DEGREE OF DOCTOR OF PHILOSOPHY IN
ELECTRONICS AND TELECOMMUNICATIONS

DOCTORATE SCHOOL IN
INFORMATION AND COMMUNICATION TECHNOLOGIES

XXV Cycle

UNIVERSITY OF MODENA AND REGGIO EMILIA

DEPARTMENT OF ENGINEERING "Enzo Ferrari"

Ph.D. DISSERTATION

Modeling and Control of Multi-phase Synchronous Motors for Automotive Application

Candidate:
Marco Fei
Advisor:
Prof. Roberto Zanasi
The Director of the School:
Prof. Giorgio M. Vitetta

DOTTORATO DI RICERCA IN
ELECTRONICS AND TELECOMMUNICATIONS

SCUOLA DI DOTTORATO IN
INFORMATION AND COMMUNICATION TECHNOLOGIES

XXV Ciclo

UNIVERSITÀ DEGLI STUDI DI MODENA E REGGIO EMILIA

DIPARTIMENTO DI INGEGNERIA "Enzo Ferrari"

TESI PER IL CONSEGUIMENTO DEL TITOLO DI DOTTORE DI RICERCA

Modellistica e Controllo di Motori Sincroni Polifase per Applicazioni Automotive

Tesi di:
Marco Fei
Relatore:
Prof. Roberto Zanasi
Il Direttore:
Prof. Giorgio M. Vitetta

to Chiara, the love of my life.

Contents

Abstract

In the last two decades the interest in electrical machines with more than three phases for variable speed applications is increased worldwide.
The fault tolerant capability of multi-phase motor drives and the possibility to enhance the motor torque by injecting an higher order of stator current harmonics, make the multi-phase synchronous machines suitable for Electric and Hybrid Electric Vehicles where reliability and power density are very important issues.
Thus, this dissertation addresses the modeling and the control of multi-phase permanent magnet synchronous motor in order to improve the efficiency and the safety of the new Electric and Hybrid Electric Vehicles. As regard these two topics the first part of this thesis deals with the multi-phase synchronous motors in healthy condition, while the second part investigates this type of motors under the open-phase fault condition.
The Power-Oriented Graphs modeling technique with a vectorial notation is exploited obtaining an approach as general as possible. All the electrical and mechanical lumped parameters of the motor (i.e. the number of phases, the type of stator connection, the shape of the rotor flux, the number of faults, etc..) can be modified without changing the structure of the models which can be directly implemented in the Matlab/Simulink environment. Starting from these models and using a vectorial approach the optimal current reference which provides the desired torque minimizing the dissipation and satisfying the limit current in healthy and fault condition is proposed. The presented controls can be used for any shape of the rotor flux, for a generic odd number of phases and in presence of one or more phase failures. The simulation results validate the effectiveness of the control techniques addressed in this dissertation.
At the end of this thesis the proposed models and controls are employed in the dynamic power control of the Toyota Hybrid System. The simulation results of the proposed hybrid vehicle set the basis for future studies on new architectures for Electric and Hybrid Electric Vehicles which exploit the advantages brought by the use of this type of motors.

Chapter 1

Introduction

1.1 Multi-phase synchronous motors

The development of modern power electronic devices and the improvement in the control techniques allow to consider the number of phases of the electrical motors as one of the design variables. Moreover, although the availability of three phase electrical motors makes them customarily adopted for variable speed applications, there are several specialized applications where the use of multi-phase machines is considerably growing such as: electrical and hybrid vehicles, aerospace applications, electrical ship propulsion, locomotive traction, high-power industrial applications. Indeed multi-phase machines offer some advantages and greater number of degrees of freedom compared to three-phase ones, see [1] and [2].
Among the main types of electrical machines (i.e. induction, switched reluctance, etc..) the permanent magnet synchronous motors combine high efficiency, high torque, high power density, robustness, reduced maintenance, compactness and low weight; then they have found wide use in powertrain application, see [3].
Due to these reasons, multi-phase permanent magnet synchronous motors are treated in this dissertation and their main advantages compared to three-phase one are resumed in Tab. 1.1. The most important advantage of this type of motors over the three-phase ones is the fault-tolerant capability of the motor drive. The major types of faults which may occur within the drive system are: winding open circuit, power device open circuit, terminal open circuit, winding inter-turn short circuit, winding terminal short circuit, power device short circuit and DC-link capacitor failure, see [4].
When a fault occurs in a conventional three-phase motor drive, the system can not continue to work properly because the fault introduces a constraint on stator currents that does not allow to control the remaining two phases. Therefore in this type of motor drive the reliability is reached increasing the redundancy of the actuator system. A first expensive solution is to double the motors and the inverters (doubling also the volume and the weight), see [5]. A second solution

Propriety	3-phase machine	multi-phase machine	
		sinusoidal bef	rectangular bef
Fault Tolerant	No	Yes	Yes
Torque ripple frequency	$6f$	$2m_s f$	$2m_s f$
Current harmonics of higher order	5 and 7	$2m_s \pm 1$	$2m_s \pm k$, $k \in \{1:2:m_s-2\}$
Power torque per phase	$P/3$	P/m_s	P/m_s
Multi harmonic injection	No	No	Yes
Multi-motor multi-phase drive	No	Yes	No

Table 1.1: Main advantages of multi-phase synchronous motors where m_s is the number of phases and f is the supply frequency.

is to modify the power converter topology such as: doubling the number of power electronic devices in a separate H-bridge inverter to drive the phases or using a fourth leg to drive the neutral of the machine, see [6] and [7].
Instead the increase of the phases number makes the multi-phase machine more reliable. Minimizing the electrical, magnetic and thermal coupling between the windings, see [4] and [8], one or more phase failures do not affect the operation of the remaining windings and the multi-phase motor can still work by using the healthy phases. Therefore, unlike the classical three-phase system, using a proper fault tolerant control the multi-phase motor continues operating safely under a phase-fault without any additional hardware connections, see [9]- [14].
Increasing the number of phases the total electrical power is split across a grater number of inverter legs, so the same power level can be achieved reducing the voltage and the current ratings of the semiconductors devices or a higher power level can be achieved without increasing the converter rating.
Moreover a higher number of phases leads to decrease the amplitude of the torque ripple and increase its frequency. As shown in Tab. 1.1, the torque ripple frequency is $2m_s$ times higher than the supply frequency f because it is due to the inverter output harmonics of order $2m_s \pm 1$. This last advantage is nowadays less important because the pulsewidth modulation enables to control the harmonic content of the output voltages.
Besides these advantages, the presence of more phases increases the number of degrees of freedom improving the overall performance of the system. A first possibility consists in the injection of higher order current harmonics for machines with concentrated winding and nearly rectangular back-emf, see [15] and [16]. In this way the torque production capability of the machine increases, leading to high torque density motor drives (i.e. it is possible to increase the torque per rms ampere for the same volume machine). This feature, together with the advantages brought by the multi-phase structure, makes these kinds of machines more suitable for high-power applications.
A second possibility is the independent control of multi-motor multi-phase drive systems for

machines with distributed windings and a sinusoidal back-emf, see [17] and [18]. Connecting in series or in parallel, with an appropriate phase transposition, a set of $(m_s - 1)/2$ m_s-phase machines it is possible to control separately each machine by a single inverter. Therefore multi-motor multi-phase drive systems may become a viable solution for all applications that require more than one variable-speed electric drive, such as in industrial manipulators or wind farms.
Despite the above benefits the cost of the multi-phase motor drive is high because both the electronic and the machines are custom products which are not available on the market. This is the main drawback of this type of motors and it is the reason why nowadays the multi-phase motor drives are restricted to specialized niche applications.

1.2 Motivation and Contribution

The automotive companies worldwide use the modeling and the simulation to develop new control strategies and/or new system architectures reducing the effort and the cost in the design and testing phases. Furthermore, the multidisciplinary nature of the automotive field requires a modular approach where the model of a complex physical system can be obtained by interconnecting the models of its subsystems (modeled with an adequate level of accuracy and completeness).
In the literature a general model of a multi-phase synchronous motor has not been provided yet (almost all published works refer to the dynamic equations of five-phase or seven-phase machines). Moreover in many papers the Finite Element methods are used to validate the proposed control although the computational heaviness of these analysis makes these proposed models difficult to use in the simulations of more complex systems.
From the above discussions, this dissertation aims to develop the models and the control of multi-phase permanent magnet synchronous motor in healthy and in faulty condition . Unlike the models proposed in the literature (e.g. [15] and [19]), the vectorial notation and the Power-Oriented Graphs technique, see [20] and [21], adopted in this thesis allow to obtain general models which can be directly implemented in Matlab/Simulink environment whatever the number of phases is. A Simulink library is provided in order to have a collection of high level model blocks suitable in a modular approach. Thanks to the graphical interface the user can modify the electrical and mechanical lumped parameters of the motor (i.e. the number of phases, the type of stator connection, the shape of the rotor flux, the number of faults, etc..) without changing the structure of the models. Moreover the simulation time is quite short also in faulty condition because the open-phase failure is simulated by an additional voltage instead of a variable resistance, as done in [22].

1.3 Outline

The first part of this thesis is focused on the modeling and control of multi-phase synchronous motors in healthy condition. Two different power invariant transformations (one real and one complex) are used to write the dynamic equations of the system in a very compact and vectorial form. Such transformations are in bijective correspondence each other and therefore they are equivalent. The respective dynamic models are obtained using the Power-Oriented Graphs modeling technique and they can be directly implemented in Matlab/Simulink environment whatever the number of phases is. In order to complete the multi-phase synchronous motor modeling and make it as general as possible, both the star and delta stator connections are addressed. The comparison between these types of connections is carried out by discussing the differences among the dynamic equations. Starting from the transformed dynamic equations and using a vectorial approach to describe the voltage and current limits, the optimal current references in healthy condition are obtained. The proposed control allows to enhance the motor torque satisfying the voltage and current limits by injecting a higher order of stator current harmonics. The Simulink implementation of the motor models and the control schemes are shown and discussed together with the simulation results.
The second part of the thesis covers the open-phase faulty condition of multi-phase synchronous motors. The proposed models simulate the failure by an additional voltage in order to impose a zero current in the open-phases, without increasing their resistance, allowing in this way a short simulation time. The failure effects on the motor torque are shown and discussed in simulation results. These models constitute the basics of the subsequent fault tolerant control; indeed a deep study on the open-phase constraint leads to extend the minimum dissipation torque control also in faulty condition. The proposed post-fault controls ensure safe motor operations by using only the remaining healthy phases without any additional hardware connection.
Finally, the advantages brought by the use of this type of motors in electric and hybrid vehicles are investigated referring to the Toyota Hybrid System. The dynamic models of the main subsystems composing the powertrain (i.e. planetary gear, engine, multi-phase motors etc..) are given using the Power-Oriented Graphs modeling technique. Then the dynamic model of the whole powertrain is obtained by interconnecting the models of these main subsystems that interact each other through their power ports. The analysis of the simulation results sets the basis for future studies on new architectures for electric and hybrid vehicles based on the multi-phase permanent magnet synchronous motor.

This thesis is organized as follows. In the **Chap.2** the POG models of the multi-phase permanent magnet synchronous motor are obtained, using two different real and complex state space transformations which are invariant with respect to the power.
The **Chap.3** contains considerations about the star and delta connected motors.

The **Chap.4** describes the vectorial control where also the current and voltage limits are taken into account. The injection of a higher order of stator current harmonics to increase the motor torque is studied in depth.
In the **Chap.5** two new models of multi-phase synchronous motor under open-phase faulty condition are carried out. These models allow to obtain a quite short simulation time because the open-phase failure is simulated by an additional voltage such that the faulty phase steady-state current is zero.
The **Chap.6** is focused on the fault tolerant control. Using the proposed post-fault control strategies the multi-phase motor continues to operate safely (generating the same desired torque without ripple) under a phase-fault without any additional hardware connection.
The **Chap.7** covers a preliminary study of the dynamic model of the power-split Toyota Hybrid System where the two three-phase electric machines, that are commonly used in THS, are replaced by two five-phase machines.
Simulation results are shown in every chapter and in the **Conclusions** the main results are summarized.

Chapter 2

Multi-phase synchronous motors

The dynamic model of three-phase synchronous machines is well known in the literature and usually the Park [23], Clarke [24] and Fortescue [25] transformations are exploited in order to write the equations of the system in a compact and suitable form. These coordinate transformations can be extended to the case of multi-phase machines, where the number of phases is greater than three. The extended Park and Clarke transformations are based on a real matrix (see [16] and [26]), the Fortescue transformation is based on a complex matrix which contains complex vectors and their complex conjugate (see [27]), while in the space vector approach (see [28]) only one half of the Fortescue matrix is considered (i.e. without the complex conjugate part). All these transformations *are not power invariant*, so after the transformations the power flows cannot be expressed as the scalar product of the transformed conjugate power variables, but always a correction coefficient must be used.
The aim of this chapter is to propose new dynamic models for the multi-phase electrical machines based on the use of real and complex state space transformations which are invariant with respect to power. The dynamic models of the motor are obtained using the Power-Oriented Graphs modeling technique. This graphical modeling technique shows the power flows within the system, allows to write the state space equations of the system in a very compact form and provides a model which can be directly implemented in Simulink whatever the number of phases is and without the need of rewriting the model when the number of phase changes.
The main contents of this chapter have been published in [29] and [30].

2.1 Electrical motors modeling

The basic structure of a multi-phase synchronous motor is shown in Fig. 2.1. In this paper we refer to a permanent magnet synchronous motor with an *odd* number m_s of concentrated windings [31]-[32] characterized by the electrical and mechanical parameters shown in Tab. 2.1. The assumption of no iron saturation and the regularity of the design (constant air-gap width

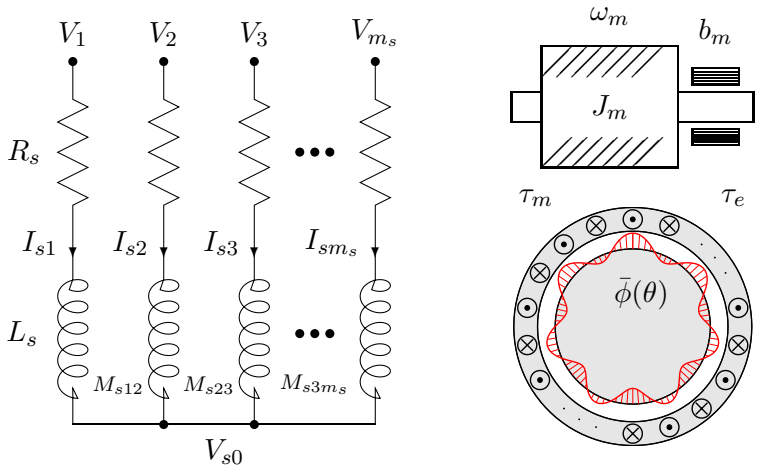

Figure 2.1: Basic structure of a multi-phase synchronous motor.

and identical windings with angular displacement) will be considered in this analysis. Using a "Lagrangian" approach, see [31]-[33], the dynamic model S_t of the considered electric motor with respect to the external fixed frame Σ_t is the following:

$$\left[\begin{array}{c|c} {}^t\mathbf{L}_s & \mathbf{0} \\ \hline \mathbf{0} & J_m \end{array}\right]\left[\begin{array}{c} {}^t\dot{\mathbf{I}}_s \\ \hline \dot{\omega}_m \end{array}\right] = -\left[\begin{array}{c|c} {}^t\mathbf{R}_s & {}^t\mathbf{K}_\tau(\theta) \\ \hline -{}^t\mathbf{K}_\tau^{\mathrm{T}}(\theta) & b_m \end{array}\right]\left[\begin{array}{c} {}^t\mathbf{I}_s \\ \hline \omega_m \end{array}\right] + \left[\begin{array}{c} {}^t\mathbf{V}_s \\ \hline -\tau_e \end{array}\right] \tag{2.1}$$

where ${}^t\mathbf{I}_s$ and ${}^t\mathbf{V}_s$ are the phase current and voltage vectors, respectively. Note that the superscript "^{t}" in (2.1) indicates that matrices and vectors are defined in the fixed reference frame Σ_t. Moreover the proposed vectorial notation, described in App. B, allows to write the matrices and the vectors of system (2.1) in a general and compact form. The resistance matrix ${}^t\mathbf{R}_s = R_s\,\mathbf{I}_{m_s}$ is diagonal and the inductance matrix ${}^t\mathbf{L}_s$ is:

$${}^t\mathbf{L}_s \;=\; L_{s0}\,\mathbf{I}_{m_s} + M_{s0}\left|\left|\left[\sum_{n=1:2}^{m_s-2} a_{Mn}\,\cos(n\,(i-h)\gamma_s)\right]_{1:m_s}^{i}\right|\right|_{1:m_s}^{h}$$

where the self inductance L_{s0} is $L_{s0} = L_s - M_{s0}$ and, according to [16], the first $m_s - 2$ odd components a_{Mn} of the mutual inductance M_{hi}, between the phases i and h, are considered. The rotor flux linkage vector is defined as:

$$\mathbf{\Phi}_c(\theta) = \varphi_c\left|\left[\bar{\phi}(\theta - h\,\gamma)\right]_{0:m-1}^{h}\right| = \varphi_c\left|\left[\sum_{n=1:2}^{\infty} a_n\cos[n(\theta - h\,\gamma_s)]\right]_{0:m-1}^{h}\right|. \tag{2.2}$$

where the parameters a_n are the coefficients of the normalized periodic rotor flux function $\bar{\phi}(\theta)$ expressed in Fourier series. According to the magnetic co-energy method, the motor torque τ_m

m_s	number of motor phases
p	number of polar expansions
N_c	number of coils for each phase
θ, θ_m	electric and rotor angular positions: $\theta = p\,\theta_m$
ω, ω_m	electric and rotor angular velocities: $\omega = p\,\omega_m$
R_s	i-th stator phase resistance
L_s	i-th stator phase self induction coefficient
M_{s0}	maximum value of mutual inductance
M_{hi}	mutual induction coefficient between the phases h and i $M_{hi} = M_{s0} \sum_{n=1:2}^{m_s-2} a_{Mn} \cos(n(h-i)\gamma_s)$
J_m	rotor moment of inertia
b_m	rotor linear friction coefficient
τ_m	electromotive torque acting on the rotor
τ_e	external load torque acting on the rotor
γ_s	basic angular displacement ($\gamma_s = 2\pi/m_s$)
$\phi_c(\theta)$	total rotor flux chained with stator phase 1
φ_r	maximum value of the rotor flux
φ_c	maximum value of function $\phi_c(\theta)$: $\varphi_c = p\,N_c\,\varphi_r$
$\bar{\phi}(\theta)$	normalized total rotor flux: $\bar{\phi}(\theta) = \dfrac{\phi_c(\theta)}{\varphi_c} = \sum_{n=1:2}^{\infty} a_i \cos(n\,\theta)$

Table 2.1: Main parameters of a multi-phase synchronous motor.

and the back-electromotive force ${}^t\mathbf{E}$ are:

$$\tau_m = {}^t\mathbf{K}_\tau\,{}^t\mathbf{I}_s\,, \quad {}^t\mathbf{E}_s = \frac{d\,{}^t\mathbf{\Phi}_c(\theta)}{dt} = \overbrace{\frac{\partial\,{}^t\mathbf{\Phi}_c(\theta)}{\partial\theta}\underbrace{\frac{\partial\theta}{\partial\theta_m}}_{p}}^{{}^t\mathbf{K}_\tau(\theta)}\underbrace{\frac{d\theta_m}{dt}}_{\omega_m} = {}^t\mathbf{K}_\tau(\theta)\,\omega_m\,. \tag{2.3}$$

where the torque vector ${}^t\mathbf{K}_\tau(\theta)$ (also known as speed normalized back electromotive force vector) is obtained as:

$${}^t\mathbf{K}_\tau(\theta) = \frac{\partial\,{}^t\mathbf{\Phi}_c(p\,\theta_m)}{\partial\theta_m} = p\,\varphi_c \left|\left[-\sum_{n=1:2}^{\infty} n\,a_n \sin\left(n(\theta - h\gamma_s)\right) \right]\right|_{0:m_s-1}^{h}. \tag{2.4}$$

The POG block scheme of the synchronous motor in the fixed reference frame Σ_t, see eq. (2.1),

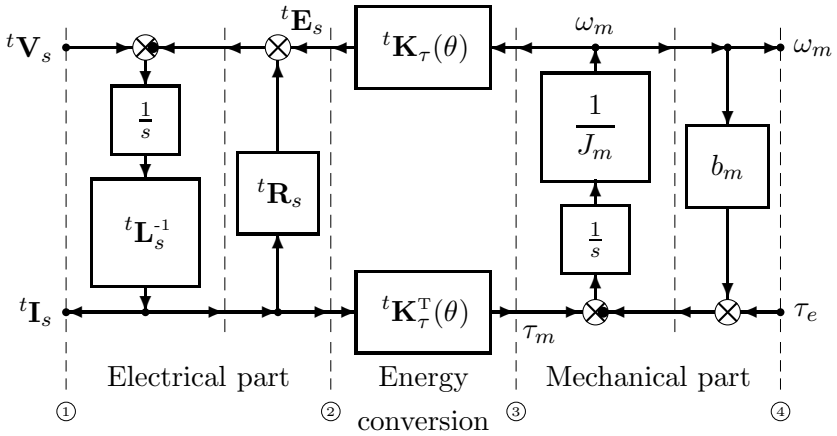

Figure 2.2: POG block scheme of the dynamic model of a multi-phase synchronous motor in the fixed reference frame Σ_t.

is shown in Fig. 2.2. The POG scheme clearly puts in evidence four different power sections. The *elaboration blocks* between the power sections ① and ② represent the *Electrical part* of the system, while the blocks between sections ③ and ④ represent the *Mechanical part* of the system. The *connection block* between sections ② and ③ represents the energy and power conversion (without accumulation nor dissipation) between the electrical and mechanical parts of the motor. Pre-multiplying system (2.1) by vector $\left[{}^t\mathbf{I}_s \,|\, \omega_m\right]$, one obtains the following relation:

$$\underbrace{\left[{}^t\mathbf{I}_s \,|\, \omega_m\right]\left[\begin{array}{c|c} {}^t\mathbf{L}_s & 0 \\ \hline 0 & J_m \end{array}\right]\left[\begin{array}{c} {}^t\dot{\mathbf{I}}_s \\ \hline \dot{\omega}_m \end{array}\right]}_{\dot{E}} = \underbrace{-\left[{}^t\mathbf{I}_s \,|\, \omega_m\right]\left[\begin{array}{c|c} {}^t\mathbf{R}_s & 0 \\ \hline 0 & b_m \end{array}\right]\left[\begin{array}{c} \mathbf{I} \\ \hline \omega_m \end{array}\right]}_{P_d} + \underbrace{\left[{}^t\mathbf{I}_s \,|\, \omega_m\right]\left[\begin{array}{c|c} 0 & -{}^t\mathbf{K}_\tau \\ \hline {}^t\mathbf{K}_\tau^{\mathrm{T}} & 0 \end{array}\right]\left[\begin{array}{c} {}^t\mathbf{I}_s \\ \hline \omega_m \end{array}\right]}_{P_r = 0} + \underbrace{\left[{}^t\mathbf{I}_s \,|\, \omega_m\right]\left[\begin{array}{c} {}^t\mathbf{V}_s \\ \hline -\tau_e \end{array}\right]}_{P_e}$$

$\dot{E}$	P_d	$P_r = 0$	P_e
Stored energy variation	Dissipating power	Redistributed power	Input/Output power

Each term of this expression has a physical meaning: term $\dot{E}$ represents the variation of energy stored within the system, term P_d represents the dissipating power, $P_r = 0$ is a null term representing the power redistributed within the system by connection block ${}^t\mathbf{K}_\tau(\theta)$ and last term P_e represents the input/output power.

2.2 State Space Transformations

In the modeling of multi-phase machines a variety of transformations has been proposed, see [15], [16], [26]-[28], [34] and [35]-[39]. A first general formulation of the possible state space transformations has been given in [36].

This section presents two different state space transformations compared with the main transformations typically used in the literature.

2.2.1 System S_ω in the rotating frame Σ_ω

The dynamic model (2.1) of the multi-phase synchronous motor can be expressed in a rotating frame Σ_ω using a state space transformation ${}^t\mathbf{I}_s = {}^t\mathbf{T}_{\underline{\omega}}\,{}^{\underline{\omega}}\mathbf{I}_s$ based on the following orthonormal matrix ${}^t\mathbf{T}_{\underline{\omega}} \in \mathbb{R}^{m_s \times m_s}$:

$$ {}^t\mathbf{T}_{\underline{\omega}} = \left[\begin{array}{cc} {}^t\mathbf{T}_\omega & \mathbf{z}_{m_s} \end{array}\right] \tag{2.5} $$

where the matrix ${}^t\mathbf{T}_\omega \in \mathbb{R}^{m_s \times (m_s-1)}$ and the homopolar vector $\mathbf{z}_{m_s} \in \mathbb{R}^{m_s}$ have the form:

$$ {}^t\mathbf{T}_\omega = \sqrt{\frac{2}{m_s}} \underset{0:m_s-1}{\overset{h}{\left\|\left[\begin{array}{c} \cos(k(h\gamma_s-\theta)) \end{array}\right.\right.}} \underset{1:2:m_s-2}{\overset{k}{\left.\left.\begin{array}{c} , \sin(k(h\gamma_s-\theta)) \end{array}\right]\right\|}} \qquad \mathbf{z}_{m_s} = \underset{0:m_s-1}{\overset{h}{\left\|\left[\begin{array}{c} \sqrt{\frac{1}{m_s}} \end{array}\right]\right\|}}. \tag{2.6} $$

Matrix ${}^t\mathbf{T}_\omega$ is a function of the electrical angle θ and transforms the system variables from the original fixed reference frame Σ_t to a rotating reference frame Σ_ω. Applying the congruent state space transformation ${}^t\mathbf{I}_s = {}^t\mathbf{T}_{\underline{\omega}}\,{}^{\underline{\omega}}\mathbf{I}_s$ to system (2.1), one obtains the following transformed system S_ω expressed in the rotating frame Σ_ω:

$$ \left[\begin{array}{c|c} {}^{\underline{\omega}}\mathbf{L}_s & \mathbf{0} \\ \hline \mathbf{0} & J_m \end{array}\right] \left[\begin{array}{c} {}^{\underline{\omega}}\dot{\mathbf{I}}_s \\ \hline \dot{\omega}_m \end{array}\right] = - \left[\begin{array}{c|c} {}^{\underline{\omega}}\mathbf{R}_s + {}^{\underline{\omega}}\mathbf{L}_s\,{}^{\underline{\omega}}\mathbf{J}_s & {}^{\underline{\omega}}\mathbf{K}_\tau(\theta) \\ \hline -{}^{\underline{\omega}}\mathbf{K}_\tau^{\mathrm{T}}(\theta) & b_m \end{array}\right] \left[\begin{array}{c} {}^{\underline{\omega}}\mathbf{I}_s \\ \hline \omega_m \end{array}\right] + \left[\begin{array}{c} {}^{\underline{\omega}}\mathbf{V}_s \\ \hline -\tau_e \end{array}\right] \tag{2.7} $$

where the terms ${}^{\underline{\omega}}\mathbf{L}_s\,{}^{\underline{\omega}}\mathbf{J}_s\,{}^{\underline{\omega}}\mathbf{I}_s$ and ${}^{\underline{\omega}}\mathbf{K}_\tau(\theta)\omega_m$ represent the back-emf voltages which are induced by the flux rotation due to the stator currents and the permanent magnets, respectively. Note that the superscript "$\underline{\omega}$" in (2.7) means that matrices and vector are defined in the rotating reference frame Σ_ω where also the last m_s-th differential equation is used. Instead when the stator phases are star-connected the superscript "$^\omega$" will be used. As shown in the Sec.3.2, the last m_s-th differential equation becomes a static equation for a star-connected motor, then the homopolar vector $\mathbf{z}_{m_s}$ can be eliminated reducing the matrices ${}^t\mathbf{T}_{\underline{\omega}}$ to the rectangular matrix ${}^t\mathbf{T}_\omega$. The dynamic models of a star-connected multi-phase synchronous motor in the rotating frame Σ_ω for $m_s = 3$ and $m_s = 5$ are shown in Fig. 2.3. The square resistance, inductance and coupling matrices ${}^{\underline{\omega}}\mathbf{R}_s$, ${}^{\underline{\omega}}\mathbf{L}_s$ and ${}^{\underline{\omega}}\mathbf{J}_s$ have the following simplified structure: ${}^{\underline{\omega}}\mathbf{R}_s = {}^t\mathbf{T}_{\underline{\omega}}^{\mathrm{T}}\,{}^t\mathbf{R}_s\,{}^t\mathbf{T}_{\underline{\omega}} = {}^t\mathbf{R}_s$,

$$ {}^{\underline{\omega}}\mathbf{L}_s = = {}^t\mathbf{T}_{\underline{\omega}}^{\mathrm{T}}\,{}^t\mathbf{L}_s\,{}^t\mathbf{T}_{\underline{\omega}} = \left[\begin{array}{cc} \underset{1:2:m_s-2}{\overset{k}{\left\|\left[\begin{array}{cc} L_{sk} & 0 \\ 0 & L_{sk} \end{array}\right]\right\|}} & \mathbf{0} \\ \mathbf{0} & L_{s0} \end{array}\right], \quad {}^{\underline{\omega}}\mathbf{J}_s = {}^t\mathbf{T}_{\underline{\omega}}^{\mathrm{T}}\,{}^t\dot{\mathbf{T}}_{\underline{\omega}} = \left[\begin{array}{cc} \underset{1:2:m_s-2}{\overset{k}{\left\|\left[\begin{array}{cc} 0 & -k\omega \\ k\omega & 0 \end{array}\right]\right\|}} & \mathbf{0} \\ \mathbf{0} & 0 \end{array}\right], $$

where $L_{sk} = L_{s0} + \frac{m_s}{2} a_{Mk} M_{s0}$ for $k \in \{3, 5, \ldots, m_s-2\}$ and $\omega = \dot{\theta}$ is the time-derivative of the electric angle θ. Since the transformed matrices have a block diagonal structure, the electrical equations of system (2.1) are decoupled. Therefore the original system S_t is divided into $(m_s-1)/2$ two-dimensional orthogonal and decoupled subspaces $\Sigma_{\omega k}$ with $k \in \{1:2:m_s-2\}$ (i.e. for

m_s	Dynamic model
3	$\left[\begin{array}{cc\|c} L_{s1} & 0 & 0 \\ 0 & L_{s1} & 0 \\ \hline 0 & 0 & J_m \end{array}\right]\left[\begin{array}{c} \dot{I}_{d1} \\ \dot{I}_{q1} \\ \hline \dot{\omega}_m \end{array}\right] = -\left[\begin{array}{cc\|c} R_s & -p\,\omega_m\,L_{s1} & 0 \\ p\,\omega_m\,L_{s1} & R_s & p\varphi_c\sqrt{\frac{3}{2}}\,a_1 \\ \hline 0 & -p\varphi_c\sqrt{\frac{3}{2}}\,a_1 & b_m \end{array}\right]\left[\begin{array}{c} I_{d1} \\ I_{q1} \\ \hline \omega_m \end{array}\right] + \left[\begin{array}{c} V_{d1} \\ V_{q1} \\ \hline -\tau_e \end{array}\right]$
5	$\left[\begin{array}{cccc\|c} L_{s1} & 0 & 0 & 0 & 0 \\ 0 & L_{s1} & 0 & 0 & 0 \\ 0 & 0 & L_{s3} & 0 & 0 \\ 0 & 0 & 0 & L_{s3} & 0 \\ \hline 0 & 0 & 0 & 0 & J_m \end{array}\right]\left[\begin{array}{c} \dot{I}_{d1} \\ \dot{I}_{q1} \\ \dot{I}_{d3} \\ \dot{I}_{q3} \\ \hline \dot{\omega}_m \end{array}\right] = -\left[\begin{array}{cccc\|c} R_s & -p\,\omega_m\,L_{s1} & 0 & 0 & 0 \\ p\,\omega_m\,L_{s1} & R_s & 0 & 0 & p\varphi_c\sqrt{\frac{5}{2}}\,a_1 \\ 0 & 0 & R_s & -3\,p\,\omega_m\,L_{s3} & 0 \\ 0 & 0 & 3\,p\,\omega_m\,L_{s3} & R_s & p\varphi_c\sqrt{\frac{5}{2}}\,3\,a_3 \\ \hline 0 & -p\varphi_c\sqrt{\frac{5}{2}}\,a_1 & 0 & -p\varphi_c\sqrt{\frac{5}{2}}\,3\,a_3 & b_m \end{array}\right]\left[\begin{array}{c} I_{d1} \\ I_{q1} \\ I_{d3} \\ I_{q3} \\ \hline \omega_m \end{array}\right] + \left[\begin{array}{c} V_{d1} \\ V_{q1} \\ V_{d3} \\ V_{q3} \\ \hline -\tau_e \end{array}\right]$

Figure 2.3: Dynamic models of a star-connected multi-phase synchronous motor in the rotating reference frame Σ_ω for $m_s = 3$ and $m_s = 5$.

$m_s = 5$ there are two subspaces $\Sigma_{\omega 1}$ and $\Sigma_{\omega 3}$, see Fig. 2.3). The transformed current and voltage vectors ${}^{\underline{\omega}}\mathbf{I}_s$ and ${}^{\underline{\omega}}\mathbf{V}_s$ in (2.7) are:

$$ {}^{\underline{\omega}}\mathbf{I}_s = {}^{t}\mathbf{T}_{\underline{\omega}}^{\mathrm{T}}\,{}^{t}\mathbf{I}_s = \left[\begin{array}{c} \overset{k}{\left\|\begin{bmatrix} {}^{\omega}I_{dk} \\ {}^{\omega}I_{qk} \end{bmatrix}\right\|} \\ {}_{1:2:m_s-2} \\ {}^{\omega}I_{sm_s} \end{array}\right], \qquad {}^{\underline{\omega}}\mathbf{V}_s = {}^{t}\mathbf{T}_{\underline{\omega}}^{\mathrm{T}}\,{}^{t}\mathbf{V}_s = \left[\begin{array}{c} \overset{k}{\left\|\begin{bmatrix} {}^{\omega}V_{dk} \\ {}^{\omega}V_{qk} \end{bmatrix}\right\|} \\ {}_{1:2:m_s-2} \\ {}^{\omega}V_{sm_s} \end{array}\right] \tag{2.8} $$

where I_{dk}, I_{qk}, V_{dk} and V_{qk} are, respectively, the *direct* and *quadrature* components of the current and voltage vectors ${}^{\underline{\omega}}\mathbf{I}_s$ and ${}^{\underline{\omega}}\mathbf{V}_s$ in the rotating reference frame Σ_ω. The last components ${}^{\omega}I_{sm_s} = \mathbf{z}_{m_s}^{\mathrm{T}}\,{}^{t}\mathbf{I}_s$ and ${}^{\omega}V_{sm_s} = \mathbf{z}_{m_s}^{\mathrm{T}}\,{}^{t}\mathbf{V}_s$ of vectors ${}^{\underline{\omega}}\mathbf{I}_s$ and ${}^{\underline{\omega}}\mathbf{V}_s$ are proportional to the sum of the m_s stator currents I_{sh} and the m_s stator voltages V_{sh}, respectively:

$$ {}^{\omega}I_{sm_s} = \sqrt{\frac{1}{m_s}}\sum_{h=1}^{m_s} I_{sh}, \qquad {}^{\omega}V_{sm_s} = \sqrt{\frac{1}{m_s}}\sum_{h=1}^{m_s} V_{sh}. \tag{2.9} $$

Note that ${}^{\omega}I_{sm_s} = 0$ when the stator phases are star-connected and ${}^{\omega}V_{sm_s} = 0$ when the input stator voltages are balanced. The transformed torque vector ${}^{\underline{\omega}}\mathbf{K}_\tau(\theta)$ in the rotating frame Σ_ω

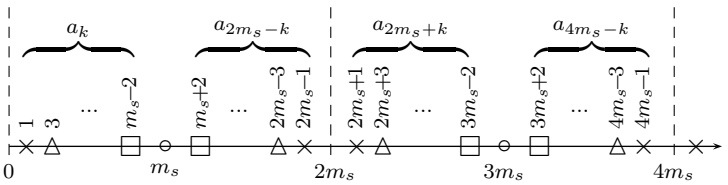

Figure 2.4: Harmonic characterization of the torque vector ${}^{\omega}\mathbf{K}_{\tau}$: $\times \leftrightarrow k=1$, $\triangle \leftrightarrow k=3$, $\square \leftrightarrow k=m_s-2$, $\circ \leftrightarrow k=m_s$.

has the following form (see [31]):

$$\underline{{}^{\omega}}\mathbf{K}_{\tau}(\theta) = {}^{t}\mathbf{T}^{\mathrm{T}}_{\underline{\omega}}\,{}^{t}\mathbf{K}_{\tau} = \begin{bmatrix} \Big\|_{1:2:m_s-2}^{k} \begin{bmatrix} {}^{\omega}K_{dk} \\ {}^{\omega}K_{qk} \end{bmatrix} \Big\| \\ {}^{\omega}K_{\tau m_s} \end{bmatrix} = p\varphi_c\sqrt{\frac{m_s}{2}} \begin{bmatrix} \Big\|_{1:2:m_s-2}^{k} \begin{bmatrix} \sum_{n=0:2m_s}^{\infty} -\left[(n+k)\,a_{n+k}+(n-k)\,a_{n-k}\right]\sin(n\theta) \\ \sum_{n=0:2m_s}^{\infty} \left[(n+k)\,a_{n+k}-(n-k)\,a_{n-k}\right]\cos(n\theta) \end{bmatrix} \Big\| \\ -\sqrt{2}\sum_{n=m_s:2m_s}^{\infty} n a_n \sin(n\theta) \end{bmatrix}. \tag{2.10}$$

This expression is function of the coefficients a_n of the rotor flux Fourier series, so it is suitable for any shape of the normalized rotor flux $\bar{\phi}(\theta)$ shown in Tab 2.1. The harmonic characterization of the torque components is shown in Fig. 2.4: the *direct* and *quadrature* components, ${}^{\omega}K_{dk}$ and ${}^{\omega}K_{qk}$ with $k \in \{1:2:m_s-2\}$, depend only on the coefficients a_n of order $n = 2m_s h \pm k$ where $h = 0, 1, 2..$, while the last component ${}^{\omega}K_{\tau m_s}$ depends only on the coefficients a_n of order $n = hm_s$ with odd h. When the normalized rotor flux $\bar{\phi}(\theta)$ is characterized by the first odd m_s-2 harmonics:

$$\bar{\phi}(\theta) = \sum_{i=1:2}^{m_s-2} a_i \cos(i\,\theta)\,. \tag{2.11}$$

the transformed torque vector $\underline{{}^{\omega}}\mathbf{K}_{\tau}$ is constant (not function of the electric angle θ), see [32] and [33]:

$$\underline{{}^{\omega}}\mathbf{K}_{\tau}(\theta) = \underline{{}^{\omega}}\mathbf{K}_{\tau} = p\,\varphi_c\,\sqrt{\frac{m_s}{2}} \begin{bmatrix} \Big\|_{1:2:m_s-2}^{k} \begin{bmatrix} 0 \\ k a_k \end{bmatrix} \Big\| \\ 0 \end{bmatrix}. \tag{2.12}$$

and each *quadrature* component ${}^{\omega}K_{qk}$ is defined by the coefficient a_n of the same order k. In this case the motor torque $\tau_m = \underline{{}^{\omega}}\mathbf{K}^{\mathrm{T}}_{\tau}\,\underline{{}^{\omega}}\mathbf{I}_s$ depends only on the *quadrature* components ${}^{\omega}I_{qk}$ of the current vector $\underline{{}^{\omega}}\mathbf{I}_s$ and it is possible to generate a constant torque, in all the other cases an

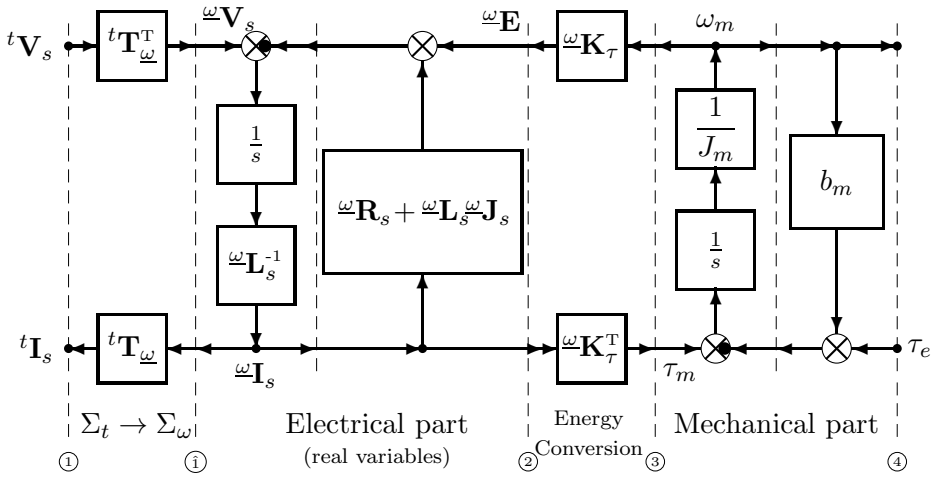

Figure 2.5: POG block scheme of the dynamic model of a multi-phase synchronous motor in the rotating frame Σ_ω.

undesired torque ripple is always present. Note that (2.12) holds for a generic number of phases m_s, while usually in the literature only some particular cases for the torque vector $^{\underline{\omega}}\mathbf{K}_\tau$ can be found, see for example [16] and [37].

The POG scheme of the multi-phase synchronous motor in rotating frame Σ_ω, see (2.7), is shown in Fig. 2.5. The *connection block* between sections ① and ⓘ represents the state space transformation $^t\mathbf{T}_{\underline{\omega}}$ between the fixed reference frame Σ_t and the rotating reference frame Σ_ω. Summarizing, the presented congruent state space transformation $^t\mathbf{I}_s = {}^t\mathbf{T}_{\underline{\omega}}{}^{\underline{\omega}}\mathbf{I}_s$ splits the original system S_t into $(m_s-1)/2$ two-dimensional orthogonal and decoupled subspaces $\Sigma_{\omega k}$ with $k \in \{1:2:m_s-2\}$ characterized by a specific set of the rotor flux harmonics, see Tab. 2.2. Then the m_s-phase motor can be seen as a set of $(m_s-1)/2$ independent electrical machines, rotating at different velocity $k\omega_m$ and characterized by the k-th coefficient of the rotor flux. The equivalence of a m-phase wye-connected machine to a set of $(m-1)/2$ fictitious independent two-phase machines is also shown in [15] and this concept is used in [16] in the case of five-phase

	Set of harmonics		
Subspaces	$m_s = 3$	$m_s = 5$	$m_s = 7$
$\Sigma_{\omega 1}$	$\mathbf{1}, 5, 7, \cdots, 6h \pm 1$	$\mathbf{1}, 9, 11, \cdots, 10h \pm 1$	$\mathbf{1}, 13, 15, \cdots, 14h \pm 1$
$\Sigma_{\omega 3}$	na	$\mathbf{3}, 7, 13, \cdots, 10h \pm 3$	$\mathbf{3}, 11, 17, \cdots, 14h \pm 3$
$\Sigma_{\omega 5}$	na	na	$\mathbf{5}, 9, 19, \cdots, 14h \pm 5$

Table 2.2: Subspaces Harmonic characterization for star-connected 3-phase, 5-phase and 7-phase motors.

machine. Particularly in [16] a pseudo orthogonal transformation is introduced to simplify the model of a five-phase machine and the original five-dimensional space is mapped into two two-dimensional orthogonal subspaces.

It can be easily proved that the congruent transformation ${}^{t}\mathbf{T}_{\underline{\omega}}$ is *power-invariant*, indeed the power $p(t) = {}^{t}\mathbf{V}_s^T\,{}^{t}\mathbf{I}_s$ in section ① is equal to the power $s(t) = {}^{\underline{\omega}}\mathbf{V}_s^T\,{}^{\underline{\omega}}\mathbf{I}_s$ in section ①̂:

$$p(t) \;=\; {}^{t}\mathbf{V}_s^T\,{}^{t}\mathbf{I}_s \;=\; {}^{\underline{\omega}}\mathbf{V}_s^T\,{}^{t}\mathbf{T}_{\underline{\omega}}^T\,{}^{t}\mathbf{T}_{\underline{\omega}}\,{}^{\underline{\omega}}\mathbf{I}_s = {}^{\underline{\omega}}\mathbf{V}_s^T\,{}^{\underline{\omega}}\mathbf{I}_s \;=\; s(t).$$

Comparison with Park and Clarke transformations

The transformation ${}^{t}\mathbf{T}_{\underline{\omega}}$ is similar to the *Park transformation* typically used in the literature and also known as $dq0$ transformation, see [27]. The generalized Park transformation is based on the following matrix ${}^{\underline{\omega}}\mathbf{P}_t$:

$${}^{\underline{\omega}}\mathbf{P}_t = {}^{t}\mathbf{P}_{\underline{\omega}}^{-1} = \frac{2}{m_s}\begin{bmatrix} k & & & h \\ \left\|\begin{bmatrix}\cos(k(h\gamma_s-\theta))\\ \sin(k(h\gamma_s-\theta))\end{bmatrix}\right\| & & & \\ 1{:}2{:}m_s-2 & & & 0{:}m_s-1 \\ & & h & \\ & & [\![\; c \;]\!] & \\ & & 0{:}m_s-1 & \end{bmatrix} = \frac{2}{5}\left[\begin{array}{ccccc} \cos(-\theta) & \cos(\gamma_s-\theta) & \cos(2\gamma_s-\theta) & \cos(3\gamma_s-\theta) & \cos(4\gamma_s-\theta) \\ \sin(-\theta) & \sin(\gamma_s-\theta) & \sin(2\gamma_s-\theta) & \sin(3\gamma_s-\theta) & \sin(4\gamma_s-\theta) \\ \cos(-3\theta) & \cos(3\gamma_s-3\theta) & \cos(6\gamma_s-3\theta) & \cos(9\gamma_s-3\theta) & \cos(12\gamma_s-3\theta) \\ \underline{\sin(-3\theta)} & \underline{\sin(3\gamma_s-3\theta)} & \underline{\sin(6\gamma_s-3\theta)} & \underline{\sin(9\gamma_s-3\theta)} & \underline{\sin(12\gamma_s-3\theta)} \\ c & c & c & c & c \end{array}\right]_{m_s=5}$$

where c is a constant: $c = \frac{1}{\sqrt{2}}$ in [16] and $c = \frac{1}{2}$ in [37]. The Clarke transformation ${}^{\underline{\omega}}\mathbf{C}_t$ (see [24] and [27]) can be obtained as a particular case from the Park transformation putting $\theta = 0$. Applying the Park similarity transformation ${}^{P}\mathbf{I}_s = {}^{t}\mathbf{P}_{\underline{\omega}}^{-1}\,{}^{t}\mathbf{I}_s$ to system (2.1), one obtains an equivalent transformed system expressed in a rotating reference frame.

Matrices ${}^{t}\mathbf{P}_{\underline{\omega}}$ and ${}^{t}\mathbf{T}_{\underline{\omega}}$ are related by the following relations:

$${}^{t}\mathbf{P}_{\underline{\omega}}^{-1} = \mathbf{A}\,{}^{t}\mathbf{T}_{\underline{\omega}}^{\mathrm{T}}, \quad {}^{t}\mathbf{P}_{\underline{\omega}} = \mathbf{A}^{-1}\,{}^{t}\mathbf{T}_{\underline{\omega}}\;, \;\text{ with } \mathbf{A} = \sqrt{\frac{2}{m_s}}\begin{bmatrix}\mathbf{I}_{m_s-1} & \mathbf{0} \\ \mathbf{0} & \frac{1}{\sqrt{2}c}\end{bmatrix} \tag{2.13}$$

where the conversion matrix $\mathbf{A}$ is needed to adjust the power. Indeed one can verify that the Park similarity transformation *is not power-invariant* because the instantaneous powers $p(t) = {}^{t}\mathbf{V}_s^{\mathrm{T}}{}^{t}\mathbf{I}_s$ and $s(t) = {}^{P}\mathbf{V}_s^{\mathrm{T}}{}^{P}\mathbf{I}_s$ are related as follows:

$$p(t) \;=\; (\mathbf{A}^{-1})^2 s(t) \;=\; \frac{m_s}{2}\,{}^{P}\mathbf{V}_s^{\mathrm{T}}\,{}^{P}\mathbf{I}_s - \Big(\frac{m_s}{2} - \frac{m_s}{4\,c^2}\Big)\,{}^{P}V_0\,{}^{P}I_0$$

where ${}^{P}V_0$ and ${}^{P}I_0$ are the last components of the voltage and current vectors ${}^{P}\mathbf{V}_s$ and ${}^{P}\mathbf{I}_s$, respectively. In case of star-connected phases the last column of matrix ${}^{t}\mathbf{P}_{\underline{\omega}}^{-1}$ can be eliminated, so the relation between the matrices ${}^{t}\mathbf{P}_{\omega}$, ${}^{t}\mathbf{T}_{\omega}$ and the instantaneous powers $p(t)$ and $s(t)$ can be rewritten as:

$${}^{t}\mathbf{P}_{\omega}^{-1} = \sqrt{\frac{2}{m_s}}\,{}^{t}\mathbf{T}_{\omega}^{\mathrm{T}}, \qquad {}^{t}\mathbf{P}_{\omega} = \sqrt{\frac{m_s}{2}}\,{}^{t}\mathbf{T}_{\omega}, \qquad p(t) = \frac{m_s}{2}s(t). \tag{2.14}$$

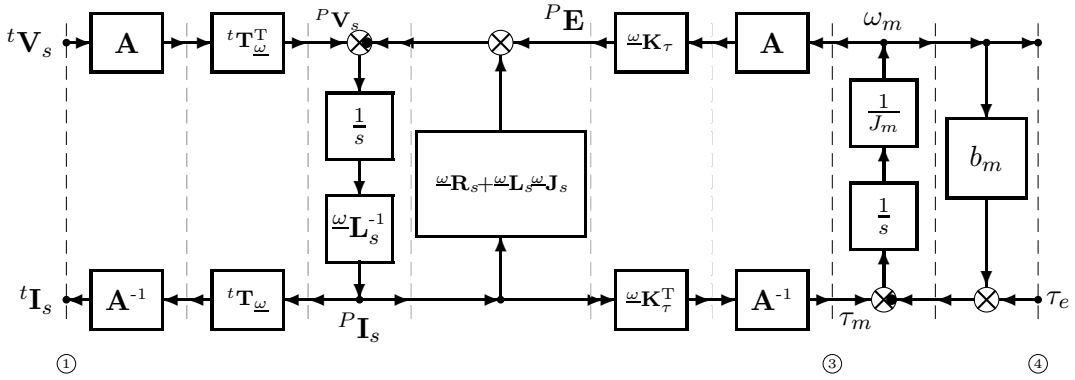

Figure 2.6: POG-like scheme of a multi-phase synchronous motor in the Park rotating reference frame.

Fig. 2.6 shows a "POG-like" scheme of the electrical motor obtained with the Park transformation. Note that this scheme is similar to the POG scheme of Fig. 2.5 but the part between power sections ① and ③ does not keep the meaning of power because the Park similarity transformation *is not power-invariant*. The main disadvantage of using this transformation is that a particular conversion matrix $\mathbf{A}$ and its inverse $\mathbf{A}^{-1}$ are needed. On the contrary considering a power invariant transformation the meaning of power is kept even in the transformed system. The block scheme of Fig. 2.6 is equivalent to the block scheme of Fig. 2.7 typically used in the literature (see [15]) where the $(m_s-1)/2$ fictitious machines are kept separated and $\mathbf{R}(\theta)$ is the rotation matrix.

The scheme given in Fig. 2.7 needs to be rearranged when the number of phases m_s changes while with the POG vectorial approach a unique general model is used whatever the number of phases m_s is. Moreover the system S_ω in Fig. 2.5 is obtained using a congruent transformation which uses the transpose of the transformation matrix ($^t\mathbf{T}_{\underline{\omega}}^{\mathrm{T}}$) while the system in Fig. 2.7 is obtained using a similarity transformation which uses the inverse of the transformation matrix ($^t\mathbf{C}_{\underline{\omega}}^{\text{-1}}$). The main features of the two transformations are summarized in the following Table: A very important advantage of exploiting the POG technique with vectorial notation is that the POG scheme of Fig. 2.5 can be directly implemented in Simulink without the need to consider separate fictitious machines. Moreover from the vectorial notation a better control can be

Transf.	Power invariant	Dynamic equations	Fictitious machines	Variables	Vectorial notation
$^t\mathbf{T}_{\underline{\omega}}$	Yes	general m_s	$\frac{m_s+1}{2}$	real	Yes
$^t\mathbf{P}_{\underline{\omega}}$	No	fixed m_s	$\frac{m_s+1}{2}$	real	No

Table 2.3: Resume table of the difference between the proposed and the Park transformations: $^t\mathbf{T}_{\underline{\omega}}$ and $^t\mathbf{P}_{\underline{\omega}}$, respectively.

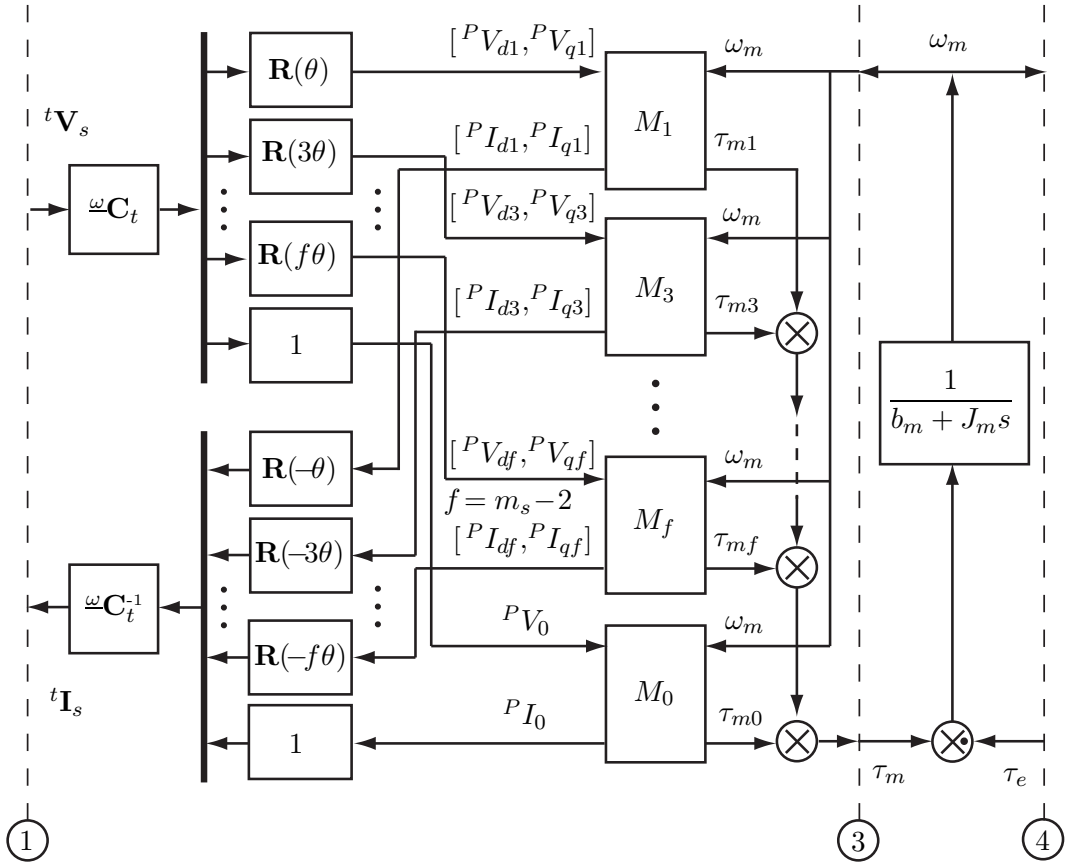

Figure 2.7: Block scheme of a m_s-phase motor in the Park rotating reference frame.

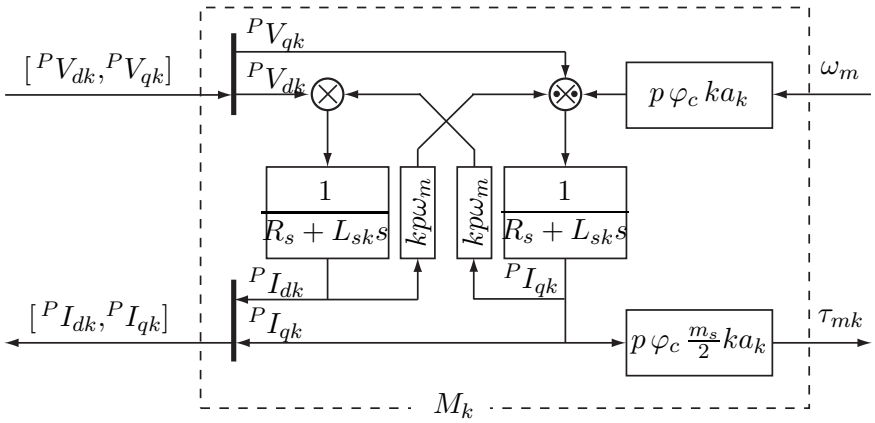

Figure 2.8: Block scheme of the k-th machine M_k in Park rotating frame for $k \in \{1:2:m_s-2\}$.

implemented, as it will be shown in Section 2.3.

2.2.2 System $\overline{S}_\omega$ in the reduced complex rotating frame $\overline{\Sigma}_\omega$

A complex and reduced model of the multi-phase synchronous motor expressed in a complex rotating reference frame $\overline{\Sigma}_\omega$ can be obtained using a state space pseudo-transformation ${}^t\mathbf{I}_s = \mathfrak{Re}\big({}^t\overline{\mathbf{T}}_{\underline{\omega}N}{}^{\underline{\omega}}\overline{\mathbf{I}}_s\big)$ based on the following complex rectangular matrix ${}^t\overline{\mathbf{T}}_{\underline{\omega}N} \in \mathbb{C}^{\,m_s \times \frac{m_s+1}{2}}$:

$$ {}^t\overline{\mathbf{T}}_{\underline{\omega}N} = {}^t\overline{\mathbf{T}}_{\underline{\omega}}\,\mathbf{N} = \left[\begin{array}{cc} {}^t\overline{\mathbf{T}}_{\omega} & \mathbf{z}_{m_s} \end{array}\right]\mathbf{N} \tag{2.15} $$

where:

$$ {}^t\overline{\mathbf{T}}_{\omega} = \sqrt{\frac{1}{m_s}} \underset{0:m_s-1}{\overset{h}{\Big\|\Big[}} e^{jk(\theta - h\gamma_s)} \underset{1:2:m_s-2}{\overset{k}{\Big]\Big\|}}, \qquad \mathbf{z}_{m_s} = \underset{0:m_s-1}{\overset{h}{\Big\|\Big[}} \sqrt{\tfrac{1}{m_s}} \Big]\Big\|, \qquad \mathbf{N} = \left[\begin{array}{cc} \sqrt{2}\,\mathbf{I}_{\frac{m_s-1}{2}} & \mathbf{0} \\ \mathbf{0} & 1 \end{array}\right]. $$

Applying the pseudo-transformation ${}^t\mathbf{I}_s = \mathfrak{Re}\big({}^t\overline{\mathbf{T}}_{\underline{\omega}N}{}^{\underline{\omega}}\overline{\mathbf{I}}_s\big)$ to system (2.1), one obtains the following transformed system $\overline{S}_\omega$ expressed in the complex and reduced rotating frame $\overline{\Sigma}_\omega$:

$$ \left[\begin{array}{c|c} {}^{\underline{\omega}}\overline{\mathbf{L}}_s & \mathbf{0} \\ \hline \mathbf{0} & J_m \end{array}\right]\left[\begin{array}{c} {}^{\underline{\omega}}\dot{\overline{\mathbf{I}}}_s \\ \hline \dot{\omega}_m \end{array}\right] = -\left[\begin{array}{c|c} {}^{\underline{\omega}}\overline{\mathbf{R}}_s + {}^{\underline{\omega}}\overline{\mathbf{L}}_s\,{}^{\underline{\omega}}\overline{\mathbf{J}}_s & {}^{\underline{\omega}}\overline{\mathbf{K}}_{\tau N} \\ \hline -{}^{\underline{\omega}}\overline{\mathbf{K}}^*_{\tau N} & b_m \end{array}\right]\left[\begin{array}{c} {}^{\underline{\omega}}\overline{\mathbf{I}}_s \\ \hline \omega_m \end{array}\right] + \left[\begin{array}{c} {}^{\underline{\omega}}\overline{\mathbf{V}}_s \\ \hline -\tau_e \end{array}\right] \tag{2.16} $$

The dynamic models of a star-connected multi-phase synchronous motor in the reduced complex rotating frame $\overline{\Sigma}_\omega$ for $m_s = 3$ and $m_s = 5$ are shown in Fig. 2.9. The mathematical calculations about the transformed matrices and vectors are reported in App.C.2.
The resistance, coupling and inductance matrices ${}^{\underline{\omega}}\overline{\mathbf{R}}_s$, ${}^{\underline{\omega}}\overline{\mathbf{J}}_s$ and ${}^{\underline{\omega}}\overline{\mathbf{L}}_s$ have a diagonal structure and they are obtained using matrix ${}^t\overline{\mathbf{T}}_{\underline{\omega}}$ as follows: ${}^{\underline{\omega}}\overline{\mathbf{R}}_s = {}^t\overline{\mathbf{T}}^*_{\underline{\omega}}\,{}^t\mathbf{R}_s\,{}^t\overline{\mathbf{T}}_{\underline{\omega}} = R_s\mathbf{I}_{\frac{m_s+1}{2}}$,

$$ {}^{\underline{\omega}}\overline{\mathbf{J}}_s = {}^t\overline{\mathbf{T}}^*_{\underline{\omega}}\,{}^t\dot{\overline{\mathbf{T}}}_{\underline{\omega}} = \begin{bmatrix} {}^{\omega}\overline{\mathbf{J}}_s & \mathbf{0} \\ \mathbf{0} & 0 \end{bmatrix} = \begin{bmatrix} \overset{k}{\Big\|\Big[}\, j\,kp\,\omega_m \,\underset{1:2:m_s-2}{\Big]\Big\|} & \mathbf{0} \\ \mathbf{0} & 0 \end{bmatrix}, \tag{2.17} $$

$$ {}^{\underline{\omega}}\overline{\mathbf{L}}_s = {}^t\overline{\mathbf{T}}^*_{\underline{\omega}}\,{}^t\mathbf{L}_s\,{}^t\overline{\mathbf{T}}_{\underline{\omega}} = \begin{bmatrix} {}^{\omega}\overline{\mathbf{L}}_s & \mathbf{0} \\ \mathbf{0} & L_{s0} \end{bmatrix} = \begin{bmatrix} \overset{k}{\Big\|\Big[}\, L_{sk} \,\underset{1:2:m_s-2}{\Big]\Big\|} & \mathbf{0} \\ \mathbf{0} & L_{s0} \end{bmatrix}. \tag{2.18} $$

Note that the transformed matrices in the system (2.16) have dimension $(m_s+1)/2$, while they have dimension m_s in the system (2.7). Moreover the diagonal structure of these transformed matrices allows to divide the original system S_t into $(m_s-1)/2$ complex orthogonal and decoupled subspaces $\overline{\Sigma}_{\omega k}$ with $k \in \{1:2:m_s-2\}$ (i.e. for $m_s = 5$ there are two complex subspaces $\overline{\Sigma}_{\omega 1}$ and $\overline{\Sigma}_{\omega 3}$, see Fig. 2.9).

The transformed current, voltage and torque vectors ${}^{\underline{\omega}}\overline{\mathbf{I}}_s$, ${}^{\underline{\omega}}\overline{\mathbf{V}}_s$ and ${}^{\underline{\omega}}\overline{\mathbf{K}}_{\tau N}$ are obtained using matrix ${}^{t}\overline{\mathbf{T}}_{\underline{\omega} N}$ as follows:

$$
{}^{\underline{\omega}}\overline{\mathbf{I}}_s = {}^{t}\overline{\mathbf{T}}^{*}_{\underline{\omega} N}\,{}^{t}\mathbf{I}_s = \begin{bmatrix} {}^{\omega}\overline{\mathbf{I}}_s \\ {}^{\omega}I_{sm_s} \end{bmatrix} = \begin{bmatrix} \overset{k}{\underset{1:2:m_s-2}{\Big\|\Big[\,\overline{I}_{sk}\,\Big]\Big\|}} \\ {}^{\omega}I_{sm_s} \end{bmatrix} = \sqrt{\frac{2}{m_s}} \begin{bmatrix} \overset{k}{\underset{1:2:m_s-2}{\Big\|\Big[\, e^{-j\,k\,\theta} \sum_{h=1}^{m_s} I_{sh} e^{j\,k\,(h-1)\gamma_s} \,\Big]\Big\|}} \\ \dfrac{1}{\sqrt{2}} \sum_{h=1}^{m_s} I_{sh} \end{bmatrix}, \tag{2.19}
$$

$$
{}^{\underline{\omega}}\overline{\mathbf{V}}_s = {}^{t}\overline{\mathbf{T}}^{*}_{\underline{\omega} N}\,{}^{t}\mathbf{V}_s = \begin{bmatrix} {}^{\omega}\overline{\mathbf{V}}_s \\ {}^{\omega}V_{sm_s} \end{bmatrix} = \begin{bmatrix} \overset{k}{\underset{1:2:m_s-2}{\Big\|\Big[\,\overline{V}_{sk}\,\Big]\Big\|}} \\ {}^{\omega}V_{sm_s} \end{bmatrix} = \sqrt{\frac{2}{m_s}} \begin{bmatrix} \overset{k}{\underset{1:2:m_s-2}{\Big\|\Big[\, e^{-j\,k\,\theta} \sum_{h=1}^{m_s} V_{sh} e^{j\,k\,(h-1)\gamma_s} \,\Big]\Big\|}} \\ \dfrac{1}{\sqrt{2}} \sum_{h=1}^{m_s} V_{sh} \end{bmatrix}, \tag{2.20}
$$

$$
{}^{\underline{\omega}}\overline{\mathbf{K}}_{\tau N} = {}^{t}\overline{\mathbf{T}}^{*}_{\underline{\omega} N}\,{}^{t}\mathbf{K}_{\tau} = \begin{bmatrix} {}^{\omega}\overline{\mathbf{K}}_{\tau} \\ {}^{\omega}\overline{K}_{\tau m_s} \end{bmatrix} = jp\varphi_c \sqrt{\frac{m_s}{2}} \begin{bmatrix} \overset{k}{\underset{1:2:m_s-2}{\Big\|\Big[\, \sum_{n=0:2\,m_s}^{\infty} (n+k)\, a_{n+k}\, e^{j\theta n} - (n-k)\, a_{n-k}\, e^{-j\theta n} \,\Big]\Big\|}} \\ \dfrac{1}{\sqrt{2}} \sum_{n=m_s:2m_s}^{\infty} n a_n (e^{jn\theta} - e^{-jn\theta}) \end{bmatrix}. \tag{2.21}
$$

The last components ${}^{\omega}I_{sm_s}$ and ${}^{\omega}V_{sm_s}$ of vectors ${}^{\underline{\omega}}\overline{\mathbf{I}}_s$ and ${}^{\underline{\omega}}\overline{\mathbf{V}}_s$ are real and proportional to the sum of the m_s stator voltages and currents, respectively as shown in (2.9).
The expression of the torque vector ${}^{\underline{\omega}}\mathbf{K}_{\tau N}$ is still function of the coefficients a_n of the rotor flux Fourier series and therefore it is suitable for any shape of the normalized rotor flux $\bar{\phi}(\theta)$ shown in Tab 2.1. Each component $\overline{K}_{\tau k}$, with $k \in [1:2:m_s-2]$, depends only on the coefficients a_n of order $n = 2m_s h \pm k$, where $h = 0, 1, 2..$, see Fig. 2.4. While the last component ${}^{\omega}\overline{K}_{\tau m_s}$ depends only on the coefficients a_n of order $n = hm_s$ with odd h. When the rotor flux function $\bar{\phi}(\theta)$ has the structure defined in (2.11) the torque vector ${}^{\underline{\omega}}\overline{\mathbf{K}}_{\tau N}$ has a complex and constant form:

$$
{}^{\underline{\omega}}\overline{\mathbf{K}}_{\tau N}(\theta) = {}^{\underline{\omega}}\overline{\mathbf{K}}_{\tau N} = jp\varphi_c \sqrt{\frac{m_s}{2}} \begin{bmatrix} \overset{k}{\underset{1:2:m_s-2}{\big[\!\big[\, k a_k \,\big]\!\big]}} \\ 0 \end{bmatrix}. \tag{2.22}
$$

The POG scheme corresponding to the dynamic system $\overline{S}_{\omega}$ given in (2.16) is shown in Fig. 2.10. The *connection blocks* between the power sections ① -ⓘ and ② -③ take into account the function $\mathfrak{Re}(\cdot)$ which is is used to convert the transformed complex vector ${}^{\underline{\omega}}\overline{\mathbf{I}}_s$ to real vector ${}^{t}\mathbf{I}_s$:

$$
{}^{t}\mathbf{I}_s = \mathfrak{Re}\left({}^{t}\overline{\mathbf{T}}_{\underline{\omega} N}\,{}^{\underline{\omega}}\overline{\mathbf{I}}_s\right) = \mathfrak{Re}\left({}^{t}\overline{\mathbf{T}}_{\underline{\omega}}\,\mathbf{N}\,{}^{\underline{\omega}}\overline{\mathbf{I}}_s\right)
$$

m_s	Dynamic model
3	$\left[\begin{array}{c\|c} L_{s1} & 0 \\ \hline 0 & J_m \end{array}\right]\left[\begin{array}{c} {}^{\omega}\dot{\overline{I}}_{s1} \\ \hline \dot{\omega}_m \end{array}\right] = -\left[\begin{array}{c\|c} R_s + jp\,\omega_m\,L_{s1} & jp\varphi_c\sqrt{\frac{3}{2}}\,a_1 \\ \hline -\,jp\varphi_c\sqrt{\frac{3}{2}}\,a_1 & b_m \end{array}\right]\left[\begin{array}{c} {}^{\omega}\overline{I}_{s1} \\ \hline \omega_m \end{array}\right] + \left[\begin{array}{c} {}^{\omega}\overline{V}_{s1} \\ \hline -\,\tau_e \end{array}\right]$
5	$\left[\begin{array}{cc\|c} L_{s1} & 0 & 0 \\ 0 & L_{s3} & 0 \\ \hline 0 & 0 & J_m \end{array}\right]\left[\begin{array}{c} {}^{\omega}\dot{\overline{I}}_{s1} \\ {}^{\omega}\dot{\overline{I}}_{s3} \\ \hline \dot{\omega}_m \end{array}\right] = -\left[\begin{array}{cc\|c} R_s + jp\,\omega_m\,L_{s1} & 0 & jp\varphi_c\sqrt{\frac{5}{2}}\,a_1 \\ 0 & R_s + j\,3\,p\,\omega_m\,L_{s3} & jp\varphi_c\sqrt{\frac{5}{2}}\,3\,a_3 \\ \hline -\,jp\varphi_c\sqrt{\frac{5}{2}}\,a_1 & -jp\varphi_c\sqrt{\frac{5}{2}}\,3\,a_3 & b_m \end{array}\right]\left[\begin{array}{c} {}^{\omega}\overline{I}_{s1} \\ {}^{\omega}\overline{I}_{s3} \\ \hline \omega_m \end{array}\right] + \left[\begin{array}{c} {}^{\omega}\overline{V}_{s1} \\ {}^{\omega}\overline{V}_{s3} \\ \hline -\,\tau_e \end{array}\right]$

Figure 2.9: Dynamic models of a star-connected multi-phase synchronous motor in the reduced complex rotating frame $\overline{\Sigma}_\omega$ for $m_s = 3$ and $m_s = 5$.

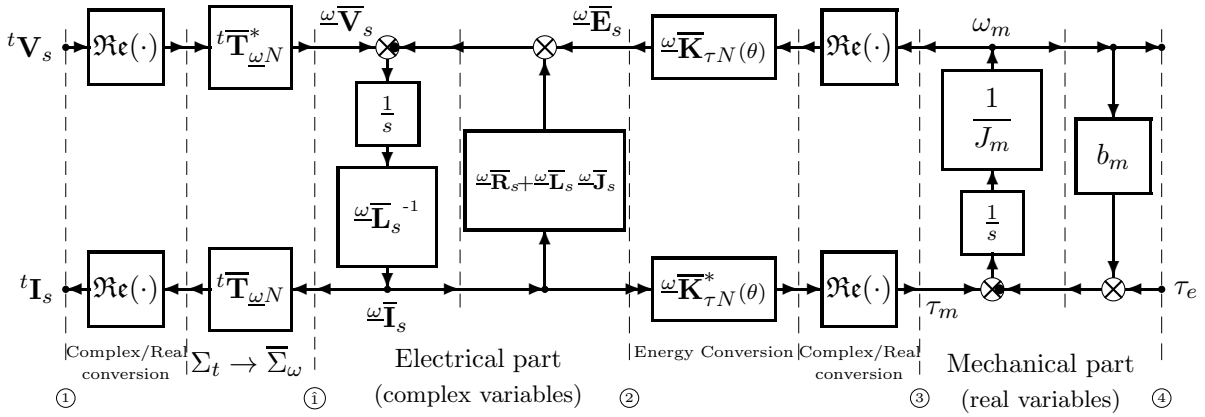

Figure 2.10: POG block scheme of the dynamic model of a multi-phase synchronous motor in the reduced complex rotating frame $\overline{\Sigma}_\omega$.

and to real motor torque τ_m:

$$\tau_m = \mathfrak{Re}\left({}^{\underline{\omega}}\overline{\mathbf{K}}^{*}_{\tau N}\,{}^{\underline{\omega}}\overline{\mathbf{I}}_s\right) = \mathfrak{Re}\left(\sum_{k=1:2}^{m_s} {}^{\omega}\overline{K}^{*}_{\tau k}\,{}^{\omega}\overline{I}_{sk}\right). \tag{2.23}$$

The mechanical part of the scheme is unchanged, while the internal variables of the electrical part (between power sections ① and ③) are complex vectors of reduced dimension.
Indeed, using the pseudo-transformation ${}^{t}\mathbf{I}_s = \mathfrak{Re}\left({}^{t}\overline{\mathbf{T}}_{\underline{\omega}N}\,{}^{\underline{\omega}}\overline{\mathbf{I}}_s\right)$ the original m_s-dimension model in the fixed frame Σ_t is transformed and reduced to a $(m_s{+}1)/2$-dimension complex model in the transformed reduced rotating frame $\overline{\Sigma}_\omega$. Then the system is decoupled into $(m_s{-}1)/2$ complex subspaces $\overline{\Sigma}_{\omega k}$ with $k \in \{1:2:m_s\}$ and the equivalence between a m_s-phase motor and a set of $(m_s{-}1)/2$ independent fictitious electrical machines remains valid also in the reduced complex rotating reference frame $\overline{\Sigma}_\omega$.

Comparison with Space Vector transformation

The transformation ${}^{t}\overline{\mathbf{T}}_{\underline{\omega}}$ is similar to the matrix proposed in the *Space Vector approach*, see [28], [38] and [39], which is based on the following transformation matrix:

$$ {}^{t}\mathbf{S}^{*}_{\underline{\omega}} = \frac{2}{m_s} \begin{bmatrix} & & h \\ & [\![\ 1\ ]\!] & \\ & 1{:}m_s & \\ k & & h \\ \left|\left[\ e^{j\,(h-1)\,k\gamma_s}\ \right]\right| & & \\ 1{:}2{:}m_s{-}1 & & 1{:}m_s \end{bmatrix} = \frac{2}{5} \left[\begin{array}{ccccc} 1 & 1 & 1 & 1 & 1 \\ \hline 1 & e^{j\gamma_s} & e^{j2\gamma_s} & e^{j3\gamma_s} & e^{j4\gamma_s} \\ 1 & e^{j3\gamma_s} & e^{j6\gamma_s} & e^{j9\gamma_s} & e^{j12\gamma_s} \end{array}\right]_{m_s=5}. $$

System $\overline{S}_{\omega}$ is described by complex variables and is obtained using the rectangular pseudo-transformation matrix ${}^{t}\overline{\mathbf{T}}_{\underline{\omega}N}$. For this reason the dimension of the transformed vectors is reduced and system $\overline{S}_{\omega}$ has a very compact form. Supposing the mechanical dynamic slower than the electrical one, i.e. assuming a constant velocity ω_m, the $m_s - 1$ eigenvalues of the considered multiphase synchronous motor coincide with the $(m_s-1)/2$ eigenvalues of system $\overline{S}_{\omega}$ (they can be easily obtained computing the complex roots of polynomial $\Delta(s) = \det\left[s\ {}^{\omega}\overline{\mathbf{L}}_s + \left({}^{\omega}\overline{\mathbf{R}}_s + {}^{\omega}\overline{\mathbf{L}}_s\,{}^{\omega}\overline{\mathbf{J}}_s\right)\right]$, and their $(m_s-1)/2$ complex conjugate values).
The pseudo-transformation matrix ${}^{t}\overline{\mathbf{T}}_{\underline{\omega}N}$ is *power-invariant*. Indeed it can be easily proved that the instantaneous power $p(t) = {}^{t}\mathbf{V}_s^{T}\,{}^{t}\mathbf{I}_s$ in section ① in Fig. 2.10 is equal to the real part of the complex instantaneous power $s(t) = \underline{{}^{\omega}\overline{\mathbf{V}}}_s^{*}\,\underline{{}^{\omega}\overline{\mathbf{I}}}_s$ in section ①:

$$ \begin{aligned} p(t) &= {}^{t}\mathbf{V}_s^{T}\,{}^{t}\mathbf{I}_s = {}^{t}\mathbf{V}_s^{T}\,\mathfrak{Re}({}^{t}\overline{\mathbf{T}}_{\underline{\omega}N}\,{}^{t}\overline{\mathbf{T}}^{*}_{\underline{\omega}N})\,{}^{t}\mathbf{I}_s \\ &= \mathfrak{Re}({}^{t}\mathbf{V}_s^{T}\,{}^{t}\overline{\mathbf{T}}_{\underline{\omega}N}\,{}^{t}\overline{\mathbf{T}}^{*}_{\underline{\omega}N}\,{}^{t}\mathbf{I}_s) = \mathfrak{Re}(\underline{{}^{\omega}\overline{\mathbf{V}}}_s^{*}\,\underline{{}^{\omega}\overline{\mathbf{I}}}_s) = \mathfrak{Re}(s(t)). \end{aligned} $$

The Space Vector approach *is not power-invariant*, indeed the instantaneous power $p(t) = {}^{t}\mathbf{V}_s^{\mathrm{T}}\,{}^{t}\mathbf{I}_s$ is not equal (but proportional) to the real part of the complex power $s(t) = {}^{S}\mathbf{V}_s^{*}\,{}^{S}\mathbf{I}_s$:

$$ p(t) \;=\; m_s\,\mathfrak{Re}(s(t)) \;=\; m_s\,\mathfrak{Re}({}^{S}\mathbf{V}_s^{*}\,{}^{S}\mathbf{I}_s). $$

2.2.3 Comparison among the proposed transformations

The two state space transformations (2.5) and (2.15) presented in the previous sections have been applied to system S_t obtaining two different dynamic systems S_{ω} and $\overline{S}_{\omega}$ which are equivalent from a mathematical point of view. It is possible to pass from one dynamic model to the others using the transformation matrices shown in Fig. 2.11. The transformation matrix $\underline{{}^{\omega}\overline{\mathbf{T}}}_{\underline{\omega}N}$ which links together the dynamic systems S_{ω} and $\overline{S}_{\omega}$ is related to matrices ${}^{t}\mathbf{T}_{\underline{\omega}}$ and ${}^{t}\overline{\mathbf{T}}_{\underline{\omega}N}$ as follows:

$$ \underline{{}^{\omega}\overline{\mathbf{T}}}_{\underline{\omega}N} \;=\; {}^{t}\mathbf{T}^{\mathrm{T}}_{\underline{\omega}}\,{}^{t}\overline{\mathbf{T}}_{\underline{\omega}N} = \begin{bmatrix} k & & l \\ \left|\left[\ \delta(l)|_k^{m_s}\ \right]\right| & & \mathbf{0} \\ \left|\left[\ -j\,\delta(l)|_k^{m_s}\ \right]\right| & & \\ 1{:}2{:}m_s{-}2 & 1{:}2{:}m_s{-}2 & \\ \mathbf{0} & & 1 \end{bmatrix} = \left[\begin{array}{ccc} 1 & 0 & 0 \\ -j & 0 & 0 \\ 0 & 1 & 0 \\ 0 & -j & 0 \\ 0 & 0 & 1 \end{array}\right]_{m_s=5}. $$

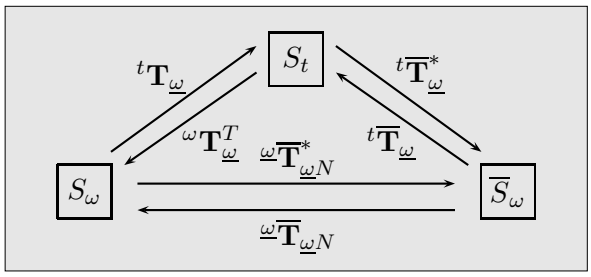

Figure 2.11: Transformation matrices relating the systems S_t, S_ω and $\overline{S}_\omega$.

Therefore one can obtain the current vector ${}^{\underline{\omega}}\overline{\mathbf{I}}_s$ as follows:

$$ {}^{\underline{\omega}}\overline{\mathbf{I}}_s = {}^{\underline{\omega}}\overline{\mathbf{T}}^*_{\underline{\omega}N}\,{}^{\underline{\omega}}\mathbf{I}_s = \begin{bmatrix} \overset{l}{\underset{1:2:m_s-2}{\left\|\left[\delta(l)|_k^{m_s} \;\; j\,\delta(l)|_k^{m_s}\right]\right\|}} & \mathbf{0} \\ \mathbf{0} & 1 \end{bmatrix} \begin{bmatrix} \overset{k}{\underset{1:2:m_s-2}{\left\|\begin{bmatrix} {}^{\omega}I_{dk} \\ {}^{\omega}I_{qk} \end{bmatrix}\right\|}} \\ {}^{\omega}I_{sm_s} \end{bmatrix} = \begin{bmatrix} \overset{k}{\underset{1:2:m_s-2}{\left\|\left[\, I_{dk} + jI_{qk} \,\right]\right\|}} \\ {}^{\omega}I_{sm_s} \end{bmatrix} \tag{2.24} $$

From (2.24) one concludes that the system (2.16) can also be obtained from system (2.7) using the bijective correspondences between two-dimensional vectors, complex numbers and two-dimensional matrices:

$$ \begin{bmatrix} \alpha \\ \beta \end{bmatrix} \quad \leftrightarrow \quad \alpha + j\beta \quad \leftrightarrow \quad \begin{bmatrix} \alpha & -\beta \\ \beta & \alpha \end{bmatrix}. $$

Thus, the *direct* and *quadrature* variables are still available in the complex reference frame $\overline{\Sigma}_\omega$, then the current, voltage and torque complex components $\overline{I}_{sk}$, $\overline{V}_{sk}$ and $\overline{K}_{\tau k}$ can be written as: $\overline{I}_{sk} = I_{dk} + jI_{qk}$, $\overline{V}_{sk} = V_{dk} + jV_{qk}$ and $\overline{K}_{\tau k} = K_{dk} + jK_{qk}$. The three systems S_t, S_ω and $\overline{S}_\omega$ are equivalent from a mathematical point of view, but they have different features from a practical point of view that are summarized in Table 2.4. The most compact and effective transformed systems is $\overline{S}_\omega$ obtained using the rectangular complex transformation matrix ${}^t\overline{\mathbf{T}}_{\underline{\omega}}$ given in (2.15), so it will be used in the following Chapters of this thesis.

System		S_t	S_ω	$\overline{S}_\omega$
Transformations		none	${}^t\mathbf{T}_{\underline{\omega}}$	${}^t\overline{\mathbf{T}}_{\underline{\omega}}$
Power invariant		/	Yes	Yes
Variables	type	real time variant	real constant	complex constant
	dimension	m_s	m_s	$\frac{m_s+1}{2}$
Fictitious machines		/	$\frac{m_s-1}{2}$	$\frac{m_s-1}{2}$

Table 2.4: Resume table of the transformed systems features

2.3 Simulation

D All the POG models of a multi-phase electric motor shown from Fig. 2.2 to Fig. 2.10 and the model with Park transformation (see Fig. 2.7) have been implemented in Simulink.
The Simulink scheme reported in Fig. 2.12 is the implementation of the POG model shown in Fig. 2.10. It has a vectorial structure that does not need to consider the fictitious machines; therefore, thanks to the graphical interface shown in Fig. 2.12.b, the user can modify the number of phases and other parameters of the model without changing the structure of the model. The Simulink scheme of the motor drive is shown in Fig. 2.12.a where the masked block of the electrical motor contains the Simulink scheme of Fig. 2.12.c.
The system has been fed with the following open-loop input:

$$ {}^{t}\mathbf{V}_{s0} = \mathfrak{Re}\left({}^{t}\overline{\mathbf{T}}_{\omega N}\, {}^{\omega}\overline{\mathbf{V}}_{s0} \right) , \qquad \text{where: } {}^{\omega}\overline{\mathbf{V}}_{s0} = \left({}^{\omega}\overline{\mathbf{R}}_{s} + {}^{\omega}\overline{\mathbf{J}}_{s}\, {}^{\omega}\overline{\mathbf{L}}_{s} \right) {}^{\omega}\overline{\mathbf{I}}_{d} + {}^{\omega}\overline{\mathbf{K}}_{\tau}\, \omega_{md} $$

where ${}^{\omega}\overline{\mathbf{I}}_{d}$ is the desired current vector in frame $\overline{\Sigma}_{\omega}$ and ω_{md} is the desired motor velocity. The simulation results shown in this section have been obtained considering the same five-phase star connected motor used in [37].
The electrical and mechanical lumped parameters of the motor are: $m_s = 5$, $p = 8$, , $N_c = 10$ $R_s = 0.11\,\Omega$, $L_s = 2.1$ mH, $M_{s0} = 0.7$ mH, $\varphi_r = 0.0025$ Wb, $J_m = 1.6$ kg m^2, $b_m = 2.06$ Nm s/rad, $a_1 = 0.71$, $a_3 = 0.04$ and the external torque $\tau_e = 0$ Nm.
Three different models are compared:

1) Park model,
2) POG model in the rotating frame Σ_{ω},
3) POG model in the reduced complex rotating frame $\overline{\Sigma}_{\omega}$.

The three desired current vectors, according to [37], are:

1) ${}^{P}\mathbf{I}_{d} = [\,0 \;\; 15 \;\; 0 \;\; 3.75\,]^{\mathrm{T}}$ $[A]$
2) ${}^{\omega}\mathbf{I}_{d} = \frac{1}{a}\,{}^{P}\mathbf{I}_{d} = [\,0 \;\; 23.72 \;\; 0 \;\; 5.93\,]^{\mathrm{T}}$ $[A]$
3) ${}^{\omega}\overline{\mathbf{I}}_{d} = j[\,23.72 \;\; 5.93\,]^{\mathrm{T}}$ $[A]$.

The dynamic time behaviors of the motor velocity ω_m, motor torque τ_m are shown in Fig. 2.13. The motor torque response is a typical step response of a second order system because the torque transient is deeply related to the electrical dominant pole of the system. While the motor velocity transient is related to the mechanical pole located in $\lambda_m = -b_m/J_m = -1.28$, then the mechanical settling time is: $T_{am} = 3/|\mathrm{Re}(\lambda_m)| \approx 2.34$ s. the first phase current vector I_{s1} in the steady state condition for the three controlled motors are shown in Fig. 2.14. The order of the error between the three simulation results is 10^{-14}.
The current vectors ${}^{P}\overline{I}_{sk}$ and ${}^{\omega}\overline{I}_{sk}$ in the two-dimensional subspaces $\Sigma_{\omega k}$ are shown in Fig. 2.15.

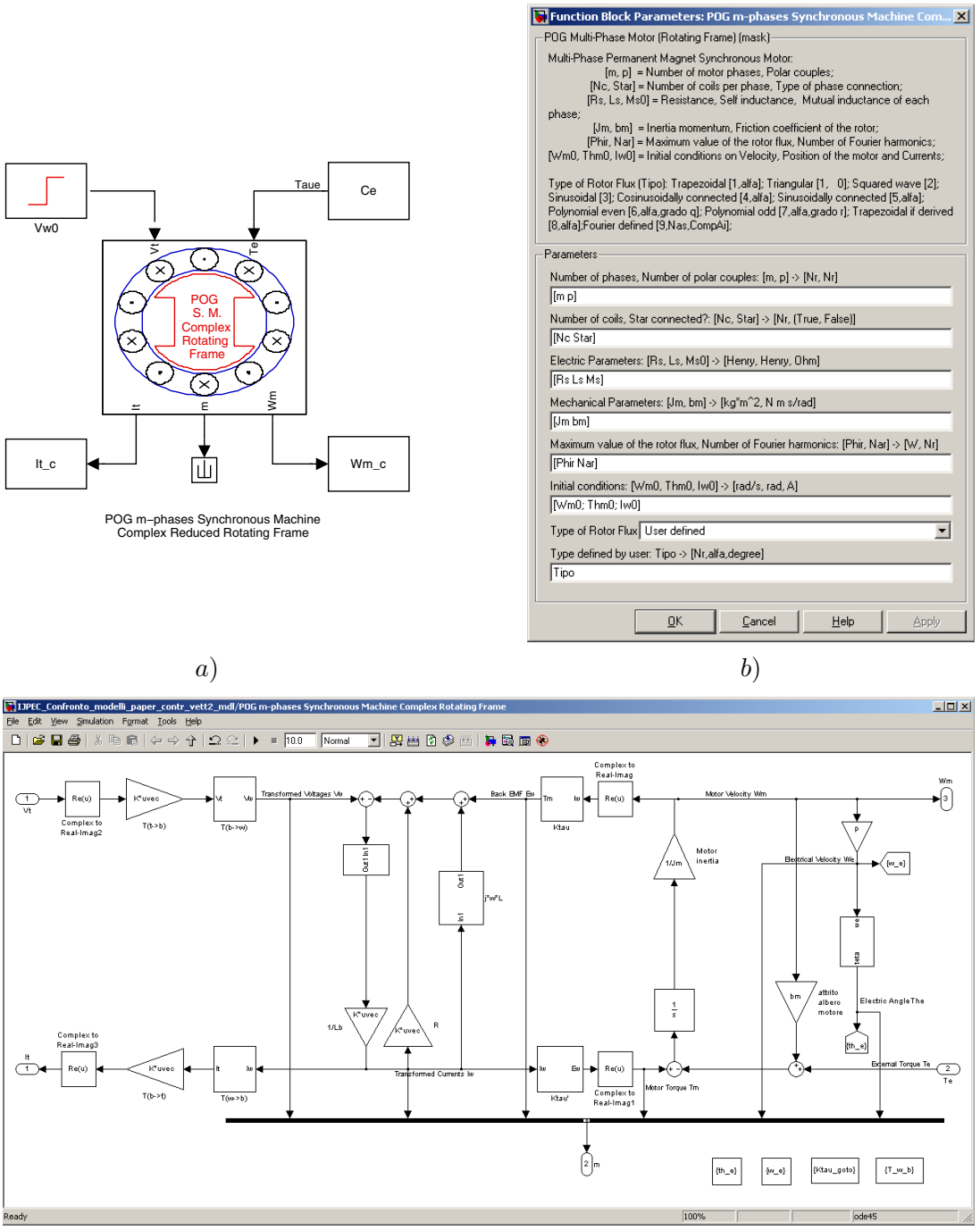

Figure 2.12: Simulink schemes: a) Simulink scheme of the controlled electric motor, b) User interface c) POG Simulink scheme of a multi-phase electrical motor in the frame $\overline{\Sigma}_\omega$.

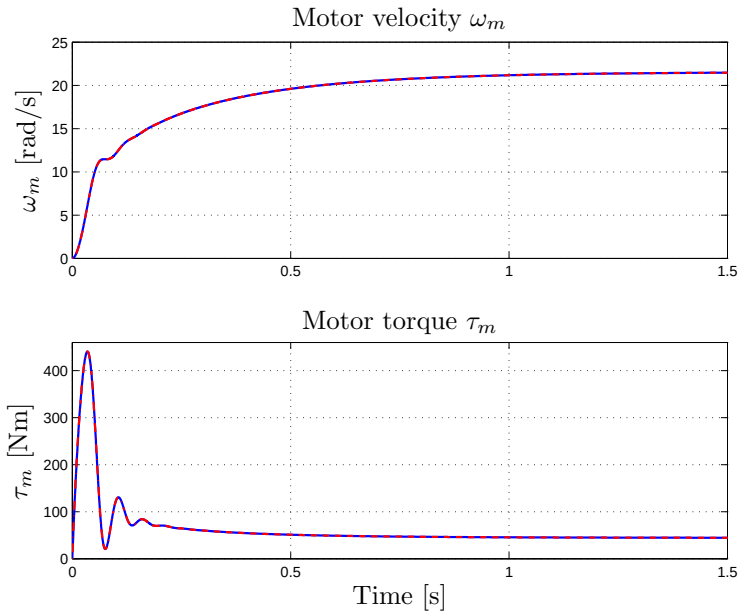

Figure 2.13: Motor velocity ω_m and motor torque τ_m.

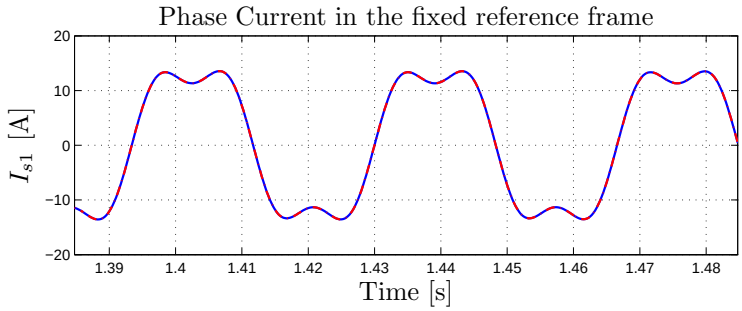

Figure 2.14: Real phase current in the fixed reference frame Σ_t.

Note that, according to (2.13), the relation between the previous current vectors is:

$$ {}^{P}\overline{I}_{sk} = a\,{}^{\omega}\overline{I}_{sk}\,, \qquad a = \sqrt{\frac{2}{m_s}} $$

The reference current vectors do not minimize the current dissipation. Using a vectorial notation it is evident that the optimal current vector that provides the desired torque τ_d minimizing the current dissipation is the current vector parallel to the torque vector ${}^{\omega}\overline{\mathbf{K}}_{\tau}$:

$$ {}^{\omega}\overline{\mathbf{I}}_{do} = \frac{{}^{\omega}\overline{\mathbf{K}}_{\tau}}{|{}^{\omega}\overline{\mathbf{K}}_{\tau}|^2}\,\tau_d = [\,0 \;\; 15.1996 \;\; 0 \;\; 2.5689\,]. $$

The first phase current component I_{s1} in steady state condition is shown in Fig. 2.16 respectively for the vectors ${}^{\omega}\overline{\mathbf{I}}_{d}$ (in red) and ${}^{\omega}\overline{\mathbf{I}}_{do}$ (in blue). Unlike ${}^{\omega}\overline{\mathbf{I}}_{d}$, the shape of the desired current ${}^{\omega}\overline{\mathbf{I}}_{d0}$ is linked to the shape of the rotor flux $\phi_c(\theta)$

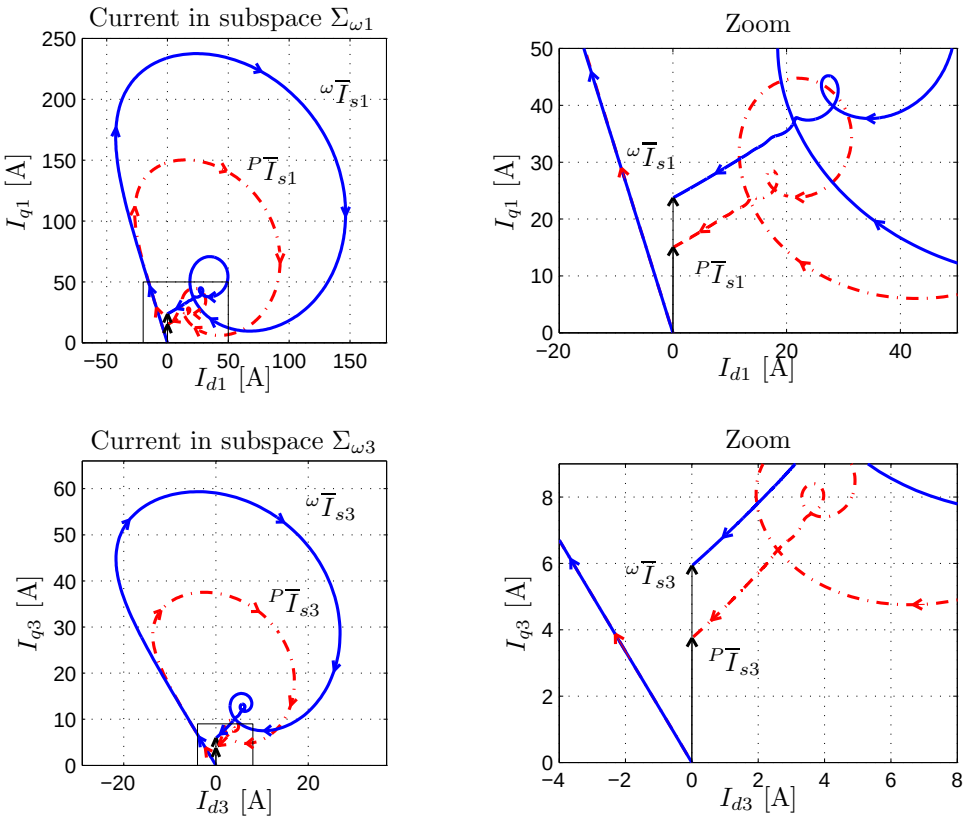

Figure 2.15: Current vectors $^{P}\overline{I}_{sk}$ and $^{\omega}\overline{I}_{sk}$ in the two-dimensional subspaces $\Sigma_{\omega k}$.

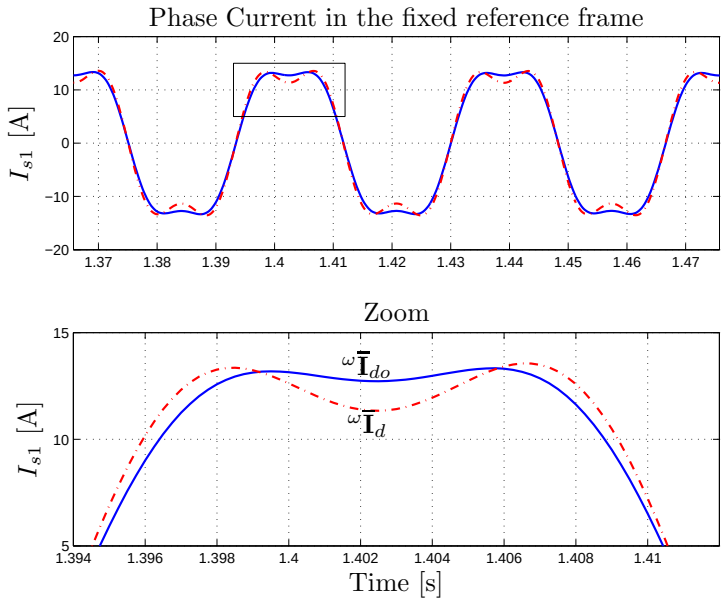

Figure 2.16: Real phase current in the fixed reference frame Σ_t.

Chapter 3

Star and Delta Multi-phase Synchronous Motors

Since the type of stator connection modifies the relation between the terminal variables and the phase ones, in order to obtain a model as general as possible both the star and delta stator connections are investigated in this chapter. The comparison between the types of connections is carried out by discussing the possible differences of the dynamic equations and of the internal complex models. Using a vectorial approach the optimal current references minimizing the dissipation are obtained and used in the control law. This approach is suitable for both star and delta connected stator phases. Finally some simulation results are reported in order to show the dynamic differences between the connection cases. The main contents of this chapter have been published in [40].

3.1 Star and Delta complex dynamic model

In this chapter we refer to a permanent magnet synchronous motor with an *odd* number m_s of concentrated winding in star or delta connection, see Fig. 3.1, characterized by the same parameters shown in Tab. 2.1.
Let ${}^t\mathbf{I}_l$, ${}^t\mathbf{V}_l$, ${}^t\mathbf{I}_s$ and ${}^t\mathbf{V}_s$ denote the following current and voltage terminal and phase vectors:

$$
\begin{aligned}
{}^t\mathbf{I}_l &= \Big[I_1 \cdots I_{m_s} \Big]^{\mathrm{T}}, \qquad & {}^t\mathbf{V}_l &= \Big[V_1 \cdots V_{m_s} \Big]^{\mathrm{T}}, \\
{}^t\mathbf{I}_s &= \Big[I_{s1} \cdots I_{sm_s} \Big]^{\mathrm{T}}, \qquad & {}^t\mathbf{V}_s &= \Big[V_{s1} \cdots V_{sm_s} \Big]^{\mathrm{T}}.
\end{aligned}
$$

The type of windings connection modifies the relation between the phase vectors ${}^t\mathbf{V}_s$ and ${}^t\mathbf{I}_s$ and the terminal vectors ${}^t\mathbf{V}_l$ and ${}^t\mathbf{I}_l$. Indeed, as shown in Fig. 3.1, in the star-connected motor the current flowing into the terminal is the same that flows into the phase while in a delta-connected motor the terminal current is the difference of the currents flowing into the two adjacent phases

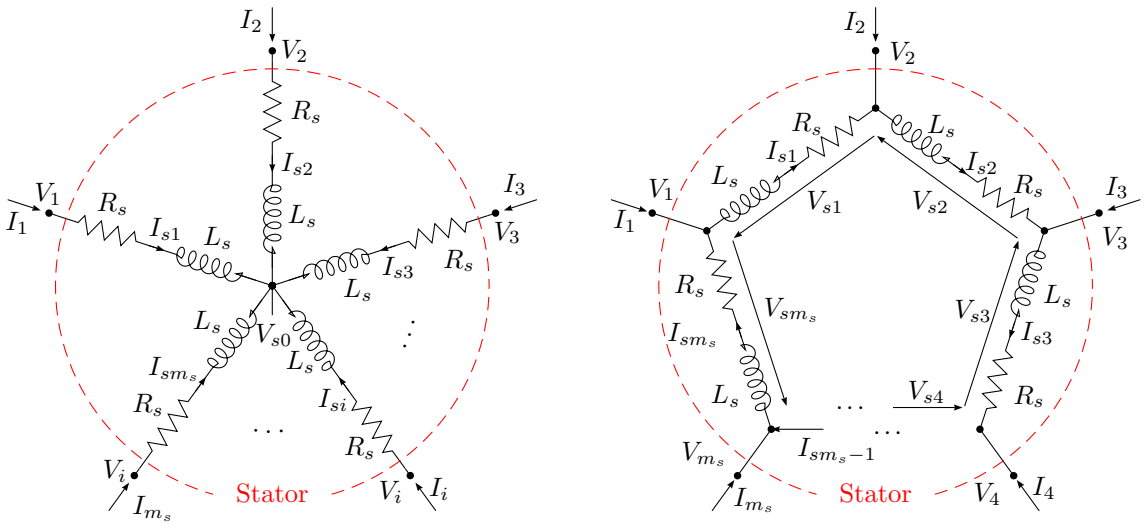

Figure 3.1: Star and delta-connected stator phases.

(connected to the same terminal). The relation between the phase and current vectors are:

$$ {}^t\mathbf{I}_l = {}^t\mathbf{T}\,{}^t\mathbf{I}_s, \qquad {}^t\mathbf{V}_s = {}^t\mathbf{T}^{\mathrm{T}}\,{}^t\mathbf{V}_l - {}^t\mathbf{V}_{s0}, \tag{3.1} $$

where the connection matrix ${}^t\mathbf{T}$ and the common voltage vector ${}^t\mathbf{V}_{s0}$ depend on the type of stator connection:

$$ {}^t\mathbf{T} = \begin{cases} \mathbf{I}_{m_s} & \text{if star-connected} \\ {}^t\mathbf{T}_{\triangle} & \text{if delta-connected} \end{cases} $$

$$ {}^t\mathbf{T}_{\triangle} = \begin{bmatrix} 1 & 0 & 0 \cdots -1 \\ -1 & 1 & 0 \cdots 0 \\ 0 & -1 & 1 \cdots 0 \\ \vdots & \vdots & \vdots \ddots \vdots \\ 0 & 0 & 0 \cdots 1 \end{bmatrix} \tag{3.2} $$

$$ {}^t\mathbf{V}_{s0} = \begin{cases} [1,\ 1,\ \ldots,\ 1]^{\mathrm{T}} V_{s0} & \text{if star-connected} \\ [0,\ 0,\ \ldots,\ 0]^{\mathrm{T}} & \text{if delta-connected} \end{cases} $$

One can easily verify that matrix ${}^t\mathbf{T}_{\triangle}$ is singular: $\det({}^t\mathbf{T}_{\triangle}) = 0$ and this is a problem for the vectorial control, as will be discussed in Sec.3.3.

Since the dynamic system $\overline{S}_{\omega}$ given in (2.16) considers the phase vectors ${}^t\mathbf{I}_s$ and ${}^t\mathbf{V}_s$, introducing the connection matrix ${}^t\mathbf{T}$ as the first elaboration block of the POG scheme in Fig. 2.10 one obtains a model which takes into account also the type of stator connection, see Fig. 3.2. Since the matrix ${}^t\mathbf{T}$ present between the power sections ①-② relates the phase vectors ${}^t\mathbf{V}_s$ and ${}^t\mathbf{I}_s$ to the terminal vectors ${}^t\mathbf{V}_l$ and ${}^t\mathbf{I}_l$, the structure of the model is the same whatever the type of stator connection is. Indeed the type of stator connection modifies only the form of the connection matrix ${}^t\mathbf{T}$ between the section ①-②. Thus, a unique general model is obtained

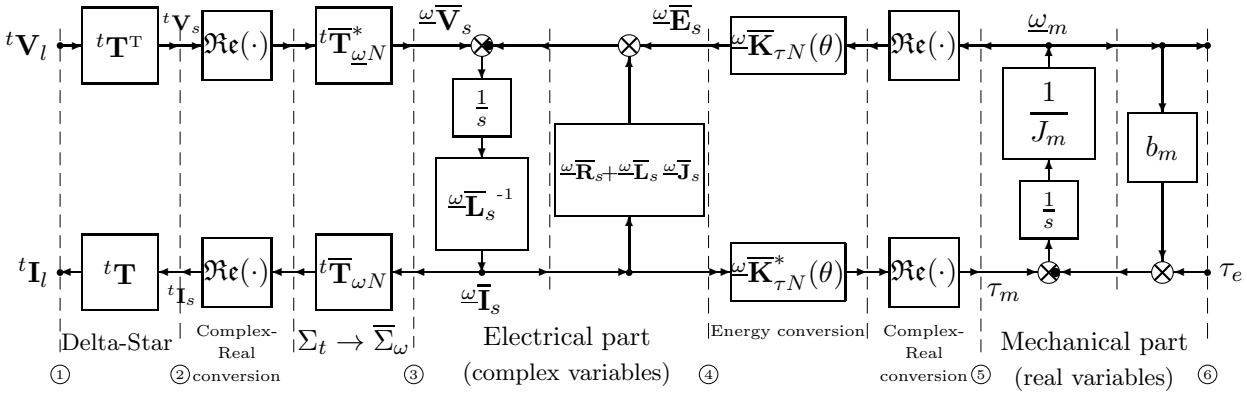

Figure 3.2: POG scheme of a multi-phase electrical motor in the reduced complex rotating reference frame $\overline{\Sigma}_\omega$.

whatever the number of phases m_s and the type of connection are. Since the value of the stator voltages V_{sh} and the stator currents I_{sh} (for the same value of the line variables V_h and I_h) change with the type of stator connection, the transformed current and voltage vectors ${}^{\underline{\omega}}\overline{\mathbf{I}}_s$ and ${}^{\underline{\omega}}\overline{\mathbf{V}}_s$ in (2.19) and (2.20) depend on the type of stator connection. Moreover the last component of current vector ${}^{\omega}I_{sm_s}$ is zero for a star-connected motor while the last component of voltage vector ${}^{\omega}V_{sm_s}$ is zero for a delta-connected motor.
In order to put in evidence the different dynamic behavior between the star and delta connected motor two different types of the normalized rotor flux for each type of stator connection will be considered in the next section. The first type of the normalized rotor flux has the shape (2.11), while the second one has also the m_s-th harmonic differen from zero:

$$\bar{\phi}(\theta) = \sum_{i=1:2}^{m_s} a_i \cos(i\,\theta). \tag{3.3}$$

When the normalized rotor flux has the structure (2.11) the transformed torque vector ${}^{\underline{\omega}}\overline{\mathbf{K}}_{\tau N}$ is constant as shown in (2.22), while when the normalized rotor flux has the structure (3.3) the transformed torque vector ${}^{\underline{\omega}}\overline{\mathbf{K}}_{\tau N}(\theta)$ is:

$${}^{\underline{\omega}}\overline{\mathbf{K}}_{\tau N}(\theta) = jp\varphi_c\sqrt{\frac{m_s}{2}}\begin{bmatrix} \Big\|_{1:2:m_s-2}^{k}\big[\!\big[\ ka_k\ \big]\!\big]\Big| \\ {}^{\omega}\overline{K}_{\tau m_s}(\theta) \end{bmatrix}.$$

where only the last component ${}^{\omega}\overline{K}_{\tau m_s}$ is function of the electric angle θ. This component is a real function that can be rewritten as:

$${}^{\omega}\overline{K}_{\tau m_s} = b_1 \sin(m_s\, p\, \omega_m t) = -p\varphi_c\sqrt{m_s} m_s a_{m_s} \sin(m_s\, p\, \omega_m t)\,. \tag{3.4}$$

In this second case the torque equation (2.23) can be rewritten as:

$$\tau_m = \mathfrak{Re}\left(\sum_{k=1:2}^{m_s-2} {}^{\omega}\overline{K}^{*}_{\tau k}\, {}^{\omega}\overline{I}_{sk}\right) + {}^{\omega}\overline{K}_{\tau m_s}(\theta)\, {}^{\omega}\overline{I}_{sm_s} = \overline{\tau}_m + \tau_{m_s}(t)$$

where the motor torque τ_m is the sum of two terms: a constant torque $\overline{\tau}_m$ and a time variant torque $\tau_{m_s}(t)$. The constant torque $\overline{\tau}_m$ is the same torque generated in the first case (when the transformed torque vector $\underline{{}^{\omega}}\overline{\mathbf{K}}_{\tau N}$ is constant), while the undesired time variant torque $\tau_{m_s}(t)$ is due to the time variant component ${}^{\omega}\overline{K}_{\tau m_s}$.

3.2 Star and Delta connected motor

The differential equations (2.16) depend on the star or delta connection of the motor. In particular the m_s-th differential equation of system (2.16) is:

$$L_{s0}\, {}^{\omega}\dot{\overline{I}}_{sm_s} = -R_s\, {}^{\omega}\overline{I}_{sm_s} + {}^{\omega}\overline{K}_{sm_s}\omega_m + {}^{\omega}\overline{V}_{sm_s}. \tag{3.5}$$

1) When the multi-phase motor is ***star connected***, the last component ${}^{\omega}I_{sm_s}$ of vector $\underline{{}^{\omega}}\bar{\mathbf{I}}_s$ is zero and the differential equation (3.5) becomes:

$${}^{\omega}\overline{K}_{sm_s}\,\omega_m + {}^{\omega}\overline{V}_{sm_s} = 0. \tag{3.6}$$

In this case the dynamic dimension of a star-connected motor is $m_s - 1$, then the homopolar vectors $\mathbf{z}_{m_s}$ in (2.5) and (2.15) can be eliminated reducing the matrices ${}^{t}\mathbf{T}_{\underline{\omega}}$ and ${}^{t}\overline{\mathbf{T}}_{\underline{\omega}N}$ to the rectangular matrices ${}^{t}\mathbf{T}_{\omega}$ and ${}^{t}\overline{\mathbf{T}}_{\omega N}$. Consequently, the generated torque is constant regardless of the last components ${}^{\omega}\overline{K}_{sm_s}$ of the transformed torque vector. Moreover, from (3.1) and (3.6) it follows that:

$$V_{s0} = \frac{1}{m_s}\sum_{h=1}^{m_s} V_h + \frac{1}{\sqrt{m_s}}\, {}^{\omega}\overline{K}_{sm_s}\,\omega_m. \tag{3.7}$$

This relation shows that the common voltage V_{s0} is zero when the input voltages V_h are balanced and when the normalized rotor flux $\bar{\phi}$ has the shape given in (2.11), i.e. when $a_{m_s} = 0$ and ${}^{\omega}\overline{K}_{sm_s} = 0$. On the contrary, the voltages V_{s0} is not zero and it is time-variant when $a_{m_s} \neq 0$.

2) When the multi-phase motor is ***delta connected***, the last component ${}^{\omega}\overline{V}_{sm_s}$ of vector $\underline{{}^{\omega}}\overline{\mathbf{V}}_s$ is zero and the differential equation (3.5) becomes:

$$L_{s0}\, {}^{\omega}\dot{\overline{I}}_{sm_s} = -R_s\, {}^{\omega}\overline{I}_{sm_s} + {}^{\omega}\overline{K}_{sm_s}\,\omega_m. \tag{3.8}$$

The last differential equation is described by this first order system where the input is the last component of torque vector and the output the last component of current vector. Therefore the dynamic dimension and the dynamic behavior are related to the type of the rotor flux. Substituting (3.4) in (3.8) one obtains:

$$L_{s0}\, {}^{\omega}\dot{\overline{I}}_{sm_s} = -R_s\, {}^{\omega}\overline{I}_{sm_s} + \omega_m b_1 \sin\left(m_s p \omega_m t\right).$$

This is a linear equation with transfer function $G(s) = \frac{\omega_m}{L_{s0}s+R_s}$ excited by a sinusoidal input with frequency $\omega_R = m_s\, p\, \omega_m$. The steady state solution of this equation can be written as follows:

$$ {}^{\omega}\overline{I}_{sm_s}(t) = b_1|G_1| \sin\left(\omega_R t + \angle G_1\right) \tag{3.9} $$

where $|G_1| = |G(j\omega_R)|$, $\angle G_1 = \angle G(j\omega_R)$ and b_1 is given in (3.4). In this case the torque τ_{m_s} corresponding to current ${}^{\omega}I_{sm_s}$ can be expressed as:

$$ \tau_{m_s}(t) = {}^{\omega}\overline{K}_{sm_s}\, {}^{\omega}\overline{I}_{sm_s} \simeq \overline{\tau_{m_s}}(t) + \widetilde{\tau}_{m_s}(t) $$

where the mean value $\overline{\tau_{m_s}}(t)$ of torque τ_{m_s} is:

$$ \overline{\tau_{m_s}}(t) = -\frac{b_1^2|G(j\omega_R)|}{2} \cos\left(\angle G(j\omega_R)\right) \tag{3.10} $$

and the ripple torque $\widetilde{\tau}_{m_s}(t)$ has the structure:

$$ \widetilde{\tau}_{m_s}(t) = -\frac{b_1^2|G(j\omega_R)|}{2} \cos\left(2\omega_R t + \angle G(j\omega_R)\right). \tag{3.11} $$

Note that when $a_{m_s} \neq 0$ and ${}^{\omega}\overline{K}_{sm_s} \neq 0$ the torque τ_{m_s} has a negative mean value $\overline{\tau_{m_s}}$, see (3.10), and a torque ripple $\widetilde{\tau}_{m_s}$ at frequency $2\omega_R$, see (3.11). When it is present the term τ_{m_s} reduces the amplitude of the total torque τ_m introducing also an undesired torque ripple. Otherwise, when the normalized rotor flux has the shape given in (2.11) the equation (3.8) becomes:

$$ L_{s0}\, {}^{\omega}\dot{\overline{I}}_{sm_s} = -R_s\, {}^{\omega}\overline{I}_{sm_s}. \tag{3.12} $$

The solution of this equation is:

$$ {}^{\omega}\overline{I}_{sm_s}(t) = {}^{\omega}\overline{I}_{sm_s}(0)\, e^{-t/\tau}, \qquad \tau = \frac{L_{s0}}{Rs} \tag{3.13} $$

and therefore in steady state condition the current ${}^{\omega}\overline{I}_{sm_s}$ is zero. In this case ${}^{\omega}\overline{K}_{sm_s} = 0$ and the torque τ_{m_s} is zero regardless of ${}^{\omega}\overline{I}_{sm_s}$. When the dynamic of equation (3.12) is disregarded the dynamic dimension of the motor is $m_s - 1$, equal to the one obtained for the star-connected case.

3.3 Vectorial Control

Torque τ_m can be controlled by the desired current vector in frame $\overline{\Sigma}_\omega$. The optimal current vector ${}^{\omega}\underline{\overline{\mathbf{I}}}_d$ which provides the desired torque τ_d minimizing the dissipation is the current vector parallel to the torque vector ${}^{\omega}\underline{\overline{\mathbf{K}}}_{\tau N}$ in frame $\overline{\Sigma}_\omega$:

$$ {}^{\omega}\underline{\overline{\mathbf{I}}}_d = \frac{{}^{\omega}\underline{\overline{\mathbf{K}}}_{\tau N}}{|{}^{\omega}\underline{\overline{\mathbf{K}}}_{\tau N}|^2}\, \tau_d, \tag{3.14} $$

When ${}^{\underline{\omega}}\overline{\mathbf{I}}_d$ is constant, the condition ${}^{\underline{\omega}}\overline{\mathbf{I}}_s = {}^{\underline{\omega}}\overline{\mathbf{I}}_d$ can be achieved using the control law:

$$ {}^{\underline{\omega}}\overline{\mathbf{V}}_s = {}^{\underline{\omega}}\overline{\mathbf{Z}}_s\, {}^{\underline{\omega}}\overline{\mathbf{I}}_s + {}^{\underline{\omega}}\overline{\mathbf{K}}_{\tau N}\, \omega_m - \mathbf{K}_c({}^{\underline{\omega}}\overline{\mathbf{I}}_s - {}^{\underline{\omega}}\overline{\mathbf{I}}_d) \tag{3.15} $$

where $\mathbf{K}_c > 0$ is a proper diagonal matrix used for the tuning of the control. The current vector ${}^{\underline{\omega}}\overline{\mathbf{I}}_s$ can be obtained from the terminal current vector ${}^{t}\mathbf{I}_l$ inverting the connection matrix ${}^{t}\mathbf{T}$:

$$ {}^{\underline{\omega}}\overline{\mathbf{I}}_s = \left({}^{t}\mathbf{T}\, {}^{t}\overline{\mathbf{T}}_{\underline{\omega}N}\right)^{-1} {}^{t}\mathbf{I}_l = {}^{t}\overline{\mathbf{T}}^{*}_{\underline{\omega}N}\, {}^{t}\mathbf{T}^{-1}\, {}^{t}\mathbf{I}_l. \tag{3.16} $$

Matrix ${}^{t}\mathbf{T}$ is invertible for a star-connected motor and is singular ($det({}^{t}\mathbf{T}_{\triangle}) = 0$) for a delta-connected motor, see (3.2). This problem can be overcome diagonalizing the connection matrix ${}^{t}\mathbf{T}$ by the matrix ${}^{t}\overline{\mathbf{T}}_{\underline{\omega}}$ as follows:

$$ {}^{\underline{\omega}}\overline{\mathbf{T}} = {}^{t}\overline{\mathbf{T}}^{*}_{\underline{\omega}}\, {}^{t}\mathbf{T}\, {}^{t}\overline{\mathbf{T}}_{\underline{\omega}}, \qquad \text{where:} \quad {}^{\underline{\omega}}\overline{\mathbf{T}} = \begin{cases} \begin{bmatrix} k & & \\ \left\| \left[1 - e^{jk\gamma_s} \right] \right\|_{1:2:m_s-2} & & \mathbf{0} \\ \mathbf{0} & & 0 \end{bmatrix} & \text{if delta-connected} \\ \mathbf{I}_{\frac{m_s+1}{2}} & & \text{if star-connected} \end{cases} $$

This equation shows that in the delta-connection the matrix ${}^{\underline{\omega}}\overline{\mathbf{T}}$ is singular because the last eigenvalue is zero. Since ${}^{t}\overline{\mathbf{T}}^{*}_{\underline{\omega}}\, {}^{t}\overline{\mathbf{T}}_{\underline{\omega}} = \mathbf{I}_{\frac{m_s+1}{2}}$, then the equation (3.16) can be rewritten as:

$$ \begin{aligned} {}^{\underline{\omega}}\overline{\mathbf{I}}_s &= \left({}^{t}\overline{\mathbf{T}}_{\underline{\omega}}\, {}^{t}\overline{\mathbf{T}}^{*}_{\underline{\omega}}\, {}^{t}\mathbf{T}\, {}^{t}\overline{\mathbf{T}}_{\underline{\omega}}\mathbf{N} \right)^{-1} {}^{t}\mathbf{I}_l = \\ &= \left({}^{t}\overline{\mathbf{T}}_{\underline{\omega}}\, {}^{\underline{\omega}}\overline{\mathbf{T}}\, \mathbf{N} \right)^{-1} {}^{t}\mathbf{I}_l \;= \left({}^{t}\overline{\mathbf{T}}_{\underline{\omega}N}\, {}^{\underline{\omega}}\overline{\mathbf{T}} \right)^{-1} {}^{t}\mathbf{I}_l = {}^{\underline{\omega}}\mathbf{T}^{-1}\, {}^{t}\overline{\mathbf{T}}^{*}_{\underline{\omega}N}\, {}^{t}\mathbf{I}_l \end{aligned} \tag{3.17} $$

where matrix ${}^{\underline{\omega}}\overline{\mathbf{T}}^{-1}$ is defined as follows:

$$ {}^{\underline{\omega}}\overline{\mathbf{T}}^{-1} = \begin{cases} \begin{bmatrix} k & & \\ \left\| \left[\dfrac{1}{1 - e^{jk\gamma_s}} \right] \right\|_{1:2:m_s-2} & & \mathbf{0} \\ \mathbf{0} & & 0 \end{bmatrix} & \text{if delta-connected} \\ \mathbf{I}_{\frac{m_s+1}{2}} & & \text{if star-connected} \end{cases} $$

Note that in the delta-connection the null eigenvalue is related to the last component ${}^{\omega}\overline{I}_{sm_s}$ of current vector ${}^{\underline{\omega}}\overline{\mathbf{I}}_s$ therefore it is not possible to control this component. However it is still possible to implement the control law (4.29) because the last current component ${}^{\omega}\overline{I}_{sm_s}$ is independent from the inputs $\big($it is zero or function of motor velocity, as shown in (3.6), (3.9) and (3.13)$\big)$. The equations (3.14), (4.29) and (3.17) are used together in the control block diagram shown in Fig. 3.3 where a P controller and feed-forward action are used.

The main differences between the two types of stator connection are summarized in Tab.3.1.

In a star-connected motor the last current component ${}^{\omega}\overline{I}_{sm_s}$ is zero therefore the dynamic dimension of the system is $m_s - 1$. In a delta-connected motor the last current component ${}^{\omega}\overline{I}_{sm_s}$ is zero in steady state condition only for a particulary shape of rotor flux otherwise the last current component is sinusoidal and undesired toque ripple is generated.

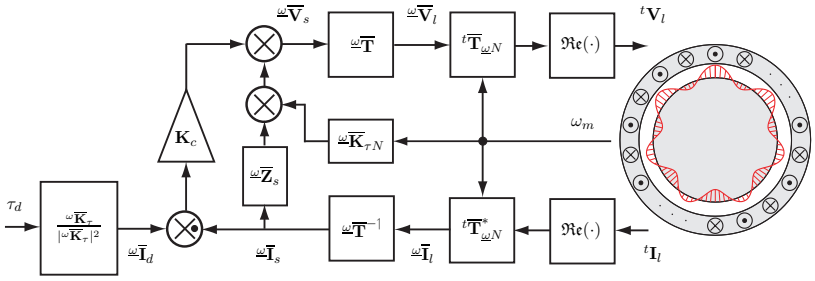

Figure 3.3: Multi-phase control motor drive scheme.

	Star		Delta	
	$a_{ms}=0$	$a_{ms}\neq 0$	$a_{ms}=0$	$a_{ms}\neq 0$
Dyn. dim.	m_s-1	m_s-1	m_s-1	m_s
τ_m	constant	constant	constant	ripple
${}^t\mathbf{T}$	invertible	invertible	singular	singular
${}^\omega\overline{I}_{sm_s}$	0 contr.	0 contr.	0 in ss uncontr.	$\sin(\cdot)$ uncontr.

Table 3.1: Resume table of the difference between the star and delta connection.

3.4 Simulation

As shown in Fig. 3.4.a both the POG model in Fig. 3.2 and the control diagram in Fig. 3.3 have been implemented in Matlab-Simulink, like a common Simulink library block. The left "Control" block in Fig. 3.3 implements the control law (3.15), while the right masked block of the electric motor contains the Simulink scheme, shown in Fig. 3.4.c. Both the masked blocks have the configuration mask window reported in Fig. 3.4.b; therefore the user can modify the motor parameters, like the number of phases, the type of stator connection, the type of the rotor flux, etc.. without changing the structure of the scheme. Note that in the field highlighted by the red box the user can select the type of stator connection.

The PWM block is not implemented in the scheme of Fig. 3.4.a and the voltage ${}^t\mathbf{V}_s$ is directly used to feed the motor. Since the low-pass characteristic of the machine inductances filters the output switched voltages of the PWM block, it is better to use directly the average voltage ${}^t\mathbf{V}_s$ reducing in this way the simulation time. Indeed the high frequency switching of the PWM block (necessary to obtain the variable-width pulse waveform from the modulating signal ${}^t\mathbf{V}_s$) increases the simulation time. Note that in this way the undesired harmonics introduced by the switching are neglected.

The simulation results shown in this section have been obtained using the following electrical and mechanical parameters: $m_s = 5$, $p = 1$, $N_c = 35$, $R_s = 1.5\,\Omega$, $L_s = 0.02$H, $M_{s0} = 0.01$ H, $a_{M1} = 1$, $a_{M3} = 1/9$, $\varphi_r = 0.02$ Wb, $J_m = 0.6$ kg m^2, $b_m = 0.25$ Nm s/rad, $a_1 = 0.25$, $a_3 = 0.75$, desired torque $\tau_d = 15$ Nm and external torque $\tau_e = 0$ Nm. In order to put in evidence the

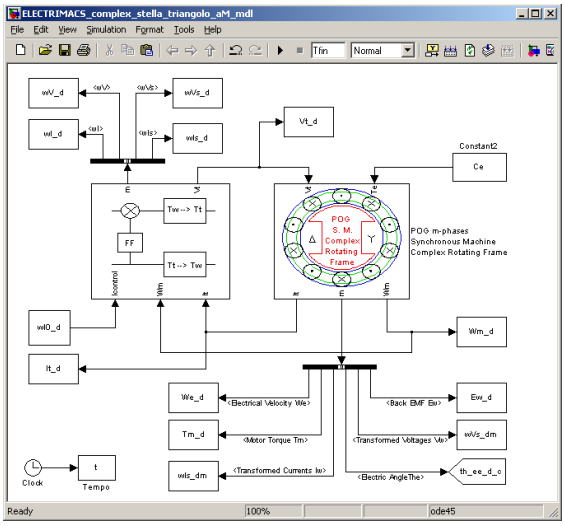

a)

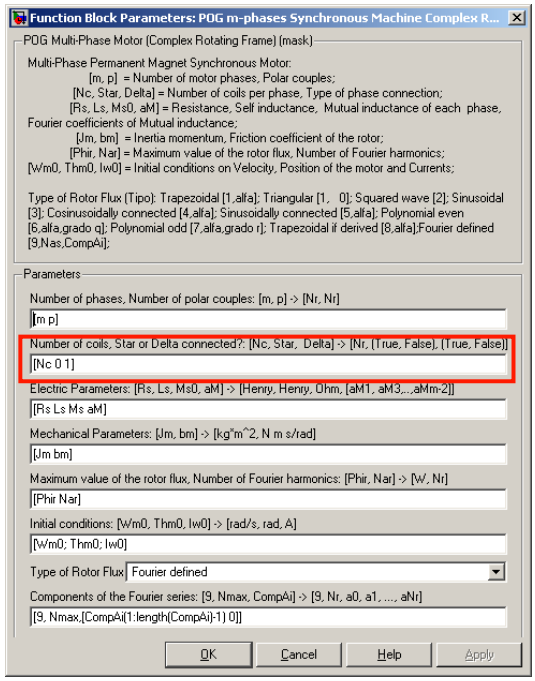

b)

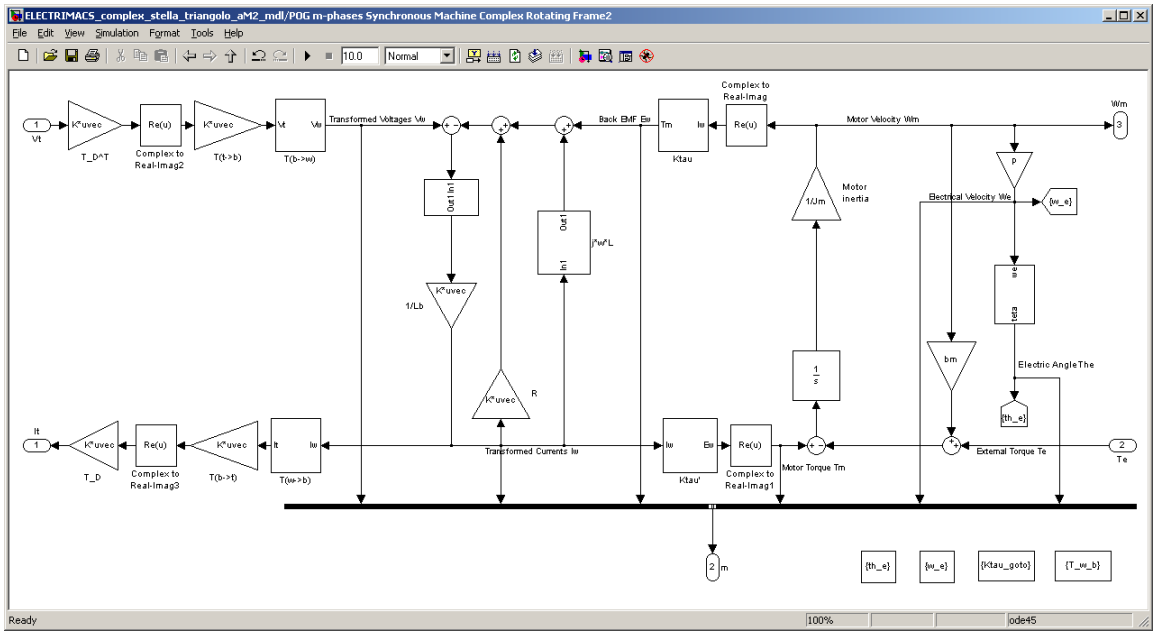

c)

Figure 3.4: Simulink schemes: a) Simulink scheme of the controlled electric motor, b) User interface c) POG Simulink scheme of a multi-phase electrical motor in the frame $\overline{\Sigma}_\omega$.

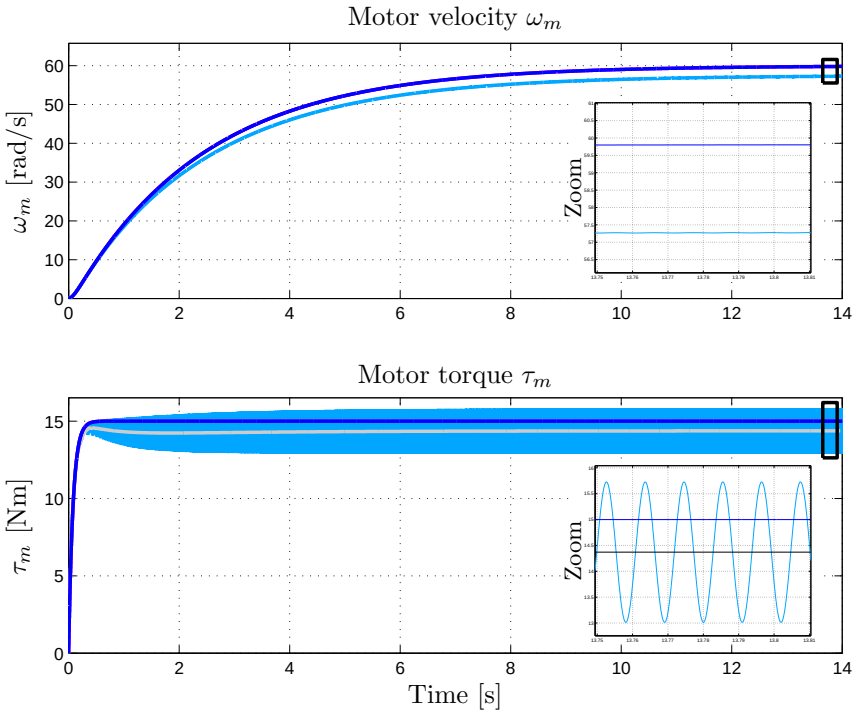

Figure 3.5: Motor velocity ω_m and motor torque τ_m

different dynamic behavior between the star and delta connected motors, three different cases are compared:

1) star-connected motor with $a_5 = 0$,
2) delta-connected motor with $a_5 = 0$,
3) delta-connected motor with $a_5 = 0.05$.

The time behaviors of the motor velocity ω_m, motor torque τ_m for the three controlled motors are shown in Fig. 3.5. The blue lines are referred to case 1 and case 2, while the cyan lines are related to case 3. The torques generated in case 1 and case 2 are equal (the order of the error is 10^{-14}), while the torque τ_m generated in case 3 is smaller then cases 1 and 2 and it is affected by ripple. Therefore in this 3-rd case the motor starts accelerating to 57.3 [rad/s] (that is a lower velocity respect to 59.8 [rad/s] reached in case 1 and case 2). According to the simulation results, the torque reduction, the ripple amplitude and its frequency, calculated by (3.10) and (3.11), are:

$$\begin{aligned} \overline{\tau_{m_s}}(t) &= -\tfrac{b_1^2|G(j\omega_R)|}{2}\cos\left(\angle G(j\omega_R)\right) = 0.6293 \text{ [Nm]}, \\ \widetilde{\tau}_{m_s}(t) &= -\tfrac{b_1^2|G(j\omega_R)|}{2}\cos\left(2\omega_R t + \angle G(j\omega_R)\right) = -1.3565\,\cos(572.8893\,t - 1.0884) \text{ [Nm]} \end{aligned}$$

where:

$$b_1 = -p^2 N_c \varphi_r \sqrt{m_s} m_s a_{m_s} = -0.3913 \text{ [Wb]}, \quad \omega_R = m_s\, p\, \omega_m = 286.4446 \text{ [rad/s]},$$

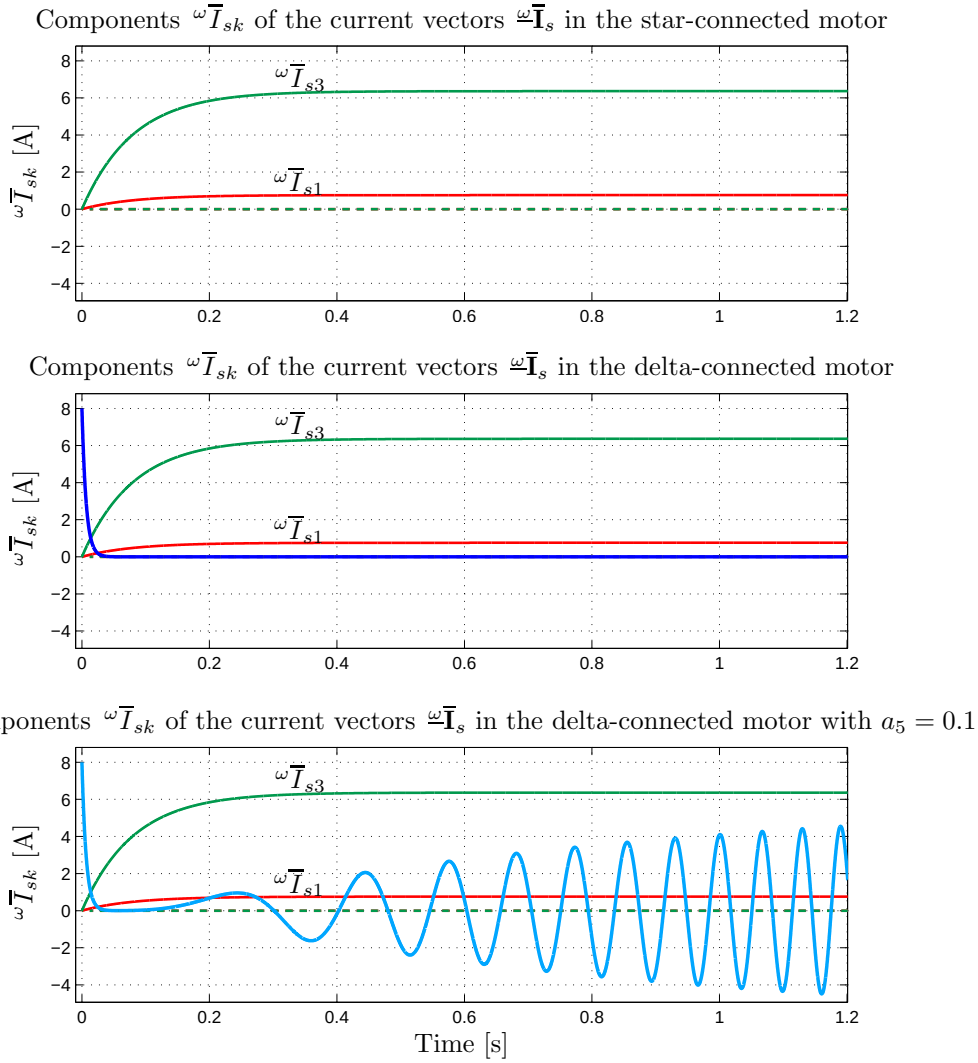

Figure 3.6: Transformed phase currents in the complex rotating reference frame $\overline{\Sigma}_{\omega}$.

$$|G(j\omega_R)| = \frac{\omega_m}{\sqrt{R_s^2+L_{s0}^2\,\omega_R^2}} = 17.7177 \text{ [rad/s}\Omega\text{]}, \quad \angle G(j\omega_R) = -\arctan\frac{L_{s0}\,\omega_R}{R_s} = -1.0884 \text{ [rad]}.$$

Using the (3.14) one obtains the desired current vector ${}^{\omega}\overline{\mathbf{I}}_d$ which provides the desired torque $\tau_d = 15$ Nm minimizing the dissipation:

$${}^{\omega}\overline{\mathbf{I}}_d = \begin{bmatrix} {}^{\omega}\overline{I}_{s1} & {}^{\omega}\overline{I}_{s3} & {}^{\omega}\overline{I}_{s5} \end{bmatrix}^T = \begin{bmatrix} 0+j1.2 & 0+j6.3 & 0 \end{bmatrix}^T.$$

The transient of the components ${}^{\omega}\overline{I}_{sk}$ of vector ${}^{\omega}\overline{\mathbf{I}}_s$ is shown in Fig. 3.6. The time behavior of components ${}^{\omega}\overline{I}_{s1}$ (red line) and ${}^{\omega}\overline{I}_{s3}$ (green line) is the same for the three motors, while it is different for ${}^{\omega}\overline{I}_{s5}$ because the control law (4.29) can not control this last component. Note that the component ${}^{\omega}\overline{I}_{s5}$ is zero in case 1, see (3.6), is zero in steady state condition (blue line) in case 2, see (3.9), and is sinusoidal (cyan line) in case 3, see (3.13). The time behaviors of

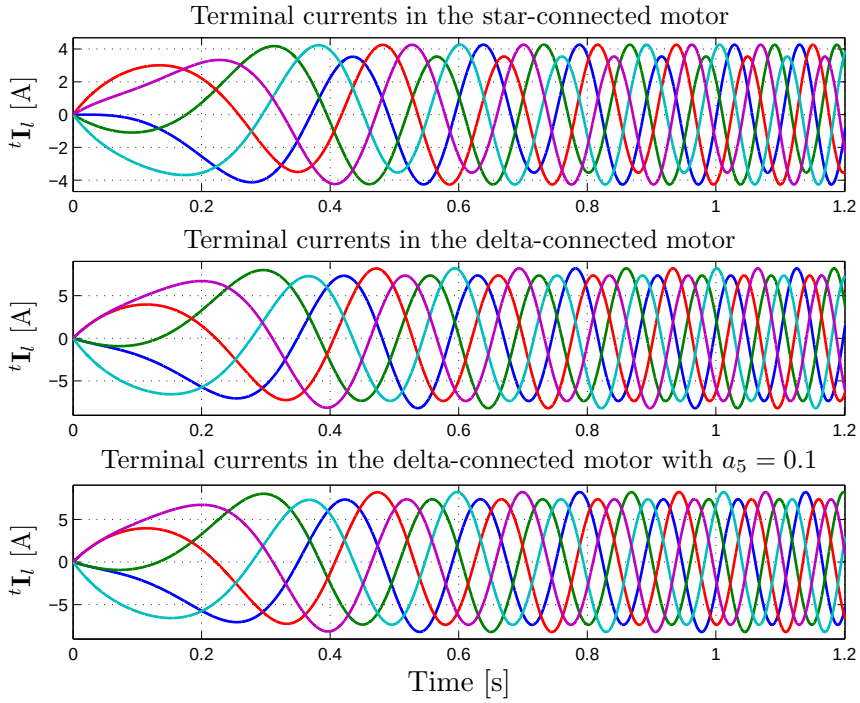

Figure 3.7: Terminal currents in the fixed reference frame Σ_t.

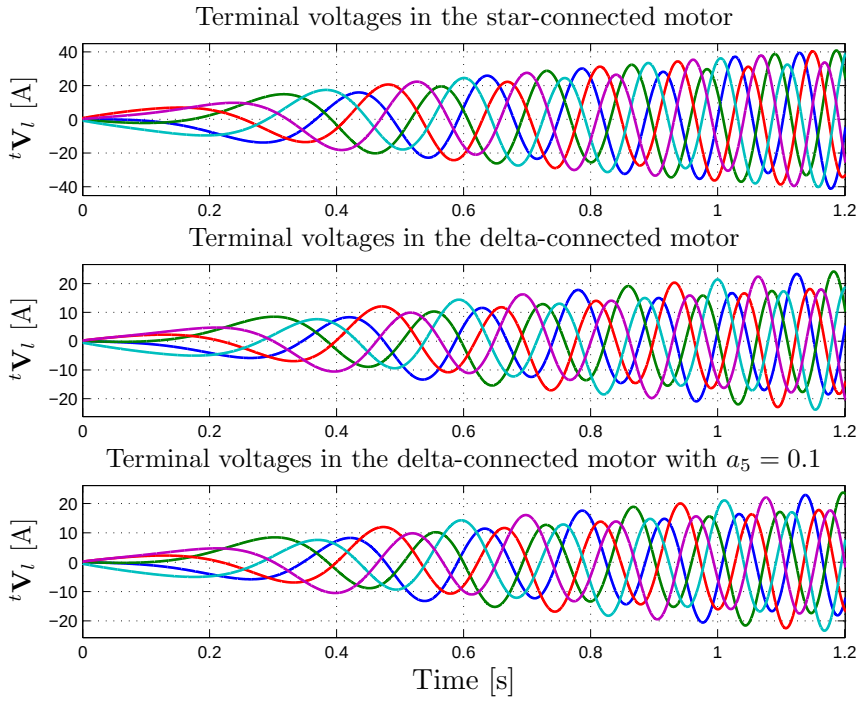

Figure 3.8: Terminal voltages in the fixed reference frame Σ_t.

the three terminal current and voltage vectors ${}^t\mathbf{I}_l$, ${}^t\mathbf{V}_l$ for the three motors are shown Fig. 3.7 and Fig. 3.8, respectively. Note that the transient of the terminal currents and the terminal voltages for a delta-connected motor is the same in both cases 2 and 3 because the control law (4.29) can not control the last component ${}^{\omega}\overline{I}_{s5}$.
In conclusion, the simulation results are agree with the differences shown in Tab.3.1.

Chapter 4

Multi-phase Vectorial Control with Currents and Voltages Saturations

Multi-phase machines have higher torque-to-volume ratio, compared to three-phase ones, due to the injection of higher order current harmonics for the machines with concentrated winding and nearly rectangular back-emf, see [15], [16], [37]. In [41] and [42] the effects of the voltage and current limits on the third harmonic injection are considered. In [41] the voltage and the current constraints are rewritten as 2-norm constraints of the transformed vectors obtaining a field weakening algorithm, while in [42] the voltage 1-norm constraint of the voltage is taken into account. Almost all the abovementioned papers consider specific motors with 5 or 7 phases where only the first and the third current harmonics are injected. Moreover although the amplitude of the injected harmonics is tied to the harmonic spectrum of the back-emf, it is not clear how the current references are obtained.
This chapter addresses the torque control of m_s-phase permanent magnet synchronous machines where the first odd harmonics below m_s are injected. A new vectorial approach to describe the voltage and current limits is proposed. Starting from the transformed dynamic equations and using the voltage and current constraints, the optimal current references is obtained. It holds for an arbitrary number of star connected phases and an arbitrary shape of the rotor flux. Some simulation results for a 7-phase motor validate the proposed control law. The main contents of this chapter have been published in [43], [44] (for a multi-phase synchronous motor) and in [45] (for a 5-phase synchronous motor).

4.1 Transformed dynamic equations

In the complex rotating reference frame $\overline{\Sigma}_\omega$ the m_s-phase star-connected motor can be seen as a set of $(m_s - 1)/2$ independent electrical fictitious machines rotating at different velocity $kp\omega_m$ and characterized by the k-th coefficient of the rotor flux, see Sec. 2.2. This concept is

the generalization of the Multi-machine representation in [15] and it is shown in Fig. 4.1 where different colors define the different machines.
Since injecting the first odd harmonics with order below m_s it is possible to increase the motor torque of a multi phase motor, let us now consider the case of balanced voltage and current stator vectors ${}^t\mathbf{V}_s$ and ${}^t\mathbf{I}_s$ composed by the first $(m_s-1)/2$ harmonics:

$$ {}^t\mathbf{V}_s = \underset{1:m_s}{{}^{h}[\![V_{sh}]\!]} = \sum_{k=1:2}^{m_s-2} \underset{1:m_s}{{}^{h}[\![V_{mk}\cos(k\theta - k(\theta_{vk} - (h-1)\gamma_s))]\!]} \tag{4.1} $$

$$ {}^t\mathbf{I}_s = \underset{1:m_s}{{}^{h}[\![I_{sh}]\!]} = \sum_{k=1:2}^{m_s-2} \underset{1:m_s}{{}^{h}[\![I_{mk}\cos(k\theta - k(\theta_{ik} - (h-1)\gamma_s))]\!]}, \tag{4.2} $$

where V_{mk} and I_{mk} are the amplitude of the balanced harmonics components of order k and θ_{vk}, θ_{ik} are proper initial phase shifts. In this case the transformed current and voltage vectors ${}^{\omega}\overline{\mathbf{I}}_s = {}^t\overline{\mathbf{T}}^*_{\omega N}\,{}^t\mathbf{I}_s$ and ${}^{\omega}\overline{\mathbf{V}}_s = {}^t\overline{\mathbf{T}}^*_{\omega N}\,{}^t\mathbf{V}_s$ are (mathematical details are reported in App.C.4):

$$ {}^{\omega}\overline{\mathbf{I}}_s = \underset{1:2:m_s-2}{{}^{k}\left|\left[\overline{I}_{sk}\right]\right|} = \underset{1:2:m_s-2}{{}^{k}\left|\left[I_{dk} + jI_{qk}\right]\right|} = \sqrt{\frac{m_s}{2}} \underset{1:2:m_s-2}{{}^{k}\left|\left[I_{mk}\, e^{jk\theta_{ik}}\right]\right|} \tag{4.3} $$

$$ {}^{\omega}\overline{\mathbf{V}}_s = \underset{1:2:m_s-2}{{}^{k}\left|\left[\overline{V}_{sk}\right]\right|} = \underset{1:2:m_s-2}{{}^{k}\left|\left[V_{dk} + jV_{qk}\right]\right|} = \sqrt{\frac{m_s}{2}} \underset{1:2:m_s-2}{{}^{k}\left|\left[V_{mk}\, e^{jk\theta_{vk}}\right]\right|} \tag{4.4} $$

where I_{dk}, I_{qk}, V_{dk} and V_{qk} are, respectively, the *direct* and *quadrature* components of the current and voltage vectors $\overline{I}_{sk}$ and $\overline{V}_{sk}$. The modulus $|\overline{I}_{sk}|$ and $|\overline{V}_{sk}|$ are related to the amplitude I_{mk} and V_{mk} by the following relations:

$$ |\overline{I}_{sk}| = \sqrt{I_{dk}^2 + I_{qk}^2} = \sqrt{\frac{m_s}{2}} I_{mk} = I_{Mk}, \tag{4.5} $$

$$ |\overline{V}_{sk}| = \sqrt{V_{dk}^2 + V_{qk}^2} = \sqrt{\frac{m_s}{2}} V_{mk} = V_{Mk} \tag{4.6} $$

Expressions (4.4), (4.3), (4.5) and (4.6) show that the harmonics of order k and amplitude V_{mk} and I_{mk} in (4.1) and (4.2) are transformed into vectors $\overline{V}_{sk}$ and $\overline{I}_{sk}$ with modulus $V_{Mk} = \sqrt{\frac{m_s}{2}}\, V_{mk}$ and $I_{Mk} = \sqrt{\frac{m_s}{2}}\, I_{mk}$ which move in the complex subspace $\overline{\Sigma}_{\omega k}$. In other words each harmonic of order k is related to the fictitious electrical machine rotating at the same frequency $k\omega_m$ and characterized by the k-th coefficient a_k of the rotor flux. According to this in Fig. 4.1 the color of the 1-st voltage and current harmonics is yellow, while the color of the 3-rd voltage and current harmonics is orange.
Substituting (2.22) and (4.3) in (2.23) the motor torque can be rewritten as:

$$ \tau_m = \mathfrak{Re}\left({}^{\omega}\overline{\mathbf{K}}^*_{\tau N}\,{}^{\omega}\overline{\mathbf{I}}_s\right) = p\varphi_c \sqrt{\frac{m_s}{2}} \sum_{k=1:2}^{m_s-2} k a_k I_{qk}. \tag{4.7} $$

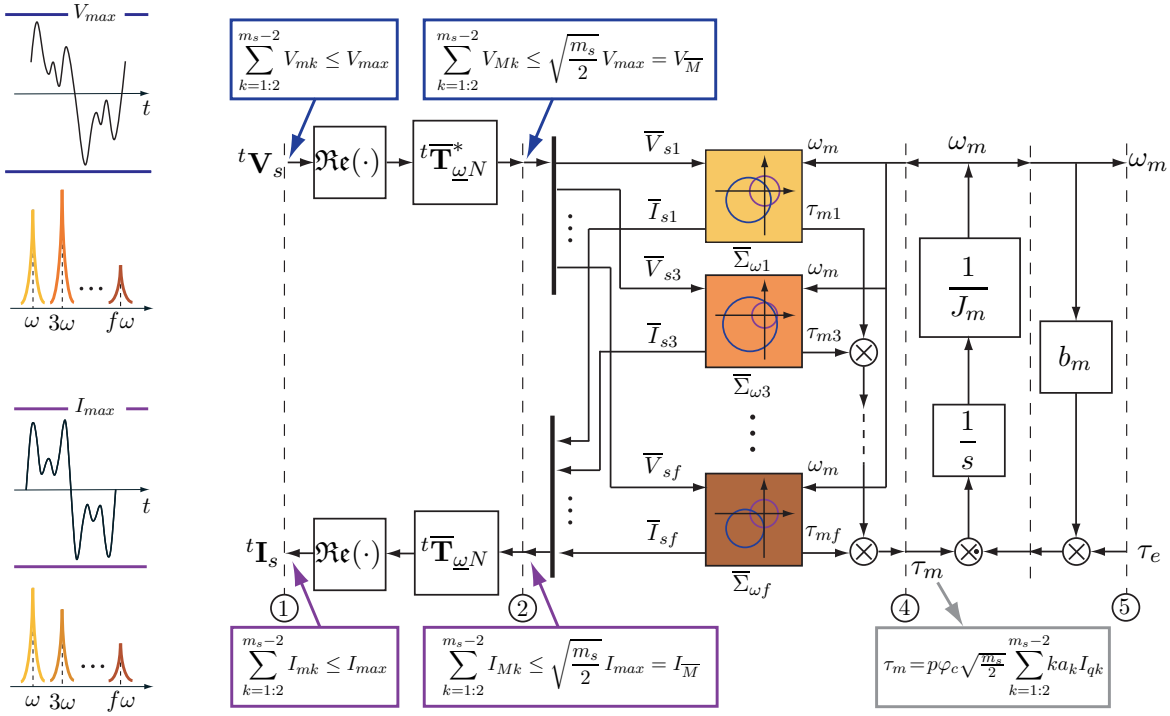

Figure 4.1: Multi subspaces scheme of a m_s-phase motor in the complex rotating frame $\overline{\Sigma}_\omega$.

This torque equation is the sum of individual contribution of each fictitious machine and it shows the dependence of torque τ_m on the quadrature components I_{qk} of the current vectors $\overline{I}_{sk}$. In (2.22) the direct components K_{dk} of the torque vectors $\overline{K}_{\tau k}$ are equal to zero therefore the direct components I_{dk} of the current vectors $\overline{I}_{sk}$ dissipate power without producing torque. From (4.7) it is clear that the torque production capability of the machine increases injecting the first odd harmonics with order below to m_s. Moreover it shows that the motor torque is generated by the interaction between the harmonics a_k of the rotor flux and the stator current harmonic with the same order k. Therefore the amplitude of the injected harmonics is tied to the harmonic spectrum of the rotor flux (it is uselfull to apply high I_{qk} in subspaces with high components ka_k).

4.2 Multi Harmonics Constraints

The amplitudes of components V_{sh} and I_{sh} of the voltage and current vectors ${}^t\mathbf{V}_s$ and ${}^t\mathbf{I}_s$ in (4.1) and (4.2) are bounded, respectively, by the maximum voltage V_{max} of the inverter DC link and the maximum rated current I_{max}, thus the following constraints hold:

$$\sum_{k=1:2}^{m_s-2} V_{mk} \le V_{max}\,, \qquad \sum_{k=1:2}^{m_s-2} I_{mk} \le I_{max}. \tag{4.8}$$

Defining the constraint vectors $\mathbf{V}_M$, $\mathbf{I}_M$ and $\mathbf{K}_\tau \in \mathbb{R}^{\frac{m_s-1}{2}}$ as:

$$\mathbf{V}_M = \underset{1:2:m_s-2}{\overset{k}{\left\|\left[\, |\overline{V}_{sk}| \,\right]\right\|}}, \quad \mathbf{I}_M = \underset{1:2:m_s-2}{\overset{k}{\left\|\left[\, |\overline{I}_{sk}| \,\right]\right\|}}, \quad \mathbf{K}_\tau = \underset{1:2:m_s-2}{\overset{k}{\left\|\left[\, |\overline{K}_{\tau k}| \,\right]\right\|}}$$

the voltage and current constraints (4.8), multiplied by constant $\sqrt{\frac{m_s}{2}}$, can be rewritten as a 1-norm constraint on vectors $\mathbf{V}_M$ and $\mathbf{I}_M$:

$$\| \mathbf{V}_M \|_1 = \sum_{k=1:2}^{m_s-2} V_{Mk} \leq \sqrt{\frac{m_s}{2}}\, V_{max} = V_{\overline{M}}, \tag{4.9}$$

$$\| \mathbf{I}_M \|_1 = \sum_{k=1:2}^{m_s-2} I_{Mk} \leq \sqrt{\frac{m_s}{2}}\, I_{max} = I_{\overline{M}}, \tag{4.10}$$

where V_{Mk} and I_{Mk} are the moduli of vectors $\overline{V}_{sk}$ and $\overline{I}_{sk}$, respectively:

$$V_{Mk} = \sqrt{V_{dk}^2 + V_{qk}^2} = \sqrt{\frac{m_s}{2}} V_{mk}\,, \qquad I_{Mk} = \sqrt{I_{dk}^2 + I_{qk}^2} = \sqrt{\frac{m_s}{2}} I_{mk}.$$

The constraint equations in (4.8) act on the power section ①, while the transformed constraints (4.9), (4.10) act on the power section ②, see Fig. 4.1.
In the design of the control law there are some degrees of freedom that will be used to decide how to distribute the maximum voltage $V_{\overline{M}}$ and current $I_{\overline{M}}$ into the components V_{Mk} and I_{Mk} to satisfy the constraints (4.9) and (4.10). In the next sections it will be shown how this defines in each subspace $\overline{\Sigma}_{\omega k}$ a specific operative zone that modifies the torque producing capability of the subspace.

4.3 Vectorial control

In steady-state condition, the dynamic equation of the electrical part is:

$${}^{\omega}\overline{\mathbf{V}}_s = ({}^{\omega}\overline{\mathbf{R}}_s + {}^{\omega}\overline{\mathbf{J}}_s\, {}^{\omega}\overline{\mathbf{L}}_s)\, {}^{\omega}\overline{\mathbf{I}}_d + {}^{\omega}\overline{\mathbf{K}}_\tau\, \omega_{md}$$

which is equivalent to the following $(m_s - 1)/2$ equations of the complex subspaces $\overline{\Sigma}_{\omega k}$:

$$\overline{V}_{sk} = \overline{Z}_{sk}\overline{I}_{sk} + jK_{qk}\omega_m\,, \quad \overline{Z}_{sk} = R_s + j\, k\, p\, \omega_m L_{sk}. \tag{4.11}$$

Introducing the current and voltage vectors $\overline{I}_{sk} = I_{dk} + jI_{qk}$ and $\overline{V}_{sk} = V_{dk} + jV_{qk}$ in (4.11) and then substituting the obtained equation in (4.6) the voltage constraint $\sqrt{V_{dk}^2 + V_{qk}^2} \leq V_{Mk}$ can be rewritten as follows:

$$(I_{dk} - X_{0k})^2 + (I_{qk} - Y_{0k})^2 \leq R_{0k}^2 \tag{4.12}$$

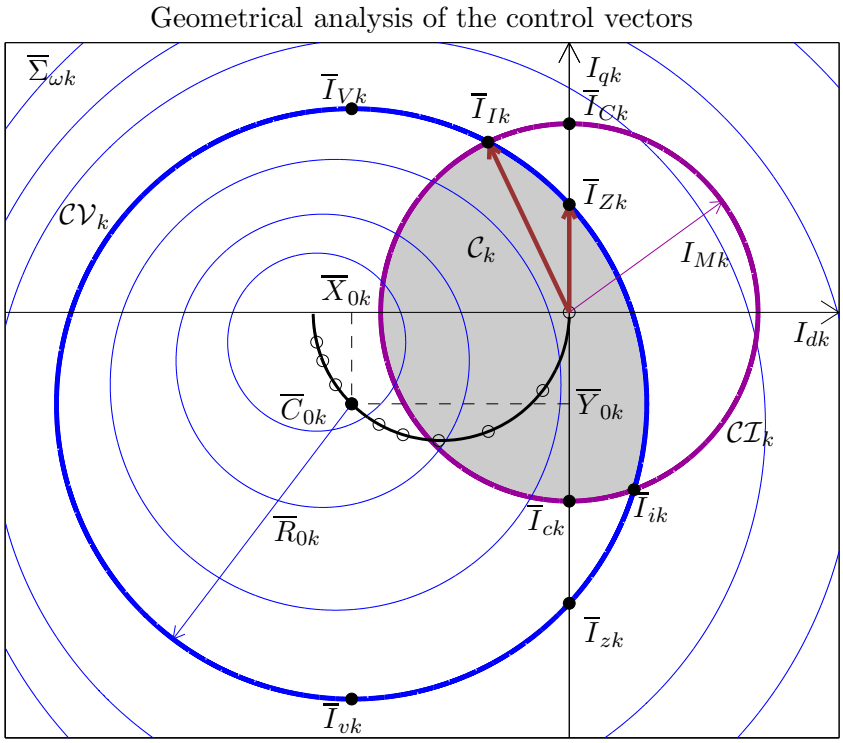

Figure 4.2: Maximum current circles $\mathcal{CV}_k$ and $\mathcal{CI}_k$ in complex subspace $\overline{\Sigma}_{\omega k}$.

where:

$$R_{0k}(\omega_m) = \left|\overline{R}_{0k}\left(\omega_m\right)\right|_{|\overline{V}_{sk}|=V_{Mk}} = \frac{V_{Mk}}{|Z_{sk}|} \tag{4.13}$$

$$X_{0k}(\omega_m) = Re(\overline{C}_{0k}) = \frac{-K_{qk}\, k\, p\, \omega_m^2 L_{sk}}{|\overline{Z}_{sk}|^2} \tag{4.14}$$

$$Y_{0k}(\omega_m) = Im(\overline{C}_{0k}) = \frac{-K_{qk}\, \omega_m R_s}{|\overline{Z}_{sk}|^2}. \tag{4.15}$$

Relation (4.12) is the mathematical expression of the maximum voltage circle $\mathcal{CV}_k$ corresponding to the value V_{Mk} that satisfies the voltage constraint (4.9). The terms $\overline{C}_{0k}(\omega_m) = X_{0k} + j\, Y_{0k}$ and $R_{0k}\left(\omega_m\right)$ represent the center and the radius of the maximum voltage circle $\mathcal{CV}_k$. These terms are function of the parameter ω_m. When velocity ω_m increases the radius R_{0k} of circle $\mathcal{CV}_k$ decreases and its center $\overline{C}_{0k}$ moves in the complex plane $\overline{\Sigma}_{\omega k}$ on a circle with center in $\left(\frac{-K_{qk}}{2\, k\, p\, L_{sk}},\, 0\right)$ and radius $\frac{K_{qk}}{2\, k\, p\, L_{sk}}$. The current vector $\overline{I}_{sk}$ satisfies the voltage constraint only if its modulus is inside the maximum voltage circle $\mathcal{CV}_k$. Therefore in order to satisfy the current constraint (4.10) the current vector $\overline{I}_{sk}$ must also stay inside the maximum circle $\mathcal{CI}_k$ having center in the origin and radius I_{Mk}:

$$I_{dk}^2 + I_{qk}^2 \leq I_{Mk}^2. \tag{4.16}$$

A graphical representation of the voltage and current circles $\mathcal{CV}_k$ and $\mathcal{CI}_k$ in the complex plane $\overline{\Sigma}_{\omega k}$ for a particular value of ω_m is shown in blue and violet in Fig. 4.2. The intersection zone $\mathcal{C}_k$ between the two circles, shown in grey in Fig. 4.2, represents the area in which both the voltage and current constraints are satisfied. Subtracting equation (4.16) from equation (4.12) one obtains the following relation:

$$-2X_{0k}I_{dk} - 2Y_{0k}I_{qk} + X_{0k}^2 + Y_{0k}^2 - R_{0k}^2 + I_{Mk}^2 = 0. \tag{4.17}$$

Using (4.17) together with (4.16), one obtains the intersection points $\overline{I}_{Ik}$ and $\overline{I}_{ik}$ of circle $\mathcal{CV}_k$ with circle $\mathcal{CI}_k$:

$$\overline{I}_{I,ik} = \frac{Y_{0k}}{|\overline{C}_{0k}|}\left[\frac{X_{0k}P_k}{|\overline{C}_{0k}|} \pm \sqrt{I_{Mk}^2 - \frac{Y_{0k}^2 P_k^2}{|\overline{C}_{0k}|^2}}\right]\left(1 - j\frac{X_{0k}}{Y_{0k}}\right) + jP_k \tag{4.18}$$

where $P_k = \frac{|\overline{C}_{0k}|^2 - R_{0k}^2 + I_{Mk}2}{2Y_{0k}}$.
The coordinates of the other points shown in Fig. 4.2 are:

$$\overline{I}_{Vk}(\omega_m) = X_{0k}(\omega_m) + jY_{0k}(\omega_m) + jR_{0k}(\omega_m) \tag{4.19}$$

$$\overline{I}_{Zk}(\omega_m) = jY_{0k}(\omega_m) + j\sqrt{R_{0k}^2(\omega_m) - X_{0k}^2(\omega_m)} \tag{4.20}$$

$$\overline{I}_{Ck} = jI_{Mk} \tag{4.21}$$

$$\overline{I}_{ck} = -jI_{Mk} \tag{4.22}$$

$$\overline{I}_{zk}(\omega_m) = jY_{0k}(\omega_m) - j\sqrt{R_{0k}^2(\omega_m) - X_{0k}^2(\omega_m)} \tag{4.23}$$

$$\overline{I}_{vk}(\omega_m) = jY_{0k}(\omega_m) - jR_{0k}(\omega_m) \tag{4.24}$$

Note that the coordinates of all points shown in Fig. 4.2 are function of the components V_{Mk} and I_{Mk}. Indeed the constraints distribution defines in each subspace $\overline{\Sigma}_{\omega k}$ a specific operative zone that modifies the torque producing capability of the subspace (the torque τ_{mk} generated in the subspace $\overline{\Sigma}_{\omega k}$ can be provided using only the current $\overline{I}_{sk} \in \mathcal{C}_k$). Since the quadrature components I_{qk} act on the motor torque while the direct components I_{dk} modify the magnetizing rotor flux, the two main control laws used in the literature [46], [47] are:

1) *field oriented control* where the direct component of the current vector is zero $I_{dk} = 0$ so $\overline{I}_{sk} = max\left\{\overline{I}_{Ck}, \overline{I}_{Zk}\right\} \in \mathcal{C}_k$;
2) *flux weakening control* where also the direct component of the current vector is used $I_{dk} \neq 0$ so $\overline{I}_{sk} = max\left\{\overline{I}_{vk}, \overline{I}_{Ik}\right\} \in \mathcal{C}_k$.

The first control produces a constant torque at low velocity while the second one ensures a constant power at high velocity. At high velocity when the back electromotive force (due to the permanent magnets) approaches the maximum voltage V_{max} the motor torque τ_M drops rapidly with the speed ω_m using the field oriented control (see the operation point $\overline{I}_{sk} = \overline{I}_{Zk}$ in Fig. 4.2).

Instead using the flux weakening control the motor velocity ω_m can be increased because the influence of permanent magnets flux linkage is reduced by the demagnetizing (negative) I_{dk} current. Since the direct component weakens the flux but it does not produce torque, the operation point $\overline{I}_{sk} = \overline{I}_{Ik}$ produces an higher torque respect to $\overline{I}_{sk} = \overline{I}_{Zk}$ dissipating power. Note that in Fig. 4.2 the points $\overline{I}_{Ck}$ and $\overline{I}_{zk}$ cannot be used in the control because they do not satisfy the constraints ($\overline{I}_{Ck}$ and $\overline{I}_{zk} \notin \mathcal{C}_k$).

4.4 Constraints distributions

The torque can be provided using only the current vectors $\overline{I}_{sk}$ inside the intersection zone $\mathcal{C}_k$ of the maximum voltage and current circles $\mathcal{CV}_k$ and $\mathcal{CI}_k$, so the voltage and current limits determine the torque producing capability of the subspace $\overline{\Sigma}_{\omega k}$. For a given ω_m, it is possible to modulate the components V_{Mk} and I_{Mk} in each subspace $\overline{\Sigma}_{\omega k}$ in order to increase or decrease the maximum voltage and current circles $\mathcal{CV}_k$ and $\mathcal{CI}_k$ satisfying the constraints (4.9) and (4.10). For a 5-phase motor, the current and voltage 1-norm constraints can be represented as planes in $\mathbb{R}^2$ as shown in Fig. 4.3 and Fig. 4.4. From (2.3) it is clear that the torque τ_m is tied to the scalar product of $\mathbf{K}_\tau$ and $\mathbf{I}_M$ and for this reason the vector $\mathbf{K}_\tau$ has been reported in the current 1-norm constraint of Fig. 4.3.a and Fig. 4.4.a. The torque control law described in the next section is a generalization, for a m_s-phase machine, of the following two cases of constraints distribution for a 5-phase machine:

Case 1) The optimal distribution of the current constraint minimizing the power dissipation is reported in Fig. 4.3.a. The vector $\mathbf{I}_{Md}$ does not satisfy the current constraint, therefore this distribution cannot be used. The scalar product of the three vectors $\mathbf{I}_{Ma}$, $\mathbf{I}_{Mb}$ and $\mathbf{I}_{Mc}$ with the vector $\mathbf{K}_\tau$ is the same but the vectors $\mathbf{I}_{Ma}$ and $\mathbf{I}_{Mb}$ do not minimize the power dissipation because their moduli are greater than the modulus of $\mathbf{I}_{Mc}$. Thus, the current constraint vector which minimizes the power dissipation is the vector $\mathbf{I}_{Mc}$ with the minimum modulus parallel to

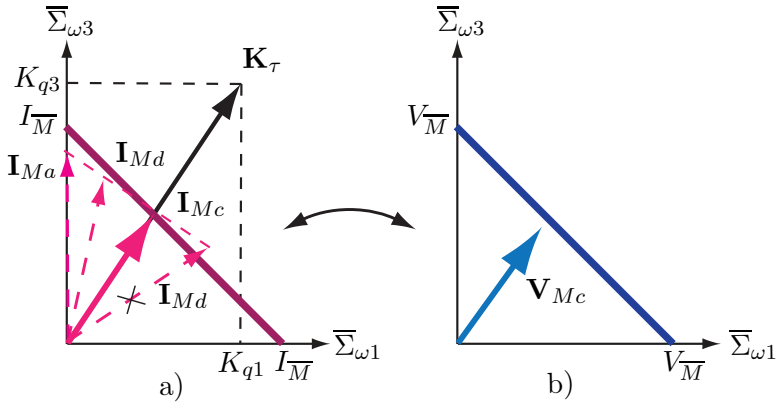

Figure 4.3: Minimum dissipation constraints, $m_s = 5$: a) current, b) voltage.

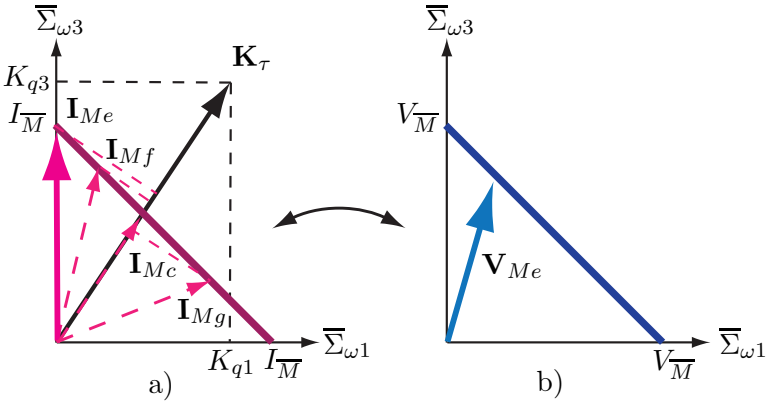

Figure 4.4: Maximum torque constraints, $m_s = 5$: a) current, b) voltage.

$\mathbf{K}_\tau$. The voltage vector $\mathbf{V}_{\overline{Mc}}$ related to the current vector $\mathbf{I}_{\overline{Mc}}$ is reported in Fig. 4.3.b.

Case 2) The optimal distribution of the current constraint maximizing the torque τ_m is reported in Fig. 4.4.a. The vectors $\mathbf{I}_{Mc}$, $\mathbf{I}_{Mf}$ and $\mathbf{I}_{Mg}$ do not maximize the torque because their projections onto $\mathbf{K}_\tau$ are smaller than the projection of vector $\mathbf{I}_{Me}$. The vector $\mathbf{I}_M = \mathbf{I}_{Me}$ that maximizes the scalar product $\mathbf{K}_\tau^{\mathrm{T}}\,\mathbf{I}_M$ is obtained giving the maximum value $I_{\overline{M}}$ to the component I_{M3} related to the maximum component K_{q3} of vector $\mathbf{K}_\tau$. The voltage vector $\mathbf{V}_{\overline{Me}}$ related to the current vector $\mathbf{I}_{\overline{Me}}$ is reported in Fig. 4.4.b.

Generalizing these two cases, four different constraints distribution into the subspaces $\overline{\Sigma}_{\omega k}$ will be considered, see Fig. 4.5. The dashed lines are the voltage and current circles $\mathcal{CV}_k$ and $\mathcal{CI}_k$ showed in Fig. 4.2, while the solid lines are the new circles $\mathcal{CV}'_k$ and $\mathcal{CI}'_k$ obtained modulating the components V_{Mk} and I_{Mk}.
In Fig. 4.5.a the operation point is $\overline{I}_{sk} = \overline{I}_{Zk} \equiv \overline{I}_{Ck} \equiv \overline{I}_{Ik}$, so the torque can be generated using only the quadrature component I_{qk}. Given the current constraint I_{Mk} and using equations (4.20) and (4.21), one obtains the component V_{Mk}:

$$V_{Mk} = |\overline{Z}_{sk}|\sqrt{X_{0k}^2 + (I_{Mk} - Y_{0k})^2}. \tag{4.25}$$

In Fig. 4.5.b the operation point is the origin $\overline{I}_{sk} = 0$ because $I_{Mk} = 0$, so the torque generated by subspace $\Sigma_{\omega k}$ is zero. The component V_{Mk} has the following structure:

$$V_{Mk} = |\overline{Z}_{sk}|\,\left|\overline{C}_{0k}\right| = K_{qk}\,\omega_m. \tag{4.26}$$

In Fig. 4.5.c the operation point is $\overline{I}_{sk} = \overline{C}_{0k}$ because $V_{Mk} = 0$, so the torque generated by subspace $\Sigma_{\omega k}$ is negative. The component I_{Mk} has the following structure:

$$I_{Mk} = \left|\overline{C}_{0k}\right| = K_{qk}\,\omega_m/|\overline{Z}_{sk}|. \tag{4.27}$$

In Fig. 4.5.d the operation point is $\overline{I}_{sk} = \overline{I}_{Ik} \equiv \overline{I}_{ik}$. Also in this case the torque generated by subspace $\Sigma_{\omega k}$ is negative. Given the current constraint I_{Mk}, from (4.18) one obtains $R_{0k} + I_{Mk} =$

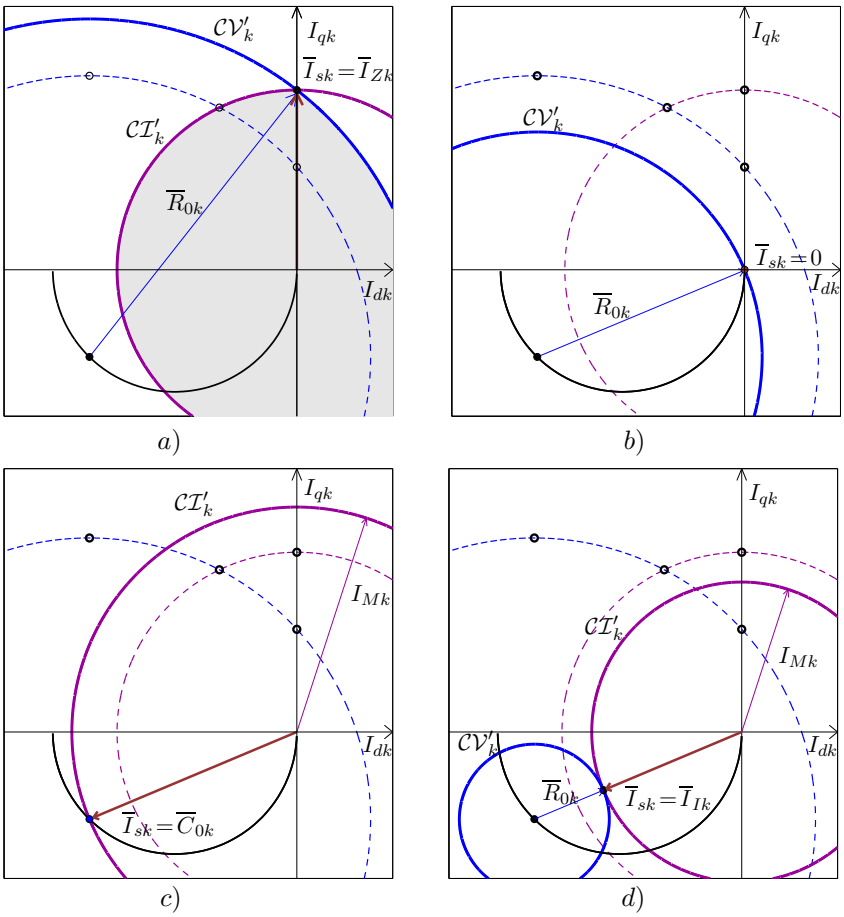

Figure 4.5: Maximum current circles $\mathcal{CV}_k$ and $\mathcal{CI}_k$ in subspace $\overline{\Sigma}_{\omega k}$ obtained modulating the components V_{Mk} and I_{Mk} .

$|\overline{C}_{0k}|$ and the component V_{Mk} is:

$$V_{Mk} = |\overline{Z}_{sk}| \left(|\overline{C}_{0k}| - I_{Mk} \right) = K_{qk}\omega_m - |\overline{Z}_{sk}| I_{Mk}. \tag{4.28}$$

These four cases show that when the operation point is defined, the components V_{Mk} and I_{Mk} are bounded by the equations (4.16) and (4.12).

4.5 Torque control

Torque τ_m can be controlled by current vectors ${}^{\omega}\overline{\mathbf{I}}_d$ in frame $\overline{\Sigma}_{\omega}$ not exceeding the constraints on the maximum input voltage and current. When ${}^{\omega}\overline{\mathbf{I}}_d$ is constant, the condition ${}^{\omega}\overline{\mathbf{I}}_s = {}^{\omega}\overline{\mathbf{I}}_d$ can be achieved using the following control law:

$${}^{\omega}\overline{\mathbf{V}}_s = {}^{\omega}\overline{\mathbf{Z}}_s \, {}^{\omega}\overline{\mathbf{I}}_s + {}^{\omega}\overline{\mathbf{K}}_{\tau N} \, \omega_m - \mathbf{K}_c({}^{\omega}\overline{\mathbf{I}}_s - {}^{\omega}\overline{\mathbf{I}}_d) \tag{4.29}$$

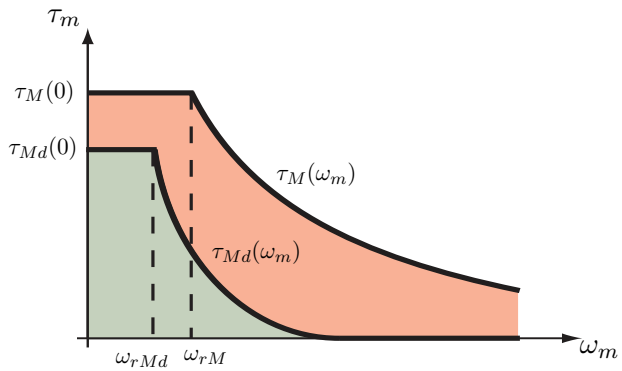

Figure 4.6: Limit torques for a multi-phase synchronous motors.

where $\mathbf{K}_c > 0$ is a control diagonal matrix and ${}^{\omega}\mathbf{I}_d$ is:

$$ {}^{\omega}\overline{\mathbf{I}}_d = \begin{cases} {}^{\omega}\overline{\mathbf{I}}_M & \text{if} \quad \tau_d \geq \tau_M(\omega_m) \\ {}^{\omega}\overline{\mathbf{I}}_{cc} & \text{if} \quad \tau_{Md}(\omega_m) < \tau_d < \tau_M(\omega_m) \\ {}^{\omega}\overline{\mathbf{I}}_{md} & \text{if} \quad 0 \leq \tau_d \leq \tau_{Md}(\omega_m) \end{cases} \tag{4.30} $$

where τ_d is the desired torque. $\tau_{Md}(\omega_m)$ is the maximum torque with minimum dissipation while $\tau_M(\omega_m)$ is the maximum torque. These two limit torques are function of the motor parameters, the voltage and current constraints and the control law. In Fig. 4.6 the two curves $\tau_{Md}(\omega_m)$ and $\tau_M(\omega_m)$ define three zones in the (τ_m, ω_m) torque plane: the green zone represents the region where the desired torque τ_d can be provided using the *minimum dissipation torque control*; the red zone represents the region where the torque τ_d is obtained using the *convex combination torque control*; the white zone is not allowed because τ_d cannot exceed the maximum torque τ_M, in this area the *maximum torque control is used*.
This control law, used together with relation (4.29), provides the desired torque τ_d satisfying the constraints (4.9), (4.10) and minimizing, when possible, the current dissipation.

4.5.1 Minimum dissipation torque control

The current constraint vector $\mathbf{I}_M$ which minimizes the power dissipation is the vector with the minimum modulus parallel to vector $\mathbf{K}_\tau$ (see Fig. 4.3.a):

$$ \mathbf{I}_M = \frac{\tau_d}{|\mathbf{K}_\tau|}\hat{\mathbf{K}}_\tau = \frac{\mathbf{K}_\tau}{|\mathbf{K}_\tau|^2}\tau_d = \Big\| \Big[\tau_d \widetilde{K}_k \Big] \Big\|_{1:2:m_s-2}^{k} \tag{4.31} $$

where $\widetilde{K}_k = \dfrac{K_{qk}}{|{}^{\omega}\mathbf{K}_\tau|^2} = \dfrac{ka_k}{p\varphi_c\sqrt{\dfrac{m_s}{2}\displaystyle\sum_{k=1:2}^{m_s-2}(ka_k)^2}}$

are the distribution coefficients of the current constraint $I_{\overline{M}}$ into the subspaces $\overline{\Sigma}_{\omega k}$. Only the

quadrature components I_{qk} of the current vectors $\overline{I}_{sk}$ are used to generate torque (see Fig. 4.5.a), therefore the current vector ${}^{\omega}\overline{\mathbf{I}}_{md}$ which minimizes the power dissipation is:

$$ {}^{\omega}\mathbf{I}_{md} = \Big\| \Big[\; j\tau_d \, \widetilde{K}_k \; \Big] \Big\|_{1:2:m_s-2}^{k} = \frac{{}^{\omega}\overline{\mathbf{K}}_{\tau N}}{|{}^{\omega}\overline{\mathbf{K}}_{\tau N}|^2} \, \tau_d. \tag{4.32} $$

Note that the current vector ${}^{\omega}\overline{\mathbf{I}}_{md}$ is parallel to the torque vector ${}^{\omega}\overline{\mathbf{K}}_{\tau}$. Substituting (4.31) in (4.25) and using the voltage constraint (4.9), one obtains the following equation:

$$ \sum_{k=1:2}^{m_s-2} \underbrace{|\overline{Z}_{sk}| \sqrt{X_{0k}^2 + (\tau_d \, \widetilde{K}_k - Y_{0k})^2}}_{V_{\overline{M}k}} = V_{\overline{M}}. \tag{4.33} $$

At low velocity the current constraint limits the torque. Using (4.31) and the current constraint (4.10) the maximum torque with minimum dissipation at low velocity is:

$$ \tau_{Md}(0) = \frac{I_{\overline{M}}}{\sum_{k=1:2}^{m_s-2} \widetilde{K}_k}. $$

Substituting $\tau_{Md}(0)$ in (4.33) one obtains the rated velocity ω_{rMd}. When $\omega_m > \omega_{rMd}$, the limit torque decreases and it is limited by the voltage constraint. Given $\omega_m > \omega_{rMd}$, equation (4.33) can be numerically solved with respect to τ_d in order to obtain the maximum torque $\tau_{Md}(\omega_m)$ satisfying minimum dissipation and the voltage and current constraints.
The desired torque τ_d can be obtained with minimum current vector ${}^{\omega}\mathbf{I}_{md}$ only if $\tau_d < \tau_{Md}(\omega_m)$. In Fig. 4.6 the curve $\tau_{Md}(\omega_m)$ defines the green zone representing the region where the desired torque τ_d can be provided minimizing the power dissipation.

4.5.2 Maximum torque control

The maximum torques $\tau_M(\omega_m)$ can be obtained maximizing the projection of the vector $\mathbf{I}_M$ onto the torque vector $\mathbf{K}_{\tau}$, see Fig. 4.4.a. To reach this goal it is necessary to sort the components K_{qk} of the vector $\mathbf{K}_{\tau}$ and apply the following current and voltage constraints distribution:

$$ \begin{cases} I_{Mk} = I_M, & V_{Mk} = |\overline{Z}_{sG}| \sqrt{X_{0G}^2 + (I_M - Y_{0G})^2} & \text{if } k = G \\ I_{Mk} = |\overline{C}_{0k}|, & V_{Mk} = 0 & \text{if } k \in N_g \\ I_{Mk} = I_{Mg}, & V_{Mk} = K_{qk} \, \omega_m \; - \; |\overline{Z}_{sg}| \, I_{Mg} & \text{if } k = g \\ I_{Mk} = 0, & V_{Mk} = K_{qk} \, \omega_m & \text{if } k \in O_g \end{cases} \tag{4.34} $$

where $I_M = I_{\overline{M}} - \sum_{k \in N_g} |\overline{C}_{0k}| - I_{Mg}$ and:

- G is the index of the maximum component of $\mathbf{K}_{\tau}$,

- O_g is the set of the subspaces not jet considered,
- N_g is the set of the subspaces already considered,
- g is the index of the considered subspace univocally defined from the motor velocity ω_m (the reason will be explained later).

The subspace $\Sigma_{\omega G}$ related to the maximum component K_{qk} of the torque vector is shown in Fig. 4.2, the subspace $\Sigma_{\omega g}$ is shown in Fig. 4.5.d and the subspaces not yet considered and already considered are shown, respectively, in Fig. 4.5.b and Fig. 4.5.c. Substituting the components V_{Mk} of (4.34) in the voltage constraint (4.9) one obtains the following equation:

$$\sum_{k\in[g,Og]} K_{qk}\omega_m + |\overline{Z}_{sG}|\sqrt{X_{0G}^2+(I_M-Y_{0G})^2} - |\overline{Z}_{sg}|I_{Mg} = V_{\overline{M}} \tag{4.35}$$

Given ω_m, equation (5.19) can be rewritten as:

$$\sqrt{X_{0G}^2+\left(I_{\overline{M}}-\sum_{k\in N_g}|\overline{C}_{0k}|-I_{Mg}-Y_{0G}\right)^2} = \frac{V_{\overline{M}}-\sum\limits_{k\in[g,Og]}K_{qk}\,\omega_m}{|\overline{Z}_{sG}|}+\frac{|\overline{Z}_{sg}|}{|\overline{Z}_{sG}|}\,I_{Mg}$$

This relation can be solved with respect to I_{Mg} obtaining the voltage V_{Mg} of the considered subspaces. The components $\overline{I}_{sk}$ of the maximum current vector ${}^{\omega}\overline{\mathbf{I}}_M$ are univocally defined from the constraints distribution:

$${}^{\omega}\overline{\mathbf{I}}_M = \left|\left[\overline{I}_{sk}\right]\right|_{1:2:m_s-2}^{k},\quad \overline{I}_{sk}=\begin{cases}\max\{\overline{I}_{vk},\overline{I}_{Ik},\overline{I}_{Zk}\}\in\mathcal{C}_k & \text{if } k=G\\ X_{0k}+jY_{0k} & \text{if } k\in N_g\\ \overline{I}_{Ik} & \text{if } k=g\\ 0 & \text{if } k\in O_g\end{cases} \tag{4.36}$$

Note that $\Sigma_{\omega G}$ is the only subspace that generates torque because the current components in the other subspaces are negative or equal to zero.

When $\omega_m \le \omega_{rM}$ the current constraint limits the torque and the maximum value $I_{\overline{M}}$ is given only by the subspace $\Sigma_{\omega k}$ related to the maximum component K_{qk} of vector $\mathbf{K}_\tau$ (see Case 2 of Sec.4.4), then $g=0$, $N_g=\emptyset$ and in this case the equation (4.34) can be rewritten as:

$$\begin{cases} I_{Mk}=I_{\overline{M}},\ V_{Mk}=|\overline{Z}_{sG}|\sqrt{X_{0G}^2+(I_{\overline{M}}-Y_{0G})^2} & \text{if } k=G\\ I_{Mk}=0,\quad V_{Mk}=K_{qk}\,\omega_m & \text{if } k\in O_g\end{cases}$$

and the maximum torque at low velocity is:

$$\tau_M(0)=p\varphi_c\sqrt{\frac{m_s}{2}}Ga_G I_{\overline{M}}.$$

When the velocity ω_m increases the components V_{Mk} increase and there is a velocity ω_{rM} for which the voltage constraint is exactly satisfied. The rated velocity ω_{rM} can be obtained substituting the components V_{Mk} in (4.9). When $\omega_m > \omega_{rM}$ the voltage constraint limits the torque then it is necessary to redistribute the current constraint $I_{\overline{M}}$ into the other subspaces to reduce the components V_{Mk}, see (4.28). Since this operation causes a reduction of the torque (see vector I_{Mf} in Fig. 4.4.a), the current constraint $I_{\overline{M}}$ is redistributed only into the subspaces $\overline{\Sigma}_{\omega k}$ with $k \in [N_g, g]$ minimizing in this way the torque reduction. The current and voltage constraints distribution (4.34) must be applied starting from the subspace $\Sigma_{\omega k}$ related to the minimum component K_{qk} up to the subspace $\Sigma_{\omega G}$. The index g is univocally defined by motor velocity ω_m: it is the first subspace $\Sigma_{\omega g}$ where $V_{Mg} > 0$. At the end, when $g = G$ and $O_g = \emptyset$, the equation (4.34) can be rewritten as:

$$\begin{cases} I_{Mk} = I_{\overline{M}} - \sum_{k \neq G} |\overline{C}_{0k}|, & V_{Mk} = V_{\overline{M}} \quad \text{if } k = G \\ I_{Mk} = |C_{0k}|, & V_{Mk} = 0 \quad \text{if } k \in N_g \end{cases}$$

Summarizing this constraint distribution is a trade off between the torque reduction and the constraints. The maximum torque is obtained when the constraint $I_{\overline{M}}$ is given to the subspace $\Sigma_{\omega G}$ but there is a velocity in which to satisfy the voltage constraint it is necessary to redistribute the current constraint $I_{\overline{M}}$ into the other subspaces. In this way both the constraints are satisfied but the generated torque decreases because the projection of the current vector $\mathbf{I}_{\overline{M}}$ onto the torque vector ${}^{\omega}\mathbf{K}_{\tau}$ does, see vector I_{Mf} in Fig. 4.4.a.
At low velocity the current constraint limits the torque, so the maximum value $I_{\overline{M}}$ is given to the subspace $\Sigma_{\omega G}$ and in the other subspaces the voltage constraint is used to hold the operation point in the origin, then $g = 0$ the set O_g is full and the set N_g is empty.
Instead at high velocity the voltage constraint limits the torque, so the maximum value $V_{\overline{M}}$ is given to the subspace $\Sigma_{\omega G}$ and in the other subspaces the current constraint is used to hold the operation point in the center C_{0k}, then $g = 0$ and the set O_g is empty.
The maximum torque control is obtained choosing ${}^{\omega}\overline{\mathbf{I}}_d = {}^{\omega}\overline{\mathbf{I}}_M$ when $\tau_d \geq \tau_M(\omega_m)$. In Fig. 4.6 the curve τ_M defines the white region that represents the zone not allowed because τ_d cannot exceed the maximum torque.

4.5.3 Convex combination torque control

In Fig. 4.6 the curves τ_{Md} and τ_M define a red zone that represents the region where the two previous control laws cannot be used. In this region the optimal control law which satisfies the constraints (4.9), (4.10) and minimizes the current dissipation is quite complex and difficult to be found. In this case we propose the following suboptimal control law obtained as a convex combination of the maximum current vector ${}^{\omega}\mathbf{I}_M$, see (4.36), and the maximum current vector with minimum dissipation ${}^{\omega}\mathbf{I}_{Md} = \frac{{}^{\omega}\overline{\mathbf{K}}_{\tau}}{|{}^{\omega}\overline{\mathbf{K}}_{\tau}|^2}\tau_{Md}$, see (4.32). When $\tau_{Md} < \tau_d < \tau_M$ the torque τ_d

is obtained using the following current vector:

$$^{\omega}\overline{\mathbf{I}}_{cc} = {}^{\omega}\mathbf{I}_{Md} + \alpha\,({}^{\omega}\mathbf{I}_{M} - {}^{\omega}\mathbf{I}_{Md})$$

where $\alpha = \dfrac{\tau_d - \tau_N(\omega_m)}{\tau_M(\omega_m) - \tau_N(\omega_m)}$.

4.6 Simulation results

The proposed control has been implemented in Matlab/Simulink environment as swhon in Fig. 4.7. Particularly the masked-block on the left implements the saturated vectorial control proposed in this Chapter, while the other two masked-blocks refer to scheme of Sec.3.4. The simulation results have been obtained considering a 7-phase motor with the following electrical and mechanical lumped parameters: $m_s = 7$, $p = 1$, $N_c = 30$, $R_s = 2\,\Omega$, $L_s = 0.03$ H, $M_{s0} = 0.025$ H, $a_{M1} = 1$, $a_{M3} = 1/9$, $a_{M5} = 1/25$, $\varphi_r = 0.02$ Wb, $J_m = 1.6$ kg m^2, $b_m = 0.15$ Nm s/rad, $V_{max} = 100$V, $I_{max} = 35$A $a_1 = 0.40$, $a_3 = 0.3$, $a_5 = 0.25$. The external torque τ_e is zero until $t = 10$ s then $\tau_e = 45$ Nm (see the black dashed line in Fig. 4.8).

The time behaviors of motor velocity ω_m, motor torque τ_m, desired torque τ_d, external torque τ_e and maximum torques τ_M and τ_N with their corresponding trajectories on the torque plane (τ_m, ω_m) are reported in Fig. 4.8. The letters A, B, C, D and E refer to the critical points for the control: A when $\tau_d = \tau_{Md}$, B and D when $\tau_d = \tau_M$, C when the external torque τ_e is

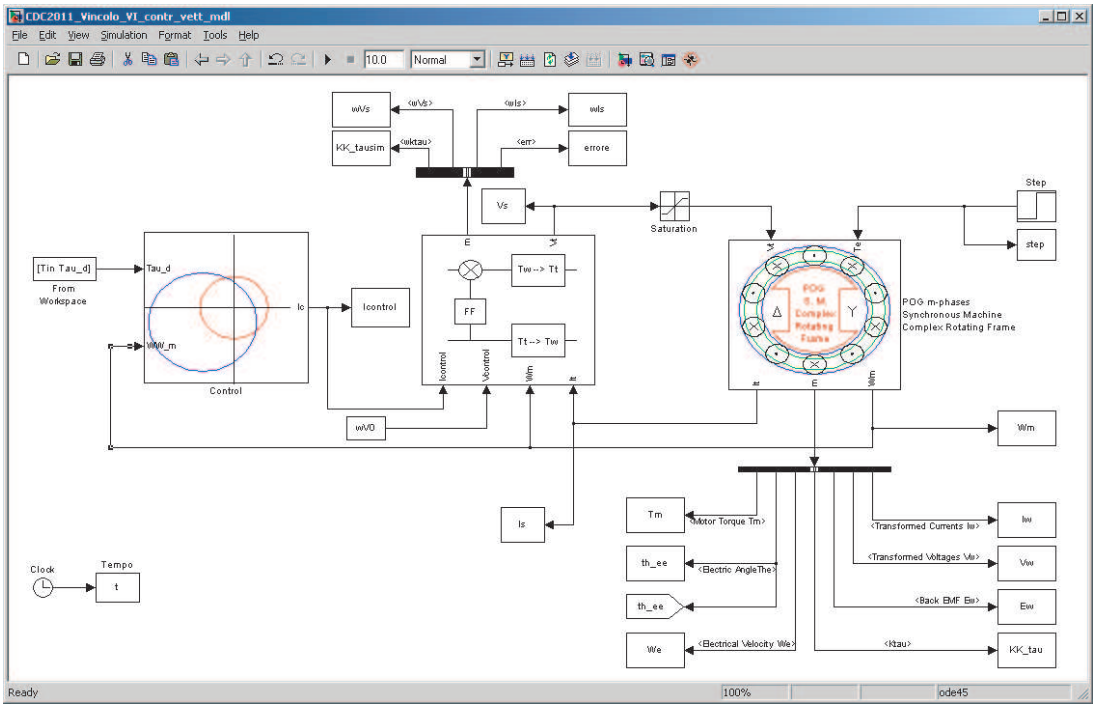

Figure 4.7: Scheme of the control diagram implemented in Simulink environment.

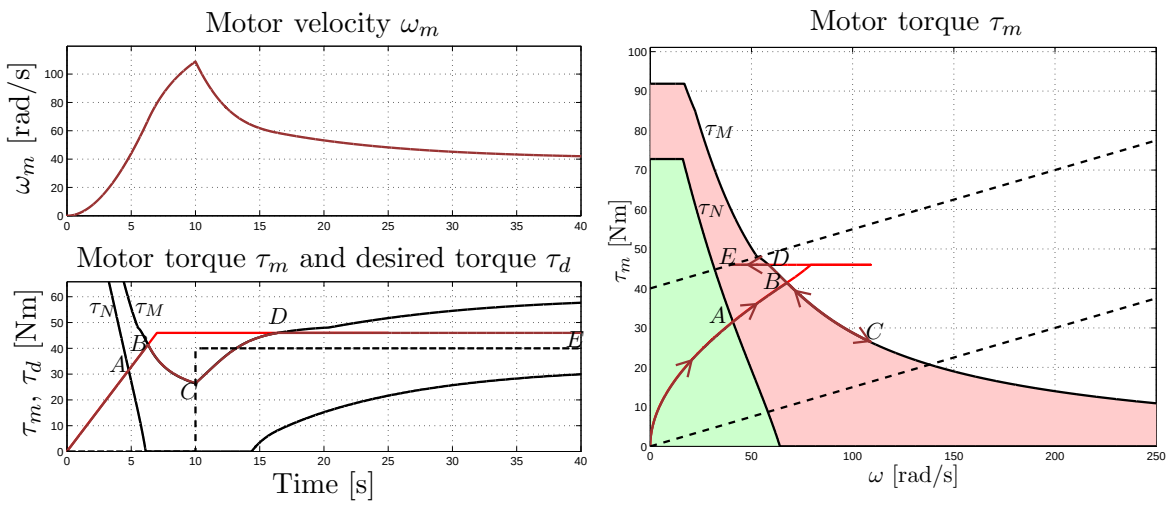

Figure 4.8: Time behaviors of motor velocity ω_m, motor torque τ_m (brown), desired torque τ_d (red), external torque τ_e (dashed-black), maximum torques τ_M and τ_N (black) with their corresponding trajectories on the torque plane (τ_m, ω_m).

applied and E the final steady-state condition. Note that for $\tau_d \leq \tau_M$, i.e. from point 0 to point B and from point D to point E, the control law (4.29) and the torque control (4.30) guarantee $\tau_m = \tau_d$. The constraints (4.9) and (4.10) are always satisfied as it is shown in Fig. 4.9.
Fig. 4.10 shows the phase current and voltage waveforms in the steady-state condition and their corresponding spectrum. It is clear that the phase voltage and phase current waveforms satisfy (4.8) and they are obtained injecting the 1-st, the 3-rd and the 5-th harmonics.
The current vectors $\overline{I}_{sk}$ in the complex subspaces $\overline{\Sigma}_{\omega 1}$, $\overline{\Sigma}_{\omega 3}$ and $\overline{\Sigma}_{\omega 5}$ are shown in Fig. 4.11. The desired torque τ_d is provided only by the quadrature components I_{qk} of the current vectors $\overline{I}_{sk}$ until it is $\tau_d = \tau_N$ in point A.
Note that from A to B, where the convex combination control ${}^{\omega}\mathbf{I}_{cc}$ is used and the current vectors $\overline{I}_{sk}$ remain within the intersection zones $\mathcal{C}_k$. From point B to point D the maximum torque control ${}^{\omega}\mathbf{I}_M$ is used, the desired torque τ_d is generated only by the current component I_{q5M} and

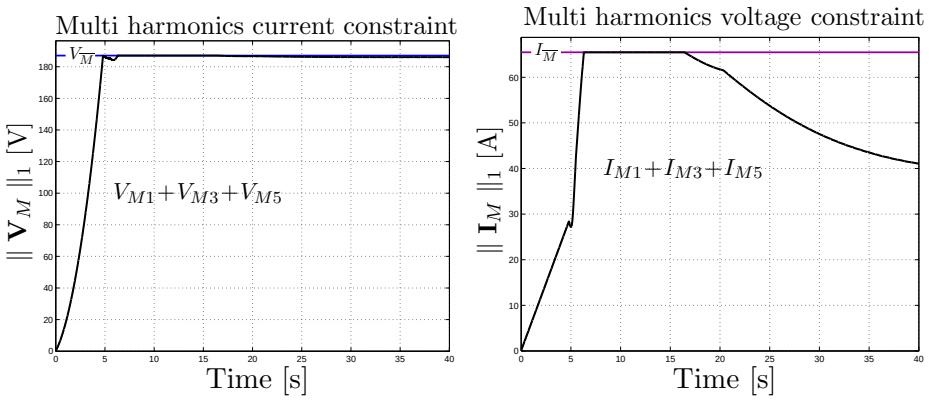

Figure 4.9: Sum of the components V_{Mk} and I_{Mk} of vectors $\mathbf{V}_M$ and $\mathbf{I}_M$.

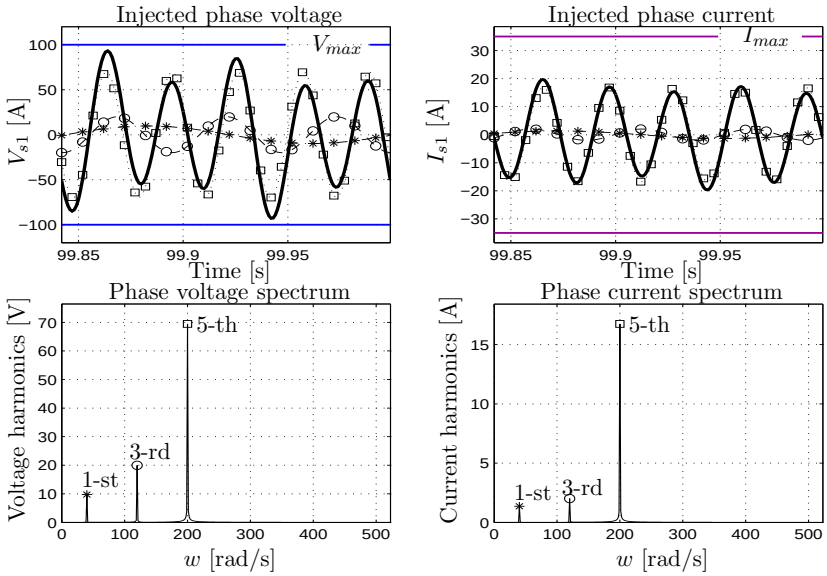

Figure 4.10: Phase current and voltage waveform with their corresponding harmonic spectrum in steady-state condition.

the maximum voltage constraint $V_{\overline{M}}$ is applied only to the component V_{M5} of the subspace $\Sigma_{\omega 5}$. From D to E the desired torque τ_d is provided by the convex combination torque control.

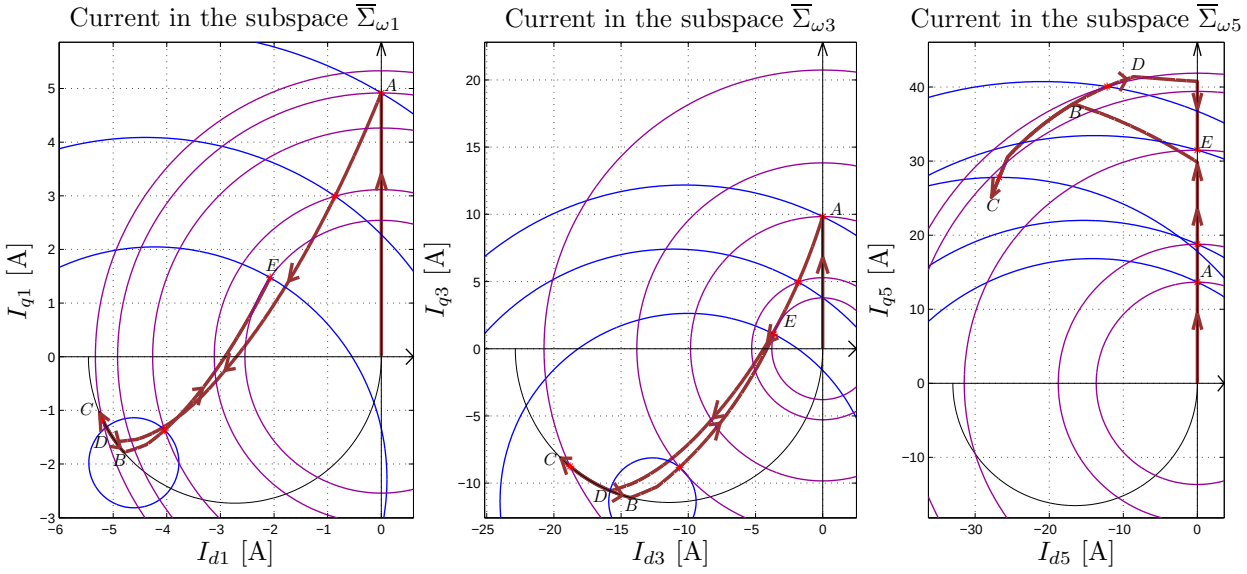

Figure 4.11: Current and voltage circles $\mathcal{CV}_k$, $\mathcal{CI}_k$ and current vectors $\overline{I}_{sk}$ in the complex subspaces $\overline{\Sigma}_{\omega k}$.

Chapter 5

Modeling of Open-phase Fault Condition

This chapter deals with the modeling of multi-phase permanent magnet synchronous motors under open-phase fault condition. Multi-phase electrical motors offer high reliability thanks to their capability to operate safely even in case of faults such the loss of some phase.
The major types of faults which may occur within the drive system are: winding open circuit, power device open circuit, terminal open circuit, winding inter-turn short circuit, winding terminal short circuit, power device short circuit and DC-link capacitor failure, see [4]. Nevertheless the open circuit fault is the most commonly found because it has the highest failure rate as reported in Tab.5.1 and even when a short-circuit occurs the fuse (commonly used as series short-circuit protection in the inverter, see [6]) automatically opens the connection.
In the literature any effective model for the faulty motor has been provided yet. Indeed, although in [22] and [48] the open circuited phase failure is simulated by a variable resistor as opening element the value of this resistance is a trade-off between the model accuracy and the simulation time.
In this chapter two models of a multi phase PM machine in the case of open phase fault condition are proposed. These models simulate the failure by an additional voltage in order to impose a zero current in the open-phases, without increasing their resistance, allowing in this way a short simulation time. The open circuit fault can occur to any of the phases and both cases of adjacent and non-adjacent open phases may be simulated. We consider the star stator connection case but this approach can be extended also for delta connected motors. Moreover the models hold for any shape of the rotor flux and for a generic odd number of phases.
The advantages of Power-Oriented Graphs modeling technique allow to directly implement the proposed models in a general-type simulator. Thanks to these models the different control strategies for faulty operation of the motor can be tested before the implementation on a real motor drive. The main contents of this chapter have been published in [50] and [51].

Cause of Failure	Failure rate/phase [per hr]	No. Phases	Total failure rate [per hr]
Short circuit between phases	6.7×10^{-6}	3	20.1×10^{-6}
Open circuit in windings/joints	13.4×10^{-6}	3	40.2×10^{-6}
Open circuit in connections	1.0×10^{-6}	3	3.0×10^{-6}
Short circuit in connections	1.0×10^{-6}	3	3.0×10^{-6}

Table 5.1: Resume table of the failure rates in a three-phase motor, see [49].

5.1 Open phase fault condition

In this section the model of the motor in open-phase fault condition is introduced. The simulation of an open-phase fault has been proposed in [22] and [48] where the open circuited phase failure is simulated by a variable resistor as opening element as shown in Fig. 5.1a. Although the implementation of this model is easier, the value of the faulty resistance is a trade-off between the model accuracy and the simulation time.
Indeed, in simulation, the computation step time of the numerical solver is chosen in regard to the smallest time constant of the simulated system. In open-circuited conditions, the open-phase time constant becomes very small, so a large value of R_{sf} reduces the computation step time increasing the simulation time, see [22]. When the resistance R_{sf} grows up continuously to infinite the pole $p_i = -R_{sf}/L_s$, related to the faulty phase, moves towards minus infinite and the system time constant $\tau_i = L_s/R_{sf}$ becomes very small. In this condition the system simulations can be performed only using a very small integration step, thus increasing the simulation time. Using this method the value of the resistance R_{sf} is a trade-off between the expected model accuracy and the overall computation time. Moreover, since R_{sf} can not tend to infinity the current of the open-phase does not tend to zero.

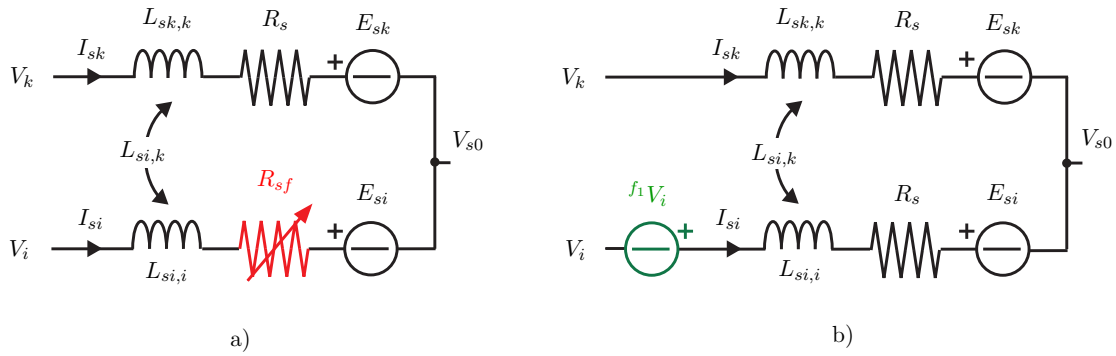

Figure 5.1: Representation of two different ways to simulate an open phase fault: a) variable resistor as opening element b) additional voltage.

To avoid these problems we propose to simulate the open-phase failure by supplying the faulty phase with an additional voltage, as shown in Fig. 5.1b, such that its steady-state current is zero. In this way it is possible to impose a zero current without increasing the phase resistance, allowing a short simulation time (it is the same respect to the healthy condition) because the faulty phase pole $p_i = -R_s/L_s$ and the time constant $\tau_i = L_s/R_s$ remain unchanged.

5.2 Modeling of Open-phase fault condition in the fixed reference frame

In order to simulate the open phase in the fixed reference frame it is necessary to impose a zero steady state current and this can be done by giving to the faulty phase the voltage such that the corresponding current is zero. Moreover also the common voltage V_{s0} must be computed. We first consider an open-phase fault occurring on a single phase and then generalize the obtained equations for a multi-fault occurring on n-phases, with $n < m_s - 2$.

5.2.1 Open-phase fault on a single phase

The electrical equations of the system (2.1) in the fixed reference frame Σ_t are:

$$ {}^t\mathbf{L}_s\, {}^t\dot{\mathbf{I}}_s = -\,{}^t\mathbf{R}_s\, {}^t\mathbf{I}_s - {}^t\mathbf{E}_s + {}^t\mathbf{V}_l - {}^tV_{s0}, \tag{5.1} $$

where the i-th phase equation can be written as:

$$ \sum_{k=1}^{m_s} L_{si,k}\dot{I}_{sk} = -R_s I_{si} - E_{si} + \underbrace{V_i - V_{s0}}_{V_{si}}. \tag{5.2} $$

In (5.2) R_s and $L_{si,i}$ are the resistance and the self-inductance of the i-th phase respectively, $L_{si,k}$ is the mutual inductance between the phases i and k, E_{si} is the back-emf voltage, V_i is the terminal voltage applied on the i-th phase and V_{s0} is the common voltage.
When i-th phase is open the corresponding current I_{si} must be zero. To achieve this condition it is sufficient to add to i-th phase the following additional voltage ${}^{f_1}V_i$:

$$ {}^{f_1}V_i = \sum_{k=1,k\neq i}^{m_s} L_{si,k}\dot{I}_{sk} + E_{si} - V_i + V_{s0}. \tag{5.3} $$

The first two terms on the right-hand side compensate the back-emf voltages due to the mutual inductances and the rotor flux rotation while the last two terms compensate the phase voltage V_{si}. Adding (5.3) to the left-hand side of equation (5.2) one obtains this first order differential equation:

$$ L_{si,i}\dot{I}_{si} = -R_s I_{si}, \tag{5.4} $$

so the current falls down with an exponential law. Therefore this equation guarantees $I_{si} = 0$ in steady state condition without modifying the value of R_s.
Introducing the transformation matrix ${}^{f_1}\mathbf{T}_t$ (equal to the identity matrix of dimension m_s in which the i-th column has been eliminated) the equation (5.3) can be rewritten in vectorial form as:

$$ {}^{f_1}V_i = (\mathbf{e}_i^{m_s})^{\mathrm{T}} \left[{}^{t}\mathbf{L}_s \, {}^{f_1}\mathbf{T}_t \, {}^{f_1}\dot{\mathbf{I}}_s + {}^{t}\mathbf{E}_s - {}^{t}\mathbf{V}_l + \mathbf{1}^{m_s} V_{s0} \right] \tag{5.5} $$

where $\mathbf{e}_i^{m_s}$ is the i-th vector of the standard basis of space $\mathbb{R}^{m_s}$ which selects only the i-th component of the corresponding right vector.
The additional voltage ${}^{f_1}V_i$ is function of unknown variables: time derivative of healthy stator currents ${}^{f_1}\dot{\mathbf{I}}_s$ and the common voltage V_{s0}. The time derivative of healthy stator currents ${}^{f_1}\dot{\mathbf{I}}_s$ can be computed considering the reduced system obtained from (5.1) eliminating the i-th equation, while the common voltage can be computed taking into account also the additional voltage ${}^{f_1}V_i$ added to the i-th phase.
Applying the transformation matrix ${}^{f_1}\mathbf{T}_t$ to system (5.1) one obtains the following reduced system:

$$ {}^{f_1}\mathbf{L}_s \, {}^{f_1}\dot{\mathbf{I}}_s = - {}^{f_1}\mathbf{R}_s \, {}^{f_1}\mathbf{I}_s - {}^{f_1}\mathbf{E}_s + {}^{f_1}\mathbf{V}_l - \mathbf{1}^{m_s-1} V_{s0}. \tag{5.6} $$

The transformed vectors ${}^{f_1}\mathbf{I}_s$, ${}^{f_1}\mathbf{V}_s$ and ${}^{f_1}\mathbf{E}_s$, belonging to $\mathbb{R}^{m_s-1}$, are obtained from vectors ${}^{t}\mathbf{I}_s$, ${}^{t}\mathbf{V}_l$ and ${}^{t}\mathbf{E}_s$ eliminating their i-th component:

$$ {}^{f_1}\mathbf{I}_s = {}^{f_1}\mathbf{T}_t^{\mathrm{T}} \, {}^{t}\mathbf{I}_s \ , \quad {}^{f_1}\mathbf{V}_s = {}^{f_1}\mathbf{T}_t^{\mathrm{T}} \, {}^{t}\mathbf{V}_s = {}^{f_1}\mathbf{V}_l - \mathbf{1}^{m_s-1} V_{s0} \ , \quad {}^{f_1}\mathbf{E}_s = {}^{f_1}\mathbf{T}_t^{\mathrm{T}} \, {}^{t}\mathbf{E}_s. $$

Similarly, the transformed matrices ${}^{f_1}\mathbf{R}_s$ and ${}^{f_1}\mathbf{L}_s$ are obtained from ${}^{t}\mathbf{R}_s$ and ${}^{t}\mathbf{L}_s$ eliminating the i-th row and column:

$$ {}^{f_1}\mathbf{R}_s = {}^{f_1}\mathbf{T}_t^{\mathrm{T}} \, {}^{t}\mathbf{R}_s \, {}^{f_1}\mathbf{T}_t \ , \qquad {}^{f1}\mathbf{L}_s = {}^{f_1}\mathbf{T}_t^{\mathrm{T}} \, {}^{t}\mathbf{L}_s \, {}^{f_1}\mathbf{T}_t. $$

Then the time derivative of the reduced current vector ${}^{f1}\dot{\mathbf{I}}_s$ can be calculated from system (5.6) as follows:

$$ {}^{f_1}\dot{\mathbf{I}}_s = {}^{f_1}\mathbf{L}_s^{-1} (- {}^{f_1}\mathbf{R}_s \, {}^{f_1}\mathbf{I}_s - {}^{f_1}\mathbf{E}_s + {}^{f_1}\mathbf{V}_l - \mathbf{1}^{m_s-1} V_{s0}). \tag{5.7} $$

Substituting (5.7) in (5.5) one obtains the following expression of the additional voltage ${}^{f_1}V_i$:

$$ {}^{f_1}V_i = (\mathbf{e}_i^{m_s})^{\mathrm{T}} [\mathbf{V}_p + \boldsymbol{\alpha}_p \, V_{s0}] \tag{5.8} $$

where the voltage vector $\mathbf{V}_p$ and the dimensionless vector $\boldsymbol{\alpha}_p$ have the following structure:

$$ \mathbf{V}_p = {}^{t}\mathbf{E}_s - {}^{t}\mathbf{V}_l + {}^{t}\mathbf{L}_s \, {}^{f_1}\mathbf{T}_t \, {}^{f_1}\mathbf{L}_s^{-1} \left({}^{f_1}\mathbf{V}_l - {}^{f_1}\mathbf{E}_s - {}^{f_1}\mathbf{R}_s \, {}^{f_1}\mathbf{I}_s \right) \tag{5.9} $$

$$ \boldsymbol{\alpha}_p = \mathbf{1}^{m_s} - {}^{t}\mathbf{L}_s \, {}^{f_1}\mathbf{T}_t \, {}^{f_1}\mathbf{L}_s^{-1} \mathbf{1}^{m_s-1} \tag{5.10} $$

The equation (3.7) in Sec.3 shows how the common voltage V_{s0} is function of the terminal voltages V_h and the back-electromotive forces E_{sh}:

$$ V_{s0} = \frac{1}{m_s} \left(\sum_{h=1}^{m_s} V_h - \sum_{h=1}^{m_s} E_{sh} \right) = \frac{(\mathbf{1}^{m_s})^{\mathrm{T}} \left({}^{t}\mathbf{V}_l - {}^{t}\mathbf{E}_s \right)}{m_s} \tag{5.11} $$

Accordingly, the common voltage V_{s0} can be obtained in faulty condition taking into account in (5.11) the additional voltage ${}^{f_1}V_i$ added to the i-th phase:

$$m_s V_{s0} = (\mathbf{1}^{m_s})^{\mathrm{T}} \left({}^{t}\mathbf{V}_l - {}^{t}\mathbf{E}_s \right) + (\mathbf{e}_i^{m_s})^{\mathrm{T}} [\mathbf{V}_p + \boldsymbol{\alpha}_p V_{s0}] .$$

From this equation one obtains the expression of the common voltage V_{s0} in faulty condition:

$$V_{s0} = \frac{(\mathbf{1}^{m_s})^{\mathrm{T}} \left({}^{t}\mathbf{V}_l - {}^{t}\mathbf{E}_s \right) + (\mathbf{e}_i^{m_s})^{\mathrm{T}} \mathbf{V}_p}{m_s - (\mathbf{e}_i^{m_s})^{\mathrm{T}} \boldsymbol{\alpha}_p}. \tag{5.12}$$

Substituting (5.12) in (5.8) one obtains the equation of the additional faulty voltage:

$${}^{f_1}V_i = (\mathbf{e}_i^{m_s})^{\mathrm{T}} \left[\mathbf{V}_p + \boldsymbol{\alpha}_p \frac{(\mathbf{1}^{m_s})^{\mathrm{T}} \left({}^{t}\mathbf{V}_l - {}^{t}\mathbf{E}_s \right) + (\mathbf{e}_i^{m_s})^{\mathrm{T}} \mathbf{V}_p}{m_s - (\mathbf{e}_i^{m_s})^{\mathrm{T}} \boldsymbol{\alpha}_p} \right] \tag{5.13}$$

this equation is only function of known variables such as terminal voltage, back-electromotive force, reduced stator current and known parameters such as inductance and resistance matrices. Finally, the open-phase condition $I_{si} = 0$ can be obtained by adding the following voltage vector ${}^{t}\mathbf{V}_{Fs}$ to system (2.1):

$$\left[\begin{array}{c|c} {}^{t}\mathbf{L}_s & \mathbf{0} \\ \hline \mathbf{0} & J_m \end{array} \right] \left[\begin{array}{c} {}^{t}\dot{\mathbf{I}}_s \\ \hline \dot{\omega}_m \end{array} \right] = - \left[\begin{array}{c|c} {}^{t}\mathbf{R}_s & {}^{t}\mathbf{K}_\tau(\theta) \\ \hline -{}^{t}\mathbf{K}_\tau^{\mathrm{T}}(\theta) & b_m \end{array} \right] \left[\begin{array}{c} {}^{t}\mathbf{I}_s \\ \hline \omega_m \end{array} \right] + \left[\begin{array}{c} {}^{t}\mathbf{V}_s \\ \hline -\tau_e \end{array} \right] + \left[\begin{array}{c} {}^{t}\mathbf{V}_{Fs} \\ \hline 0 \end{array} \right] \tag{5.14}$$

where:

$${}^{t}\mathbf{V}_{Fs} = \left[\, 0 \cdots 0 \;\; {}^{f_1}V_i \;\; 0 \cdots 0 \, \right]^{\mathrm{T}} \tag{5.15}$$

The vector ${}^{t}\mathbf{V}_{Fs}$ has only the i-th component, related to the broken phase, different from zero and in vectorial form it can be obtained as:

$${}^{t}\mathbf{V}_{Fs} = \mathbf{F}_p \left[\mathbf{V}_p + \boldsymbol{\alpha}_p \frac{(\mathbf{1}^{m_s})^{\mathrm{T}} \left({}^{t}\mathbf{V}_l - {}^{t}\mathbf{E}_s \right) + (\mathbf{e}_i^{m_s})^{\mathrm{T}} \mathbf{V}_p}{m_s - (\mathbf{e}_i^{m_s})^{\mathrm{T}} \boldsymbol{\alpha}_p} \right] \tag{5.16}$$

where matrix $\mathbf{F}_p = \mathbf{I}_{m_s} - {}^{f_1}\mathbf{T}_t \, {}^{f_1}\mathbf{T}_t^{\mathrm{T}}$ is a matrix in which only the the i-th diagonal elements are different from zero.

5.2.2 Multi open-phase fault condition

The method shown in Sec. 5.2.1 can also be used in the case of multi open-phase fault condition. Let $\mathcal{S}$ denote the set of the faulty phases: $\mathcal{S} = \{i_1, i_2, ..., i_n\}$ with $n < m_s - 2$ and where the indices i_i define the order of the faults i.e. i_1 is the 1-st phase that faults, i_2 is the 2-nd phase that faults and so on.. .The proposed method can be described as follows:

1. Eliminating from (5.1) the rows and the columns corresponding to the indices belonging to $\mathcal{S}$, obtain the reduced system in a vectorial form similar to (5.6) and then calculate the time derivative of the reduced current vector ${}^{f_n}\dot{\mathbf{I}}_s$.

2. Substitute ${}^{f_n}\dot{\mathbf{I}}_s$ in the equation of the additional voltages ${}^{f_n}V_{i_1}$, ${}^{f_n}V_{i_2}$, ... , ${}^{f_n}V_{i_n}$ putting in evidence the common voltage V_{s0}.

3. Recalculate voltage V_{s0} considering also the additional voltages ${}^{f_n}V_{i_1}$, ${}^{f_n}V_{i_2}$, ..., ${}^{f_n}V_{i_n}$.

4. Substitute V_{s0} in the equation of the additional voltages obtaining the components different from zero of the additional voltage vector ${}^{t}\mathbf{V}_{Fs}$.

In this case the reduced system has the following structure:

$$ {}^{f_n}\mathbf{L}_s\,{}^{f_n}\dot{\mathbf{I}}_s = -\,{}^{f_n}\mathbf{R}_s\,{}^{f_n}\mathbf{I}_s - {}^{f_n}\mathbf{E}_s + {}^{f_n}\mathbf{V}_l - \mathbf{1}^{m_s-n}V_{s0}. \tag{5.17} $$

It is obtained from (2.1) eliminating the rows and the columns of the open phases by using a transformation matrix ${}^{f_n}\mathbf{T}_t$ which is equal to an identity matrix of dimension m_s without the n columns related to the n faulty phases. Inverting the matrix ${}^{f_n}\mathbf{L}_s$ in (5.17) one obtains the time derivative of the reduced current vector ${}^{f_n}\dot{\mathbf{I}}_s$:

$$ {}^{f_n}\dot{\mathbf{I}}_s = {}^{f_n}\mathbf{L}_s^{-1}(-\,{}^{f_n}\mathbf{R}_s\,{}^{f_n}\mathbf{I}_s - {}^{f_n}\mathbf{E}_s + {}^{f_n}\mathbf{V}_l - \mathbf{1}^{m_s-n}V_{s0}) $$

In the multi fault case the adding voltages functions can be expressed as follows:

$$ \begin{cases} {}^{f_n}V_{i_1} &= (\mathbf{e}_{i_1}^{m_s})^{\mathrm{T}}[\mathbf{V}_p + \boldsymbol{\alpha}_p\,V_{s0}] \\ {}^{f_n}V_{i_2} &= (\mathbf{e}_{i_2}^{m_s})^{\mathrm{T}}[\mathbf{V}_p + \boldsymbol{\alpha}_p\,V_{s0}] \\ & \vdots \\ {}^{f_n}V_{i_n} &= (\mathbf{e}_{i_n}^{m_s})^{\mathrm{T}}[\mathbf{V}_p + \boldsymbol{\alpha}_p\,V_{s0}] \end{cases} $$

where:

$$ \mathbf{V}_p = {}^{t}\mathbf{E}_s - {}^{t}\mathbf{V}_l + {}^{t}\mathbf{L}_s\,{}^{f_n}\mathbf{T}_t\,{}^{f_n}\mathbf{L}_s^{-1}\Big({}^{f_n}\mathbf{V}_l - {}^{f_n}\mathbf{E}_s - {}^{f_n}\mathbf{R}_s\,{}^{f_n}\mathbf{I}_s\Big) \tag{5.18} $$

$$ \boldsymbol{\alpha}_p = \mathbf{1}^{m_s} - {}^{t}\mathbf{L}_s\,{}^{f_n}\mathbf{T}_t\,{}^{f_n}\mathbf{L}_s^{-1}\mathbf{1}^{m_s-n} \tag{5.19} $$

Introducing these voltages in (5.11) one obtains the common voltage V_{s0} under multi fault-phase condition:

$$ V_{s0} = \frac{(\mathbf{1}^{m_s})^{\mathrm{T}}\left({}^{t}\mathbf{V}_l - {}^{t}\mathbf{E}_s\right) + (\mathbf{e}_{\mathcal{S}}^{m_s})^{\mathrm{T}}\mathbf{V}_p}{m_s - (\mathbf{e}_{\mathcal{S}}^{m_s})^{\mathrm{T}}\boldsymbol{\alpha}_p} \tag{5.20} $$

where the components e_i of vector $\mathbf{e}_{\mathcal{S}}^{m_s}$ are defined as follows: $e_i = \{1 \text{ if } i \in \mathcal{S}\,,\, 0 \text{ otherwise}\}$. Finally, the voltage vector ${}^{t}\mathbf{V}_{Fs}$ added to system (2.1) is:

$$ {}^{t}\mathbf{V}_{Fs} = \mathbf{F}_p\left[\mathbf{V}_p + \boldsymbol{\alpha}_p\frac{(\mathbf{1}^{m_s})^{\mathrm{T}}\left({}^{t}\mathbf{V}_l - {}^{t}\mathbf{E}_s\right) + (\mathbf{e}_{\mathcal{S}}^{m_s})^{\mathrm{T}}\mathbf{V}_p}{m_s - (\mathbf{e}_{\mathcal{S}}^{m_s})^{\mathrm{T}}\boldsymbol{\alpha}_p}\right] \tag{5.21} $$

where $\mathbf{F}_p = \mathbf{I}_{m_s} - {}^{f_n}\mathbf{T}_t\,{}^{f_n}\mathbf{T}_t^{\mathrm{T}}$. The generalized equations (5.20) and (5.21) have the same structure of (5.12) and (5.16). Note that in (5.12) and (5.16) the standard basis vector $\mathbf{e}_i^{m_s}$ is used to

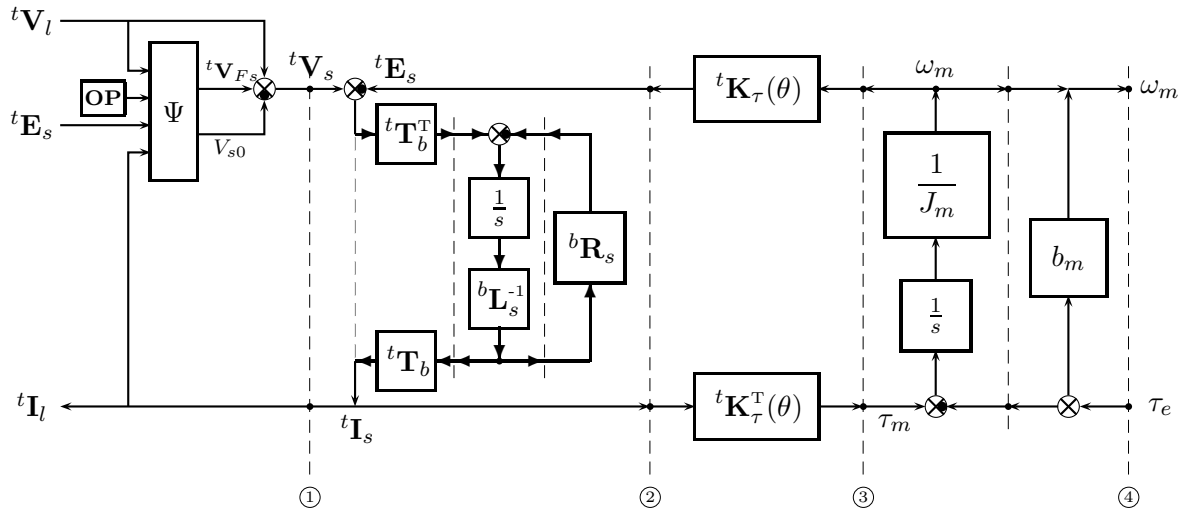

Figure 5.2: POG block scheme of the motor in the fixed reference frame Σ_t under open-phase fault condition.

select the i-th component of the calculated vectors $\mathbf{V}_p$ and $\boldsymbol{\alpha}_p$, while in (5.20) and (5.21) the vector $\mathbf{e}_{\mathcal{S}}^{m_s}$ is used to select only the components of vectors $\mathbf{V}_p$ and $\boldsymbol{\alpha}_p$ related to the faulty phases.

The POG block scheme representing the dynamics of the motor in fault condition is shown in Fig. 5.2: the *mechanical part* between sections ③-④ and the *connection blocks* between sections ② and ③ (named torque vector) are unchanged, while the *electrical part* is modified compared to the POG model shown in Fig. 2.2.

Matrix $^t\mathbf{T}_b$ is a power-invariant transformation, similar to generalized Clarke transformation (see Sec.2) used to impose the star connection constraint:

$$^t\mathbf{T}_b = {}^t\mathbf{T}_\omega\big|_{\theta=0} = \sqrt{\frac{2}{m_s}} \left\| \left[\underset{0:m_s-1}{\cos(kh\gamma_s)} \ , \ \underset{1:2:m_s-2}{\sin(kh\gamma_s)} \right] \right\|_{h}^{k}.$$

As shown in Sec.2 the transformed matrices $^b\mathbf{R}_s = {}^t\mathbf{T}_b^{\mathrm{T}}\,{}^t\mathbf{R}_s\,{}^t\mathbf{T}_b$ and $^b\mathbf{L}_s = {}^t\mathbf{T}_b^{\mathrm{T}}\,{}^t\mathbf{L}_s\,{}^t\mathbf{T}_b$ have a diagonal structure.

The element denoted by **OP** is an internal input which defines the instants at which the faults occur and provides the indexes of the open phases. The block $\Psi(\cdot)$ is the function that calculates the common voltage V_{s0} and the adding voltage vector $^t\mathbf{V}_{Fs}$ starting from the knowledge of vectors $^t\mathbf{I}_s$, $^t\mathbf{V}_l$ and $^t\mathbf{E}_s$.

In healthy condition the adding vector $^t\mathbf{V}_{Fs}$ is zero and the common voltage V_{s0} is zero or time variant with small oscillations, see Sec.3. In faulty condition the common voltage V_{s0} is time variant, see (5.20), and the adding vector $^t\mathbf{V}_{Fs}$ is the voltage vector which guarantees zero currents through the faulty phases, see (5.21).

5.2.3 Simulations of a 7-phase motor

Fig. 5.3.a. shows the motor drive and the masked-block contains the POG model of Fig. 5.2. Particularly the electrical part of the system is shown in Fig. 5.3.c where a Matlab function is used to implement the block $\Psi(\cdot)$. Note that the time instant of the faults and the indeces of the open-phases must be inserted in the last field (highlighted by the red box) of the graphical user interface shown in Fig. 5.3.b.

The simulation results shown in this section have been obtained considering a 7-phase permanent magnet synchronous motor with three open-phase failures. The motor is controlled using the minimum dissipation torque control described in Sec.4.5.1 also when the three open-phase failures occur (both adjacent and non adjacent open phases are simulated). The control is unchanged to put in evidence the torque reduction with ripple due to the faults.

The main electrical and mechanical lumped parameters of the 7-phase machine are: $m_s = 7$, $p = 1$, $N_c = 30$, $R_s = 2\,\Omega$, $L_s = 0.03$ H, $M_{s0} = 0.02$ H, $\varphi_r = 0.02$ Wb, $J_m = 1.6$ kg m^2, $b_m = 0.8$ Nm s/rad, $V_{max} = 100$ V, $a_1 = 0.7$, $a_3 = 0.2$, $a_5 = 0.1$ and the external torque $\tau_e = 0$ Nm. The phase $i_1 = 3$ opens at time $t_1 = 8$ s, phase $i_2 = 1$ opens at time $t_2 = 12$ s and phase $i_3 = 4$ opens at time $t_3 = 16$ s. Therefore the three congruent transformation matrices ${}^{f_1}\mathbf{T}_c$, ${}^{f_2}\mathbf{T}_c$ and ${}^{f_3}\mathbf{T}_c$ have the following structure:

$$ {}^{f_1}\mathbf{T}_t = \begin{bmatrix} 1&0&0&0&0&0\\ 0&1&0&0&0&0\\ 0&0&0&0&0&0\\ 0&0&1&0&0&0\\ 0&0&0&1&0&0\\ 0&0&0&0&1&0\\ 0&0&0&0&0&1 \end{bmatrix}, \quad {}^{f_2}\mathbf{T}_t = \begin{bmatrix} 0&0&0&0&0\\ 1&0&0&0&0\\ 0&0&0&0&0\\ 0&1&0&0&0\\ 0&0&1&0&0\\ 0&0&0&1&0\\ 0&0&0&0&1 \end{bmatrix}, \quad {}^{f_3}\mathbf{T}_t = \begin{bmatrix} 0&0&0&0\\ 1&0&0&0\\ 0&0&0&0\\ 0&0&0&0\\ 0&1&0&0\\ 0&0&1&0\\ 0&0&0&1 \end{bmatrix}. $$

At time $t = t_1$, when the first fault occurs, matrix ${}^{f_1}\mathbf{T}_c$ is used to eliminate the 3rd row and the 3rd column. At time $t = t_2$ matrix ${}^{f_2}\mathbf{T}_c$ is used to eliminate the 1st and 3rd rows and columns. Finally, at $t = t_3$, matrix ${}^{f_3}\mathbf{T}_c$ is used to eliminate from the system the 1st, 3rd and 4th rows and columns. Therefore the reduced system obtained at $t = t_3$ using matrix ${}^{f_3}\mathbf{T}_c$ is:

$$ \underbrace{\begin{bmatrix} L_{11} & L_{14} & L_{14} & L_{13}\\ L_{14} & L_{11} & L_{12} & L_{13}\\ L_{14} & L_{12} & L_{11} & L_{12}\\ L_{13} & L_{13} & L_{12} & L_{11} \end{bmatrix}}_{{}^{f_3}\mathbf{L}_s} \underbrace{\begin{bmatrix} \dot{I}_{s2}\\ \dot{I}_{s5}\\ \dot{I}_{s6}\\ \dot{I}_{s7} \end{bmatrix}}_{{}^{f_3}\dot{\mathbf{I}}_s} = - \underbrace{\begin{bmatrix} R_s & 0 & 0 & 0\\ 0 & R_s & 0 & 0\\ 0 & 0 & R_s & 0\\ 0 & 0 & 0 & R_s \end{bmatrix}}_{{}^{f_3}\mathbf{R}_s} \underbrace{\begin{bmatrix} I_{s2}\\ I_{s5}\\ I_{s6}\\ I_{s7} \end{bmatrix}}_{{}^{f_3}\mathbf{I}_s} - \underbrace{\begin{bmatrix} E_{s2}\\ E_{s5}\\ E_{s6}\\ E_{s7} \end{bmatrix}}_{{}^{f_3}\mathbf{E}_s} + \underbrace{\begin{bmatrix} V_2\\ V_5\\ V_6\\ V_7 \end{bmatrix}}_{{}^{f_3}\mathbf{V}_l} - \underbrace{\begin{bmatrix} 1\\ 1\\ 1\\ 1 \end{bmatrix}}_{\mathbf{1}^{7-3}} V_{s0} $$

The time behaviors of common voltage V_{s0} and adding vector ${}^{c}\mathbf{V}_{Fs}$ and their corresponding zoom are shown in Fig. 5.4. The common voltage V_{s0} is zero in healthy condition and is time variant in faulty condition, see Fig. 5.4; moreover the amplitude of its oscillations increases with

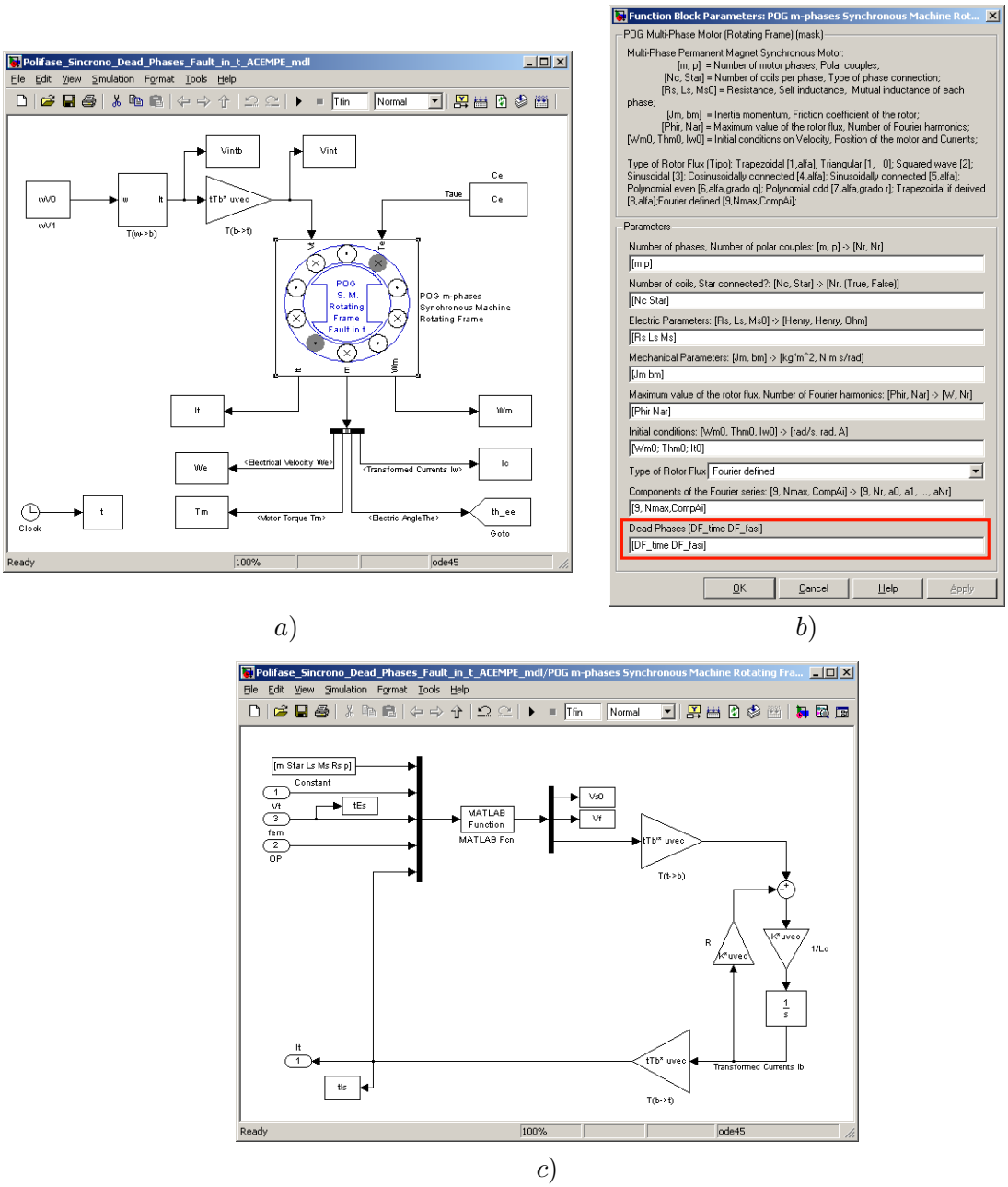

a) b)

c)

Figure 5.3: Simulink schemes: a) Simulink scheme of the controlled electric motor, b) User interface c) POG Simulink scheme of the electrical part modified to simulate the open-phase failures.

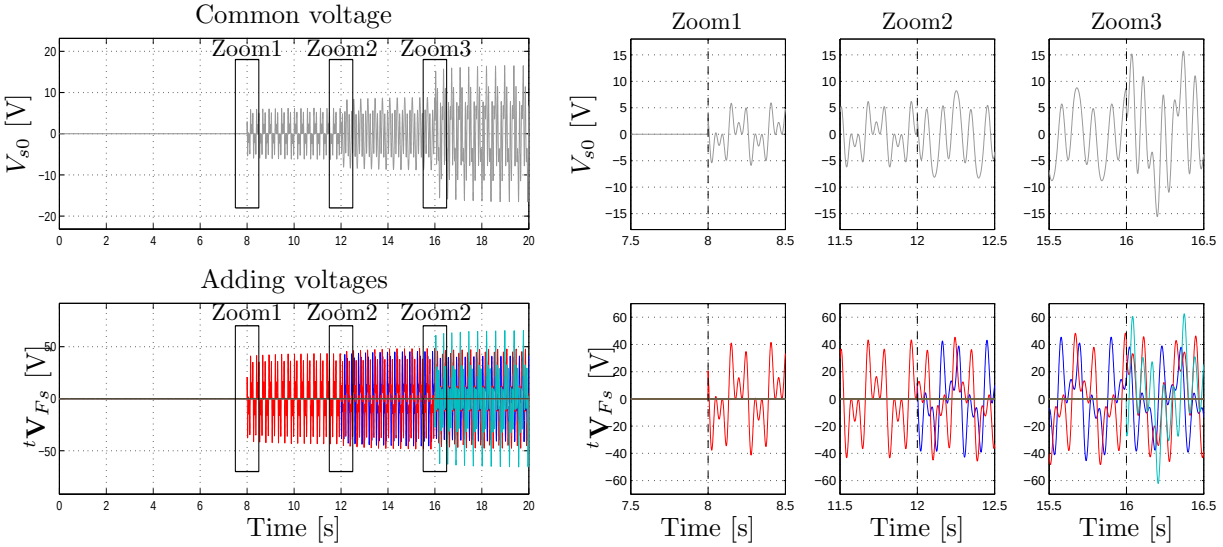

Figure 5.4: Common voltage V_{s0} and adding voltage vector ${}^t\mathbf{V}_{Fs}$.

the number of failures. The adding vector ${}^c\mathbf{V}_{Fs}$ has only the component ${}^{f_1}V_3$ different from zero when $t_1 \leq t < t_2$, it has both the components ${}^{f_2}V_1$ and ${}^{f_2}V_3$ different from zero with ${}^{f_2}V_3 \neq {}^{f_1}V_3$ when $t_2 \leq t < t_3$ and finally it is:

$${}^t\mathbf{V}_{Fs} = \begin{bmatrix} {}^{f_3}V_1 & 0 & {}^{f_3}V_3 & {}^{f_3}V_4 & 0 & 0 & 0 \end{bmatrix}^{\mathrm{T}}, \qquad \text{for } t > t_3.$$

In this final faulty condition the matrix $\mathbf{F}_p$ and the vectors $\mathbf{e}^7_{\mathcal{S}}$, $\boldsymbol{\alpha}_p$ and $\mathbf{V}_p$ have the following structure:

$$\mathbf{F}_p = \begin{bmatrix} 1&0&0&0&0&0&0 \\ 0&0&0&0&0&0&0 \\ 0&0&1&0&0&0&0 \\ 0&0&0&1&0&0&0 \\ 0&0&0&0&0&0&0 \\ 0&0&0&0&0&0&0 \\ 0&0&0&0&0&0&0 \end{bmatrix}, \quad \mathbf{e}^7_{\mathcal{S}} = \begin{bmatrix} 1 \\ 0 \\ 1 \\ 1 \\ 0 \\ 0 \\ 0 \end{bmatrix}, \quad \boldsymbol{\alpha}_p = \begin{bmatrix} \alpha_{p1} \\ 0 \\ \alpha_{p3} \\ \alpha_{p4} \\ 0 \\ 0 \\ 0 \end{bmatrix}, \quad \mathbf{V}_p = \begin{bmatrix} V_{p1} \\ V_{p2} \\ V_{p3} \\ V_{p4} \\ V_{p5} \\ V_{p6} \\ V_{p7} \end{bmatrix}.$$

The stator currents ${}^t\mathbf{I}_s$, the sum I_{s0} of the stator currents (always equal to zero because the motor is star-connected), the number n of faulty phases ($i_1 = 3$, $i_2 = 1$, $i_3 = 4$) and the zoom of the stator currents ${}^t\mathbf{I}_s$ when the faults occur are shown in Fig. 5.11. Note that at time $t = 8$ s the phase 3 opens and the current I_{s3} goes to zero, then at time $t = 12$ s the phase 1 opens and the current I_{s1} goes to zero and finally at time $t = 16$ s the phase 4 opens and the current I_{s4} goes to zero. During the faulty transient the old broken phases currents are slightly different from zero because, to simplify the computation, in the reduced system (5.17) the last faulty phase current ${}^{f_n}I_{i_n}$ is considered zero even if it is different from zero during the transient. Therefore to keep the current in the old faulty phase equal to zero ${}^{f_n}I_{i_1} = {}^{f_n}I_{i_2} = \ldots = {}^{f_n}I_{i_{n-1}} = 0$, the additional voltage ${}^{f_n}V_{i_1}, {}^{f_n}V_{i_2}, \ldots, {}^{f_n}V_{i_{n-1}}$ must be recalculated taking into account the current

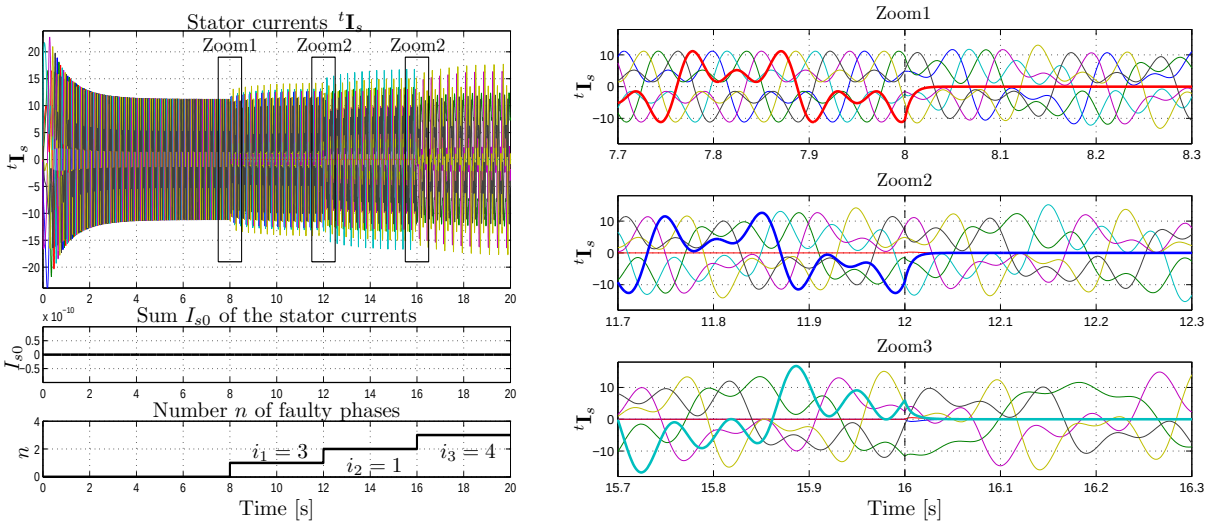

Figure 5.5: Stator currents ${}^t\mathbf{I}_s$ and their zoom when the faults occur.

${}^{f_n}I_{i_n}$ and the additional voltage ${}^{f_n}V_{i_n}$ applied to the last broken phase.

The motor velocity ω_m and the motor torque τ_m are shown in Fig. 5.6. When the 1st fault occurs the mean value of the torque decreases to 84.34% and the torque ripple (calculated as the peak to peak value normalized with respect to the mean value) is 75.01%. When the 2*nd* fault occurs on a non adjacent phase ($i_1 = 3$ and $i_2 = 1$) the mean value of the torque decreases to 67.32% and the torque ripple rises to 155.93%. Finally, when the 3rd fault occurs on an adjacent phase ($i_1 = 3$ and $i_3 = 4$) the mean value of the torque decreases to the 59.8% and the torque ripple is 175.55%. Contrarily to three-phase wye-connected machines, the loss of one phase is

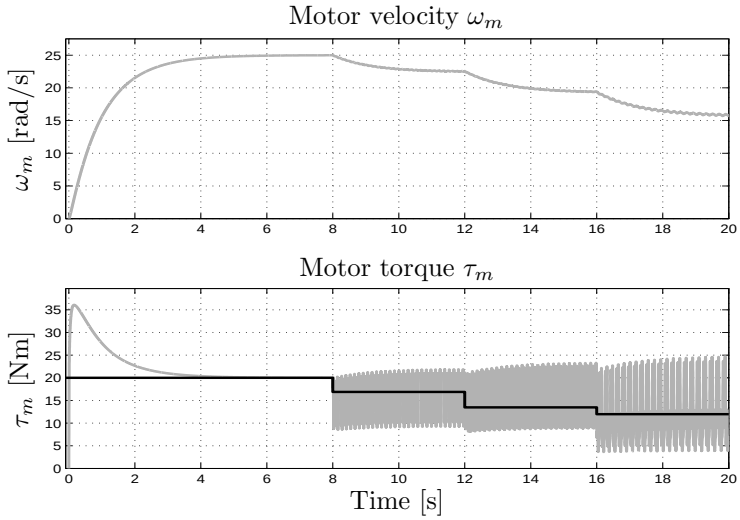

Figure 5.6: Motor velocity ω_m and motor torque τ_m (the solid line indicates the mean value of the torque in steady state condition).

not critical for seven-phase machines.
However, torque ripples appear when classic vector control of the machine is implemented. This ripple comes from the interaction between the unbalanced magnetic field of the stator currents in faulty condition (the remaining healthy phases are displaced asymmetrically) and the symmetrical magnetic field of the rotor, see [52]. The cause of this undesired torque pulsation is clear in the transformed reference frames Σ_ω and $\overline{\Sigma}_\omega$. Indeed in these rotating reference frames the transformed torque vectors $\underline{^{\omega}\mathbf{K}}_\tau$ and $\underline{^{\omega}\overline{\mathbf{K}}}_{\tau N}$ remain constant also in faulty condition while the current vectors $\underline{^{\omega}\mathbf{I}}_s$ and $\underline{^{\omega}\overline{\mathbf{I}}}_s$ become function of the electric angle θ as shown in [48] and [53]. Therefore the torque ripple is traced back to the even harmonics $\big($at frequencies 2ω, 4ω, ... , $(m_s-1)\omega\big)$ of the direct and quadrature components I_{dk} and I_{qk}.
The zoom of the direct and quadrature components I_{dk} and I_{qk} in Fig. 5.7 shows how these components are constant in healthy condition while they are function of the electric angle θ in faulty condition.

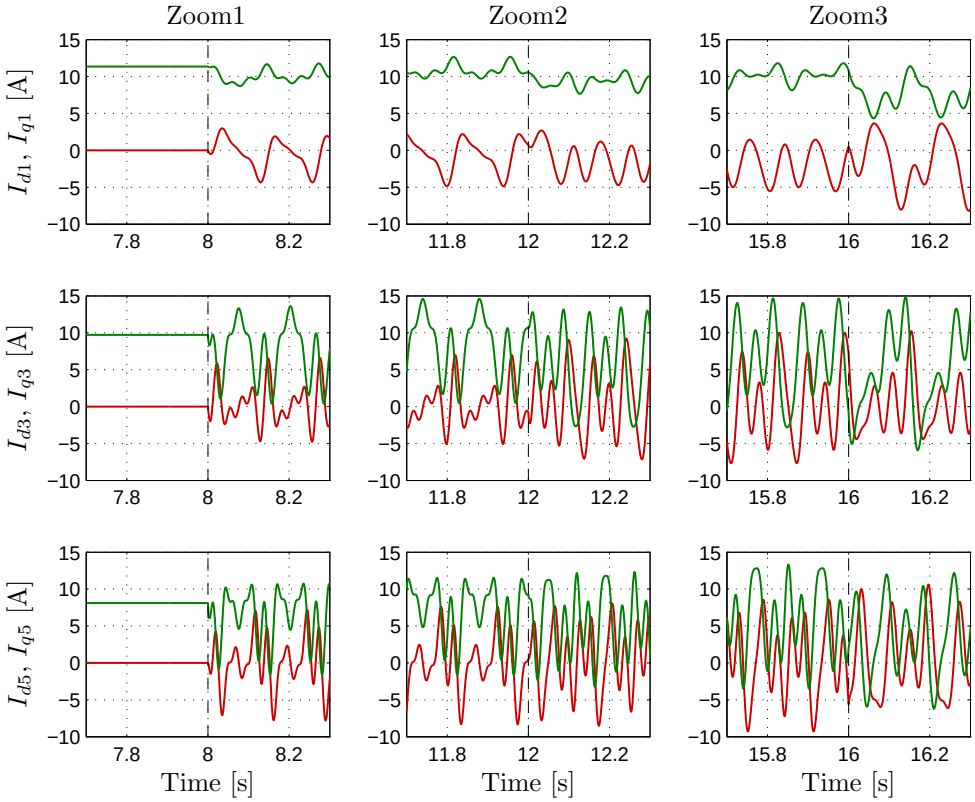

Figure 5.7: Zoom of the direct and quadrature components I_{dk} (red) and I_{qk} (green) in the rotating reference frame Σ_ω when the faults occur.

5.3 Modeling of Open-phase fault condition using a transformation

In order to compute the faulty voltage in the fixed reference frame it is necessary to compute the common voltage V_{s0}, but this calculation is quite complex. Moreover the star connection constraint must be taken into account. To overcome these problems a transformation is now introduced. Let us consider the following transformation matrix ${}^{\underline{t}}\mathbf{T}_c$ and its inverse:

$${}^{\underline{t}}\mathbf{T}_c = \left[\begin{array}{c|c} \mathbf{I}_{m_s-1} & \mathbf{0} \\ \hline -\mathbf{1} & 1 \end{array}\right], \qquad {}^{\underline{t}}\mathbf{T}_c^{-1} = \left[\begin{array}{c|c} \mathbf{I}_{m_s-1} & \mathbf{0} \\ \hline \mathbf{1} & 1 \end{array}\right].$$

Applying the transformation ${}^{\underline{t}}\mathbf{T}_c$ to the electrical equations (5.1), one obtains the following transformed current and voltage vectors ${}^{\underline{c}}\mathbf{I}_s$ and ${}^{\underline{c}}\mathbf{V}_s$:

$${}^{\underline{c}}\mathbf{I}_s = {}^{\underline{t}}\mathbf{T}_c^{-1}\,{}^{t}\mathbf{I}_s = \left[\begin{array}{ccc|c} I_{s1} & I_{s2} & \dots & I_{sm_s-1} \end{array} \left| \sum_{i=1}^{m_s} I_{si} \right.\right]^{\mathrm{T}}, \qquad {}^{\underline{c}}\mathbf{V}_s = {}^{\underline{t}}\mathbf{T}_c^{\mathrm{T}}\,{}^{t}\mathbf{V}_s = \left[\begin{array}{c} V_{s1} - V_{sm_s} \\ V_{s2} - V_{sm_s} \\ \vdots \\ \hline V_{sm_s-1} - V_{sm_s} \\ \hline V_{sm_s} - V_{s0} \end{array}\right].$$

The last component of current vector ${}^{\underline{c}}\mathbf{I}_s$ represents the star-connection constraint, while the other components are unchanged. The last component of voltage vector ${}^{\underline{c}}\mathbf{V}_s$ is referred to the common voltage V_{s0}, while the other components are referred to the last phase voltage V_{sm_s}. Therefore using this transformation the star connection constraint is put in evidence and the common voltage is hidden in the last phase voltage.

When the multi-phase motor is star-connected the last component of vector ${}^{\underline{c}}\mathbf{I}_s$ is zero then the last differential equation of the transformed system becomes a static equation that can be solved obtaining the common voltage V_{s0}. Since the dynamic dimension of a star connected motor is $m_s - 1$, then it is necessary to eliminate the last column of matrix ${}^{\underline{t}}\mathbf{T}_c$ (to satisfy this constraint) and consider only matrix ${}^{t}\mathbf{T}_c$ defined as:

$${}^{t}\mathbf{T}_c = {}^{\underline{t}}\mathbf{T}_c\,\mathbf{S}_{m_s} = \begin{bmatrix} \mathbf{I}_{m_s-1} \\ -\mathbf{1} \end{bmatrix} \quad \text{where} \quad \mathbf{S}_{m_s} = \begin{bmatrix} \mathbf{I}_{m_s-1} \\ \mathbf{0} \end{bmatrix}.$$

In this case applying the transformation ${}^{t}\mathbf{T}_c$ to the electrical equations (5.1), one obtains the following transformed system:

$${}^{c}\mathbf{L}_s\;{}^{c}\dot{\mathbf{I}}_s = -\,{}^{c}\mathbf{R}_s\;{}^{c}\mathbf{I}_s - {}^{c}\mathbf{E}_s + {}^{c}\mathbf{V}_s \tag{5.22}$$

characterized by the following transformed vectors ${}^{c}\mathbf{I}_s$, ${}^{c}\mathbf{V}_s$ and ${}^{c}\mathbf{E}_s$ defined as:

$${}^{c}\mathbf{I}_s = \mathbf{S}_{m_s}^{\mathrm{T}}\,{}^{\underline{t}}\mathbf{T}_c^{-1}\,{}^{t}\mathbf{I}_s = \underset{1:m_s-1}{\overset{i}{[\![}\;{}^{c}I_{si}\;]\!]}, \quad {}^{c}\mathbf{V}_s = {}^{t}\mathbf{T}_c^{\mathrm{T}}\,{}^{t}\mathbf{V}_s = \underset{1:m_s-1}{\overset{i}{[\![}\;{}^{c}V_{si}\;]\!]}, \quad {}^{c}\mathbf{E}_s = {}^{t}\mathbf{T}_c^{\mathrm{T}}\,{}^{t}\mathbf{E}_s = \underset{1:m_s-1}{\overset{i}{[\![}\;{}^{c}E_{si}\;]\!]},$$

where: ${}^cI_{si} = I_{si}$, ${}^cV_{si} = V_{si} - V_{sm_s}$, ${}^cE_{si} = E_{si} - E_{sm_s}$. The transformed resistance and inductance matrices ${}^c\mathbf{R}_s$ and ${}^c\mathbf{L}_s$ have the following form:

$${}^c\mathbf{R}_s = {}^t\mathbf{T}_c^{\mathrm{T}}\,{}^t\mathbf{R}_s\,{}^t\mathbf{T}_c = \underset{1:m_s-1}{\overset{i}{\underset{1:m_s-1}{\overset{k}{[\![\ {}^cR_{si,k}\ ]\!]}}}} = R_s \underset{1:m_s-1}{\overset{i}{\underset{1:m_s-1}{\overset{k}{\left\|\left[\ 1+\delta_{i,k}\ \right]\right\|}}}}, \quad {}^c\mathbf{L}_s = {}^t\mathbf{T}_c^{\mathrm{T}}\,{}^t\mathbf{L}_s\,{}^t\mathbf{T}_c = \underset{1:m_s-1}{\overset{i}{\underset{1:m_s-1}{\overset{k}{[\![\ {}^cL_{si,k}\ ]\!]}}}}$$

where $\delta_{i,k} = \{1 \text{ if } i=k, 0 \text{ otherwise}\}$ and ${}^cL_{si,k} = L_{s0}(1+\delta_{i,k}) + 4M_{s0}\sin(k\frac{\gamma_s}{2})\sin(i\frac{\gamma_s}{2})\cos((i-k)\frac{\gamma_s}{2})$.

Compared to the electrical equations (5.1) in the external fixed frame Σ_t:

- The dynamic dimension is $m_s - 1$
- The components of the transformed current vector ${}^c\mathbf{I}_s$ are unchanged
- The components of the transformed voltage and bef vector ${}^c\mathbf{V}_s$ and ${}^c\mathbf{I}_s$ are respectively referred to the last phase voltage V_{sm_s} and the last bef E_{sm_s}.
- Unlike the resistance matrix ${}^t\mathbf{R}_s$, the transformed resistance matrix ${}^c\mathbf{R}_s$ is full, so also this matrix creates a coupling between the phases.
- Like the inductance matrix ${}^t\mathbf{L}_s$, the transformed inductance matrix ${}^c\mathbf{L}_s$ is symmetric with respect to both the main and secondary diagonals:
  ${}^cL_{si,k} = {}^cL_{sk,i} = {}^cL_{s(m_s-i)+1,(m_s-k)+1} = {}^cL_{s(m_s-k)+1,(m_s-i)+1}$.

The method proposed in Sec. 5.2 can still be used, therefore also in this transformed system the open-phase failure is simulated by supplying the faulty phase with an additional voltage, as shown in Fig. 5.8, such that its steady-state current is zero.

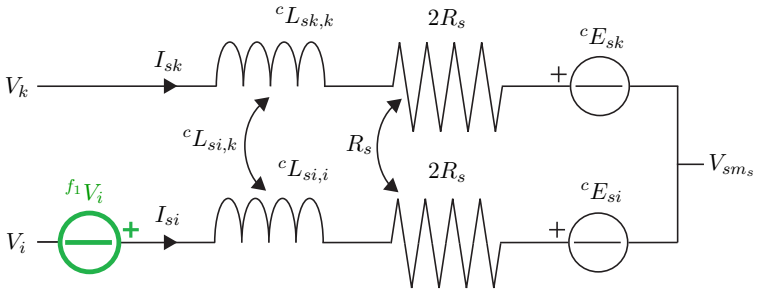

Figure 5.8: Representation of an open circuited phase in the transformed frame.

5.3.1 Open-phase fault on a single phase

Let i denote the index of the faulty phase. The i-th equation of system (5.22) can be written as:

$$\sum_{k=1}^{m_s-1} {}^cL_{si,k}\,{}^c\dot{I}_{sk} = -\sum_{k=1}^{m_s-1} {}^cR_{si,k}\,{}^cI_{sk} - {}^cE_{si} + {}^cV_{si}. \tag{5.23}$$

When i-th phase is open the corresponding current I_{si} must be zero. To achieve this condition it is sufficient to add to i-th phase the following additional voltage ${}^{f_1}V_i$:

$$ {}^{f_1}V_i = \sum_{k=1,k\neq i}^{m_s-1} {}^{c}L_{si,k}\, {}^{c}\dot{I}_{sk} + \sum_{k=1,k\neq i}^{m_s-1} {}^{c}R_{si,k}\, {}^{c}I_{sk} + {}^{c}E_{si} - {}^{c}V_{si}. \tag{5.24} $$

Adding (5.24) to the left part of equation (5.23) one obtains:

$$ {}^{c}L_{si,i}\, {}^{c}\dot{I}_{si} = -2R_s\, {}^{c}I_{si}. \tag{5.25} $$

This equation guarantees ${}^{c}I_{si} = I_{si} = 0$ in steady state condition doubling the value of R_s. Putting ${}^{c}\dot{I}_{si} = {}^{c}I_{si} = 0$ in system (5.22) and eliminating the i-th equation one obtains the following reduced system:

$$ {}^{f_1}\mathbf{L}_s\, {}^{f_1}\dot{\mathbf{I}}_s = -\,{}^{f_1}\mathbf{R}_s\, {}^{f_1}\mathbf{I}_s - {}^{f_1}\mathbf{E}_s + {}^{f_1}\mathbf{V}_s. \tag{5.26} $$

This system can also be obtained from (5.22) using the transformation ${}^{c}\mathbf{I}_s = {}^{f_1}\mathbf{T}_c\, {}^{f_1}\mathbf{I}_s$, with matrix ${}^{f_1}\mathbf{T}_c$ defined as the identity matrix of dimension $m_s - 1$ in which the i-th column has been eliminated. The transformed vectors ${}^{f_1}\mathbf{I}_s$, ${}^{f_1}\mathbf{V}_s$ and ${}^{f_1}\mathbf{E}_s$, belonging to $\mathbb{R}^{m_s-2}$, are obtained from vectors ${}^{c}\mathbf{I}_s$, ${}^{c}\mathbf{V}_s$ and ${}^{c}\mathbf{E}_s$ eliminating their i-th component:

$$ {}^{f_1}\mathbf{I}_s = {}^{f_1}\mathbf{T}_c^{\mathrm{T}}\, {}^{c}\mathbf{I}_s \ , \quad {}^{f_1}\mathbf{V}_s = {}^{f_1}\mathbf{T}_c^{\mathrm{T}}\, {}^{c}\mathbf{V}_s \ , \quad {}^{f_1}\mathbf{E}_s = {}^{f_1}\mathbf{T}_c^{\mathrm{T}}\, {}^{c}\mathbf{E}_s. $$

Similarly, the transformed resistance and inductance matrices ${}^{f_1}\mathbf{R}_s$ and ${}^{f_1}\mathbf{L}_s$ are obtained from ${}^{c}\mathbf{R}_s$ and ${}^{c}\mathbf{L}_s$ eliminating the i-th row and the i-th column:

$$ {}^{f_1}\mathbf{R}_s = {}^{f_1}\mathbf{T}_c^{\mathrm{T}}\, {}^{c}\mathbf{R}_s\, {}^{f_1}\mathbf{T}_c \ , \qquad {}^{f1}\mathbf{L}_s = {}^{f_1}\mathbf{T}_c^{\mathrm{T}}\, {}^{c}\mathbf{L}_s\, {}^{f_1}\mathbf{T}_c. $$

Equation (5.24) can be rewritten in vectorial notation as:

$$ {}^{f_1}V_i = (\mathbf{e}_i^{m_s-1})^{\mathrm{T}} \left[{}^{c}\mathbf{L}_s\, {}^{f_1}\mathbf{T}_c\, {}^{f_1}\dot{\mathbf{I}}_s + {}^{c}\mathbf{R}_s\, {}^{f_1}\mathbf{T}_c\, {}^{f_1}\mathbf{I}_s + {}^{c}\mathbf{E}_s - {}^{c}\mathbf{V}_s \right] \tag{5.27} $$

where the time derivative of the reduced current vector ${}^{f1}\dot{\mathbf{I}}_s$ can be calculated from the reduced system (5.26) as follows:

$$ {}^{f_1}\dot{\mathbf{I}}_s = {}^{f_1}\mathbf{L}_s^{-1}(-\,{}^{f_1}\mathbf{R}_s\, {}^{f_1}\mathbf{I}_s - {}^{f_1}\mathbf{E}_s + {}^{f_1}\mathbf{V}_s). \tag{5.28} $$

Therefore the open-phase condition ${}^{c}I_{si} = I_{si} = 0$ can be obtained adding the following voltage vector ${}^{c}\mathbf{V}_{Fs}$ to system (5.22):

$$ {}^{c}\mathbf{V}_{Fs} = \left[{}^{c}\mathbf{L}_s\, {}^{f_1}\mathbf{T}_c^{f_1 f_1}\mathbf{L}_s^{-1} \left(-\,{}^{f_1}\mathbf{R}_s {}^{f_1}\mathbf{I}_s - {}^{f_1}\mathbf{E}_s + {}^{f_1}\mathbf{V}_s \right) + {}^{c}\mathbf{R}_s {}^{f_1}\mathbf{T}_c {}^{f_1}\mathbf{I}_s + {}^{c}\mathbf{E}_s - {}^{c}\mathbf{V}_s \right] = \left[0 \cdots 0\ {}^{f_1}V_i\ 0 \cdots 0 \right]^{\mathrm{T}}. \tag{5.29} $$

Since the voltage vector has only the i-th component (related to the broken phase) different from zero, it is useless to replace the standard basis vector $\mathbf{e}_i^{m_s-1}$ with the matrix $\mathbf{F}_p = \mathbf{I}_{m_s-1} - {}^{f_1}\mathbf{T}_c\, {}^{f_1}\mathbf{T}_c^{\mathrm{T}}$ (as done in (5.16)).

5.3.2 Open-phase fault on two phases

Using the same method it is possible to simulate also a second fault occurring at the j-th phase by the following reduced system:

$$ {}^{f_2}\mathbf{L}_s \, {}^{f_2}\dot{\mathbf{I}}_s = - {}^{f_2}\mathbf{R}_s \, {}^{f_2}\mathbf{I}_s - {}^{f_2}\mathbf{E}_s + {}^{f_2}\mathbf{V}_s \tag{5.30} $$

obtained from (5.22) using a transformation matrix ${}^{f_2}\mathbf{T}_c$ which is equal to the identity matrix of dimension m_s without the i-th and j-th columns. The reduced vectors ${}^{f_2}\mathbf{I}_s$, ${}^{f_2}\mathbf{V}_s$ and ${}^{f_2}\mathbf{E}_s$, belonging to $\mathbb{R}^{m_s-3}$, are obtained from vectors ${}^{c}\mathbf{I}_s$, ${}^{c}\mathbf{V}_s$ and ${}^{c}\mathbf{E}_s$ eliminating the i-th and j-th components, while the reduced inductance and resistance matrices ${}^{f_2}\mathbf{R}_s$ and ${}^{f_2}\mathbf{L}_s$ are obtained from ${}^{c}\mathbf{R}_s$ and ${}^{c}\mathbf{L}_s$ eliminating the i-th and j-th rows and columns. In this case the additional vector ${}^{c}\mathbf{V}_{Fs}$ added to the system (5.22) is:

$$ {}^{c}\mathbf{V}_{Fs} = \Big[{}^{c}\mathbf{L}_s \, {}^{f_2}\mathbf{T}_c \, {}^{f_2}\dot{\mathbf{I}}_s + {}^{c}\mathbf{R}_s \, {}^{f_2}\mathbf{T}_c \, {}^{f_2}\mathbf{I}_s + {}^{c}\mathbf{E}_s - {}^{c}\mathbf{V}_s \Big] = \Big[\mathbf{0} \;\; {}^{f_2}V_i \;\; \mathbf{0} \;\; {}^{f_2}V_j \;\; \mathbf{0} \Big]^{\mathrm{T}}. \tag{5.31} $$

Note that in (5.31) the relative position of the two non-zero elements ${}^{f_2}V_i$ and ${}^{f_2}V_j$ depends on the values of indices i and j. The additional voltages ${}^{f_2}V_i$ and ${}^{f_2}V_j$ added to the i-th and j-th phases of system (5.22) can be obtained as:

$$ {}^{f_2}V_i = (\mathbf{e}_i^{m_s-1})^{\mathrm{T}} \Big[{}^{c}\mathbf{L}_s \, {}^{f_2}\mathbf{T}_c \, {}^{f_2}\dot{\mathbf{I}}_s + {}^{c}\mathbf{R}_s \, {}^{f_2}\mathbf{T}_c \, {}^{f_2}\mathbf{I}_s + {}^{c}\mathbf{E}_s - {}^{c}\mathbf{V}_s \Big], \tag{5.32} $$

$$ {}^{f_2}V_j = (\mathbf{e}_j^{m_s-1})^{\mathrm{T}} \Big[{}^{c}\mathbf{L}_s \, {}^{f_2}\mathbf{T}_c \, {}^{f_2}\dot{\mathbf{I}}_s + {}^{c}\mathbf{R}_s \, {}^{f_2}\mathbf{T}_c \, {}^{f_2}\mathbf{I}_s + {}^{c}\mathbf{E}_s - {}^{c}\mathbf{V}_s \Big]. \tag{5.33} $$

Adding (5.31) to (5.22) one obtains zero currents of the two faulty phases in steady state condition but in the faulty transient the first broken phase current is different from zero because in the calculation of the component ${}^{f_2}V_i$ the current I_{sj} has been considered zero even if it is different from zero.

During this second fault transient in order to hold the current in the first faulty phase equal to zero ${}^{c}I_{si} = I_{si} = 0$, the additional voltage ${}^{f_2}V_i$ must be recalculated taking into account the current I_{sj}. Therefore also the current I_{sj} and the voltage ${}^{f_2}V_j$ (computed in (5.33)) must be introduced in the reduced system (5.27) as follows:

$$ {}^{f_1}\mathbf{L}_s \, {}^{f_1}\dot{\mathbf{I}}_s = - {}^{f_1}\mathbf{R}_s \, {}^{f_1}\mathbf{I}_s - {}^{f_1}\mathbf{E}_s + {}^{f_1}\mathbf{V}_s + {}^{f_1}\mathbf{V}_{Fs}. \tag{5.34} $$

where the vector ${}^{f_1}\mathbf{V}_{Fs} \in \mathbb{R}^{m_s-2}$ is defined as: ${}^{f_1}\mathbf{V}_{Fs} = \Big[0 \cdots 0 \;\; {}^{f_2}V_j \;\; 0 \cdots 0 \Big]^{\mathrm{T}}$.

Note that the only component different from zero of ${}^{f_1}\mathbf{V}_{Fs}$ is the j-th component ${}^{f_2}V_j$ related to the second broken phase when $j > i$ and it is $j-1$-th component when $j < i$. One can obtain this vector using the matrices $\mathbf{F}_j$ and ${}^{f_1}\mathbf{T}_c$ as follows:

$$ {}^{f_1}\mathbf{V}_{Fs} = {}^{f_1}\mathbf{T}_c^{\mathrm{T}} \, \mathbf{F}_j \, {}^{c}\mathbf{V}_{Fs} \tag{5.35} $$

The matrix $\mathbf{F}_j$ (in which only the j-th diagonal elements are different from zero) selects the component ${}^{f_2}V_j$, while the matrix ${}^{f_1}\mathbf{T}_c$ reduces the dimension of the vector $\mathbf{F}_j\,{}^{c}\mathbf{V}_{Fs}$.
Now the additional voltage ${}^{f_1}V_i$ is:

$${}^{f_1}V_i = (\mathbf{e}_i^{m_s-1})^{\mathrm{T}}\left[{}^{c}\mathbf{L}_s\,{}^{f_1}\mathbf{T}_c\,{}^{f_1}\mathbf{L}_s^{-1}\left(-\,{}^{f_1}\mathbf{R}_s\,{}^{f_1}\mathbf{I}_s - {}^{f_1}\mathbf{E}_s + {}^{f_1}\mathbf{V}_s + {}^{f_1}\mathbf{V}_{Fs}\right) + {}^{c}\mathbf{R}_s\,{}^{f_1}\mathbf{T}_c\,{}^{f_1}\mathbf{I}_s + {}^{c}\mathbf{E}_s - {}^{c}\mathbf{V}_s\right] \tag{5.36}$$

and the voltage vector ${}^{c}\mathbf{V}_{Fs}$ added to system (5.22) has the following form:

$${}^{c}\mathbf{V}_{Fs} = \begin{bmatrix}\mathbf{0} & {}^{f_1}V_i & \mathbf{0} & {}^{f_2}V_j & \mathbf{0}\end{bmatrix}^{\mathrm{T}} \tag{5.37}$$

where the additional voltage ${}^{f_2}V_i$ in (5.31) is replaced with the new voltage ${}^{f_1}V_i$. Like equation (5.31), also in (5.37) the relative position of the two non-zero elements ${}^{f_1}V_i$ and ${}^{f_2}V_j$ depends on the values of indices i and j.

5.3.3 Multi open-phase fault condition

The shown method can be generalized in the case of multi open-phase fault condition. Let $\mathcal{S}$ denote the set of the faulty phases: $\mathcal{S} = \{i_1, i_2, ..., i_n\}$ with $n < m_s - 2$ and where the indices i_i define the order of the faults, i.e. i_1 is the 1-st phase that faults, i_2 is the 2-nd phase that faults and so on.. . The proposed method can be described in five steps as follows:

1. Eliminate from (2.1) the rows and columns corresponding to the indices belonging to $\mathcal{S}$, obtain the reduced system in a vectorial form similar to (5.26) and calculate the time derivative of the reduced current vector ${}^{f_n}\dot{\mathbf{I}}_s$.
   The reduced system is obtained from (5.22) eliminating the rows and columns of the open phases by using a transformation matrix ${}^{f_n}\mathbf{T}_c$ which is equal to an identity matrix of dimension $m_s - n$ without the n columns related to the n faulty phases.

   $${}^{f_n}\mathbf{L}_s\,{}^{f_n}\dot{\mathbf{I}}_s = -\,{}^{f_n}\mathbf{R}_s\,{}^{f_n}\mathbf{I}_s - {}^{f_n}\mathbf{E}_s + {}^{f_n}\mathbf{V}_s$$

   Then, compute the time derivative of the reduced current vector ${}^{f_n}\dot{\mathbf{I}}_s$ as follows:

   $${}^{f_n}\dot{\mathbf{I}}_s = {}^{f_n}\mathbf{L}_s^{-1}(-\,{}^{f_n}\mathbf{R}_s\,{}^{f_n}\mathbf{I}_s - {}^{f_n}\mathbf{E}_s + {}^{f_n}\mathbf{V}_s)$$

2. Substitute the time derivative of current vector ${}^{f_n}\dot{\mathbf{I}}_s$ in the equation of the additional voltage vector ${}^{c}\mathbf{V}_{Fs}$:

   $${}^{c}\mathbf{V}_{Fs} = \left[{}^{c}\mathbf{L}_s\,{}^{f_n}\mathbf{T}_c\,{}^{f_n}\mathbf{L}_s^{-1}\left(-\,{}^{f_n}\mathbf{R}_s\,{}^{f_n}\mathbf{I}_s - {}^{f_n}\mathbf{E}_s + {}^{f_n}\mathbf{V}_s\right) + {}^{c}\mathbf{R}_s\,{}^{f_n}\mathbf{T}_c\,{}^{f_n}\mathbf{I}_s + {}^{c}\mathbf{E}_s - {}^{c}\mathbf{V}_s\right] \tag{5.38}$$

3. Define the subsets $\mathcal{S}_o$ and $\mathcal{S}_g$ of $\mathcal{S}$ as: $\mathcal{S}_o = \{i_1, i_2, ..., i_o\}$, $\mathcal{S}_g = \{i_{o+1}, ..., i_n\}$ with $o = 1, n-1$. The steady-state set $\mathcal{S}_o$ is the set in which the faulty currents are zero: $i_1 = i_2 = \cdots = i_o = 0$ (in steady-state condition), while the transient set $\mathcal{S}_g$ is the set in which the faulty currents fall to zero: $i_o \neq i_{o+1} \neq, ..., \neq i_n \neq 0$ (transient condition). In this way a multi failure occurring at the same time or at the near time can be simulated. The most common case is that only one failure occurs at instant t_n so the set $\mathcal{S}_g$ is defined by the last faulty phase current while $\mathcal{S}_o$ is defined by all old broken phases currents; i.e. $o = n-1$, $\mathcal{S}_o = \{i_1, i_2, ..., i_{n-1}\}$ and $\mathcal{S}_g = \{i_n\}$.

4. Recalculate the voltage components of ${}^{c}\mathbf{V}_{Fs}$ computed for the phases $i_1, i_2, ..., i_o$ taking into account the phase currents $i_{o+1}, \ldots, i_n$ that are different from zero.

   - Select the voltage components of ${}^{c}\mathbf{V}_{Fs}$ computed for the phases $i_{o+1}, \ldots, i_n$ by the matrix $\mathbf{F}_g$ in which only the diagonal elements belonging to $\mathcal{S}_g$ are different from zero.

$$ {}^{c}\mathbf{V}_{Fsg} = \mathbf{F}_g \left[{}^{c}\mathbf{L}_s \, {}^{f_n}\mathbf{T}_c \, {}^{f_n}\mathbf{L}_s^{-1} \left(- {}^{f_n}\mathbf{R}_s \, {}^{f_n}\mathbf{I}_s - {}^{f_n}\mathbf{E}_s + {}^{f_n}\mathbf{V}_s \right) + {}^{c}\mathbf{R}_s \, {}^{f_n}\mathbf{T}_c \, {}^{f_n}\mathbf{I}_s + {}^{c}\mathbf{E}_s - {}^{c}\mathbf{V}_s \right] $$

   - Consider the reduced system taking into account also the currents and the voltages of phases belonging to $\mathcal{S}_g$

$$ {}^{f_o}\mathbf{L}_s \, {}^{f_o}\dot{\mathbf{I}}_s = - {}^{f_o}\mathbf{R}_s \, {}^{f_o}\mathbf{I}_s - {}^{f_o}\mathbf{E}_s + {}^{f_o}\mathbf{V}_s + {}^{f_o}\mathbf{V}_{Fs} $$

     where ${}^{f_o}\mathbf{V}_{Fs} = {}^{f_o}\mathbf{T}_c^{\mathrm{T}} \, \mathbf{F}_g \, {}^{c}\mathbf{V}_{Fs}$ is the extension of (5.35). This reduced system is obtained from (5.22) eliminating the rows and columns of the phases belonging to $\mathcal{S}_o$ by using the transformation matrix ${}^{f_o}\mathbf{T}_c$ which is equal to an identity matrix of dimension $m_s - o$ without the o columns related to the old faulty phases.

   - Calculate the voltage vector ${}^{c}\mathbf{V}_{Fso}$ selecting the components by the matrix $\mathbf{F}_o$ in which only the diagonal elements belonging to $\mathcal{S}_o$ are different from zero.

$$ {}^{c}\mathbf{V}_{Fso} = \mathbf{F}_o \left[{}^{c}\mathbf{L}_s \, {}^{f_o}\mathbf{T}_c \, {}^{f_o}\dot{\mathbf{I}}_s + {}^{c}\mathbf{R}_s \, {}^{f_o}\mathbf{T}_c \, {}^{f_o}\mathbf{I}_s + {}^{c}\mathbf{E}_s - {}^{c}\mathbf{V}_s \right] $$

     where the time derivative of the reduced current vector ${}^{f_o}\dot{\mathbf{I}}_s$, considering the voltage vector ${}^{f_o}\mathbf{V}_{Fs}$, can be computed as follows:

$$ {}^{f_o}\dot{\mathbf{I}}_s = {}^{f_o}\mathbf{L}_s^{-1} (- {}^{f_o}\mathbf{R}_s \, {}^{f_o}\mathbf{I}_s - {}^{f_o}\mathbf{E}_s + {}^{f_o}\mathbf{V}_s + {}^{f_o}\mathbf{V}_{Fs}) \tag{5.39} $$

   - Add the vectors ${}^{c}\mathbf{V}_{Fsg}$ and ${}^{c}\mathbf{V}_{Fso}$ obtaining the voltage vector ${}^{c}\mathbf{V}_{Fs}$:

$$ {}^{c}\mathbf{V}_{Fs} = {}^{c}\mathbf{V}_{Fsg} + {}^{c}\mathbf{V}_{Fso} \tag{5.40} $$

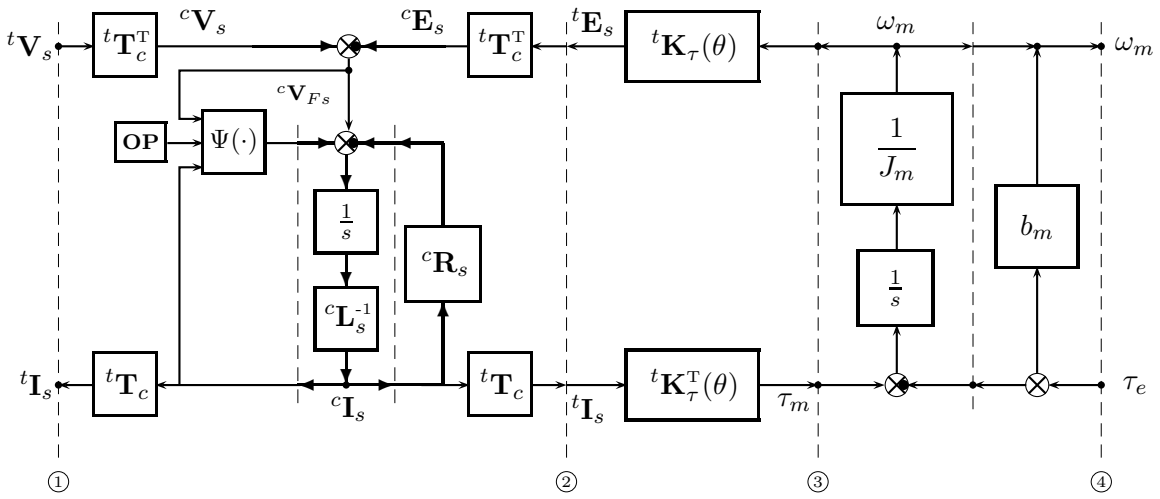

Figure 5.9: POG block scheme of the motor in the transformed frame under open-phase fault condition.

This equation is the generalization of (5.37) indeed the components ${}^{f_g}V_{i_1}$, ${}^{f_g}V_{i_1}$, .., ${}^{f_g}V_{i_o}$ of vector ${}^c\mathbf{V}_{Fs}$ are replaced with the voltage ${}^{f_o}V_{i_1}$, ${}^{f_o}V_{i_1}$, .., ${}^{f_o}V_{i_o}$ that are the components (different from zero) of vector ${}^c\mathbf{V}_{Fso}$

5. Add to the system (5.22) the final voltage ${}^c\mathbf{V}_{Fs}$.

In App. C.5 the proposed approach is applied to a five-phase and seven-phase synchronous motor, respectively. In both examples all the previous computations are written explicitly.
The POG block scheme representing the dynamics of the motor in faulty condition is shown in Fig. 5.9: the *mechanical part* between sections ③-④ and the *connection blocks* between sections ② and ③ (named torque vector) are unchanged, while the electrical part is modified respect to the POG model shown in Fig. 2.2.
Matrix ${}^t\mathbf{T}_c$ in Fig. 5.9 is the transformation used to impose the star connection constraint. The element denoted by **OP** is an internal input which defines the instants at which the faults occur and the indexes of the open phases. The block $\Psi(\cdot)$ is the function that calculates the voltage vector ${}^c\mathbf{V}_{Fs}$ added to the system starting from the vectors ${}^c\mathbf{I}_s$, ${}^c\mathbf{V}_s$ and ${}^c\mathbf{E}_s$.
In healthy condition vector ${}^c\mathbf{V}_{Fs}$ is zero, while in faulty condition it is given by equations (5.40) and it is the voltage vector having the components related to the faulty phases different from zero which guarantees zero currents through the faulty phases.

5.3.4 Simulation of a 5-phase motor

The Simulink block-mask of the POG model of Fig. 5.9 is shown in Fig. 5.10.a and in particular the electrical part is shown in Fig. 5.10.b. The user interface is not shown because it has the

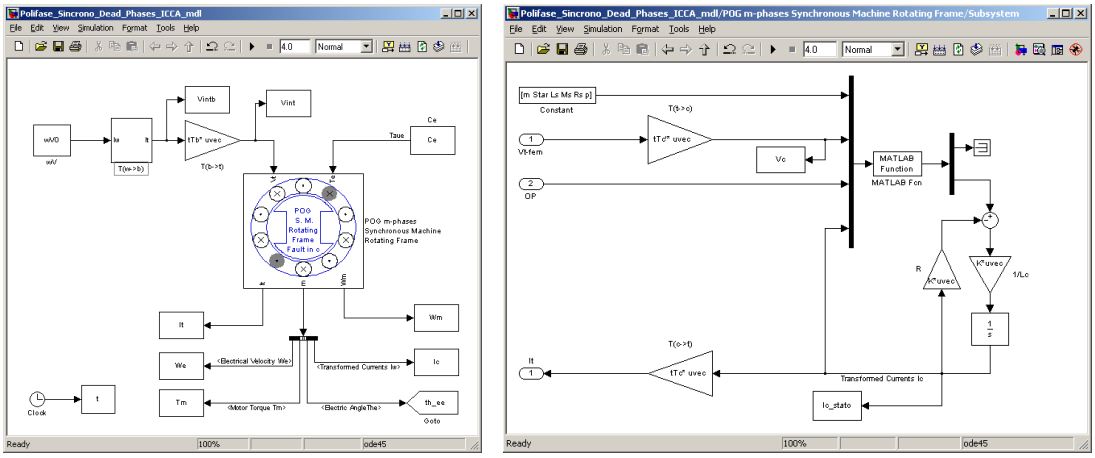

a) *b)*

Figure 5.10: Simulink schemes: a) Simulink scheme of the controlled electric motor, b) POG Simulink scheme of the electrical part modified to simulate the open-phase failures.

same structure of the one shown in Fig. 5.3.b.

The minimum dissipation torque control described in Sec.4.5.1 is used also in faulty condition to show the undesired faulty effects. The motor considered for simulations is a 5-phase permanent magnet synchronous motor characterized by the following electrical and mechanical lumped parameters: $m_s = 5$, $p = 1$, $N_c = 30$, $R_s = 2\,\Omega$, $L_s = 0.03$ H, $M_{s0} = 0.02$ H, $\varphi_r = 0.02$ Wb, $J_m = 1.6$ kg m^2, $b_m = 0.8$ Nms/rad, $V_{max} = 100$ V, $a_1 = 0.87$, $a_3 = 0.13$ and the external torque $\tau_e = 0$ Nm. Both the open-phase fault of two adjacent and non adjacent phases are

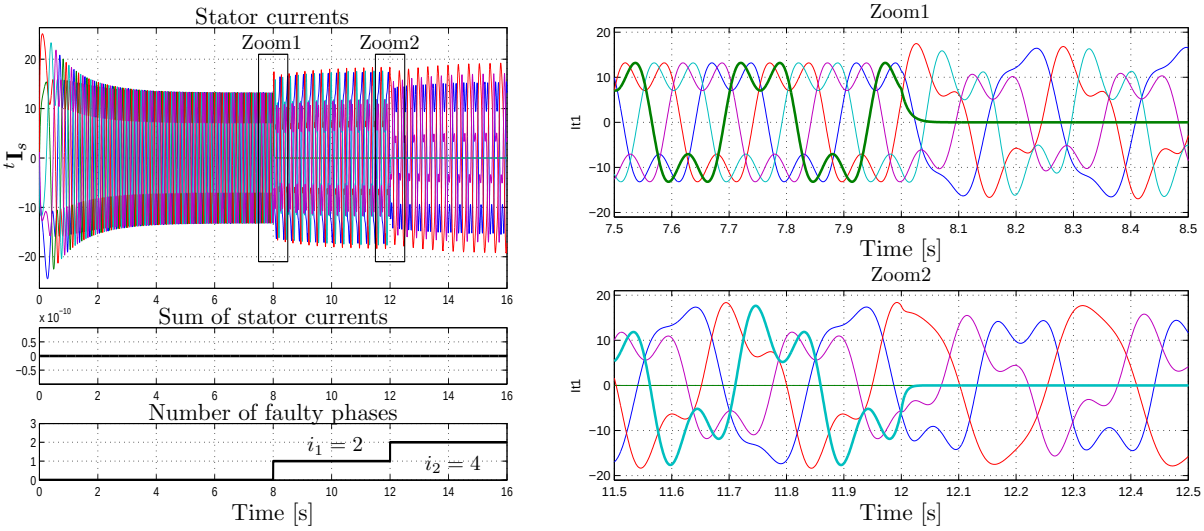

Figure 5.11: Stator currents ${}^t\mathbf{I}_s$ and their zoom when the faults occur: phase $i_1 = 2$ opens at time $t = 8$ s and phase $i_2 = 4$ opens at time $t = 12$ s.

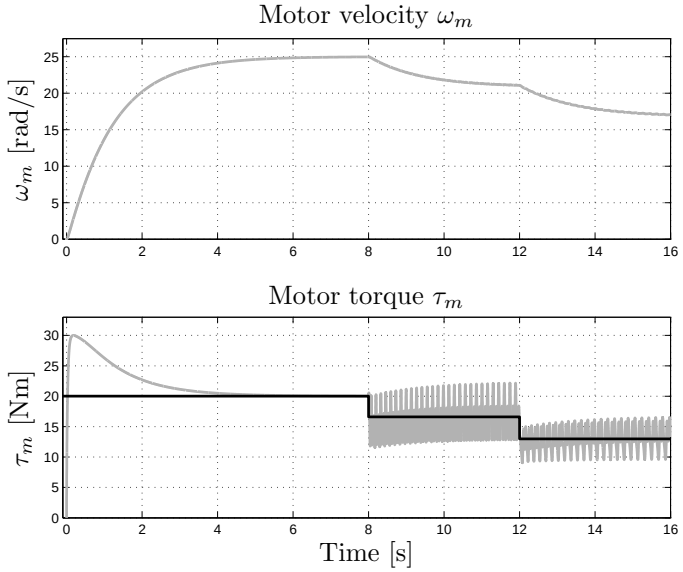

Figure 5.12: Motor velocity ω_m and motor torque τ_m (the black line is the torque mean value).

simulated and the faults occur at $t_1 = 8$ s and $t_2 = 12$ s, respectively.

The simulation results shown in Fig. 5.11-5.12 correspond to the case of two open-phase faults occurring at two non-adjacent phases, in particular phase $i_1 = 2$ opens at time $t = 8$ s and phase $i_2 = 4$ opens at time $t = 12$ s. When $t_1 \leq t \leq t_2$ $n = 1$, $\mathcal{S}_o = \{\,\}$, $\mathcal{S}_g = \{i_1 = 2\}$, while when $t > t_2$ $n = 2$, $o = 1$, $\mathcal{S}_o = \{i_1 = 2\}$, $\mathcal{S}_g = \{i_2 = 4\}$.
Fig. 5.11 shows the stator currents ${}^t\mathbf{I}_s$, the sum of stator currents (always equal to zero because the motor is star-connected), the number of faulty phases ($i = 2$, $j = 4$) and the zoom of the stator currents ${}^t\mathbf{I}_s$ when the faults occur. Note that at time $t = 8$ s the phase 2 opens and the current I_{s2} goes to zero, then at time $t = 12$ s the phase 4 opens and the current I_{s4} goes to zero with zero current in I_{s2}.
When the faults occur the motor decelerates, as show in Fig. 5.12, because when the first open-phase fault occurs the mean value of the torque reduces to the 82.9% and it reduces to the 64.9% when also the second phase is open. The torque ripple (calculated as the peak to peak value normalized with respect to the mean value) is about the same in both the faulty conditions: it is of 56.6% in the first faulty case and it is 57.6% in the second ones.

The second set of simulation results is shown in Fig. 5.13-5.14, corresponding to the case of open-phase fault occurring at two adjacent phases: phase $i_1 = 3$ opens at $t = 8$ s and phase $i_2 = 2$ opens at $t = 12$ s. When $t_1 \leq t \leq t_2$ $n = 1$, $\mathcal{S}_o = \{\,\}$, $\mathcal{S}_g = \{i_1 = 3\}$, while when $t > t_2$ $n = 2$, $o = 1$, $\mathcal{S}_o = \{i_1 = 3\}$, $\mathcal{S}_g = \{i_2 = 3\}$.
Fig. 5.13 shows the stator currents ${}^t\mathbf{I}_s$, the sum of stator currents, the number of faulty phases and the zoom of stator currents when the faults occur. Note that also in this case during the transient of the second fault the current in the first broken phase is zero.

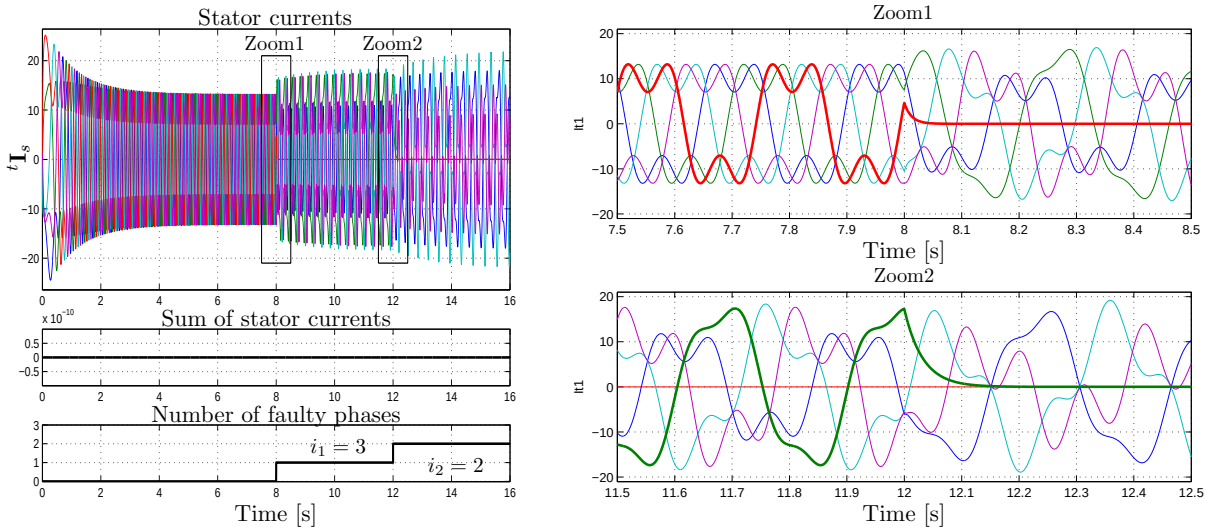

Figure 5.13: Stator currents ${}^t\mathbf{I}_s$ and their zoom when the faults occur: phase $i = 3$ opens at time $t = 8$ s and phase $j = 2$ opens at time $t = 12$ s.

The motor velocity ω_m and the motor torque τ_m (with its mean value) are shown in Fig. 5.14. When the first open-phase fault occurs the mean value of the torque reduces to the 82.8% and the torque ripple is 56.7%, while when the second fault occurs at an adjacent phase the torque mean value reduces to the 54.9% and the torque ripple is 192.4%.
This simulation shows how the torque reduction with two adjacent open-phases is higher than the case with two non-adjacent phases. Then, the fault effects on the motor torque depend on both the number and the relative spatial distribution of the open-phase faults.

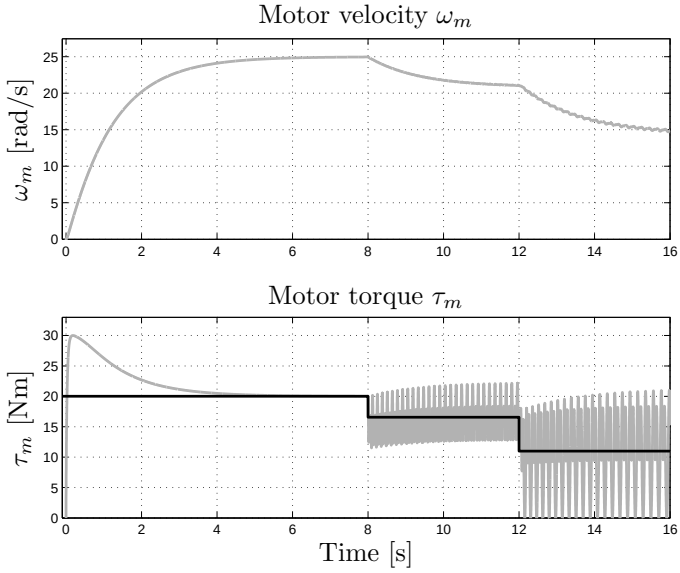

Figure 5.14: Motor velocity ω_m and motor torque τ_m (the black line is the torque mean value).

Chapter 6

Minimum Dissipation Fault-Tolerant Controls

Multi-phase motor drives are more reliable than the traditional three-phase ones because they can continue to operate even in case of faults such as the loss of one or more phases. In [4] and [8] a multi-phase synchronous motor is designed with a modular approach minimizing the electrical, magnetic and thermal coupling between the windings. Thus, a failure in one winding will not affect the operation of the remaining windings. However, as shown in Chap.5, if the control is not modified the mean value of the torque reduces and a torque ripple appears. Therefore a reconfiguration of the control strategy for the remaining healthy phases is necessary to compensate the fault effect maintaining unaffected the performance of the system.
Several fault-tolerant controls have been proposed in the fixed reference frame [9]-[12] and in the rotating reference frame [13] and [14], in order to make the motor able to operate safely even in case of fault (in particular obtaining ripple-free torque and minimizing losses).
In [9] the healthy-phase balanced currents are calculated keeping the magneto motive force (MMF) unchanged under the faults. Although a solution is obtained for a 5-phase synchronous motor where the 1-st and the 3-rd are injected, it is quite complex to generalize the proposed approach for machines with higher number of phases where the number of injected harmonics increases. Moreover this method does not minimize the global Joule losses and the torque ripple. In [10] the symmetry of the healthy-phase currents with respect to the location of the faulty phases is used reducing the torque pulsation and satisfying the star-connection constraint. An optimal solution is obtained for a 5-phase synchronous motor but also in this case the generalization of the control strategy is quite complex. In [11] the current vector in faulty conditions is obtained using the Lagrangian multipliers with the minimum dissipation function subject to the open phase and the minimum torque ripple constraints. Also in [12] a similar result is obtained with a different approach: the dimension of the *speed normalized back electromotive force* vector is adapted to the dimension of the remaining healthy-phases. These

two methods hold for machines with a generic odd number of phases but the constraint on the maximum phase current limit is not taken into account. In [13] different control strategies are compared for a seven phase induction motor but it is not clear how the current references are obtained. In [14] a seven-phase synchronous motor with a particular shape of the rotor flux is used. Then the higher number of degrees of freedom of the drive is used in the post-fault strategy. Although this method is very interesting, it can be used only for a particular type of machines.
In this chapter the minimum dissipation control of a multi-phase PM machine in the case of open circuited phases is studied. Using a vectorial approach the optimal current references in fault condition which provide the desired torque (without ripple) minimizing the dissipation are obtained in the fixed and rotating reference frame, respectively. Moreover the maximum phase current limit is taken into account. The approach is quite general: the proposed control law can be used for any shape of the rotor flux, for a generic odd number of phases and it works in presence of one or more failures.
The main contents of this chapter have been published in [54] and [55].

6.1 Minimum dissipation torque control in fault condition

In this chapter we refer to a permanent magnet synchronous motor with an *odd* number m_s of concentrated winding in star connection, see Fig. 2.1, characterized by the same parameters shown in Tab. 2.1.
Assuming that the failures do no affect the operation of the remaining healthy windings when f open-phase faults occur the related phase currents fall down to zero and they do not contribute any more to the torque generation. Therefore the open phase constraints must be taken into account to mitigate the fault effects.
This section covers only the fault tolerant control; however monitoring the stator current (in the fixed or rotating reference frame) and its harmonic spectrum it is possible to detect the open phase fault. More details about fault detection and fault diagnosis can be found in [56]-[59].

6.1.1 Control in the fixed reference frame

In healthy condition the current vector ${}^t\mathbf{I}_d$ which provides the desired torque τ_d minimizing the power dissipation is the vector with the minimum modulus parallel to the torque vector ${}^t\mathbf{K}_\tau(\theta)$:

$$ {}^t\mathbf{I}_d(\theta) = \frac{{}^t\mathbf{K}_\tau(\theta)}{|\,{}^t\mathbf{K}_\tau(\theta)|^2}\,\tau_d. \tag{6.1} $$

When f phase-faults occur the open phase constraints must be taken into account projecting the torque vector onto the $m_s-(f+1)$ dimensional subspace generated by the healthy currents.

Let $\mathcal{S} = \{i_1, i_2, ..., i_f\}$ denote the index set of the faulty phases with $f \leq m_s - 3$. In the case of a star connected motor the open phase constraints can be written as:

$$ {}^{\underline{t}}\mathbf{B}^{\mathrm{T}}\, {}^{t}\mathbf{I}_s = \left[\sum_{i=1}^{m_s} I_{si}\,,\, I_{si_1}\,,\, I_{si_2}\,,\cdots,\, I_{si_f} \right]^{\mathrm{T}} = (\mathbf{0}^{f+1})^{\mathrm{T}} $$

where matrix ${}^{\underline{t}}\mathbf{B}$ is defined as follows:

$$ {}^{\underline{t}}\mathbf{B} = \left[\mathbf{1}^{m_s}\ \ {}^{t}\mathbf{B}\right], \qquad {}^{t}\mathbf{B} = [\ \mathbf{e}_{i_1}^{m_s}\ \mathbf{e}_{i_2}^{m_s}\ \cdots\ \mathbf{e}_{i_f}^{m_s}]. \tag{6.2} $$

Note that in matrix ${}^{\underline{t}}\mathbf{B}$ the vector $\mathbf{1}^{m_s}$ is used to consider the star connection constraint, while matrix ${}^{t}\mathbf{B}$ selects the faulty component (the i-th standard basis vector $\mathbf{e}_i^{m_s}$ of space $\mathbb{R}^{m_s}$ is used to select the i-th fault component I_{si} of the current vector ${}^{t}\mathbf{I}_s$). The vectors $\mathbf{1}^{m_s}, \mathbf{e}_{i_1}^{m_s}, \mathbf{e}_{i_2}^{m_s}, \cdots$ and $\mathbf{e}_{i_f}^{m_s}$ form a basis of the $(f+1)$-dimensional forbidden subspace $\mathrm{Im}({}^{\underline{t}}\mathbf{B})$. The subspace of the remaining healthy currents that can be used to generate torque is $\ker({}^{\underline{t}}\mathbf{B}^{\mathrm{T}})$ because it is orthogonal to the forbidden subspace $\mathrm{Im}({}^{\omega}\mathbf{B})$. Indeed the null-space of the constraint matrix transpose is the orthogonal complement of its row space: $\ker({}^{\underline{t}}\mathbf{B}^{\mathrm{T}}) = (\mathrm{Im}({}^{\omega}\mathbf{B}))^{\perp}$.
Then the current constraints are satisfied if the torque vector ${}^{t}\mathbf{K}_\tau(\theta)$ is projected on $\ker({}^{\underline{t}}\mathbf{B}^{\mathrm{T}})$ along $\mathrm{Im}({}^{\underline{t}}\mathbf{B})$ as follows:

$$ \begin{aligned} {}^{t_f}\mathbf{K}_\tau(\theta) &= {}^{t}\mathbf{K}_\tau(\theta) - {}^{\underline{t}}\mathbf{B}\left({}^{\underline{t}}\mathbf{B}^{\mathrm{T}}\,{}^{\underline{t}}\mathbf{B}\right)^{-1}{}^{\underline{t}}\mathbf{B}^{\mathrm{T}}\,{}^{t}\mathbf{K}_\tau(\theta) \\ &= \left[\mathbf{I}_{m_s} - {}^{\underline{t}}\mathbf{B}\left({}^{\underline{t}}\mathbf{B}^{\mathrm{T}}\,{}^{\underline{t}}\mathbf{B}\right)^{-1}{}^{\underline{t}}\mathbf{B}^{\mathrm{T}}\right]{}^{t}\mathbf{K}_\tau(\theta) \\ &= \mathbf{P}\,{}^{t}\mathbf{K}_\tau(\theta) \end{aligned} \tag{6.3} $$

where $\mathbf{P}$ is the projection matrix on $\ker({}^{\underline{t}}\mathbf{B}^{\mathrm{T}})$ along $\mathrm{Im}({}^{\underline{t}}\mathbf{B})$.
A graphical representation of equation (6.3) is shown in Fig. 6.1 where the torque vector ${}^{t}\mathbf{K}_\tau(\theta)$, the forbidden subspace $\mathrm{Im}({}^{\underline{t}}\mathbf{B})$ and the projected torque vector ${}^{t_f}\mathbf{K}_\tau(\theta)$ are respectively described by the violet, black and red vectors. Note that the projected torque vector ${}^{t_f}\mathbf{K}_\tau(\theta)$ describes a complex symmetrical trajectory on the subspace $\ker({}^{\underline{t}}\mathbf{B}^{\mathrm{T}})$ of the healthy currents because it is a nonsymmetrical vector with zeros in correspondence of the components related to the faulty phases. Moreover if the rotor flux function is characterized by the first odd $m_s - 2$ harmonics, the modulus of torque vector $|\,{}^{t}\mathbf{K}_\tau(\theta)|$ is constant while the modulus of the projected torque vector $|\,{}^{t_f}\mathbf{K}_\tau(\theta)|$ is a periodic function of the electric angle. Substituting equation (6.3) in (6.1) one obtains in fault condition the current vector ${}^{t_f}\mathbf{I}_d(\theta)$ which provides the desired torque τ_d satisfying the constraints and minimizing the power dissipation:

$$ {}^{t_f}\mathbf{I}_d(\theta) = \frac{{}^{t_f}\mathbf{K}_\tau(\theta)}{|\,{}^{t_f}\mathbf{K}_\tau(\theta)|^2}\,\tau_d. \tag{6.4} $$

Since in the fixed reference frame Σ_t the current and voltage vectors ${}^{t}\mathbf{I}_s(\theta)$ and ${}^{t}\mathbf{V}_s(\theta)$ are functions of the electrical position θ and the magnetic coupling between the phases (described by

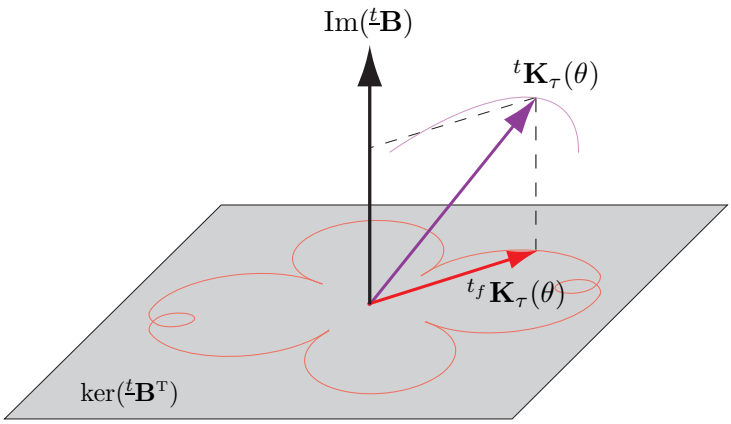

Figure 6.1: Projection of a torque vector onto the subspace of healthy currents in the fixed reference frame Σ_t.

the full inductance matrix $^t\mathbf{L}_s$) makes difficult the achievement of the control scheme, then an hysteresis current controller is used in order to follow the time variant reference current vector $^{t_f}\mathbf{I}_d(\theta)$, see Fig. 6.2.

Equation (6.4) has been found with different approach in [11] and [12]. In [11] the current vector in faulty conditions is obtained using the Lagrangian multipliers with the minimum dissipation function subject to the open phase and the star connection constraints.

In [12] a vectorial approach is used to directly project the torque vector (named *speed normalized back electromotive force*) on the subspace of the healthy currents and imposing the star connection constraint.

The main difference of the approach proposed in this paper compared to the others in [11] and [12] is that our approach can be extended also in the rotating reference frame (also known as *dq-reference frame*) where a constant torque can be reached using a feed-forward action and a PI controller.

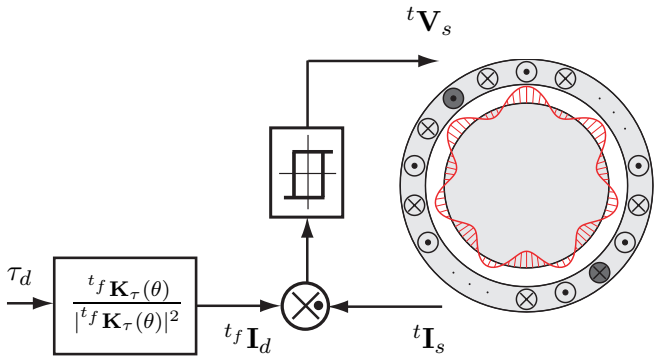

Figure 6.2: Multi-phase control motor drive scheme under fault condition in the fixed reference frame Σ_t.

6.1.2 Control in the rotating reference frame

The dynamic model (2.1) of the multi-phase synchronous motor can be expressed in the rotating frame Σ_ω using the transformation ${}^t\mathbf{T}_\omega \in \mathbb{R}^{m_s \times m_s - 1}$, as reported in Sec.2.2.1. The transformed current vector ${}^\omega\mathbf{I}_d$ which provides, in healthy condition, the desired torque τ_d minimizing the power dissipation is the vector with the minimum modulus parallel to the transformed torque vector ${}^\omega\mathbf{K}_\tau$:

$$ {}^\omega\mathbf{I}_d = \frac{{}^\omega\mathbf{K}_\tau}{|{}^\omega\mathbf{K}_\tau|^2}\,\tau_d. \tag{6.5} $$

Since the transformed current vector is ${}^\omega\mathbf{I}_s = {}^t\mathbf{T}_\omega^{\mathrm{T}}\,{}^t\mathbf{I}_s$, then the open phase constraint can be written as:

$$ {}^t\mathbf{B}^{\mathrm{T}}\,{}^t\mathbf{I}_s = {}^t\mathbf{B}^{\mathrm{T}}\,{}^t\mathbf{T}_\omega\,{}^\omega\mathbf{I}_s = (\mathbf{0}^f)^{\mathrm{T}} \tag{6.6} $$

where matrix ${}^t\mathbf{B}$ is defined in (6.2). Therefore the constraint matrix ${}^\omega\mathbf{B}$ in the rotating reference frame can be written as follows:

$$ {}^\omega\mathbf{B} = ({}^t\mathbf{B}^{\mathrm{T}}\,{}^t\mathbf{T}_\omega)^{\mathrm{T}} = {}^t\mathbf{T}_\omega^{\mathrm{T}}\,{}^t\mathbf{B} = {}^\omega\mathbf{T}_t\,{}^t\mathbf{B}. \tag{6.7} $$

Substituting (2.6) and (6.2) in (6.7) one obtains:

$$ {}^\omega\mathbf{B} = \underset{1:2:m_s-2}{\overset{k}{\left|\left[\begin{array}{c}\cos(k((h-1)\gamma_s-\theta))\\ \sin(k((h-1)\gamma_s-\theta))\end{array}\right]\right|}}_{h\in\mathcal{S}} = \left[\mathbf{w}_{i_1}\,\mathbf{w}_{i_2}\,\cdots\,\mathbf{w}_{i_f}\right], $$

where the vectors $\mathbf{w}_{i_1}$, $\mathbf{w}_{i_2}$, $\cdots$ and $\mathbf{w}_{i_f}$ (that are the columns of the transformation ${}^\omega\mathbf{T}_t$ related to the faulty phases) form a basis of the f-dimensional forbidden subspace $\mathrm{Im}({}^\omega\mathbf{B})$ in the rotating reference frame.

One first difference with the previous approach is that matrix ${}^\omega\mathbf{B}$ imposes only the fault constraints because it is the transformation matrix ${}^t\mathbf{T}_\omega$ that imposes the star connection constraint. On the contrary, in the fixed frame Σ_t matrix ${}^t\mathbf{B}$ imposes both the constraints.

The subspace $\ker({}^\omega\mathbf{B}^{\mathrm{T}})$, which is orthogonal to the forbidden subspace $\mathrm{Im}({}^\omega\mathbf{B})$, is the subspace of the healthy currents that satisfies the constraints. Therefore the current constraints are satisfied if the transformed torque vector ${}^\omega\mathbf{K}_\tau$ is projected on $\ker({}^\omega\mathbf{B}^{\mathrm{T}})$ along $\mathrm{Im}({}^\omega\mathbf{B})$. Now the projection matrix is:

$$ {}^\omega\mathbf{P} = \mathbf{I}_{m_s-1} - {}^\omega\mathbf{B}\left({}^\omega\mathbf{B}^{\mathrm{T}}\,{}^\omega\mathbf{B}\right)^{-1}{}^\omega\mathbf{B}^{\mathrm{T}}. $$

Using this projection matrix ${}^\omega\mathbf{P}$ one can obtain the following projected torque vector ${}^{\omega_f}\mathbf{K}_\tau(\theta)$:

$$ {}^{\omega_f}\mathbf{K}_\tau(\theta) = {}^\omega\mathbf{P}\,{}^\omega\mathbf{K}_\tau = \underset{1:2:m_s-2}{\overset{k}{\left|\left[\begin{array}{c}{}^fK_{dk}(\theta)\\ {}^fK_{qk}(\theta)\end{array}\right]\right|}}. \tag{6.8} $$

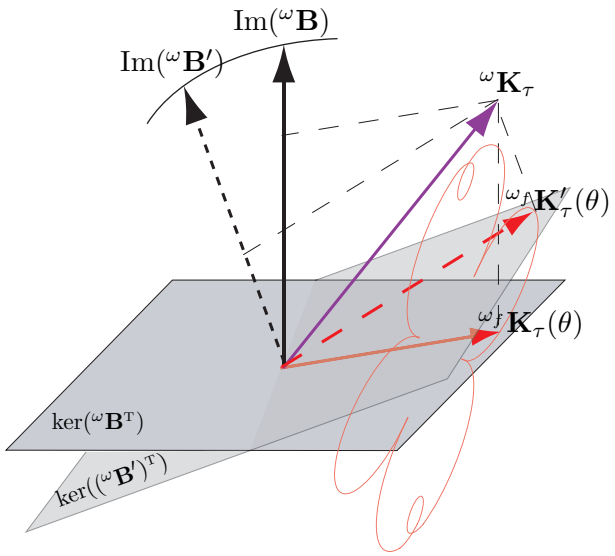

Figure 6.3: Projection of a torque vector onto the subspace of healthy currents in the rotating reference frame Σ_ω.

Note that the vectors $\mathbf{w}_{i_1}$, $\mathbf{w}_{i_2}$ $\cdots$ and $\mathbf{w}_{i_f}$ are function of the electric angle θ, then also the forbidden subspace $\mathrm{Im}({}^{\omega}\mathbf{B})$ is function of θ. Consequently the projected torque vector ${}^{\omega_f}\mathbf{K}_\tau(\theta)$ is a periodic function of the electric angle θ.

A graphical representation of equation (6.8) at two different time t and t', with $t < t'$, is shown in Fig. 6.3: the transformed torque vector ${}^{\omega}\mathbf{K}_\tau(\theta)$ (the violet vector) is constant while the forbidden subspace $\mathrm{Im}({}^{\omega}\mathbf{B})$ (the black vector) is function of the electric angle θ. This is the second difference compared to the previous approach (where the forbidden subspace $\mathrm{Im}({}^{t}\mathbf{B})$ is constant and the torque vector ${}^{t}\mathbf{K}_\tau(\theta)$ is time variant).

The variation of the forbidden subspace from $\mathrm{Im}({}^{\omega}\mathbf{B})$ to $\mathrm{Im}({}^{\omega}\mathbf{B}')$ modifies from $\ker({}^{\omega}\mathbf{B}^{\mathrm{T}})$ to $\ker({}^{\omega}\mathbf{B}'^{\mathrm{T}})$ the subspace of the healthy currents satisfying the fault constraints. In Fig. 6.3, the projection of the transformed torque vector ${}^{\omega_f}\mathbf{K}_\tau(\theta)$ (the red vector) is a periodic function of the electric angle and it describes a periodic trajectory (the red line). Note that the trajectory is the same of Fig. 6.1 because it is possible to prove that the following relation holds:

$$|{}^{t_f}\mathbf{K}_\tau(\theta)| = |{}^{\omega_f}\mathbf{K}_\tau(\theta)|.$$

Substituting equation (6.8) in (6.5) one obtains the desired current vector ${}^{\omega_f}\mathbf{I}_d$ in frame Σ_ω under fault condition which provides the desired torque τ_d minimizing the power dissipation:

$${}^{\omega_f}\mathbf{I}_d(\theta) = \frac{{}^{\omega_f}\mathbf{K}_\tau(\theta)}{|{}^{\omega_f}\mathbf{K}_\tau(\theta)|^2}\,\tau_d = \left\| \begin{bmatrix} {}^{f}I_{dk}(\theta) \\ {}^{f}I_{qk}(\theta) \end{bmatrix} \right\|_{1:2:m_s-2}^{k}, \tag{6.9}$$

where the direct ${}^{f}I_{dk}$ and quadrature ${}^{f}I_{qk}$ are:

$$ {}^{f}I_{dk}(\theta) = \frac{{}^{f}K_{dk}(\theta)}{|{}^{\omega_f}\mathbf{K}_\tau(\theta)|^2}\,\tau_d\,, \quad {}^{f}I_{qk}(\theta) = \frac{{}^{f}K_{qk}(\theta)}{|{}^{\omega_f}\mathbf{K}_\tau(\theta)|^2}\,\tau_d. \tag{6.10} $$

The direct component ${}^{f}I_{dk}$ of the current vectors $\overline{I}_{sk}$ must be used to satisfy the faulty constraint despite they dissipate power without producing torque (in (2.12) the direct components K_{dk} of the torque vectors $\overline{K}_{\tau k}$ are zero). Indeed the direct components are related to the rotor-magnetizing flux and they are necessary to balance the asymmetrical magnetic field of the stator currents in fault condition due to the asymmetrical displaced of the remaining healthy phases.

The condition ${}^{\omega}\mathbf{I}_s = {}^{\omega_f}\mathbf{I}_d$ cannot be achieved using the control law (4.29) because the desired current is a periodic function of the electric angle θ. Therefore an undesired torque ripple (due to the tracking error) appears if the block diagram shown in Fig. 6.4 is used. This problem can be overcome using the following control:

$$ {}^{\omega}\mathbf{V}_s = ({}^{\omega}\mathbf{R}_s + {}^{\omega}\mathbf{J}_s\,{}^{\omega}\mathbf{L}_s)\,{}^{\omega}\mathbf{I}_s + {}^{\omega}\mathbf{K}_\tau\,\omega_m - \mathbf{K}_c({}^{\omega}\mathbf{I}_s - {}^{\omega_f}\mathbf{I}_d) \tag{6.11} $$

where $\mathbf{K}_c$ is a diagonal matrix, used for the control design, defined as follows:

$$ \mathbf{K}_c = K\frac{(2\omega)^2}{s^2 + (2\omega)^2}(s + 2\omega)^2\mathbf{I}_{m_s - 1}. \tag{6.12} $$

Matrix $\mathbf{K}_c$ has been obtained using the Internal Model Principle because the direct and quadrature components of the current vector in (6.5) oscillate at frequencies 2ω, 4ω, ... $(m_s - l)\omega$. Note that the first part of equation (6.12) allows to track reference current vectors while the second order term $(s + 2\omega)^2$ stabilizes the system. The equations (6.5) and (6.11) are used together in the control block diagram shown in Fig. 6.4.

Another solution is to transform the desired current vector ${}^{\omega_f}\mathbf{I}_d$ in the rotating reference frame

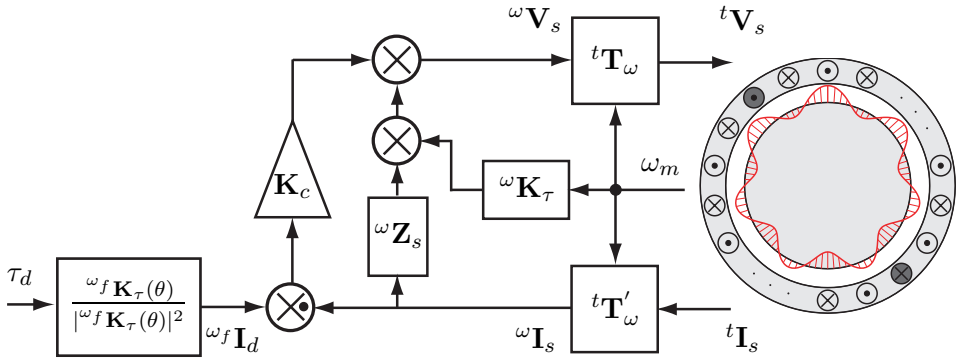

Figure 6.4: Multi-phase control motor drive scheme under fault condition in the rotating reference frame Σ_ω.

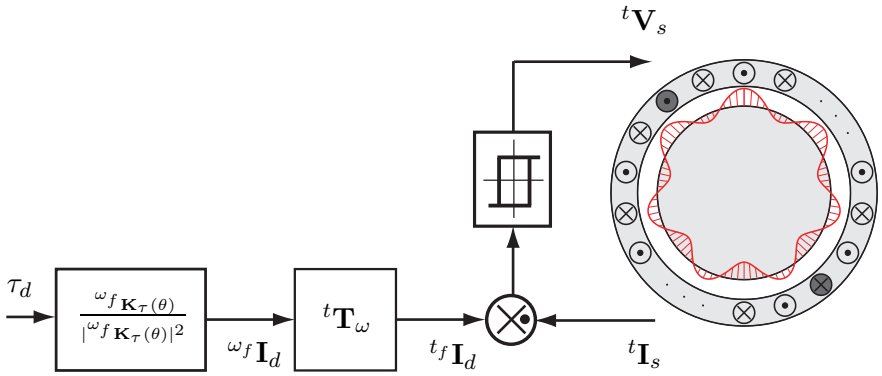

Figure 6.5: Multi-phase control motor drive scheme under fault condition in the rotating reference frame Σ_ω: the hysteresis current controller.

to the desired current vector $^{t_f}\mathbf{I}_d$ in the fixed reference frame as: $^{t_f}\mathbf{I}_d(\theta) = {}^{t}\mathbf{T}_\omega\, {}^{\omega_f}\mathbf{I}_d(\theta)$.
Then an hysteresis current controller can be used in order to follow the time variant reference current vector $^{t_f}\mathbf{I}_d(\theta)$, see Fig. 6.5. Using the proposed control the multi-phase motor continues to operate safely (generating the same desired torque without ripple) under a phase-faults without any additional hardware connections. The first solution is used in [54] while the second one is used in [55].

6.1.3 Current limit

Since the drive should continue to produce the same rated power also in fault condition, the fault-tolerant controls increase the current amplitude in the healthy phases. Therefore even if the theoretical maximum number of faults in a m_s-phase motor is $m_s - 3$ the maximum number of faults for safe operation of the motors is less of $m_s - 3$ and it is related to the maximum phase current limit because the semiconductor switches of the inverter and the motor must be able to stand operation with this increased current level. When the current limit is not satisfied to avoid any further failures the post-fault control must be modified considering that degraded performance is better than no performance.
The main advantages of the proposed control compared to the others in [11] and [12] is that the maximum current limit can be taken into account. When the amplitudes of the components of the current vectors $^{t}\mathbf{I}_s$ are bounded by the the maximum rated current I_{max} the following constraint holds:

$$\sum_{k=1:2}^{n} I_{mk} \leq I_{max} \tag{6.13}$$

where I_{mk} is the amplitude of the k-th injected harmonics in (4.2). The upper bound of summation is $n > m_s - 2$ because using the proposed fault tolerant control a higher order of odd harmonics are injected to feed the motor. Since the harmonics of order $2m_sh \pm k$ with $h = 0, 1, 2..$

and $k = 1:2:m_s-2$ are transformed into the same complex vector $\overline{I}_{sk}$, the constraint (6.13) can be rewritten as:

$$\sum_{k=1:2}^{m_s-2} |\overline{I}_{sk}| \leq \sqrt{\frac{m_s}{2}} I_{max}, \tag{6.14}$$

where the modulus of the current vectors I_{sk} is defined, from (4.5) and (6.10), as:

$$|\overline{I}_{sk}| = \sqrt{{}^fK_{dk}^2 + {}^fK_{qk}^2}\, \frac{\tau_d}{|{}^{\omega_f}\mathbf{K}_\tau(\theta)|^2}. \tag{6.15}$$

Substituting (6.15) in (6.14) one obtains the maximum torque in faulty condition minimizing the current dissipation and satisfying the maximum current limit I_{max}:

$$\tau_c(\theta) = \frac{|{}^{\omega_f}\mathbf{K}_\tau(\theta)|^2}{\sum_{k=1:2}^{m_s-2} \sqrt{{}^fK_{dk}(\theta)^2 + {}^fK_{qk}(\theta)^2}} \sqrt{\frac{m_s}{2}} I_{max}. \tag{6.16}$$

Equation (6.16) transforms the current limit in a torque limit, so when $\tau_d > \tau_c(\theta)$ the desired torque is saturated to the maximum value satisfying the maximum current limit. This value depends both on the number and the relative spatial distribution of the open-phase faults. In other words, for the same value of the current limit I_{max} the available torque $\tau_c(\theta)$ with two adjacent open-phases is lower than the case with two non-adjacent phases. Introducing (6.16) in (6.9) one obtains the desired current vector ${}^{\omega_f}\mathbf{I}_d$ in frame Σ_ω under fault condition minimizing the power dissipation and satisfying the current limit:

$${}^{\omega_f}\mathbf{I}_d(\theta) = \begin{cases} \dfrac{{}^{\omega_f}\mathbf{K}_\tau(\theta)}{|{}^{\omega_f}\mathbf{K}_\tau(\theta)|^2}\, \tau_d & \text{if} \quad \tau_d \leq \tau_c(\theta) \\ \dfrac{{}^{\omega_f}\mathbf{K}_\tau(\theta)}{|{}^{\omega_f}\mathbf{K}_\tau(\theta)|^2}\, \tau_c(\theta) & \text{if} \quad \tau_d > \tau_c(\theta) \end{cases} \tag{6.17}$$

The dependence of τ_c from θ produces a time variant motor torque τ_m. In the applications where a constant torque is required it is necessary to compute the minimum of the maximum torque $\min(\tau_c(\theta))$. It can be made in the algorithm comparing the actual value $\tau_c(\theta)$ with the stored value τ_{cs} and saving the actual value in the stored value $\tau_{cs} = \tau_c(\theta)$ if $\tau_c(\theta) < \tau_{cs}$. Therefore after a period $T = 2\pi t/\theta$ one obtains the minimum value $\tau_{cs} = \min(\tau_c(\theta))$. In this case the current vector ${}^{\omega_f}\mathbf{I}_d$ is obtained as:

$${}^{\omega_f}\mathbf{I}_d(\theta) = \begin{cases} \dfrac{{}^{\omega_f}\mathbf{K}_\tau(\theta)}{|{}^{\omega_f}\mathbf{K}_\tau(\theta)|^2}\, \tau_d & \text{if} \quad \tau_d \leq \tau_{cs} \\ \dfrac{{}^{\omega_f}\mathbf{K}_\tau(\theta)}{|{}^{\omega_f}\mathbf{K}_\tau(\theta)|^2}\, \tau_{cs} & \text{if} \quad \tau_d > \tau_{cs} \end{cases} \tag{6.18}$$

Note that there is a trade-off between the torque mean value and the torque ripple: the (6.17) provides a higher torque with ripple, while the (6.18) provides a lower torque without ripple.

6.2 Simulations of a 7-phase motor without current limit

The control diagrams in Fig. 6.2, Fig. 6.4 have been implemented in Matlab-Simulink as shown in Fig. 6.6. The masked blocks of the motors refer to the POG model in faulty of Sec. 5.3, while the green blocks implement the minimum dissipation fault tolerant control in the fixed and rotating reference frames.

The simulation results shown in this section have been obtained using the following electrical and mechanical lumped parameters: $m_s = 7$, $p = 1$, $N_c = 30$, $R_s = 2\,\Omega$, $L_s = 0.03$ H, $M_{s0} = 0.02$ H, $\varphi_r = 0.02$ Wb, $J_m = 1.6$ kg m^2, $b_m = 0.8$ Nm s/rad, $a_1 = 1$, $a_3 = 0.25$, $a_5 = 0.1$, desired torque $\tau_d = 25$ Nm and external torque $\tau_e = 0$ Nm.

The faults occur on the 6-th, 3-rd and 5-th phases at time $t_1 = 1.5$s, $t_3 = 11.5$ s and $t_5 = 22.5$ s. The fault tolerant controls (6.4) and (6.9) are activated at time $t_2 = 2.5$ s, $t_4 = 12.5$ s and $t_6 = 22.5$ s. The controls are activated after a delay time of 1 s in order to show the dynamic behaviors of the motor in fault condition although in real application the fault detection time is shorter.

The zooms of the stator current vectors ${}^t\mathbf{I}_s$ in the fixed reference frame obtained using control (6.4) and control (6.9) are shown in Fig. 6.7. Since the drive should continue to produce the same electrical power also in faulty condition, the amplitude of the currents and voltages in the healthy phases increase as the number of open phases. The stator currents waveform is modified compared to the normal operation because using the proposed fault tolerant controls the motor is fed injecting a higher order of odd harmonics.

Moreover there is a symmetry of the healthy-phase currents with respect to the displacement of

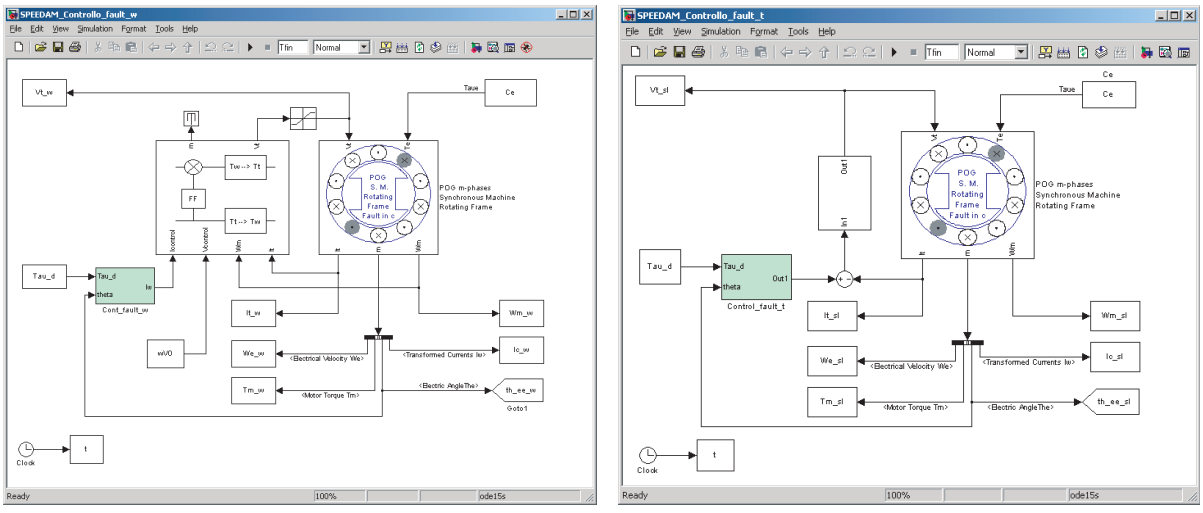

a) *b)*

Figure 6.6: Simulink schemes: a) Simulink scheme of the control diagram in Fig. 6.2, b) Simulink scheme of the control diagram in Fig. 6.4.

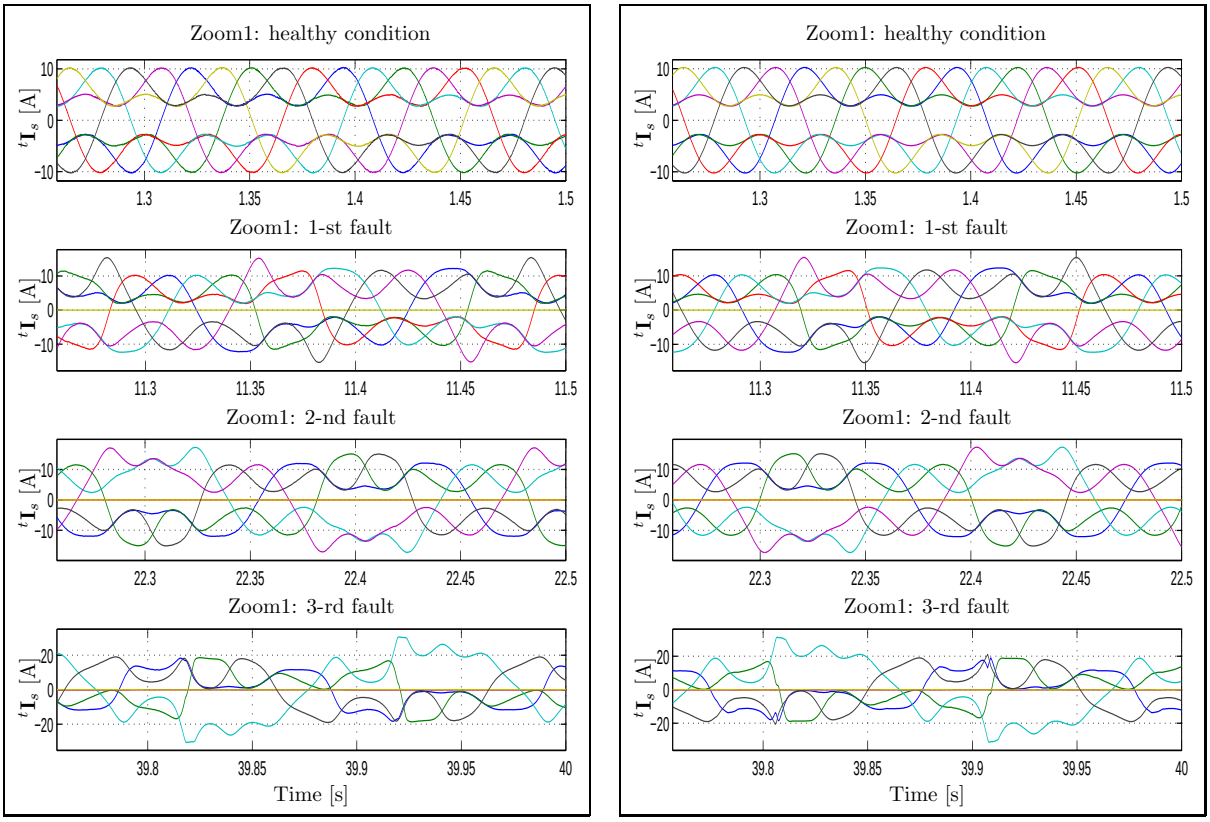

Figure 6.7: Stator currents ${}^t\mathbf{I}_s$ in the fixed reference frame obtained using the control laws described in Sec. 6.1.1 (on the left) and in Sec. 6.1.2 (on the right) .

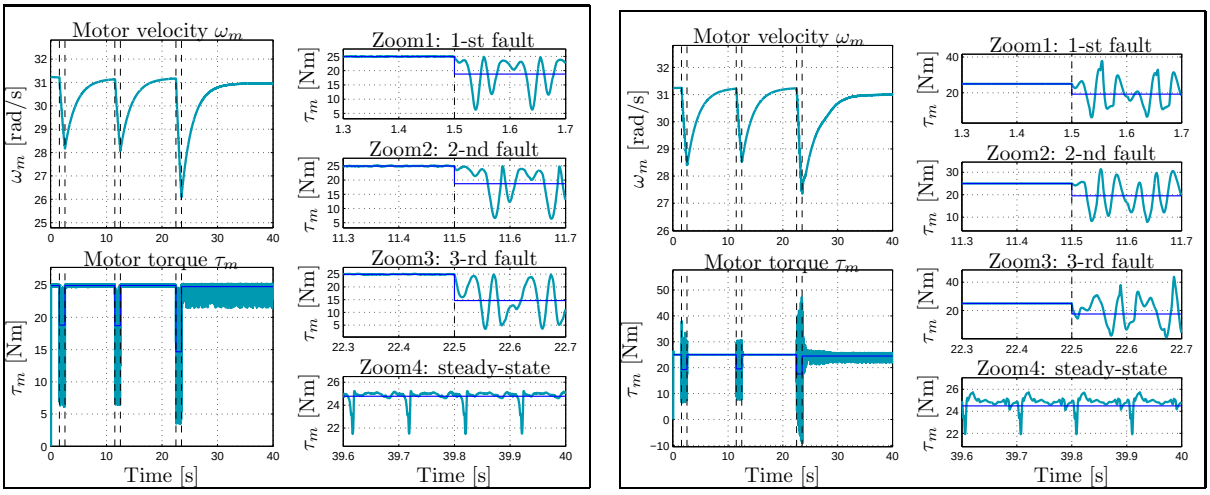

Figure 6.8: Motor velocity ω_m and motor torque τ_m using control (6.4) (on the left) and using control (6.9) (on the right).

the faulty phases. This mirror symmetry of the healthy-phase currents is used in [10] to obtain a fault-tolerant control of a five-phase permanent magnet synchronous motors with trapezoidal back-emf.

The dynamic behaviors of the motor velocity ω_m and the motor torque τ_m are shown in Fig. 6.8. During the delay time between the faults and the control reconfiguration the mean value of the torque decreases and a torque ripple appears, while when the fault tolerant control is activated the torque grows to the desired value $\tau_d = 25$ Nm without ripple for the first two faults. At time t_6, when the third fault occurs, the torque ripple does not disappear because in this case the voltage demand exceeds the maximum voltage of the inverter DC link causing a tracking error which generates the torque ripple. The different dynamic behavior of the motor torque and the motor velocity between the two fault tolerant controls is due to the two different control schemes (hysteresis for the first one and feed-forward action with controller for the second one).

6.3 Simulations of a 5-phase motor with current limit

The control diagram in Fig. 6.5 has been implemented in Matlab-Simulink as shown in Fig. 6.9. The masked blocks of the motor refer to the POG model in faulty of Sec. 5.3, while the green blocks implement the minimum dissipation in the rotating reference frames where also the current constraint is taken into account.

The simulation results shown in this section have been obtained using the following electrical and mechanical parameters: $m_s = 5$, $p = 1$, $N_c = 30$, $R_s = 2\,\Omega$, $L_s = 0.03$ H, $M_{s0} = 0.01$ H,

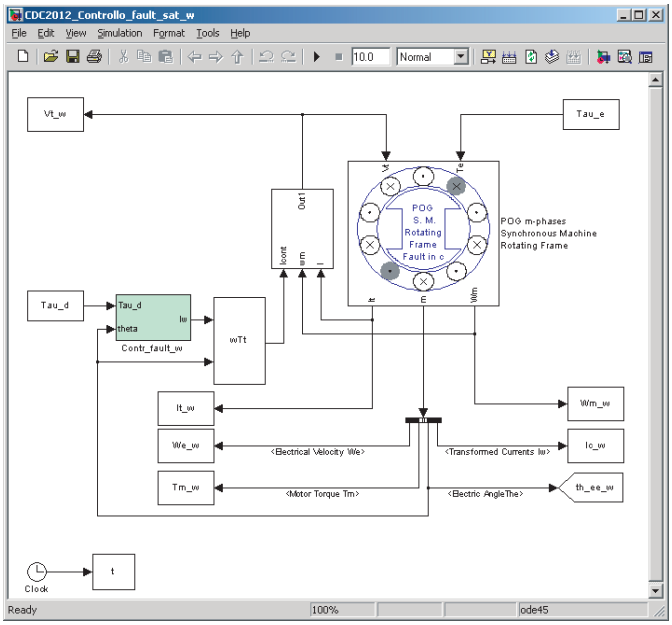

Figure 6.9: Simulink scheme of the control diagram in Fig. 6.5.

$\varphi_r = 0.02$ Wb, $J_m = 1.6$ kg m^2, $b_m = 0.8$ Nm s/rad, $a_1 = 1$, $a_3 = 0.25$, desired torque $\tau_d = 23$ Nm and an external torque $\tau_e = 5$ Nm.

The strategies (6.9), (6.17) and (6.18) are compared under two adjacent open-phase faults: the faults occur at times $t_1 = 1.5$ s and $t_3 = 10$ s on the 2-nd and the 3-rd phase, respectively; while the proposed fault tolerant controls are activated, at time $t_2 = 2.5$ s and at time $t_4 = 11$ s, after a delay time of 1 s in order to show the dynamic behaviors of the motor in fault condition. The same simulation is repeated two times in order to put in evidence the dynamic effect of the current saturation. In the first simulation the maximum current supportable by the inverter switches and by the motor is considered high, so the current limit is neglected, while in the second case the maximum current limit is $I_{max} = 35$ A.

The motor velocity ω_m and the motor torque τ_m obtained using (6.9) are shown in Fig. 6.10. When the first open-phase fault occurs the mean value of the torque decreases and the torque ripple appears (between t_1 and t_2 the control is unchanged with respect to the healthy condition). At time t_2 when the fault tolerant control is applied the torque grows up to the desired value $\tau_m = \tau_d = 23$ Nm without ripple.

When the second open-phase fault occurs the mean value of the torque decreases again and the torque ripple appears because between t_3 and t_4 there are two open phases but the control is not modified with respect to the first failure case. At time t_4 the fault tolerant control is applied and the torque grows up to the desired value τ_d without ripple.

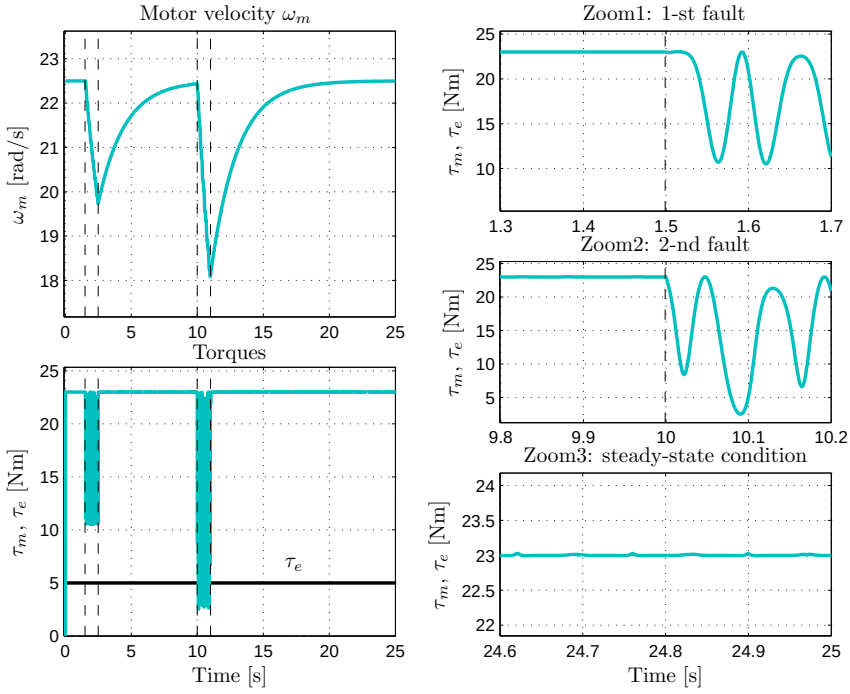

Figure 6.10: Motor velocity ω_m, motor torque τ_m and external torque τ_e (black) using control (6.9) without current limit.

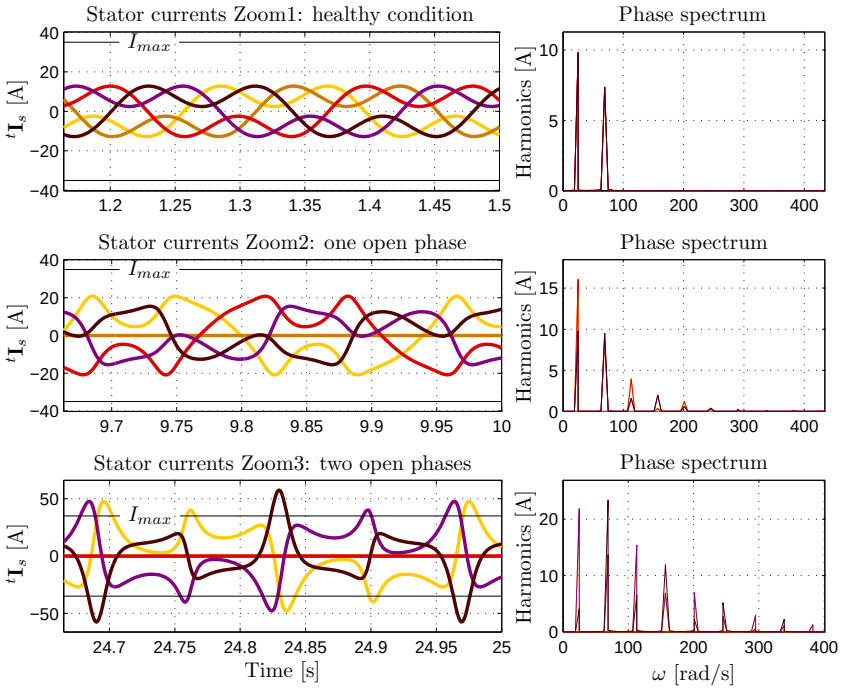

Figure 6.11: Zoom of the stator current vector $^t\mathbf{I}_s$ in the fixed reference frame with its corresponding harmonic spectrum obtained using control (6.9) .

Fig. 6.11 shows the zooms of the stator current vectors $^t\mathbf{I}_s$ in the fixed reference frame with its corresponding spectrum in healthy condition and when the fault tolerant control is activated. In healthy condition only the 1-st and the 3-rd harmonics are injected, while when the post-fault control is activated more odd harmonics of higher order are injected. Using (6.9) the amplitude of the healthy phase currents increases and the maximum phase current limit I_{max} is not satisfied when the second fault occurs (this control does not take into account the maximum current constraint).

The motor velocity ω_m and the motor torque τ_m obtained using (6.17) and (6.18) are presented in Fig. 6.12, while the zooms of the stator current vectors $^t\mathbf{I}_s$ are shown in Fig. 6.13. At time t_2 when the saturated fault tolerant controls are applied the torque reaches a lower value of τ_d in order to satisfy the maximum phase current limit I_{max} (see Fig. 6.13). Using (6.17) one obtains a torque mean value of 17.03 Nm with ripple while using (6.18) one obtains a lower torque $\tau_m = \min(\tau_c(\theta)) = 11.8$ Nm without ripple. Therefore the motor accelerates at the velocity ω_m of 20.35 rad/s when the (6.17) is used, while it decelerates at the velocity ω_m of 11.15 rad/s in the second case because the motor torque is reduced to 51%. This simulation clearly puts in evidence the trade-off between the torque mean value and the torque ripple: the (6.17) provides a higher torque with ripple, while the (6.18) provides a lower torque without ripple. In Fig. 6.14 one can see the *direct* and *quadrature* components I_{dk}, I_{qk} in the rotating reference frame: they are constant in healthy condition while they are a periodic function of the electric angle θ with

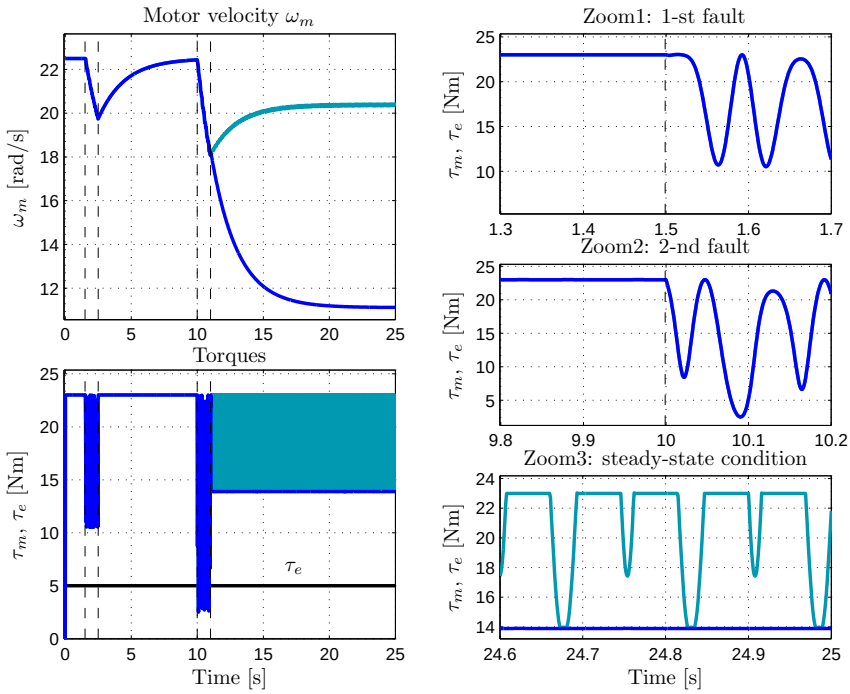

Figure 6.12: Motor velocity ω_m, motor torque τ_m and external torque τ_e (black) obtained using control (6.17) (teal) and control (6.18) (blue) with current limit.

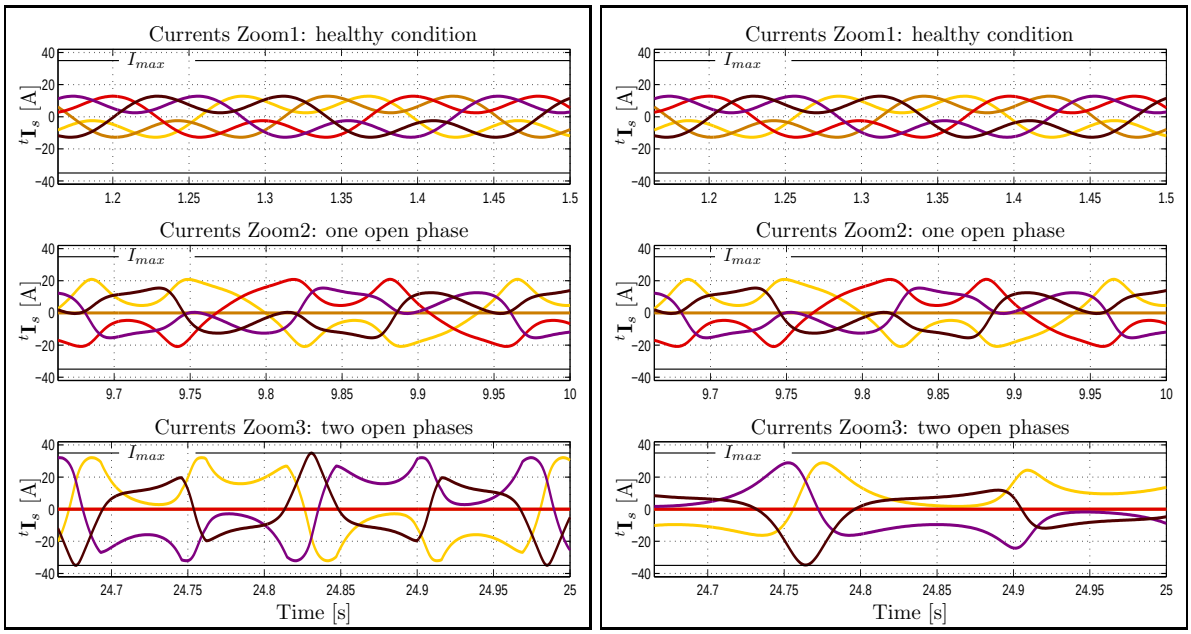

Figure 6.13: Zoom of the stator current vector ${}^t\mathbf{I}_s$ in the fixed reference frame obtained using control (6.17) (on the left) and control (6.18) (on the right).

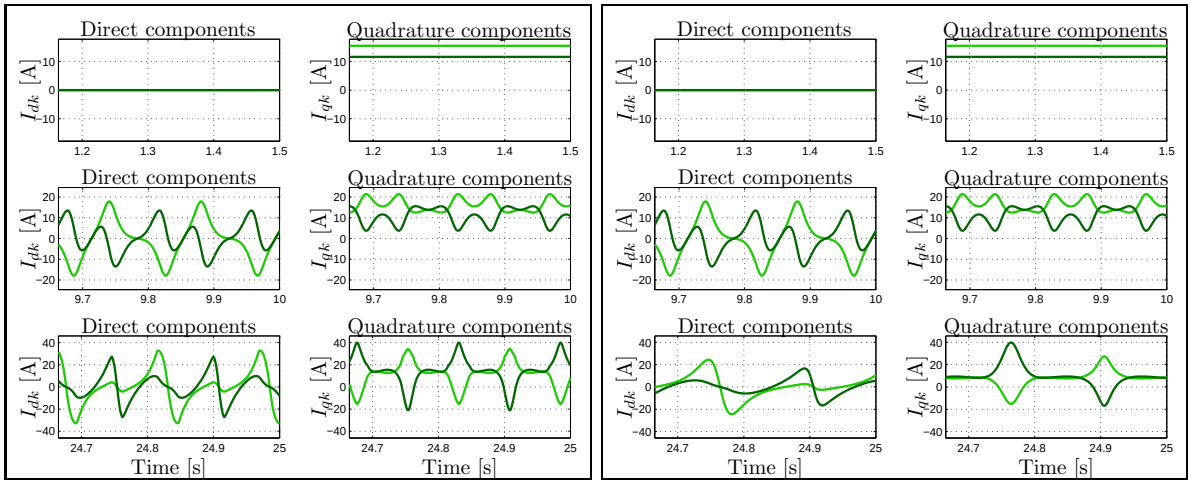

Figure 6.14: Direct and quadrature components I_{dk}, I_{qk} in the rotating frame ($k = 1$ green, $k = 3$ dark green) obtained using control (6.17) (on the left) and control (6.18) (on the right).

period T that can be obtain considering the fundamental even harmonic at frequencies $2p\omega_m$ as $T = 2\pi/2p\omega_m$. In the first-fault condition the period T is of 0.1396 s in both cases, while when the second post-fault control is activated the period T is of 0.1544 s for the control (6.17) and it is of 0.2818 s for the control (6.18).

Chapter 7

Hybrid Electric Vehicle

In safety critical applications, i.e. propulsion and traction applications, the reliability is a very important issue. When the classical three-phase motor drives are employed the reliability in case of fault is reached increasing the redundancy of the actuator system, using two motors and two inverters, see [5] or modifying the power converter topology, see [6]. The fault tolerant capability of multi-phase motor drives and the possibility to enhance the motor torque by injecting higher order stator current harmonics, see [1] and [2], make the multi-phase synchronous machines suitable for Electric and Hybrid Electric Vehicles where reliability and power density are very important issues.
In this chapter the dynamic model of the power-split Toyota Hybrid System (THS), see [60] and [61], is proposed. The two three-phase electric machines that are commonly used in THS are here replaced by two five-phase machines. The model of the whole system includes the dynamics of the engine, electric machines, planetary gear, transmission and vehicle and is realized using the Power-Oriented Graphs modeling technique. A rule-based control strategy is implemented and a fault-tolerant control is applied in the case of electrical machine failure. Simulation results are given in both healthy and fault condition to show the effectiveness of the dynamic model and the robustness of the proposed control.
The main contents of this chapter have been submitted in [62].

7.1 POG modeling of the Toyota Hybrid System

The development of new control strategies and/or new architectures for hybrid electric vehicles (HEVs) requires a deep knowledge of the dynamic behavior and the dynamic interaction among all subsystems constituting HEVs [63]. Therefore it is essential to have precise and reliable simulative models to reduce the effort and the cost in the testing phase. The interest in hybrid vehicle simulation has grown up in the past years and led to the development of many computer programs to describe the operation of hybrid powertrains. Some examples of steady and quasi-

steady simulators are: JANUS [64], ADVISOR [65], PSAT [66], Autonomie [67], CarSim from Mechanical Simulation Corporation and many others. Although steady-state or quasi-steady models allow to achieve fast computation time, they do not permit to capture transient behavior and may be unsuitable to such systems in which this is a crucial aspect. Therefore dynamic models can be used to make accurate dynamic analysis and simulation of the system and to design effective control strategies. Taking advantage from the POG modular structure, the model of the power-split Toyota Hybrid System (THS) [60] can be obtained by interconnecting the models of the subsystems that interact each other through their power ports, see Fig. 7.1. The power-split configuration includes an internal combustion engine (ICE), two multi-phase Permanent Magnet Synchronous Machines (MG1 and MG2), a transmission and the vehicle. The power-split is provided by a planetary gear: the ICE is rigidly connected to the Carrier (C), MG1 is connected to the Sun (S), MG2 and the vehicle transmission are rigidly connected to the Ring (R). The torques provided by the engine and the electrical motors are the inputs of the

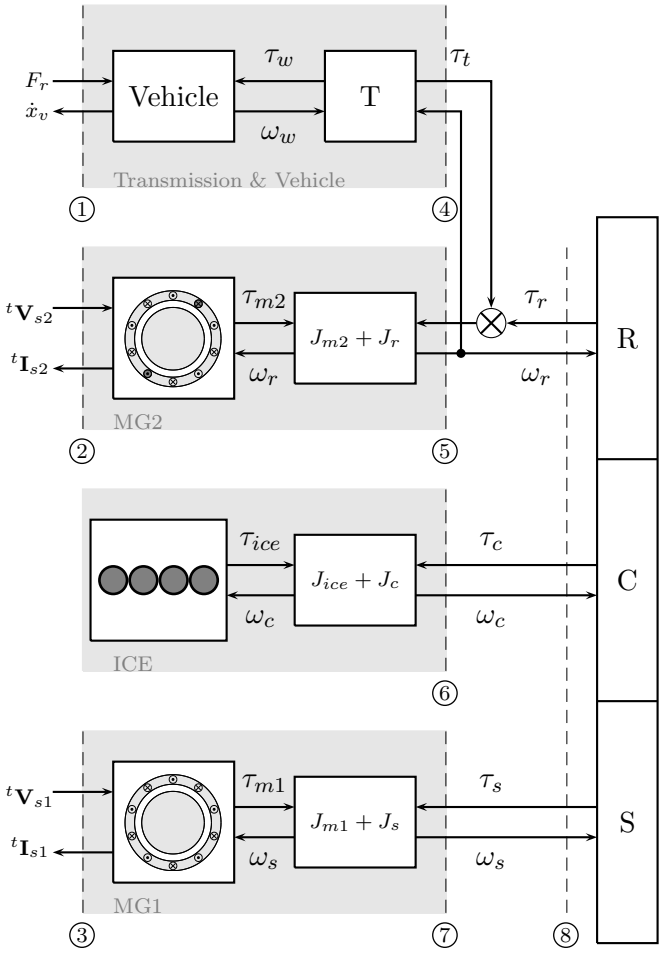

Figure 7.1: Scheme of the considered power structure of the vehicle.

powertrain system and the dynamic behavior of each block is defined by using the transmitted and the reflected torque/force.
In Fig. 7.1 the dashed lines denoted by numbers indicate the power sections, within the system, through which the power flows among the subsystems. Moreover they correspond to the power sections indicated by the same numbers in the POG schemes of the considered subsystems presented in the next part of the chapter.
In this model the input engine power passes forward through the powertrain in the direction of the physical power flow. The planetary gear splits this power into two paths: a mechanical path (also known as parallel path) and an electrical path (also known as series path). The engine power is transferred mechanically from the carrier to the ring gear, which is connected to the vehicle, via parallel path. The remaining mechanical engine power is transformed into electrical power through MG1 and it is used to charge the battery or to supply MG2. Although the electrical path is less efficient than the mechanical path it helps to improve the overall performance of the system.
Note that in this work the devices that store electrical energy such as batteries, supercapacitors and others, are not taken into account. Therefore we suppose that the electrical power which feed the machines MG1 and MG2 is always available. The machine MGi (with i=1,2) operates as motor if $P_{mi} > 0$ and as a generator if $P_{mi} < 0$.

7.1.1 Planetary Gear modeling

The planetary gears are key elements for the design of new hybrid power structures in the automotive area. In the literature it is usually considered as a static transmission gear, see [68]-

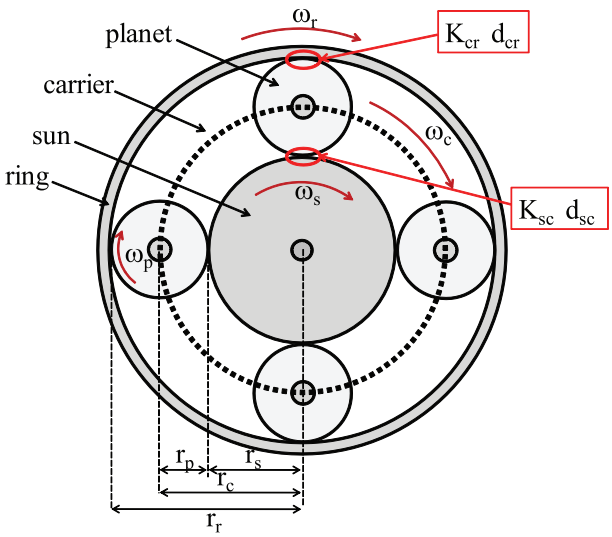

Figure 7.2: Planetary gear and related parameters.

[70]. Instead in [71] and [72] the POG technique is exploited to obtain different extended and reduced dynamic models of the planetary gear. Here a reduced elastic model of the planetary gear is given. The main parameters of the planetary gear, shown in Fig. 7.2, are: r_s, r_c, r_r and r_p are the sun, carrier, ring and planet radii; J_s, b_s, J_c, b_c, J_r, b_r, J_p and b_p are the inertia and linear friction coefficients of the sun, carrier, ring and planet, respectively. The carrier, the planets and the ring interact each other through the two elastic elements: the sun-carrier and the carrier-ring elastic elements K_{cr} and K_{sc} with the friction coefficients d_{sc} and d_{cr}.
Considering that the planetary gear inertias will be connected to the shafts of the ICE, PMSM and driving axle of the vehicle, it is convenient to provide a reduced elastic model of the planetary gear where inertias J_s, J_c and J_r are zero and considering these inertias in the shaft inertias of the motors and engine. Therefore, as shown in Fig. 7.1, these equivalent moments of inertias are considered: $J_{m2} + J_r$ for MG2 and ring, $J_{ice} + J_c$ for ICE and carrier and $J_{m1} + J_s$ for MG1 and sun.
Since the inertias J_s, J_c and J_r go to zero, the system degenerates towards a lower dynamic dimension system and the "reduced system" can be obtained by using a "congruent" transformation $\mathbf{x} = \mathbf{T}\mathbf{z}$ where $\mathbf{T}$ is a rectangular matrix obtained from some algebraic relations, see [71]. The dynamic equations of the reduced elastic model of the planetary gear in state space form are:

$$\underbrace{\begin{bmatrix} \frac{1}{K_{sc}} & 0 & 0 \\ 0 & J_p & 0 \\ 0 & 0 & \frac{1}{K_{cr}} \end{bmatrix}}_{\mathbf{L}_e} \underbrace{\begin{bmatrix} \dot{F}_{sc} \\ \dot{\omega}_p \\ \dot{F}_{cr} \end{bmatrix}}_{\dot{\mathbf{x}}} = \underbrace{\begin{bmatrix} 0 & r_p & 0 \\ -r_p & -r_p^2 d_{sc} - b_p - r_p^2 d_{cr} & -r_p \\ 0 & r_p & 0 \end{bmatrix}}_{-\mathbf{A}_e} \underbrace{\begin{bmatrix} F_{sc} \\ \omega_p \\ F_{cr} \end{bmatrix}}_{\mathbf{x}} + \underbrace{\begin{bmatrix} r_s & -r_s & 0 \\ -r_s d_{sc} r_p & r_s d_{sc} r_p - r_r d_{cr} r_p & r_r d_{cr} r_p \\ 0 & r_r & -r_r \end{bmatrix}}_{\mathbf{B}_e} \underbrace{\begin{bmatrix} \omega_s \\ \omega_c \\ \omega_r \end{bmatrix}}_{\mathbf{u}}$$

$$\underbrace{\begin{bmatrix} \tau_s \\ \tau_c \\ \tau_r \end{bmatrix}}_{\mathbf{y}} = \underbrace{\begin{bmatrix} r_s & r_s d_{sc} r_p & 0 \\ -r_s & -r_s d_{sc} r_p + r_r d_{cr} r_p & r_r \\ 0 & -r_r d_{cr} r_p & -r_r \end{bmatrix}}_{\mathbf{C}_e} \underbrace{\begin{bmatrix} F_{sc} \\ \omega_p \\ F_{cr} \end{bmatrix}}_{\mathbf{x}} + \underbrace{\begin{bmatrix} b_s + r_s^2 d_{sc} & -r_s^2 d_{sc} & 0 \\ -r_s^2 d_{sc} & b_c + r_s^2 d_{sc} + r_r^2 d_{cr} & -r_r^2 d_{cr} \\ 0 & -r_r^2 d_{cr} & b_r + r_r^2 d_{cr} \end{bmatrix}}_{\mathbf{D}_e} \underbrace{\begin{bmatrix} \omega_s \\ \omega_c \\ \omega_r \end{bmatrix}}_{\mathbf{u}} \tag{7.1}$$

Note that in the energy matrix $\mathbf{L}_e$ only the elastic coefficients K_{cr}, K_{sc} and the planet inertia J_p appear. There is a direct correspondence between the POG schemes and the state space dynamic equations, therefore equations in (7.1) can be represented by the POG schemes shown in Fig 7.3 and in Fig 7.4.
Particularly the scheme of Fig 7.4 shows clearly the reduced dynamic dimension of the system because only the friction coefficient b_s, b_r and b_c are used in the elaborator blocks of the sun, the ring and the carrier, respectively. This scheme is obtained applying the POG reduction technique to the complete POG model of the planetary gear, see [71]. Inverting the ring, the sun and the carrier paths one obtains the derivative causalities between the velocity and the torques where the angular velocities are the input and the torques are the output. Since the inertias J_s, J_c and J_r are zero the derivative path of each gear model is eliminated and only the

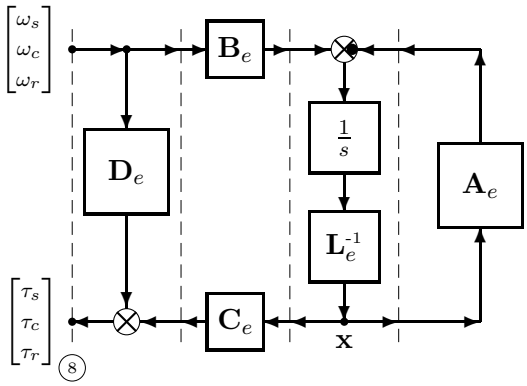

Figure 7.3: POG block scheme of the planetary gear related to the reduced elastic system (7.1).

friction coefficient b_s, b_r and b_c are used.
The compact representation of Fig 7.3 hides the structure of the system which can be shown using the POG scheme of Fig 7.4 where the reduced dimension and the elastic interaction between the gears of the epicyclic are clearly put in evidence.
The kinematics Willis relation [73] between angular velocities as function of the gear radii (7.2) can be obtained from equation (7.1) in steady-state condition (i.e. $\dot{\mathbf{x}} = 0$):

$$r_s\omega_s + r_r\omega_r = (r_s + r_r)\omega_c = 2r_c\omega_c \tag{7.2}$$

Since in (7.2) the engine speed ($\omega_c = \omega_{ice}$) is decoupled from the vehicle velocity ($\omega_r = v_v R_t / R_\omega$), then the engine can operate regardless of the vehicle velocity. This degree of freedom will be used in the control law to increase the engine efficiency.

7.1.2 Internal Combustion Engine model

In order to simulate the hybrid powertrain an engine model is needed. Since for our focus it is sufficient to consider the main mechanical dynamics of the engine, the simplified model of Fig. 7.5 is proposed. In this POG scheme the torque-speed map is associated with a first-order dynamic system that describes the equivalent dynamic behavior of the engine. In this model $J_{ice} + J_c$ are the inertias of the engine shaft and carrier, b_{ice} is the friction coefficient, τ_{ice} is the torque provided by the engine and $\tau_{ice,d}$ is the requested torque.
The engine map and the power map of the 2ZR-FXE engine (used in the 3-rd generation Toyota Prius) are shown in Fig. 7.6 where the black lines refer to the maximum torque $\tau_{ice,max}$ and power $P_{ice,max}$ for a given engine speed ω_c, the green lines refer to the optimum engine efficiency curves (where the fuel consumption is low). The maximum power delivered by the engine is 73 kW at 5200 rpm and its maximum torque is 142 Nm at 4000 rpm.
The maximum torque-speed map (black line) is used in the POG scheme of Fig. 7.5 to saturate the provided torque as $\tau_{ice} = \min\{\tau_{ice,d}, \tau_{ice,max}\}$, while the optimum torque curve (green line)

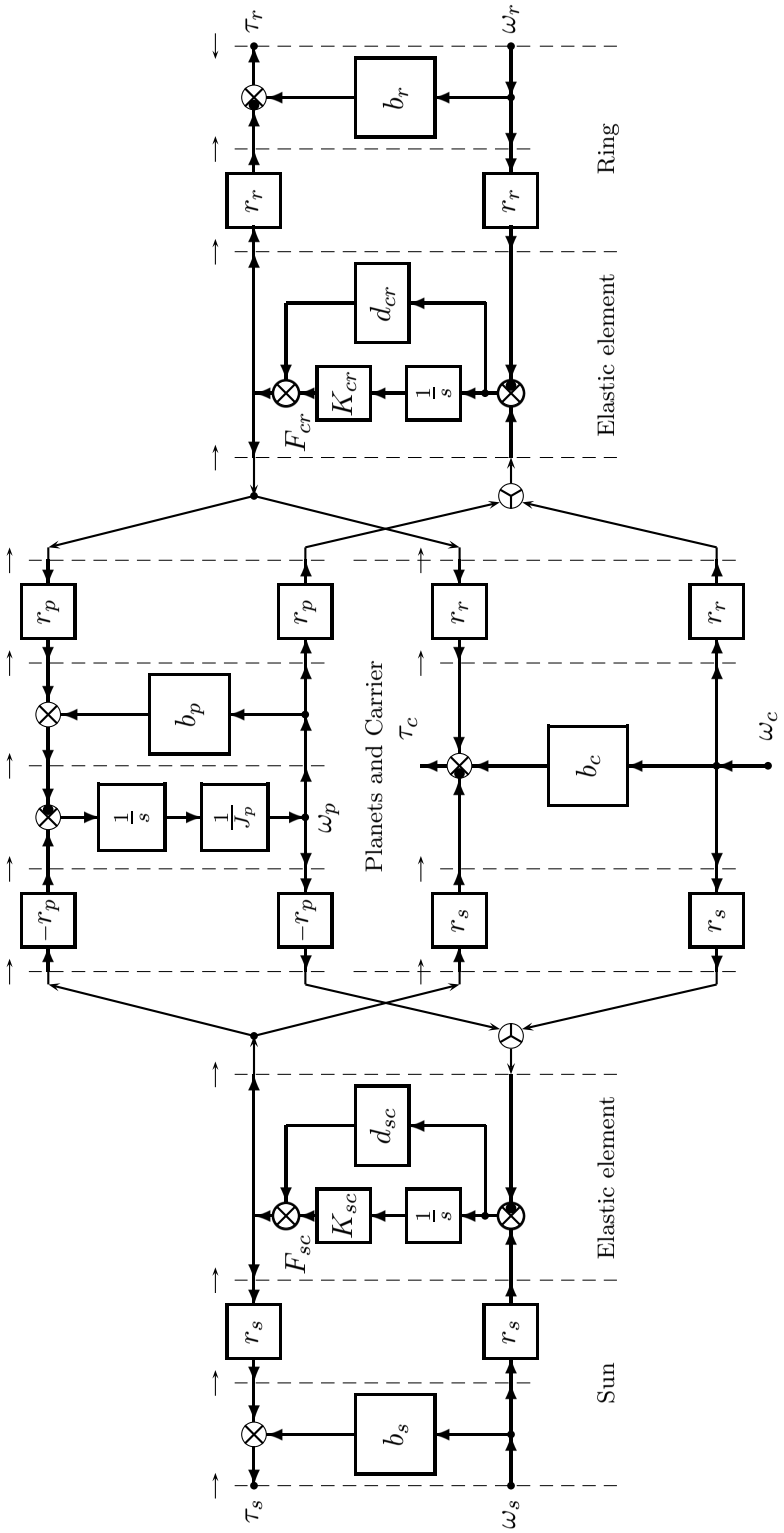

Figure 7.4: POG block diagram of the reduced planetary gear when $J_s = J_c = J_r = 0$ and the velocities are the inputs.

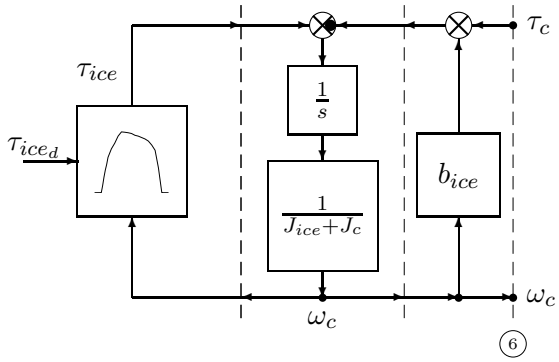

Figure 7.5: POG scheme of the ICE model.

is used in the control algorithm.
A more complete POG engine model can be found in [74] and [75] where the analogy of the internal combustion engine with electrical systems is used obtaining the differential equations of the engine dynamics in the state space form.

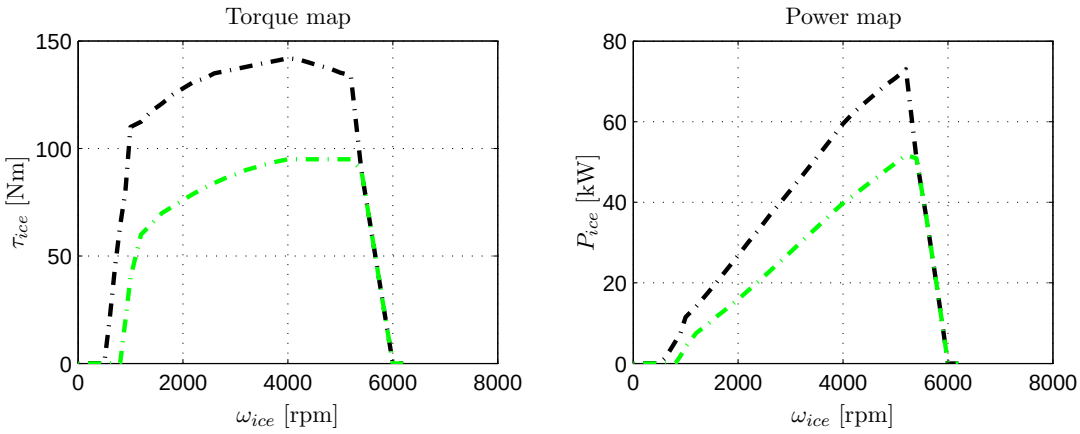

Figure 7.6: The torque-speed map (on the left) and the power-speed map (on the right) of the engine.

7.1.3 Model of the transmission and vehicle

The POG schemes of the transmission and vehicle are shown in Fig. 7.7. The transmission is modeled considering the elastic interaction between the teeth of the meshing gears, then the transmission stiffness K_t, the friction coefficient d_t and the transmission ratio R_t are used. In steady-state condition the following relations hold:

$$\begin{cases} \omega_r &= R_t\,\omega_w \\ \tau_w &= R_t\,\tau_t \end{cases}$$

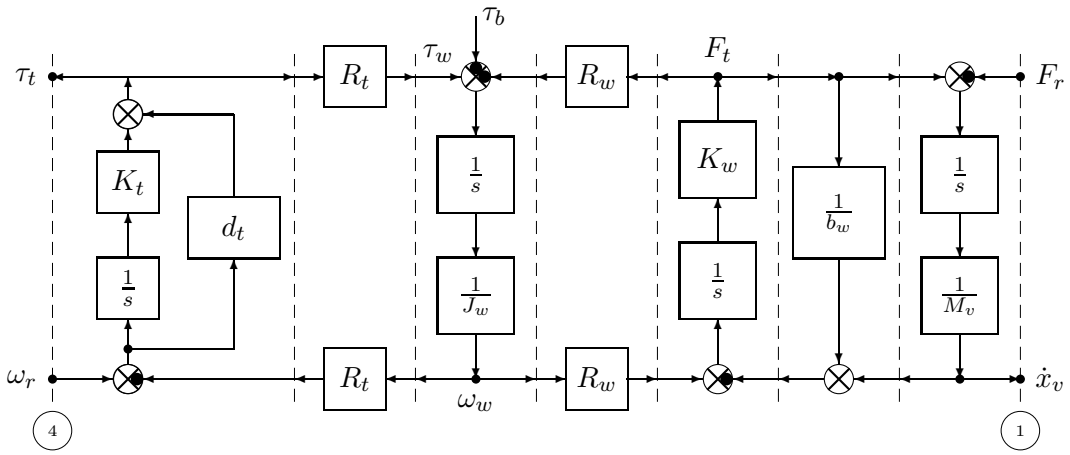

Figure 7.7: POG block scheme of the transmission and the vehicle.

where the transmission torque τ_t is the load torque for the electrical machines MG2 connected to the ring.
The wheel model is obtained neglecting the "slip" and "skid" dissipative phenomena between the tires and the ground, assuming that the wheels are solidly connected to the chassis (no suspensions) and considering only the rotation around the z axle. From the previous considerations it is possible to define the elastic tire model using: the wheel inertia J_w to describe the dynamic of the wheel and the wheel radius R_w, the tire longitudinal stiffness K_w and the friction coefficient b_w to describe the interaction between the tires and the ground. The total torque applied to the wheel can be written as:

$$\tau_T = \tau_w - \tau_b - R_w F_t$$

where τ_w is the wheel torque, τ_b is the braking torque and the product $R_w F_t$ is the load vehicle torque.
Since only the dynamic along the longitudinal direction is considered, the dynamic of the car can be modeled considering only the mass M_v of the vehicle and the traction and resistance forces F_t and F_r as follows:

$$M_v \ddot{x}_v = F_t - F_r$$

where the resistance force F_r represents the forces applied by the environment and can take into account the air resistance, the slope of the road and other effects. Assuming a flat road only the air resistance can be considered, in this case the resistance force F_r has the following form:

$$F_r = \alpha \dot{x}_{v,d}^2$$

where α is the drag coefficient which is used to quantify the air resistance of the vehicle.

7.2 Control Strategy

The adopted forward approach (also known as engine to wheel approach) to model the hybrid vehicle is very useful in the control design because the real power flows through the system are clearly put in evidence. The control strategy for the THS must be designed in two levels. The vehicle control level governs the dynamic behavior of the vehicle while the components control level actuates the reference signals from the vehicle control level to regulate the electrical motors and engine operation.

Vehicle control level

This rule-based control, see [61]-[70], generates the torque references for the electric machines $\tau_{m1,d}$ and $\tau_{m2,d}$ and for the engine $\tau_{ice,d}$ starting from the estimated required power P_{ve} and the tracking error between the reference vehicle speed $\dot{x}_{v,d}$ and real one $\dot{x}_v$. The estimated required power P_{ve} can be computed as follows:

$$P_{ve} = F_v\,\dot{x}_{v,d} + F_r\,\dot{x}_{v,d} = M_v\ddot{x}_{v,d}\,\dot{x}_{v,d} + F_r\,\dot{x}_{v,d}.$$

Since the car moves on flat road only the air resistance must be considered, then in this case the estimated power requirement P_{ve} can be rewritten as:

$$P_{ve} = M_v\ddot{x}_{v,d}\,\dot{x}_{v,d} + \alpha\,\dot{x}_{v,d}^3$$

where α is the drag coefficient.
The aim of the control is to optimize the fuel consumption, then in the control algorithm the optimum engine efficiency curves, shown in Fig. 7.6, are taken into account. The control should manage also the SOC level (State Of battery Charge), but in this work batteries are not modeled or equivalently they are considered always fully charged. Using this control the engine operates within its optimal operating region on the torque-speed plane in which the fuel efficiency is high. The different operation modes and conditions defined in [61] and [70] are listed below:

A Driving at low speed: the engine is off and the traction power is all given by MG2.

B Normal driving conditions: the traction power is supplied by the engine operating in its optimal region and by the electric motor MG2, while MG1 operates as generator to supply MG2 and/or to charge the battery (Normal energy flow).

C Boosting: during full throttle acceleration the traction power is given by the engine and by motor MG2.

D High speed cruising: to keep the engine constantly at a low speed, where engine efficiency is high, MG1 operates as motor and MG2 operates as generator (Energy recirculation flow). Note that when the vehicle cruises at high velocity the fuel consumption increases

if the engine velocity increases. Therefore it is better to keep the engine velocity constant at low speed where the fuel consumption is low even though in this way the transmission efficiency decreases (due to the double electromechanical conversion).

E Deceleration: the engine turns off and MG2 operates as generator recuperating the kinetic energy. When the braking power exceeds a limit value a friction brake is activated.

Components control level

The reference torques provided by the vehicle control level are the input of the motors and engine drives. Concerning the engine regulator, the desired torque $\tau_{ice,d}$ and cannot exceed the maximum torque $\tau_{ice,max}$ for a given engine speed ω_{ice}. Therefore the engine delivers the torque: $\tau_{ice} = \min\{\tau_{ice,d}, \tau_{ice,max}\}$, see Fig. 7.5.
Regarding the electrical motor drives the fault-tolerant control proposed in Sec. 6.1.2 is used to obtain the optimal current references in fault condition which provide the desired torque (without ripple) minimizing the dissipation and satisfying the limit current.

7.3 Simulation of the THS

The models of the ICE, Planetary Gear, electric machines MG1 and MG2, transmission, vehicle and environment forces have been implemented and masked in Matlab/Simulink environment obtaining a block library. Each masked block contains its POG model presented in the previous sections except to the masked blocks of the electrical motors that refer to the faulty model proposed in Sec. 5.3.
The system architecture implemented in Simulink is shown in Fig. 7.8. It has been obtained interconnecting the masked models like in Fig. 7.1. This "high level" approach is very useful because it allows to obtain also different architectures of electric and hybrid vehicles. Indeed using the same block and modifying the system architecture one can simulate a new powertrain dynamic model.
The orange block in Fig. 7.8 exploits the rule-based global control strategy of the vehicle and the green ones implement the minimum dissipation fault-tolerant torque control described in Sec. 6.1.2.
In order to show the advantages brought by the use of the multi-phase motors two different driving situation are simulated: a normal operation and a fault operation (the open-phase fault occurs on MG2 while it provides the traction power). Both cases are analyzed under the Extra Urban Driving Cycle (EUDC) that represents an high speed driving mode (the average speed is 62.6 km/h) in which the vehicle covers the distance of 6956 m in 400 s.
The main parameters of the system are reported in Table I. The value of the majority of the parameters is obtained from THS data sheets; otherwise when the value is not available it is estimated by using physical relations.

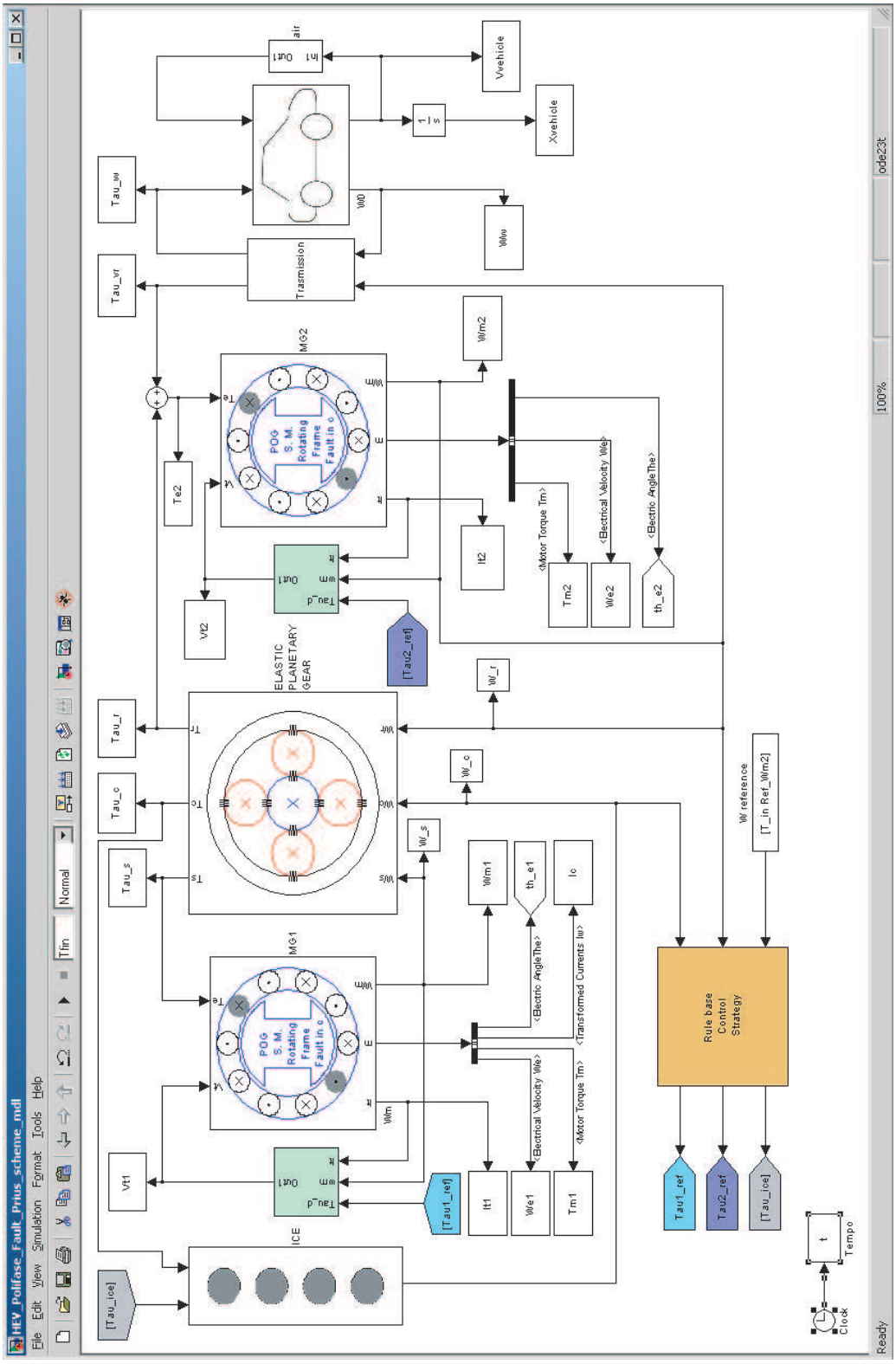

Figure 7.8: Simulink block scheme of the power-split HEV.

Table I: Main parameters of the system

Planetary Gear			
ring number of teeth	N_r	78	
sun number of teeth	N_s	30	
planet number of teeth	N_p	23	
stiffness coefficients	K_{sc}, K_{cr}	10^6	N/m
damping coefficients	d_{sc}, d_{cr}	10^5	N s/m
ring moment of inertia	J_r	0.0081	kg m^2
sun moment of inertia	J_s	1.48 10^{-4}	kg m^2
carrier moment of inertia	J_c	0.0071	kg m^2
friction coefficients	b_p, b_s, b_c, b_r	0.001	Nm s/rad
Engine			
engine moment of inertia	J_{ice}	0.2596	kg m^2
engine friction coefficient	b_{ice}	0.001	Nm s/rad
maximum torque	τ_{max} @4000rpm	142	Nm
maximum power	P_{max} @5200rpm	73	kW
Electric machines			
number of phases	m_s	5	
resistance	R_{s1}, R_{s2}	0.5,0.8	Ω
self induction	L_{s1}, L_{s2}	8, 11	mH
mutual induction	M_{s1}, M_{s2}	3, 5	mH
motors moment of inertia	J_{m1}, J_{m2}	20.1, 28.1	g m^2
motors friction coefficient	b_{m1}, b_{m2}	0.001, 0.001	Nm sec/rad
Transmission			
transmission ratio	R_t	4.113	
stiffness coefficients	K_t	10^6	N/m
damping coefficients	d_t	10^4	N s/m
Vehicle			
vehicle mass	M_v	1600	kg
wheel moment of inertia	J_w	1.06	kg m^2
wheel radius	R_w	32.55	cm
drag coefficient	α	0.254	
tires longitudinal stiffness	K_w	360000	N/m
longitudinal damping coefficient	b_w	800	kg/s

7.3.1 Simulation in normal operation

The vehicle velocity $\dot{x}_v$ and the required estimated power P_{ve} are shown in Fig. 7.9. The car starts accelerating to 70 km/h in 41 s keeping the same velocity for the following 50 s. After a short braking followed by a cruise of 50 km/h, at 188 s the vehicle slowly accelerates to 70 km/h in 13 s and maintains this velocity for other 50 s. Then the vehicle velocity increases to 100 km/h in 35 s remaining constant for the next 30 s, it increases again to the maximum velocity of 120 km/h in 20 s. Finally, after the last cruise at the maximum velocity of 10 s the car stops in 34 s and idles another 20 s. Note that a small tracking error between the desired velocity $\dot{x}_{vd}$ (green, dashed) and the vehicle one $\dot{x}_v$ (green, solid) appears only during the acceleration and deceleration.

The different operation modes are denoted by letters between vertical dashed lines in Fig. 7.9 where the horizontal red dashed line indicates the threshold speed for turning on the engine (below 15 km/h the engine is off).

These different conditions can be pointed out comparing the velocities and the torques of the planetary gear in Fig. 7.10 with the power flows into the vehicle shown in Fig. 7.11.

In mode A the vehicle is in pure electric mode then engine power $P_{ice} = 0$, MG1 power $P_{m1} = 0$ and MG2 power $P_{m2} > 0$, see Fig. 7.11 (from 20 to 30 s).

In mode C when the vehicle is accelerating and the speed is greater than 15 km/h the ICE starts to help the traction $P_{ice} > 0$.

In mode B (normal driving) the traction power is supplied by both the engine and MG2 (i.e. $P_{ice} > 0$, $P_{m2} > 0$), while in mode D (high speed cruising) MG1 operates as motor $P_{m1} > 0$ and MG2 as generator $P_{m2} < 0$ in order to make the engine operating in its optimal region. This

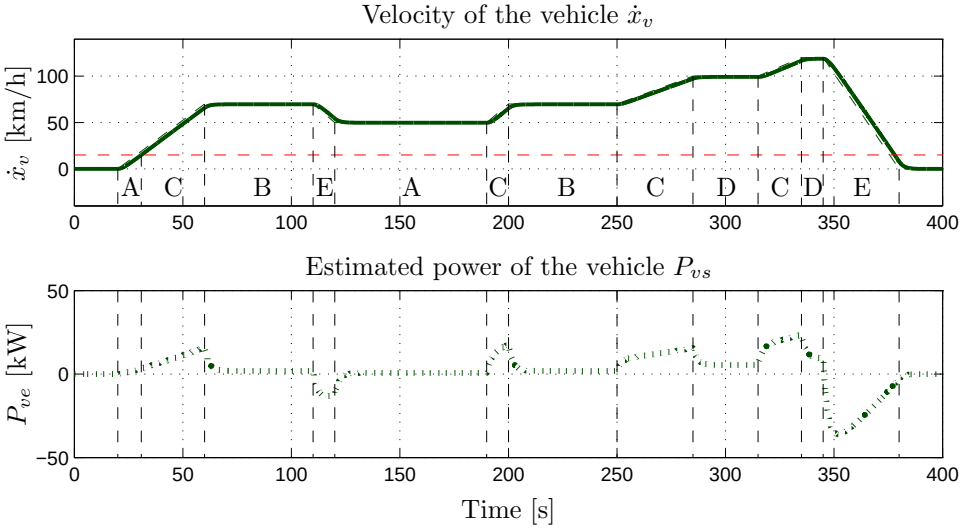

Figure 7.9: Velocity of the vehicle $\dot{x}_v$ (green, solid) with the desired velocity $\dot{x}_{vd}$ (green, dashed) and estimated power of the vehicle P_{ve} (green, dotted).

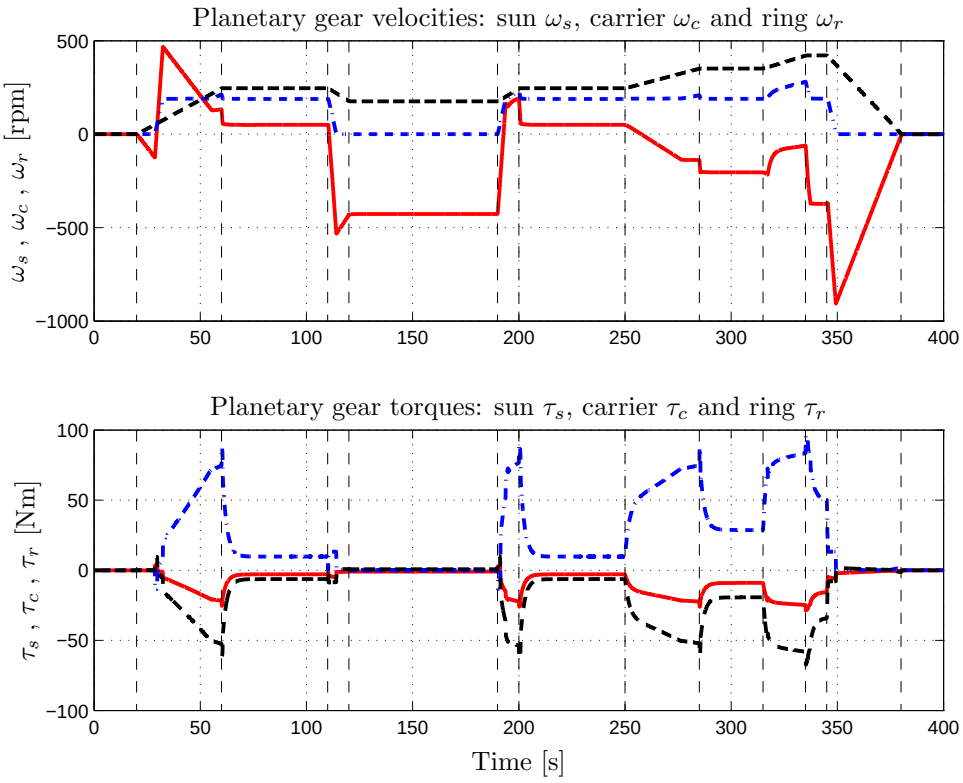

Figure 7.10: Velocities and Torques of the planetary gear: ω_s and τ_s (red, solid), ω_c and τ_c (blue, dash-dotted), ω_r and τ_r (black, dashed).

condition appears in Fig. 7.11 at 280 s and at 335 s when the car cruises at 100 km/h and 120 km/h, respectively.

In mode E (deceleration) the MG2 operates as generator $P_{m2} < 0$ and the engine is shut down until a new acceleration is requested. Therefore in constant speed condition after deceleration the traction is performed by MG2 (mode A) as shown in Fig. 7.10 between 120 and 190 s where $\omega_c = \omega_{ice} = 0$ and the car cruises at 50 km/h.

In case of strong deceleration a braking torque is activated, see the braking power P_b in Fig. 7.11 at 345 s.

The zoom of Fig. 7.11 shows the stator currents waveform of MG2 in healthy condition. The minimum dissipation torque control is used to feed the motor injecting the 1-st and the 3-rd harmonics. Increasing, in this way, the motor torque provided by MG2.

7.3.2 Simulation in fault condition

The simulated dynamic behavior of the HEV in fault condition is shown in Fig. 7.13 to 7.16. The simulated open-phase fault occurs at time 145 s and the fault-tolerant control is activated at time 160 s. The delay time of 15 s is defined in order to show the dynamic behavior of the

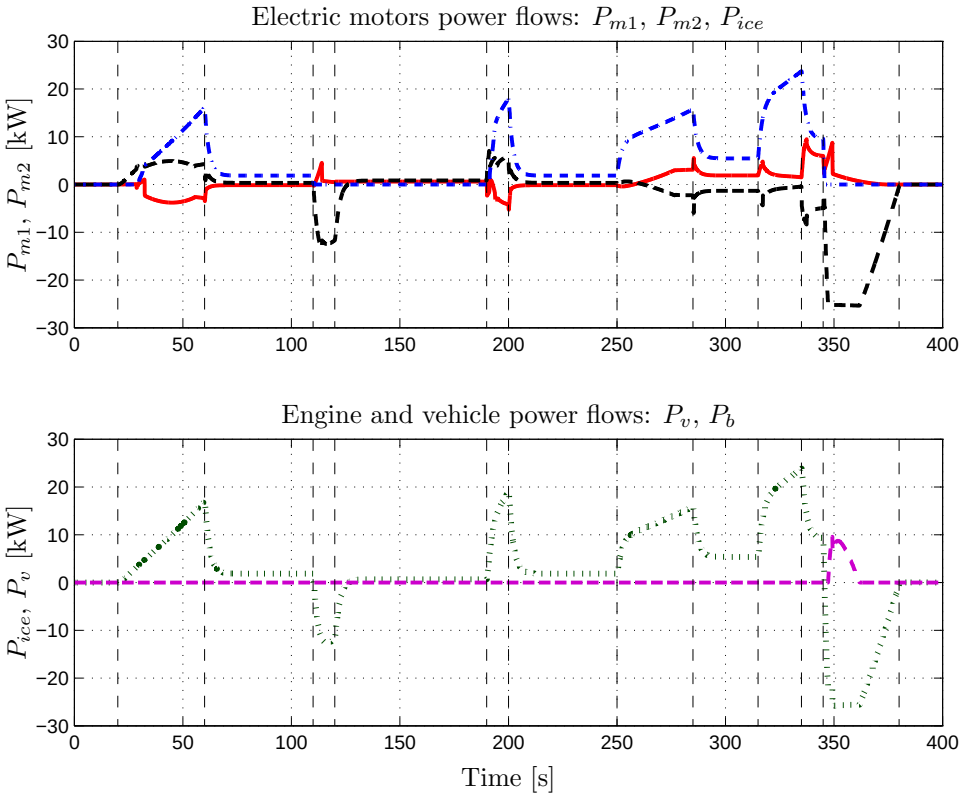

Figure 7.11: Power flows into the HEV: electric motors P_{m1} (red, solid) P_{m2} (black, dashed), engine P_{ice} (blue, dash-dotted), vehicle P_v (green, dotted), brake P_b (pink, dashed).

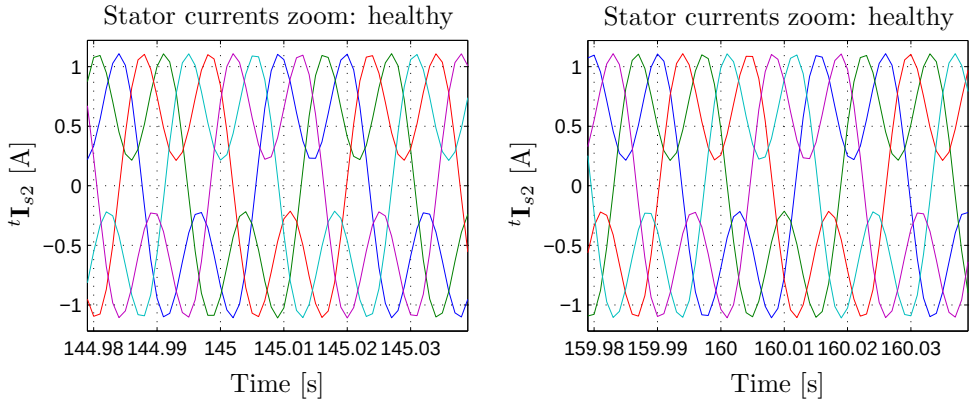

Figure 7.12: Zoom of stator currents of the electric motor MG2 connected to the ring.

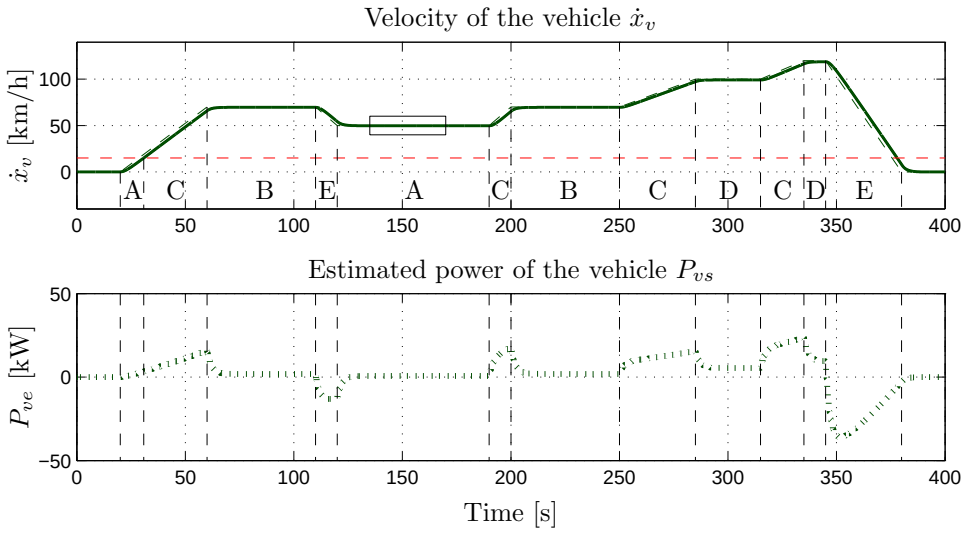

Figure 7.13: Velocity of the vehicle $\dot{x}_v$ (green, solid) with the desired velocity $\dot{x}_{vd}$ (green, dashed) and estimated power of the vehicle P_{ve} (green, dotted).

system in fault condition although in real application the fault detection time is about 1 s.
When the open-phase fault occurs on the 2-nd phase of MG2, the current I_{s2} falls down to zero as shown in Fig. 7.16 and a torque ripple appears on the planetary gears torques, see the box in Fig. 7.14 and the zoom in Fig. 7.16.
The failure does not affect the operation of the remaining windings but if the control is not modified the torque provided by MG2 decrease and a torque ripple appears, see Chap.5. Although, as shown in the box of Fig. 7.13 and in the zoom of Fig. 7.16, these fault effects seem do not not affect the HEV performances (the mean torque reduction is compensated by the ICE and the ripple is filtered by the system that behave like a first-order filter) the planetary gear torque ripple could cause severe mechanical failures. Therefore a control reconfiguration is strongly needed.
At time 160 s when the post-fault control is applied the torque ripple disappears allowing a safely vehicle operations. Using the minimum dissipation fault torque control proposed in in Sec. 6.1.2 the motor is fed injecting an higher order of odd harmonics modifying the stator currents waveform with respect to the normal operation, see Fig. 7.12 and Fig. 7.16. Note that there is a symmetry of the healthy currents with respect to the location of the faulty phase. Moreover the amplitude of the remaining currents increases because the MG2 motor drive should provide the same rated power also in fault condition.

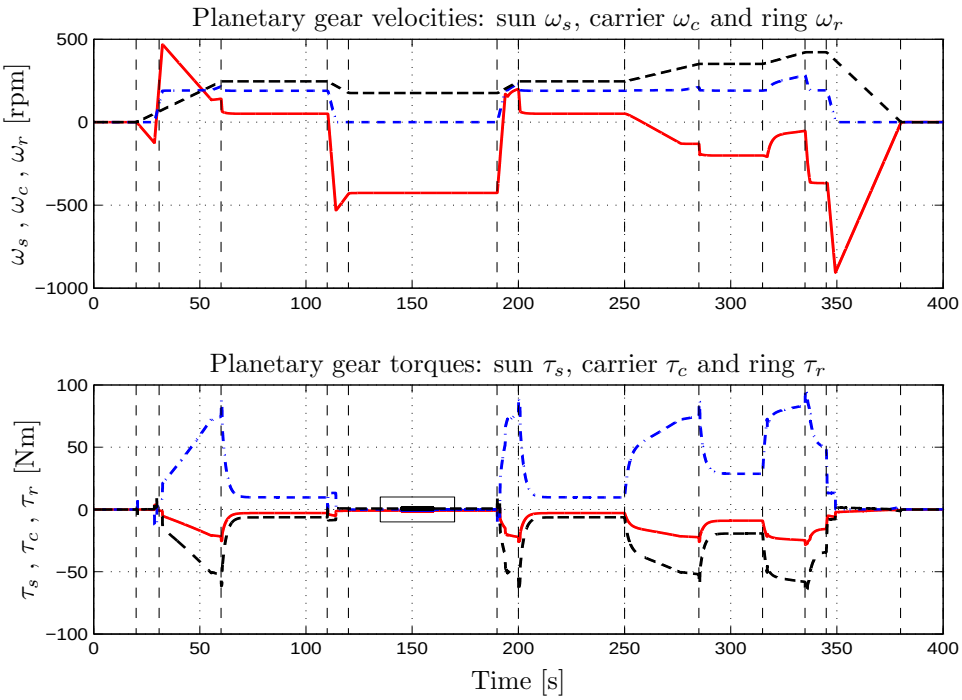

Figure 7.14: Velocities and Torques of the planetary gear: ω_s and τ_s (red, solid), ω_c and τ_c (blue, dash-dotted), ω_r and τ_r (black, dashed).

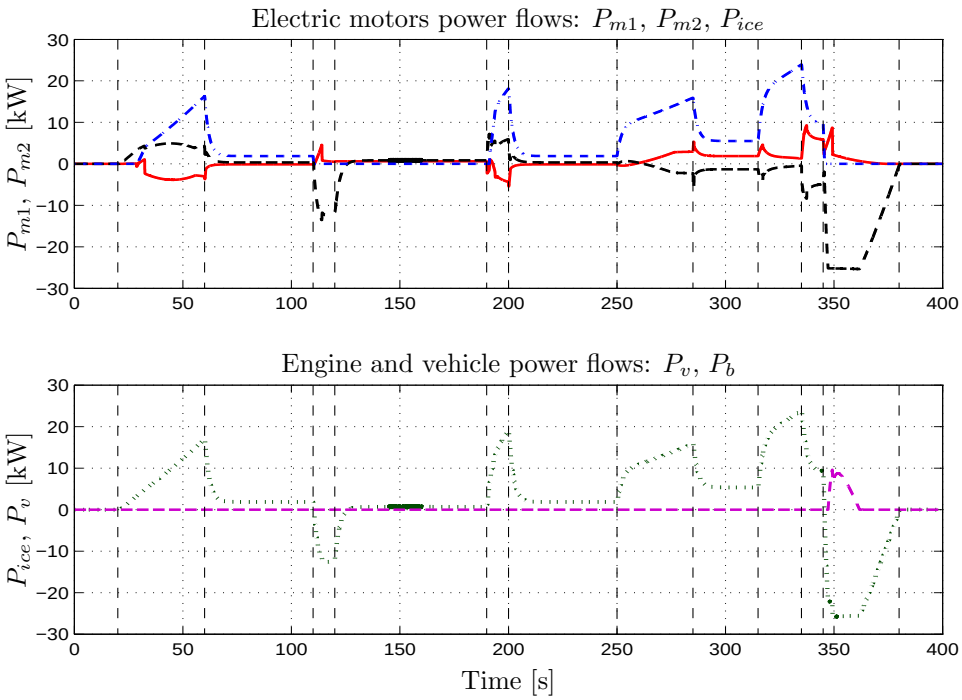

Figure 7.15: Power flows into the HEV: electric motors P_{m1} (red, solid) P_{m2} (black, dashed), engine P_{ice} (blue, dash-dotted), vehicle P_v (green, dotted), brake P_b (pink, dashed).

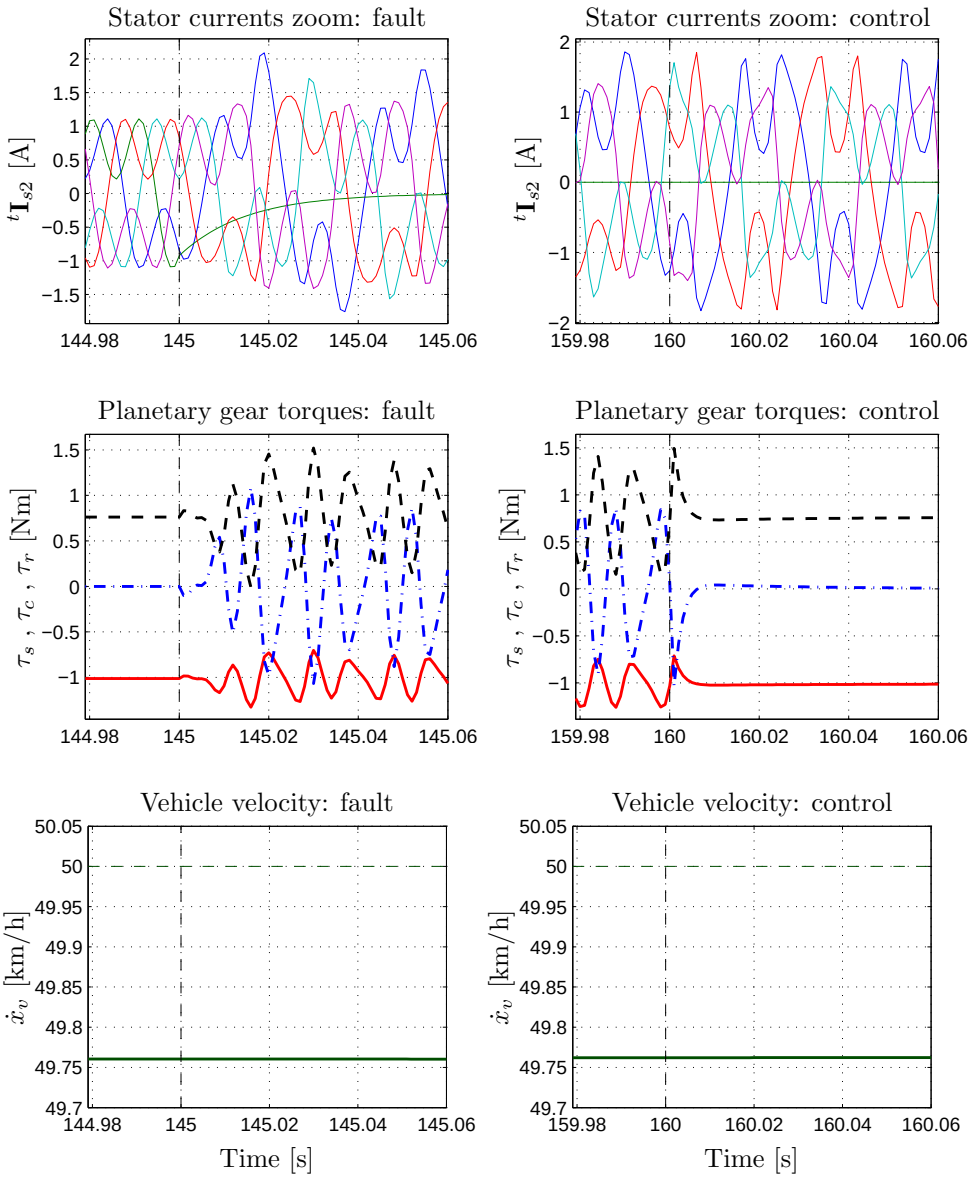

Figure 7.16: Zoom of the stator currents of the electric motor MG2 connected to the ring, zoom of the planetary gear torques and zoom of the vehicle velocity.

Conclusions

In this thesis the modeling and control of multi-phase synchronous motors in healthy and faulty conditions have been addressed.
The dynamic model of the motor has been proposed as general as possible; it holds for an arbitrary number of star or delta connected phases and for an arbitrary shape of rotor flux. Two different state space transformations, one real and one complex, are introduced: they have been analyzed in detail and compared with the classical transformations known in the literature. The proposed transformations have some important advantages with respect to those used in the literature: they are power-invariant and they make the model equations very compact, using a vectorial notation.
The exploitations of the POG schemes with vectorial notation has important advantages: the model can be directly implemented in Simulink, it provides a complete and exact dynamical description of the considered system and the model is the same whatever the number of phases and the type of stator connection are. Therefore unlike models proposed in the literature it should not be rebuilt when the number of phases or the type of stator connection change.
The vectorial control has been extended to multi-phase synchronous motor focusing on the voltage and current constraints distribution. The benefits of the harmonic injection, especially in terms of mechanical torque enhancement, have been discussed and used to propose three new different torque controls. The control equation and the scheme have been reported, discussed and implemented in Matlab-Simulink environment. The closed-loop simulation results of the motor drive show the effectiveness of the proposed control laws.
In the second part of the thesis the open-phase fault condition of multi-phase synchronous motors has been covered. Two different models of the multi-phase synchronous motor under open phase fault condition have been proposed. These models provide a good trade-off between the model accuracy and the simulation time because in these models the failure has been simulated with an additional voltage instead of using a variable resistance. Moreover the faults can occur at any phases: they can happen on one single phase or more than one phase (both adjacent and non-adjacent phases can be simulated). These models have been implemented in Simulink, creating a block library, and the simulation results have highlighted the undesired effects on the motor torque due to the faults.

A deep study on the open-phase constraint has allowed to extend the minimum dissipation torque control also to the case of faulty condition. Some post-fault controls have been proposed to compensate the fault effects by using only the remaining healthy phases; in this way the multi-phase motor continues to operate safely (generating the same desired torque without ripple) under a phase-fault without any additional hardware connections. The main advantage of the proposed controls compared to the others in the literature is that the maximum current limit can be easily taken into account. This is a very important feature because it allows to set the maximum current supportable by the inverter switches and by the motor, thus avoiding any further failures.
Finally, the advantages brought by the use of this type of motors in an electric and hybrid vehicles have been investigated referring to the Toyota Hybrid System. The dynamic models of the main subsystems composing the powertrain (i.e. planetary gear, engine, multi-phase motors etc..) have been obtained using the Power-Oriented Graphs modeling technique. Then the dynamic model of the whole powertrain has been implemented in Matlab/Simulink Environment by interconnecting the models of these main subsystems that interact each other through their power ports. This model is suitable to simulate the dynamic behavior of the vehicle in all the operating conditions. The simulation results of the proposed hybrid vehicle have shown the fault tolerant capability of multi-phase motor drives and the possibility to enhance the motor torque by injecting a higher order of stator current harmonics. These aspects make the multi-phase synchronous machines suitable for Electric and Hybrid Electric Vehicles where reliability and power density are very important issues.

The ”high level” approach adopted in the modeling proposed in this dissertation allows to simulate also different electric and hybrid architectures. Therefore the work presented in this thesis is the starting point for future studies on new architectures of electric and hybrid vehicles which exploit the advantages brought by the use of the multi-phase synchronous motors. Moreover new and safer control strategies will be designed starting from the knowledge of the dynamic behavior of the vehicle and of all subsystems constituting it.

Appendix A

Power Oriented Graphs modeling technique

Complex physical systems are usually composed by the connection of simple physical elements that can store and/or dissipate energy and interact each other by the power flow. Therefore among all the modeling techniques, the energy-based ones seem to be the best choice because they describe the main energetic domains using the power interaction between subsystems as the basic concept for modeling. Several graphical tools such as: Power-Oriented Graphs (POG) [20]-[21], Bond Graphs (BG) [82]-[84], Causal Ordering Graph (COG) [85], Energetic Macroscopic Representation (EMR) [86]- [88] have been proposed in the past years. Each one has own advantages and drawbacks and it is compared with the others in [89]-[91].
Since the POG block schemes are easy to use, easy to understand and can be directly implemented in Simulink then they are exploited in this dissertation .

A.1 System modeling using power variables

The main *energetic domains* encountered in modeling physical systems are the electrical, the mechanical (translational and rotational) and the hydraulic. Each *energetic domains* is characterized by 3 different types of physical elements PE: 2 *dynamic elements* D_e and D_f which store the energy and 1 *static element* R which dissipates, see Fig. A.1.
The dynamic elements D_e and D_f are shown in Fig. A.2, they are based on the integral causality because the derivative causality is not physically realizable and it is not useful in simulation. Therefore although the derivative causality model is still a correct mathematical model of the PE it is not used in the POG technique.
As shown in Fig. A.2 the system dynamics can be described using: the *energy variables* q_e and q_f and the *power variables* v_e and v_f. The *energy variables* define how much energy is stored within the dynamic elements, while the *power variables* describe how the energy moves within

		Electrical		Mech. Tras.		Mech. Rot.		Hydraulic	
	$\mathcal{D}_e$	C	Capacitor	M	Mass	J	Inertia	C_I	Hyd. Capacitor
	q_e	Q	Charge	p	Momentum	p	Ang. Momentum	V	Volume
Across-Var.	v_e	V	Voltage	v	Velocity	ω	Ang. Velocity	P	Pressure
	$\mathcal{D}_f$	L	Inductor	E	Spring	E	Spring	L_I	Hyd. Inductor
	q_f	ϕ	Flux	x	Displacement	θ	Ang. Displacement	ϕ_I	Hyd. Flux
Trough-Var.	v_f	I	Current	F	Force	τ	Torque	Q	Volume flow rate
	$\mathcal{R}$	R	Resistor	b	Friction	b	Ang. Friction	R_I	Hyd. Resistor

Figure A.1: The main energetic domains: the physical elements $\mathcal{D}_e$, $\mathcal{D}_f$ and $\mathcal{R}$; the energy variables q_e, q_f; the power variables v_e, v_f.

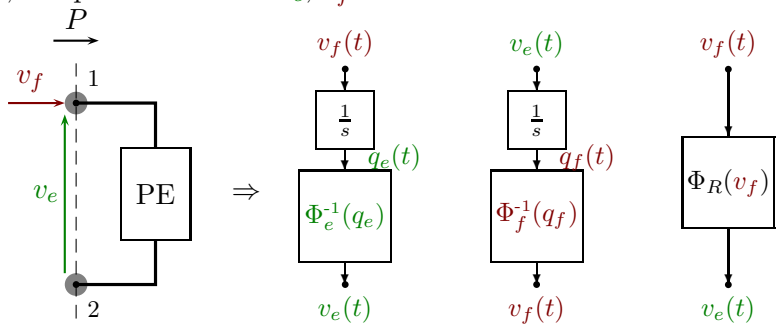

Figure A.2: Dynamic structure of the physical element PE: *Dynamic elements* D_e and D_f and *Static element* R.

the system.

Considering the *dynamic element* D_e one observes how the internal variable $q_e(t)$ is linked to the input and output variables $v_f(t)$ and $v_e(t)$ by the *differential equation* $\dot{q}_e(t) = v_f(t)$ and by the *constitutive relation* $q_e = \Phi_e(v_e)$, respectively. Moreover the energy E_e stored in the *dynamic element* D_e is function only of the internal *energy variable* q_e:

$$E_e = \int_0^t v_e(t)\, v_f(t)\, dt = \int_0^{q_e} \Phi_e^{-1}(q_e)\, dq_e = E_e(q_e).$$

Each Physical Element (PE) has two terminals (denoted 1 and 2 in Fig. A.2) and the value of the power P flowing through the section is the product of the two power variables $v_e(t)$ and $v_f(t)$: $P(t) = v_e(t)\, v_f(t)$. The *power variables* can be divided into two groups:

1) the *"across-variables"* (i.e. voltage V_p, velocity $\dot{\mathbf{x}}_p$, angular velocity ω_p and pressure P_p) which are defined *"between two points P and 0"* of the space:

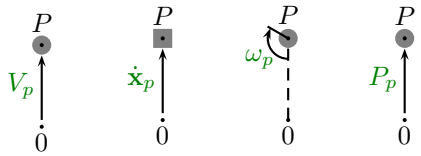

2) The *"trough-variables"* (i.e. current I_p, force F_p, torque τ_p and volume flow rate Q_p) which are defined *"in each point P"* of the space:

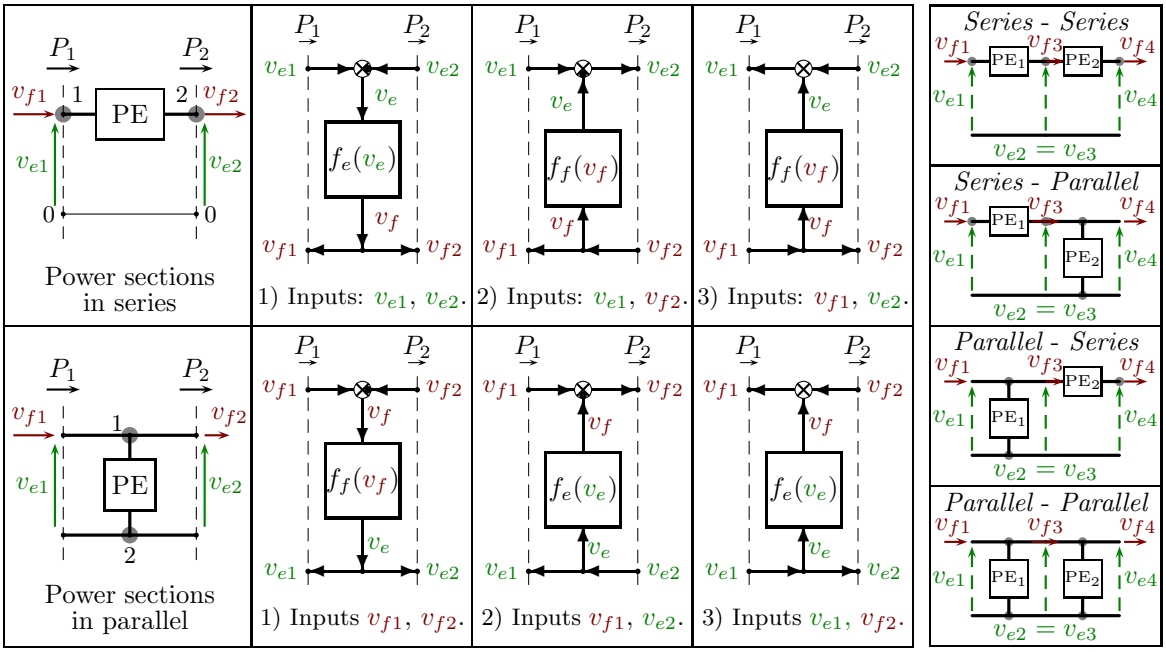

Figure A.3: The two different power connection of Physical Elements (PE) with the external world and the four types of connections of two physical elements PE_1 and PE_2

Each Physical Element (PE) interacts with the external world by means of its power section and it can be connected only in two ways: *in series* or *in parallel*. A Physical Element is connected *in series* when its terminals share the same through-variable v_f, while it is connected *in parallel* when its terminals share the same across-variable v_e, see Fig. A.3. The three different POG graphical representations of a PE connected in series or in parallel are shown in Fig. A.3. Note that it is possible to pass from one representation to the others inverting one of the input-output path.
Fig. A.3 shows also the the four possible ways of connecting two physical elements PE_1 and PE_2; when two power sections are connected, *a feedback loop always arises* in the POG graphical representation of the system.

A.2 The Power-Oriented Graphs technique

The Power-Oriented Graphs is modeling technique is based on the previous concepts regarding the system modeling using energetic approach and it is particularly suitable for modeling dynamic physical systems, see [20]-[21], [80]-[81] and [90]-[92].
The POG block schemes are normal block diagrams combined with a particular modular structure essentially based on the use of the two blocks: the *elaboration block* (e.b.) and the *connection block* (c.b.).

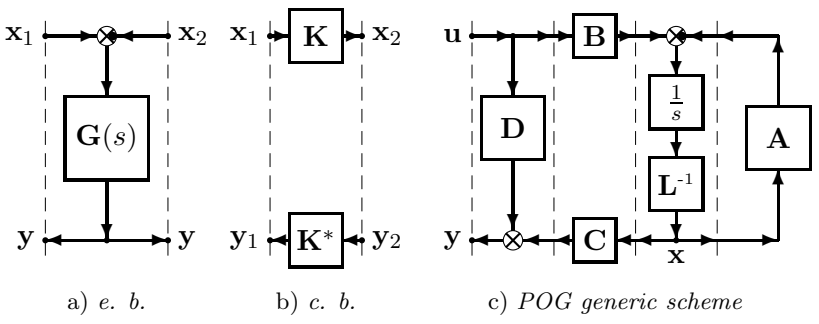

$$\begin{cases} \mathbf{L}\,\dot{\mathbf{x}} = -\mathbf{A}\,\mathbf{x} + \mathbf{B}\,\mathbf{u} \\ \mathbf{y} = \mathbf{C}\,\mathbf{x} + \mathbf{D}\,\mathbf{u} \end{cases} \tag{A.1}$$

$$\Downarrow (\mathbf{x} = \mathbf{T}\,\mathbf{z})$$

$$\begin{cases} \overline{\mathbf{L}}\,\dot{\mathbf{z}} = -\overline{\mathbf{A}}\,\mathbf{z} + \overline{\mathbf{B}}\,\mathbf{u} \\ \mathbf{y} = \overline{\mathbf{C}}\,\mathbf{z} + \overline{\mathbf{D}}\,\mathbf{u} \end{cases} \tag{A.2}$$

Figure A.4: POG basic blocks and variables: a) *elaboration block*, b) *connection block*, c) POG block scheme of a generic dynamic system.

The e.b., shown in Fig. A.4.a describes all the physical elements that stores and/or dissipates energy (i.e. springs, masses, dampers, capacities, inductances, resistances, etc.). The circle in the e.b. is a summation element and the black spot represents a minus sign that multiplies the entering variable.

The c.b., shown in and Fig. A.4.b, describes all the physical elements that redistributes the power within the system without storing nor dissipating energy (i.e. any type of gear reduction, transformers, etc.). Therefore the c.b. transforms the power variables satisfying the constraint $\mathbf{x}_1^*\mathbf{y}_1 = \mathbf{x}_2^*\mathbf{y}_2$

The e.b. and the c.b. are suitable for representing both scalar and vectorial systems. In the vectorial case, $\mathbf{G}(s)$ and $\mathbf{K}$ are matrices: $\mathbf{G}(s)$ is always a square matrix composed by positive real transfer functions, while matrix $\mathbf{K}$ can also be rectangular.

The main feature of the Power-Oriented Graphs is to keep a direct correspondence between the dashed sections of the graphs and real power sections of the modeled systems: the scalar product $\mathbf{x}^*\mathbf{y}$ of the two *power variables vectors* $\mathbf{x}$ and $\mathbf{y}$ involved in each dashed line of a POG, see Fig. A.4, has the physical meaning of *power flowing through that section.*

Another important property of the POG technique is the direct correspondence between the POG schemes and the corresponding state space dynamic equations. For example, the POG scheme shown in Fig. A.6 can be represented by the state space equations (A.1) where the *energy matrix* $\mathbf{L}$ is symmetric and positive definite: $\mathbf{L} = \mathbf{L}^* > 0$.

Using a "congruent" transformation $\mathbf{x} = \mathbf{T}\mathbf{z}$ the dynamic model (A.1) can be transformed into system (A.2) where: $\overline{\mathbf{L}} = \mathbf{T}^{\mathrm{T}}\mathbf{L}\mathbf{T}$, $\overline{\mathbf{A}} = \mathbf{T}^{\mathrm{T}}\mathbf{A}\mathbf{T}$, $\overline{\mathbf{B}} = \mathbf{T}^{\mathrm{T}}\mathbf{B}$, $\overline{\mathbf{C}} = \mathbf{C}\mathbf{T}$ and $\overline{\mathbf{D}} = \mathbf{D}$. Otherwise, when the matrix $\mathbf{T}$ is time-varying, an additional term $\mathbf{T}^{\mathrm{T}}\mathbf{L}\dot{\mathbf{T}}\mathbf{z}$ appears in the transformed system. When an eigenvalue of matrix $\mathbf{L}$ tends to zero (or to infinity), system (A.1) degenerates towards a lower dimension dynamic system. In this case the reduced and transformed system can be obtained using a "rectangular" matrix $\mathbf{T}$.

Assuming an invertible matrix $\mathbf{D}$ the POG scheme of Fig. A.4.c can also be easily input-output inverted, both graphically and mathematically, as shown in Fig. A.5. Details of how the POG

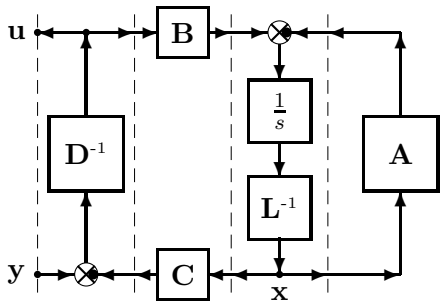

$$\begin{cases} \tilde{\mathbf{L}}\,\dot{\mathbf{x}} = -\tilde{\mathbf{A}}\,\mathbf{x} + \tilde{\mathbf{B}}\,\mathbf{y} \\ \mathbf{u} = \tilde{\mathbf{C}}\,\mathbf{x} + \tilde{\mathbf{D}}\,\mathbf{y} \end{cases} \tag{A.3}$$

where

$$\tilde{\mathbf{L}} = \mathbf{L}, \quad \tilde{\mathbf{B}} = \mathbf{B}\mathbf{D}^{-1},$$

$$\tilde{\mathbf{A}} = \mathbf{A} + \mathbf{B}\mathbf{D}^{-1}\mathbf{C},$$

$$\tilde{\mathbf{C}} = -\mathbf{D}^{-1}\mathbf{C}, \quad \tilde{\mathbf{D}} = \mathbf{D}^{-1}.$$

Figure A.5: POG block scheme of the input-output inverted system.

systems can be reduced, transformed and "input-output inverted" can be found in [92].
It can be easily shown that when $\mathbf{D} = 0$ it follows that $\mathbf{C} = \mathbf{B}^*$ and the POG systems can be represented as shown in Fig. A.6. For such a system, the energy E_s stored in the system and the dissipating power P_d are quadratic functions of matrices $\mathbf{L}$ and $\mathbf{A}_s$, respectively:

$$E_s = \frac{1}{2}\,\mathbf{x}^*\mathbf{L}\,\mathbf{x}, \qquad P_d = \mathbf{x}^*\,\mathbf{A}_s\,\mathbf{x}$$

where $\mathbf{A}_s = (\mathbf{A} + \mathbf{A}^*)/2$ is the symmetric part of the *power matrix* $\mathbf{A}$. The skew-symmetric part $\mathbf{A}_w = (\mathbf{A} - \mathbf{A}^*)/2$ of the power matrix $\mathbf{A}$ represents the power redistribution within the system "without losses", i.e. $P_d = \mathbf{x}^*\mathbf{A}_w\,\mathbf{x} = 0$. Indeed one can easily verify that all the dissipating parameters of the system appear only in matrix $\mathbf{A}_s$, while matrix $\mathbf{A}_w$ is completely characterized by all the connection parameters.
Finally the POG schemes always satisfy the following graphical rules:
1) *All the loops of a POG scheme always contains an "odd" number of minus signs* (i.e. of the black spots in the summation elements). This rule is a direct consequence of the fact that in the POG schemes a loop always appears when two physical elements are connected, see Fig.A.7 and this loop contains at least one "minus sign" for letting the powers flows have the same positive direction.
2) Chosen two generic points A and B of a POG scheme, *all the paths that go from A to B*

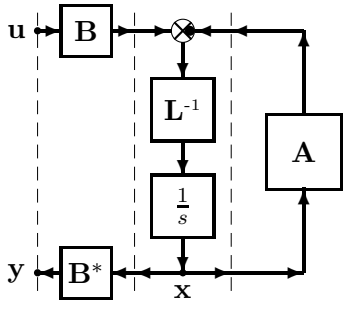

$$\begin{cases} \mathbf{L}\,\dot{\mathbf{x}} = -\mathbf{A}\mathbf{x} + \mathbf{B}\mathbf{u} \\ \mathbf{y} = \mathbf{B}^*\mathbf{x} \end{cases} \tag{A.4}$$

Figure A.6: POG scheme of a dynamic system with $\mathbf{D} = 0$ in the complex domain.

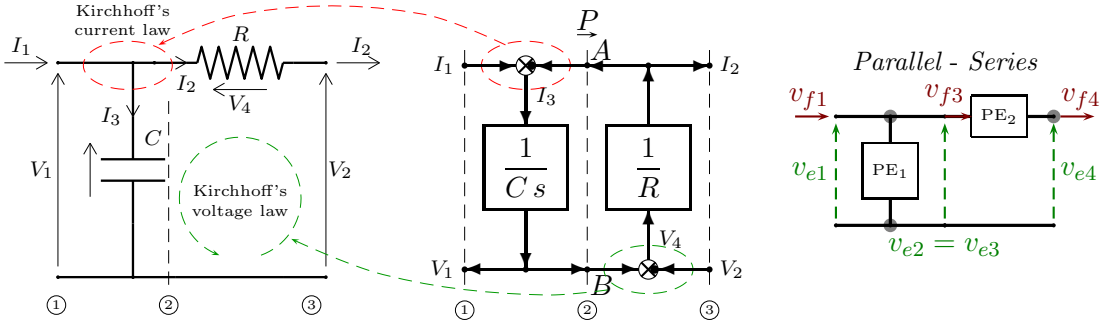

Figure A.7: POG modeling of an electrical RC circuit.

contain either an "odd" number or an "even" number of minus signs. This rule follows directly from rule 1.

3) *The direction of the power flowing through a section is positive if an "even" number of minus signs is present along one of the paths linking the input and the output of the section.*

Let us consider, fore example, the POG modeling of an electrical *RC* circuit, shown in Fig. A.7, where the C and R physical elements are described by two POG elaboration blocks. There is a direct correspondence between physical power sections and dashed sections in the POG model and the summation elements present in the elaboration blocks are a mathematical description of the current and voltage Kirchhoff's laws applied to the considered electrical system.

The positive power flows from left to right because the path that goes from B to A contains "zero" minus signs (i.e. an even number). The same result can be obtained considering the left part of section ②: the power flows from left to right because the path that goes from A to B contains "one" minus sign (i.e. an odd number). It is evident that rule 3) makes "optional", in the POG scheme, the use of the power arrow "→" drawn in the vicinity of the power sections: this direction can always be determined by direct inspection of the POG scheme.

Appendix B

Notations

The matrices and vectors in this thesis are identified by the following subscripts:

- "^{t}" refers to the fixed reference frame Σ_t.
- "$^{\underline{\omega}}$" refers to the rotating reference frame Σ_ω where also the last m_s-th differential equation is used.
- "$^{\omega}$" refers to the rotating reference frame Σ_ω in a star-connected motor.

Moreover the complex matrices and vectors are defined by the hat $\overline{\ }$. Given a complex matrix $\overline{\mathbf{A}}$, the conjugate matrix is denoted by $\overline{\mathbf{A}}^{\circ}$, the transpose matrix by $\overline{\mathbf{A}}^{\mathrm{T}}$ and the conjugate transpose matrix by $\overline{\mathbf{A}}^{*}$. Therefore the following relations hold: $\overline{\mathbf{A}}^{*} = (\overline{\mathbf{A}}^{\circ})^{\mathrm{T}} = (\overline{\mathbf{A}}^{\mathrm{T}})^{\circ}$.
The symbols **1** and **0** are used to represent a ones and zeros block matrices of proper dimensions. The full and diagonal matrices are denoted by the following notations:

$$\underset{1:n\ \ 1:m}{\overset{i\qquad j}{[\![R_{i,j}]\!]}} = \begin{bmatrix} R_{11} & R_{12} & \cdots & R_{1m} \\ R_{21} & R_{22} & \cdots & R_{2m} \\ \vdots & \vdots & \ddots & \vdots \\ R_{n1} & R_{n2} & \cdots & R_{nm} \end{bmatrix}, \qquad \underset{1:n}{\overset{i}{[\![R_i]\!]}} = \begin{bmatrix} R_1 & & & \\ & R_2 & & \\ & & \ddots & \\ & & & R_n \end{bmatrix}.$$

From these definition it follows that the column and row matrices can be expressed as:

$$\underset{1:n}{\overset{i}{[\![R_i]\!]}} = \begin{bmatrix} R_1 \\ R_2 \\ \vdots \\ R_n \end{bmatrix}, \qquad \underset{1:n}{\overset{i}{[\![R_i]\!]}} = \begin{bmatrix} R_1 & R_2 & \cdots & R_n \end{bmatrix}.$$

The symbol $\sum_{n=a:d}^{b} c_n = c_a + c_{a+d} + c_{a+2d} + \ldots$ is used to represent the sum of a succession of numbers c_n where the index n ranges from a to b with increment d, that is, using the Matlab

symbology, $n = [a : d : b]$. Using the previous notations one can represent, for example, the following matrix:

$$\overset{i}{\underset{1:a:n}{}}\overset{\quad j}{\underset{1:b:m}{}}[\![\, R_{i,j} \,]\!] = \begin{bmatrix} R_{11} & R_{1b} & \cdots & R_{1m} \\ R_{a1} & R_{ab} & \cdots & R_{am} \\ \vdots & \vdots & \ddots & \vdots \\ R_{n1} & R_{nb} & \cdots & R_{nm} \end{bmatrix}, \qquad \overset{i}{\underset{1:2:6}{}}\overset{\quad j}{\underset{3:3:11}{}}[\![\, R_{i,j} \,]\!] = \begin{bmatrix} R_{13} & R_{16} & R_{19} \\ R_{33} & R_{36} & R_{39} \\ R_{53} & R_{56} & R_{59} \end{bmatrix}.$$

The symbol $\delta(n)|_k^m$ is used to represent the following function:

$$\delta(n)|_k^m = \begin{cases} 1 & \text{for } n \in [k,\, k \pm m,\, k \pm 2m,\, k \pm 3m, \ldots] \\ 0 & \text{otherwise} \end{cases}$$

where n, k and m are integer parameters.

Appendix C

Mathematical Details

C.1 Sum of balanced vectors

The following relation about the sum of balanced vectors holds:

$$\sum_{n=h}^{k} e^{jn\gamma} = \frac{\sin(\frac{k-h+1}{2}\gamma)}{\sin(\frac{\gamma}{2})}\, e^{j\frac{k+h}{2}\gamma} \tag{C.1}$$

for $h, k \in \mathcal{Z}$ with $h \leq k$ and $\gamma \in \mathcal{R}$ with $\gamma \neq 0$.
The complex numbers $e^{j\,n\gamma}$ are two-dimensional equidistant vectors with unit modulus and phase $\varphi = n\,\gamma$. As shown in Fig. C.1 all points belong on a circle of center C and radius R where the displacement between the point is function of n.
Therefore the result of summation can be obtained rotating the vector $\mathbf{v}$ of an angle function of the lower and the upper bound h and k of summation, see zoom of Fig. C.1.

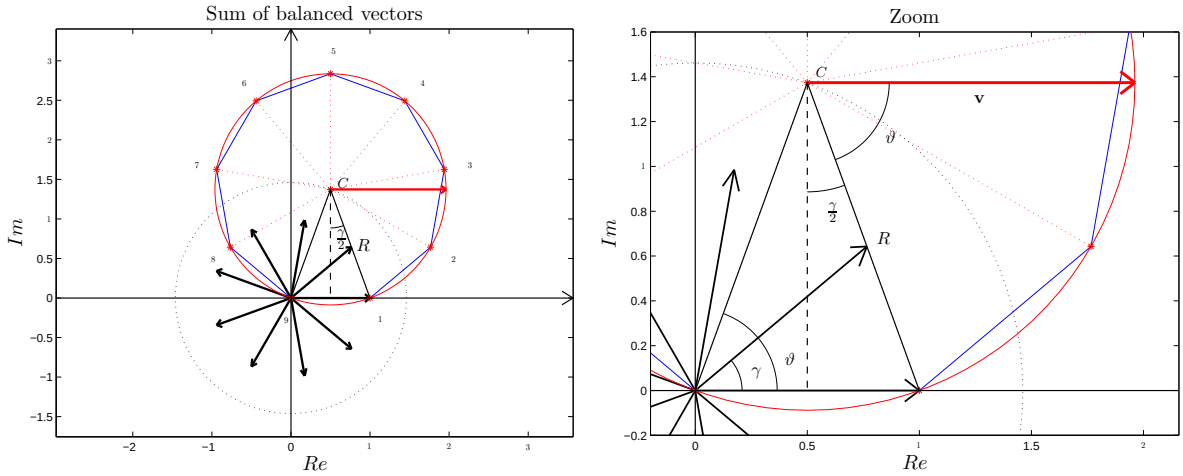

Figure C.1: Sum of $m_s = 9$ balanced vectors in the complex plane.

Consequently, the (C.1) can be be proved as follows:

$$\sum_{n=h}^{k} e^{jn\gamma} \;=\; e^{jh\gamma}\sum_{n=0}^{k-h} e^{jn\gamma} = e^{jh\gamma}\left(C + R\,e^{-j\vartheta}\,e^{j(k-h)\gamma}\right)$$

where the radius R, the center C and the angle ϑ are:

$$R = \frac{1}{2\sin\left(\frac{\gamma}{2}\right)}\,, \qquad C = \frac{1}{2} + jR\cos\left(\tfrac{\gamma}{2}\right) = R\,e^{j\vartheta}\,, \qquad \vartheta = \frac{\pi-\gamma}{2}\,.$$

Substituting, one obtains:

$$\begin{aligned}
\sum_{n=h}^{k} e^{jn\gamma} &= e^{jh\gamma}\left(R\,e^{j(\frac{\pi}{2}-\frac{\gamma}{2})} + R\,e^{j(\frac{\gamma}{2}-\frac{\pi}{2})}e^{j(k-h)\gamma}\right)\\
&= e^{jh\gamma}e^{j(k-h)\frac{\gamma}{2}}R\,\left(e^{j(\frac{\pi}{2}-\frac{\gamma}{2})}e^{-j(k-h)\frac{\gamma}{2}} + e^{-j(\frac{\pi}{2}-\frac{\gamma}{2})}e^{j(k-h)\frac{\gamma}{2}}\right)\\
&= e^{jh\gamma}e^{j(k-h)\frac{\gamma}{2}}\frac{1}{2\sin\left(\frac{\gamma}{2}\right)}\,\left(e^{j\left((k-h+1)\frac{\gamma}{2}-\frac{\pi}{2}\right)} + e^{-j\left((k-h+1)\frac{\gamma}{2}-\frac{\pi}{2}\right)}\right)\\
&= e^{jh\gamma}e^{j(k-h)\frac{\gamma}{2}}\frac{\cos\left((k-h+1)\frac{\gamma}{2}-\frac{\pi}{2}\right)}{\sin\left(\frac{\gamma}{2}\right)}\\
&= e^{j(k+h)\frac{\gamma}{2}}\,\frac{\sin\left(\frac{k-h+1}{2}\gamma\right)}{\sin\left(\frac{\gamma}{2}\right)}
\end{aligned}$$

When $\gamma = \alpha\pi$ with $\alpha \in 2\mathcal{Z}$ (i.e. $\gamma = 0,\ \pm 2\pi,\ \pm 4\pi..$) one obtains an indeterminate form:

$$\sum_{n=h}^{k} e^{jn\gamma} = \lim_{\gamma\to 0}\frac{\sin(\frac{k-h+1}{2}\gamma)}{\sin(\frac{\gamma}{2})}\,e^{j\frac{k+h}{2}\gamma} = k-h+1 \tag{C.2}$$

that it the sum of $k-h+1$ real vectors with unit modulus. Otherwise when $\gamma \neq \alpha\pi$ with $\alpha \in 2\mathcal{Z}$ the sum of balanced vectors is equal to zero if and only if:

$$\sum_{n=h}^{k} e^{jn\gamma} = \frac{\sin(\frac{k-h+1}{2}\gamma)}{\sin(\frac{\gamma}{2})}\,e^{j\frac{k+h}{2}\gamma} = 0 \qquad \Leftrightarrow \qquad k-h+1 = \frac{2\pi}{\gamma} + \alpha\pi \text{ with } \alpha \in \mathcal{Z} \tag{C.3}$$

From (C.1), (C.3), and (C.2), the following relation holds:

$$\underbrace{\sum_{n=0}^{m_s-1} e^{jn\gamma_s(r-p)}}_{=m_s \text{ if } r-p=0,\pm m_s..} = m_s\delta(r)|_p^{m_s} \tag{C.4}$$

for $\gamma_s = \frac{2\pi}{m_s}$ and $m \in \mathcal{N}$.
Indeed when $r-p = 0, \pm m_s..$ the phase $\varphi = j\,n\,\gamma_s\,(r-p) = \alpha\pi$ with $\alpha \in 2\mathcal{Z}$, and one obtains the sum of m_s real vectors with unit modulus that is equal to zero from (C.2). In all other cases the relation (C.3) is satisfied and one obtains the sum of all balanced vectors that is equal to zero. The (C.4) will be used for the calculation in the following Appendixes.

C.2 Mathematical calculations of Sec. 2.2.2

The expression of coupling matrix ${}^{\underline{\omega}}\overline{\mathbf{J}}_s$ reported in (2.17), has been obtained from the following passages:

$$
{}^{\underline{\omega}}\overline{\mathbf{J}}_s = {}^{t}\overline{\mathbf{T}}^{*}_{\omega}\, {}^{t}\dot{\overline{\mathbf{T}}}_{\omega} = \frac{1}{m_s}
\begin{bmatrix}
\overset{k}{\underset{1:2:m_s-2}{\left\| \left[\!\left[e^{-j\,k\,(\theta - h\,\gamma_s)} \right]\!\right] \right\|}} & \overset{h}{\underset{0:m_s-1}{}} \\
\overset{h}{\underset{0:m_s-1}{[\![\, 1 \,]\!]}} &
\end{bmatrix}
\begin{bmatrix}
\overset{h}{\underset{0:m_s-1}{}} & \overset{n}{\underset{1:2:m_s-2}{\left\| \left[\!\left[jn\omega e^{jn(\theta - h\gamma_s)} \right]\!\right] \right\|}} & \overset{h}{\underset{0:m_s-1}{[\![\, 0 \,]\!]}}
\end{bmatrix}
$$

$$
= \frac{1}{m_s}
\begin{bmatrix}
\overset{k}{\underset{1:2:m_s-2}{\left\| \left[\!\left[jn\omega e^{-j\theta(k-n)} \underbrace{\sum_{h=0}^{m_s-1} e^{jh\gamma_s(k-n)}}_{=m_s \text{ if } k-n=0,\pm m_s..} \right]\!\right] \right\|}} & \mathbf{0} \\
\mathbf{0} & \overset{n}{\underset{1:2:m_s-2}{\left\| \left[\!\left[jn\omega e^{j\theta n} \underbrace{\sum_{h=0}^{m_s-1} e^{jnh\gamma_s}}_{=0} \right]\!\right] \right\|}}
\end{bmatrix}
=
\begin{bmatrix}
\overset{k}{\underset{1:2:m_s-2}{[\![\, jkp\,\omega_m \,]\!]}} & \mathbf{0} \\
\mathbf{0} & 0
\end{bmatrix}
$$

The expression of transformed inductance matrix ${}^{\underline{\omega}}\overline{\mathbf{L}}_s$ reported in (2.18), has been obtained using the complex matrix ${}^{t}\overline{\mathbf{T}}_{\underline{\omega}}$ as follows:

$$
{}^{\underline{\omega}}\overline{\mathbf{L}}_s = {}^{t}\overline{\mathbf{T}}^{*}_{\underline{\omega}}\, {}^{t}\mathbf{L}_s\, {}^{t}\overline{\mathbf{T}}_{\underline{\omega}} = L_{s0}\mathbf{I}_{m_s} + {}^{t}\overline{\mathbf{T}}^{*}_{\underline{\omega}}\, M_{s0} \overset{i}{\underset{1:m_s}{\left\| \left[\!\left[\sum_{n=1:2}^{m_s-2} a_{Mn}\, \cos(n\,(i-h)\gamma_s) \right]\!\right] \right\|}} \overset{h}{\underset{1:m_s}{}}\, {}^{t}\overline{\mathbf{T}}_{\underline{\omega}}
$$

$$
= L_{s0}\mathbf{I}_{m_s} + \frac{M_{s0}}{2}\, {}^{t}\overline{\mathbf{T}}^{*}_{\underline{\omega}} \overset{i}{\underset{0:m_s-1}{\left\| \left[\!\left[\sum_{n=1:2}^{m_s-2} a_{Mn} \left(e^{j\,n\,(i-h)\gamma_s} + e^{-j\,n\,(i-h)\gamma_s} \right) \right]\!\right] \right\|}} \overset{h}{\underset{0:m_s-1}{}}\, {}^{t}\overline{\mathbf{T}}_{\underline{\omega}}
$$

$$
= L_{s0}\mathbf{I}_{m_s} + \frac{M_{s0}\sqrt{m_s}}{2}\, {}^{t}\overline{\mathbf{T}}^{*}_{\underline{\omega}}
\begin{bmatrix}
\overset{h}{\underset{0:m_s-1}{\left\| \left[\!\left[e^{jk\theta} \sum_{n=1:2}^{m_s-2} a_{Mn} e^{-jnh\gamma_s}\, \delta(k)|_n^{m_s} \right]\!\right] \right\|}} & \mathbf{0}
\end{bmatrix}
\overset{k}{\underset{1:2:m_s-2}{}}
\quad \Big\downarrow p
$$

$$
\begin{aligned}
{}^{\omega}\overline{\mathbf{L}}_s &= L_{s0}\mathbf{I}_{m_s} + \frac{M_{s0}}{2}
\begin{bmatrix}
\Big\|\Big[\, e^{-jl\theta}e^{jhl\gamma_s} \,\Big]\Big\|_{1:2:m_s-2}^{l}{}_{0:m_s-1}^{h} & \\
& \Big\|\Big[\, 1 \,\Big]\Big\|_{0:m_s-1}^{h}
\end{bmatrix}
\begin{bmatrix}
\Big\|\Big[\, e^{jk\theta}\sum_{n=1:2}^{m_s-2} a_{Mn}e^{-jnh\gamma_s}\,\delta(k)|_n^{m_s} \,\Big]\Big\|_{0:m_s-1}^{h}{}_{1:2:m_s-2}^{k} & \mathbf{0} \\
\mathbf{0} & 0
\end{bmatrix} \\
&= L_{s0}\mathbf{I}_{m_s} + \frac{M_{s0}}{2}
\begin{bmatrix}
\Big\|\Big[\, e^{-j\theta(l-n)}\sum_{n=1:2}^{m_s-2}\underbrace{\sum_{h=0}^{m_s-1} a_{Mn}\, e^{jh\gamma_s(l-n)}\,\delta(k)|_n^{m_s}}_{=m_s \text{ if } l-n=0,\pm m_s..} \,\Big]\Big\|_{1:2:m_s-2}^{l}{}_{1:2:m_s-2}^{k} & \mathbf{0} \\
\mathbf{0} & 0
\end{bmatrix} \\
&= L_{s0}\mathbf{I}_{m_s} + m_s\frac{M_{s0}}{2}
\begin{bmatrix}
\Big\|\Big[\, \sum_{n=1:2}^{m_s-2} a_{Mn}\,\delta(l)|_n^{m_s}\,\delta(k)|_n^{m_s} \,\Big]\Big\|_{1:2:m_s-2}^{l}{}_{1:2:m_s-2}^{k} & \mathbf{0} \\
\mathbf{0} & 0
\end{bmatrix} \\
&= \begin{bmatrix}
\Big\|\Big[\, L_{s0} + \frac{m_s}{2}M_{s0}a_k \,\Big]\Big\|_{1:2:m_s-2}^{k} & \mathbf{0} \\
\mathbf{0} & 0
\end{bmatrix}
= \begin{bmatrix}
{}^{\omega}\overline{\mathbf{L}}_s & \mathbf{0} \\
\mathbf{0} & L_{s0}
\end{bmatrix}
\end{aligned}
$$

where the two submatrices in the passage (p) are obtained substituting the transformation matrix ${}^{t}\widehat{\mathbf{T}}_{\underline{\omega}}$ and calculating the matrix product. The zero vector is obtained as:

$$
\begin{aligned}
&\Big\|\Big[\sum_{n=1:2}^{m_s-2} a_{Mn}\Big(e^{j\,n\,(i-h)\gamma_s} + e^{-j\,n\,(i-h)\gamma_s}\Big)\Big]\Big\|_{0:m_s-1}^{i}{}_{0:m_s-1}^{h}\ \Big\|\Big[\, 1 \,\Big]\Big\|_{0:m_s-1}^{h} = \\
&= \Big\|\Big[\underbrace{\sum_{n=1:2}^{m_s-2}\sum_{h=0}^{m_s-1} a_{Mn}\, e^{jni\gamma_s}e^{-jhk\gamma_s}}_{=0} + \underbrace{\sum_{n=1:2}^{m_s-2}\sum_{h=0}^{m_s-1} a_{Mn}\, e^{-jni\gamma_s}e^{jhk\gamma_s}}_{=0}\Big]\Big\|_{0:m_s-1}^{i}{}_{1:2:m_s-2}^{k} = \mathbf{0}
\end{aligned}
$$

and the second submatrix is computed using (C.4) in the matrix product:

$$\left\|\left[\sum_{n=1:2}^{m_s-2} a_{Mn}\left(e^{j\,n\,(i-h)\gamma_s}+e^{-j\,n\,(i-h)\gamma_s}\right)\right]\right\|_{0:m_s-1}^{i}\Bigg\|_{0:m_s-1}^{h}\left\|\left[\; e^{jk\theta}\,e^{-jhk\gamma_s}\;\right]\right\|_{1:2:m_s-2}^{h,k}=$$

$$=\left\|\left[\; e^{jk\theta}\underbrace{\sum_{n=1:2}^{m_s-2}\sum_{h=0}^{m_s-1} a_{Mn}\,e^{jni\gamma_s}e^{-jh\gamma_s(k+n)}}_{=0}+e^{jk\theta}\sum_{n=1:2}^{m_s-2}\sum_{h=0}^{m_s-1} a_{Mn}\,e^{-jni\gamma_s}e^{-jh\gamma_s(k-n)}\;\right]\right\|_{0:m_s-1}^{i,k}_{1:2:m_s-2}=$$

$$=\left\|\left[\; e^{jk\theta}\sum_{n=1:2}^{m_s-2} a_{Mn}\,e^{-jni\gamma_s}\underbrace{\sum_{h=0}^{m_s-1} e^{-jh\gamma_s(k-n)}}_{=m_s\,\text{if}\,k-n=0,\pm m_s..}\;\right]\right\|_{0:m_s-1}^{i,k}_{1:2:m_s-2}=m_s\left\|\left[\; e^{jk\theta}\sum_{n=1:2}^{m_s-2} a_{Mn}\,e^{-jni\gamma_s}\delta(k)\big|_n^{m_s}\;\right]\right\|_{0:m_s-1}^{i}{}_{1:2:m_s-2}^{k}$$

The transformed current vector ${}^{\omega}\overline{\mathbf{I}}_s = {}^{t}\overline{\mathbf{T}}^{*}_{\omega N}\,{}^{t}\mathbf{I}_s$ in (2.19) has the following structure:

$${}^{\omega}\overline{\mathbf{I}}_s=\sqrt{\frac{2}{m_s}}\begin{bmatrix}\left\|\left[\; e^{-j\,k\,(\theta\,-h\,\gamma_s)}\;\right]\right\|_{1:2:m_s-2}^{k}{}_{0:m_s-1}^{h}\\ \left\|\left[\;\frac{1}{\sqrt{2}}\;\right]\right\|_{0:m_s-1}^{h}\end{bmatrix}\Big\|_{1:m_s}^{h}\left[\!\left[\; I_{sh}\;\right]\!\right]=\sqrt{\frac{2}{m_s}}\begin{bmatrix}\left\|\left[\; e^{-j\,k\,\theta}\sum_{h=1}^{m_s} I_{sh}e^{j\,k\,(h-1)\gamma_s}\;\right]\right\|_{1:2:m_s-2}^{k}\\ \frac{1}{\sqrt{2}}\sum_{h=1}^{m_s} I_{sh}\end{bmatrix}=$$

$$=\begin{bmatrix}\left\|\left[\;{}^{\omega}\overline{I}_{sk}\;\right]\right\|_{1:2:m_s-2}^{k}\\ {}^{\omega}\overline{I}_{sm_s}\end{bmatrix}=\begin{bmatrix}\left\|\left[\; I_{dk}+j\,I_{qk}\;\right]\right\|_{1:2:m_s-2}^{k}\\ {}^{\omega}\overline{I}_{sm_s}\end{bmatrix}=\begin{bmatrix}{}^{\omega}\overline{\mathbf{I}}_s\\ {}^{\omega}I_{sm_s}\end{bmatrix}$$

and the transformed voltage vector ${}^{\omega}\overline{\mathbf{V}}_s$ (2.20) has the same structure of the current one:

$${}^{\omega}\overline{\mathbf{V}}_s=\sqrt{\frac{2}{m_s}}\begin{bmatrix}\left\|\left[\; e^{-j\,k\,\theta}\sum_{h=1}^{m_s} V_{sh}e^{j\,k\,(h-1)\gamma_s}\;\right]\right\|_{1:2:m_s-2}^{k}\\ \frac{1}{\sqrt{2}}\sum_{h=1}^{m_s} V_{sh}\end{bmatrix}=\begin{bmatrix}\left\|\left[\;{}^{\omega}\overline{V}_{sk}\;\right]\right\|_{m_s-2:-2:1}^{k}\\ {}^{\omega}\overline{V}_{sm_s}\end{bmatrix}=\begin{bmatrix}\left[\!\left[\; V_{dk}+j\,V_{qk}\;\right]\!\right]_{1:2:m_s-2}^{k}\\ {}^{\omega}\overline{V}_{sm_s}\end{bmatrix}=\begin{bmatrix}{}^{\omega}\overline{\mathbf{V}}_s\\ {}^{\omega}\overline{V}_{sm_s}\end{bmatrix}$$

The transformed torque vector ${}^{\underline{\omega}}\overline{\mathbf{K}}_{\tau N}(\theta) = {}^{t}\overline{\mathbf{T}}^{*}_{\underline{\omega} N}\mathbf{K}_{\tau}(\theta)$ in (2.21) has been obtained as follows:

$$
\begin{aligned}
{}^{\underline{\omega}}\overline{\mathbf{K}}_{\tau N}(\theta) &= -\frac{p\,\varphi_c}{j\sqrt{2\,m_s}}
\begin{bmatrix}
\overset{k}{\underset{1:2:m_s-2}{\left\|\left[\, e^{-j\,k\,(\theta - h\,\gamma_s)} \,\right]\right\|}} & \overset{h}{\underset{0:m_s-1}{}} \\
\overset{h}{\underset{0:m_s-1}{\left\|\left[\, \frac{1}{\sqrt{2}} \,\right]\right\|}}
\end{bmatrix}
\overset{h}{\underset{0:m_s-1}{\left\|\left[\, \sum_{n=-\infty;1:2}^{\infty} n\,a_n\, e^{j\,n(\theta - h\gamma_s)} \,\right]\right\|}} \\
&= \frac{j\,p\,\varphi_c}{\sqrt{2\,m_s}}
\begin{bmatrix}
\overset{k}{\underset{1:2:m_s-2}{\left\|\left[\, \sum_{n=-\infty;1:2}^{\infty} n\,a_n \sum_{h=0}^{m_s-1} e^{-j\,k\,(\theta - h\gamma_s)} e^{j\,n(\theta - h\gamma_s)} \,\right]\right\|}} \\
\frac{1}{\sqrt{2}} \sum_{n=-\infty;1:2}^{\infty} n\,a_n \sum_{h=0}^{m_s-1} e^{j\,n(\theta - h\gamma_s)}
\end{bmatrix} \\
&= \frac{j\,p\,\varphi_c}{\sqrt{2\,m_s}}
\begin{bmatrix}
\overset{k}{\underset{1:2:m_s-2}{\left\|\left[\, \sum_{n=-\infty;1:2}^{\infty} n\,a_n e^{-j\,\theta(k-n)} \underbrace{\sum_{h=0}^{m_s-1} e^{j\,h\gamma_s(k-n)}}_{=m_s \text{ if } k-n=0,\pm m_s..} \,\right]\right\|}} \\
\frac{1}{\sqrt{2}} \sum_{n=-\infty;1:2}^{\infty} n\,a_n\, e^{j\,n\,\theta} \underbrace{\sum_{h=0}^{m_s-1} e^{-j\,n\,h\gamma_s}}_{=m_s \text{ if } n=0,\pm m_s..}
\end{bmatrix} \\
&= \frac{j\,p\,\varphi_c}{\sqrt{2\,m_s}}
\begin{bmatrix}
\overset{k}{\underset{1:2:m_s-2}{\left\|\left[\, \sum_{n=-\infty;1:2}^{\infty} n\,a_n e^{-j\,\theta(k-n)}\, m_s\,\delta(n)|_k^{m_s} \,\right]\right\|}} \\
\frac{1}{\sqrt{2}} \sum_{n=-\infty;1:2}^{\infty} n\,a_n\, e^{j\,n\,\theta}\, m_s\,\delta(n)|_0^{m_s}
\end{bmatrix} \\
&= j\,\varphi_c\,p\,\sqrt{\frac{m_s}{2}}
\begin{bmatrix}
\overset{k}{\underset{1:2:m_s-2}{\left\|\left[\, \sum_{n=-\infty;k:2m_s}^{\infty} n\,a_n e^{-j\,\theta(k-n)} \,\right]\right\|}} \\
\frac{1}{\sqrt{2}} \sum_{n=-\infty;m_s:2m_s}^{\infty} n\,a_n\, e^{j\,n\,\theta}
\end{bmatrix}
\end{aligned}
$$

Operating a change of variable $\bar{n} = n - k$ and renaming $\bar{n}$ with n:

$$
\sum_{n=-\infty;k:2m_s}^{\infty} \qquad \bar{n} = n - k \;\rightarrow\; n = \bar{n} + k \qquad \sum_{\bar{n}+k=-\infty;k:2m_s}^{\infty} \qquad \sum_{\bar{n}=-\infty;0:2m_s}^{\infty}
$$

the transformed torque vector ${}^{\omega}\overline{\mathbf{K}}_{\tau N}$ is rewritten as follows:

$$ {}^{\omega}\overline{\mathbf{K}}_{\tau N}(\theta) = j\,\varphi_c\,p\,\sqrt{\frac{m_s}{2}} \begin{bmatrix} \Big\|_{1:2:m_s-2}^{k} \Big[\sum_{n=-\infty;0:2m_s}^{\infty} (n+k)\,a_{n+k}\,e^{j\,\theta\,n} \Big] \Big\| \\ \frac{1}{\sqrt{2}} \sum_{n=-\infty;m_s:2m_s}^{\infty} n\,a_n\,e^{j\,n\,\theta} \end{bmatrix} $$

Since $a_{-k} = a_k$ for real function, one obtains:

$$ {}^{\omega}\overline{\mathbf{K}}_{\tau N}(\theta) = jp\varphi_c\sqrt{\tfrac{m_s}{2}} \begin{bmatrix} \Big\|_{1:2:m_s-2}^{k} \Big[\sum_{n=0:2\,m_s}^{\infty} (n+k)\,a_{n+k}\,e^{j\theta n} - (n-k)\,a_{n-k}\,e^{-j\theta n} \Big] \Big\| \\ \frac{1}{\sqrt{2}} \sum_{n=m_s:2m_s}^{\infty} n a_n (e^{jn\theta} - e^{-jn\theta}) \end{bmatrix}. $$

The transformed torque vector ${}^{\omega}\overline{\mathbf{K}}_{\tau N}$ is constant (not function of the electric angle θ) if and only if the following relations hold:

$$ (n+k)\,a_{n+k} \neq 0 \quad \text{if} \quad n = 0 \text{ and } k \in \{1:2:m_s-2\} \tag{C.5} $$

Therefore, when the normalized rotor flux has the structure:

$$ \bar{\phi}(\theta) = \sum_{i=1:2}^{m_s-2} a_i \cos(i\,\theta) $$

the transformed torque vector ${}^{\omega}\overline{\mathbf{K}}_{\tau N}$ is constant:

$$ {}^{\omega}\overline{\mathbf{K}}_{\tau N}(\theta) = {}^{\omega}\overline{\mathbf{K}}_{\tau N} = jp\varphi_c\sqrt{\frac{m_s}{2}} \begin{bmatrix} \Big\|_{1:2:m_s-2}^{k} \Big[ka_k \Big] \Big\| \\ 0 \end{bmatrix}. $$

C.3 Mathematical calculations for Sec. 2.2.3

The transformation matrix ${}^{\omega}\overline{\mathbf{T}}_{\underline{\omega}}$ which links together the dynamic systems S_ω and $\overline{S}_\omega$ is related to matrices ${}^{t}\mathbf{T}_{\underline{\omega}}$ and ${}^{t}\overline{\mathbf{T}}_{\underline{\omega}}$ as follows:

$$
\begin{aligned}
{}^{\underline{\omega}}\overline{\mathbf{T}}_{\underline{\omega}N} &= {}^{t}\mathbf{T}_{\underline{\omega}}^{\mathrm{T}}\,{}^{t}\overline{\mathbf{T}}_{\underline{\omega}N} \\
&= \frac{2}{m_s}\begin{bmatrix} \left\|\begin{bmatrix} \cos(k(h\gamma_s-\theta)) \\ \sin(k(h\gamma_s-\theta)) \end{bmatrix}\right\|_{1:2:m_s-2}^{k}{}_{0:m_s-1}^{h} \\ \left\|\begin{bmatrix} \frac{1}{\sqrt{2}} \end{bmatrix}\right\|_{0:m_s-1}^{h} \end{bmatrix} \begin{bmatrix} \left\|\begin{bmatrix} e^{jk(\theta-h\gamma_s)} \end{bmatrix}\right\|_{0:m_s-1\ \ 1:2:m_s-2}^{h\qquad\quad k} & \left\|\begin{bmatrix} \frac{1}{\sqrt{2}} \end{bmatrix}\right\|_{0:m_s-1}^{h} \end{bmatrix} \\
&= \frac{\sqrt{2}}{m_s}\begin{bmatrix} \left\|\begin{bmatrix} \sum_{h=0}^{m_s-1}\cos(k(h\gamma_s-\theta))\,e^{jl(\theta-h\gamma_s)} \\ \sum_{h=0}^{m_s-1}\sin(k(h\gamma_s-\theta))\,e^{jl(\theta-h\gamma_s)} \end{bmatrix}\right\|_{1:2:m_s-2}^{k}{}_{1:2:m_s-2}^{l} & \left\|\begin{bmatrix} \sum_{h=0}^{m_s-1}\cos(k(h\gamma_s-\theta)) \\ \sum_{h=0}^{m_s-1}\sin(k(h\gamma_s-\theta)) \end{bmatrix}\right\|_{1:2:m_s-2}^{k} \\ \left\|\begin{bmatrix} \sum_{h=0}^{m_s-1}\frac{1}{\sqrt{2}}\,e^{jl(\theta-h\gamma_s)} \end{bmatrix}\right\|_{1:2:m_s-2}^{l} & \frac{m_s}{2} \end{bmatrix} \\
&= \frac{2}{m_s}\begin{bmatrix} \left\|\begin{bmatrix} \frac{m_s}{2}\,\delta(l)|_k^{m_s} \\ -j\,\frac{m_s}{2}\,\delta(l)|_k^{m_s} \end{bmatrix}\right\|_{1:2:m_s-2}^{k}{}_{1:2:m_s-2}^{l} & \left\|\begin{bmatrix} 0 \\ 0 \end{bmatrix}\right\|_{1:2:m_s-2}^{k} \\ [\![\,0\,]\!]_{1:2:m_s-2}^{l} & \frac{m_s}{2} \end{bmatrix} \\
&= \begin{bmatrix} \left\|\begin{bmatrix} \delta(l)|_k^{m_s} \\ -j\,\delta(l)|_k^{m_s} \end{bmatrix}\right\|_{1:2:m_s-2\qquad 1:2:m_s-2}^{k\qquad\quad l} & \mathbf{0} \\ \mathbf{0} & 1 \end{bmatrix}
\end{aligned}
$$

Indeed, using the (C.4) one obtains:

$$\begin{aligned}
\sum_{h=0}^{m_s-1} \cos(k(h\gamma_s-\theta))\, e^{jl(\theta-h\gamma_s)} &= \sum_{h=0}^{m_s-1} \frac{e^{jk(h\gamma_s-\theta)}\, e^{jl(\theta-h\gamma_s)} + e^{-jk(h\gamma_s-\theta)}\, e^{jl(\theta-h\gamma_s)}}{2} \\
&= \frac{e^{-j(k-l)\theta}}{2} \sum_{h=0}^{m_s-1} e^{j\,h\,(k-l)\,\gamma_s} + \frac{e^{j(k+l)\theta}}{2} \sum_{h=0}^{m_s-1} e^{-j\,h\,(k+l)\,\gamma_s} \\
&= \frac{m_s}{2}\,\delta(l)|_k^{m_s}
\end{aligned}$$

$$\begin{aligned}
\sum_{h=0}^{m_s-1} \sin(k(h\gamma_s-\theta))\, e^{jl(\theta-h\gamma_s)} &= \sum_{h=0}^{m_s-1} \frac{e^{jk(h\gamma_s-\theta)}\, e^{jl(\theta-h\gamma_s)} - e^{-jk(h\gamma_s-\theta)}\, e^{jl(\theta-h\gamma_s)}}{2j} \\
&= \frac{e^{-j(k-l)\theta}}{2j} \sum_{h=0}^{m_s-1} e^{j\,h\,(k-l)\,\gamma_s} - \frac{e^{j(k+l)\theta}}{2j} \sum_{h=0}^{m_s-1} e^{-j\,h\,(k+l)\,\gamma_s} \\
&= \frac{m_s}{2j}\,\delta(l)|_k^{m_s} = -j\,\frac{m_s}{2}\,\delta(l)|_k^{m_s}
\end{aligned}$$

C.4 Mathematical calculations for Sec. 4.1

Let us now consider the case of current stator vectors ${}^t\mathbf{I}_s$ composed by the first $(m_s-1)/2$ harmonics:

$${}^t\mathbf{I}_s = \sum_{k=1:2}^{m_s-2} \underset{0:m_s-1}{\overset{h}{[\![}} I_{mk} \cos(k\theta - k(\theta_{ik}+h\gamma_s)) \,]\!] = \sum_{k=1:2}^{m_s-2} \underset{0:m_s-1}{\overset{h}{\left\|\left[\!\left[\frac{I_{mk}}{2} \left(e^{j\,k(\theta-\theta_{ik}-h\gamma_s)} - e^{-j\,k(\theta-\theta_{ik}-h\gamma_s)}\right) \right]\!\right]\right\|}$$

where I_{mk} are the amplitude of the balanced current harmonic of order k and θ_{ik} is proper initial phase shifts. The expression of the transformed current vector $\underline{{}^{\omega}\overline{\mathbf{I}}}_s = {}^t\overline{\mathbf{T}}^*_{\omega N}\, {}^t\mathbf{I}_s$ reported in (4.3) has been obtained from the following passages:

$$\underline{{}^{\omega}\overline{\mathbf{I}}}_s = \sqrt{\frac{2}{m_s}} \begin{bmatrix} \underset{1:2:m_s-2}{\overset{k}{\left\|\left[\!\left[e^{-j\,k\,(\theta-h\,\gamma_s)} \right]\!\right]\right\|}} & \\ & \underset{0:m_s-1}{\overset{h}{\left\|\left[\!\left[\frac{1}{\sqrt{2}} \right]\!\right]\right\|}} \end{bmatrix} \underset{0:m_s-1}{\overset{h}{\left\|\left[\!\left[\sum_{l=1:2}^{m_s-2} \frac{I_{ml}}{2} \left(e^{j\,l(\theta-\theta_{il}-h\gamma_s)} - e^{-j\,l(\theta-\theta_{il}-h\gamma_s)}\right) \right]\!\right]\right\|} =$$

$$= \sqrt{\frac{2}{m_s}}\frac{I_{mk}}{2} \begin{bmatrix} \underset{1:2:m_s-2}{\overset{k}{\left\|\left[\!\left[\sum_{h=0}^{m_s-1} \sum_{l=1:2}^{m_s-2} e^{-j\,k\,(\theta-h\,\gamma_s)} \left(e^{j\,l(\theta-\theta_{il}-h\gamma_s)} - e^{-j\,l(\theta-\theta_{il}-h\gamma_s)}\right) \right]\!\right]\right\|} \\ \sum_{h=0}^{m_s-1} \sum_{l=1:2}^{m_s-2} \frac{1}{\sqrt{2}} \left(e^{j\,l(\theta-\theta_{il}-h\gamma_s)} - e^{-j\,l(\theta-\theta_{il}-h\gamma_s)}\right) \end{bmatrix} =$$

$$
{}^{\underline{\omega}}\overline{\mathbf{I}}_s = \sqrt{\frac{2}{m_s}}\frac{I_{mk}}{2}
\begin{bmatrix}
\Big\|_{1:2:m_s-2}^{k}\Big[\Big[\underbrace{\sum_{l=1:2}^{m_s-2} e^{j(l-k)\,\theta}e^{-jl\theta_{il}} \underbrace{\sum_{h=0}^{m_s-1} e^{-j(l-k)h\gamma_s}}_{=m_s \text{ if } l-k=0,\pm m_s,..}}_{} - \underbrace{\sum_{l=1:2}^{m_s-2} e^{-j(l+k)\,\theta}e^{jl\theta_{il}} \underbrace{\sum_{h=0}^{m_s-1} e^{j(l+k)h\gamma_s}}_{=0}}_{} \Big]\Big| \\
\underbrace{\sum_{l=1:2}^{m_s-2} \frac{1}{\sqrt{2}}e^{j\,l(\theta-\theta_{il})} \underbrace{\sum_{h=0}^{m_s-1} e^{-j\,lh\gamma_s}}_{=0}}_{} - \underbrace{\sum_{l=1:2}^{m_s-2} \frac{1}{\sqrt{2}}e^{-j\,l(\theta-\theta_{il})} \underbrace{\sum_{h=0}^{m_s-1} e^{j\,lh\gamma_s}}_{=0}}_{}
\end{bmatrix}
$$

$$
= \sqrt{\frac{2}{m_s}}\frac{I_{mk}}{2}
\begin{bmatrix}
\Big\|_{1:2:m_s-2}^{k}\Big[\Big[\sum_{l=1:2}^{m_s-2} e^{j(l-k)\,\theta}e^{-jl\theta_{il}} m_s\delta(l)\big|_k^{m_s} \Big]\Big| \\
0
\end{bmatrix}
= \sqrt{\frac{m_s}{2}}
\begin{bmatrix}
\Big\|_{1:2:m_s-2}^{k}\Big[\Big[I_{mk}e^{-jk\theta_{ik}} \Big]\Big| \\
0
\end{bmatrix}.
$$

When the motor is star-connected the last column of matrix ${}^{t}\overline{\mathbf{T}}_{\omega N}$ can be eliminated. In this case matrix ${}^{t}\overline{\mathbf{T}}_{\omega N}$ reduces to the rectangular matrix ${}^{t}\overline{\mathbf{T}}_{\omega}$ and the transformed current vector ${}^{\underline{\omega}}\overline{\mathbf{I}}_s$ reduces to ${}^{\omega}\overline{\mathbf{I}}_s$ as follows:

$$
{}^{\omega}\overline{\mathbf{I}}_s = \sqrt{\frac{m_s}{2}} \Big\|_{1:2:m_s-2}^{k}\Big[\Big[I_{mk}e^{-jk\theta_{ik}} \Big]\Big|
$$

It is possible to obtain the same result considering the balanced voltage stator vectors ${}^{t}\mathbf{V}_s$ composed by the first $(m_s-1)/2$ harmonics:

$$
{}^{t}\mathbf{V}_s = \sum_{k=1:2}^{m_s-2} \Big\|_{0:m_s-1}^{h}[\![V_{mk}\cos(k\theta - k(\theta_{vk}+h\gamma_s))]\!] = \sum_{k=1:2}^{m_s-2} \Big\|_{0:m_s-1}^{h}\Big[\Big[\frac{V_{mk}}{2}\left(e^{j\,k(\theta-\theta_{vk}-h\gamma_s)} - e^{-j\,k(\theta-\theta_{vk}-h\gamma_s)}\right) \Big]\Big|
$$

where V_{mk} are the amplitude of the balanced current harmonic of order k and θ_{vk} is proper initial phase shifts. The transformed voltage vectors ${}^{\omega}\overline{\mathbf{V}}_s = {}^{t}\overline{\mathbf{T}}^{*}_{\omega N}\,{}^{t}\mathbf{V}_s$ reported in (4.4) has the following structure:

$$
{}^{\underline{\omega}}\overline{\mathbf{V}}_s = \sqrt{\frac{m_s}{2}}
\begin{bmatrix}
\Big\|_{1:2:m_s-2}^{k}\Big[\Big[V_{mk}e^{-jk\theta_{vk}} \Big]\Big| \\
0
\end{bmatrix}
$$

C.5 Mathematical calculations for Sec. 5.3

C.5.1 Example: 5-phase motor

Let consider the example of a 5-phase motor where a first failure occurs at time t_1 at the phase $i = 2$ and a second failure occurs at time $t_2 > t_1$ at the phase $j = 4$. The transformation matrices ${}^{t}\mathbf{T}_c$, ${}^{f1}\mathbf{T}_c$ and ${}^{f2}\mathbf{T}_c$ have the following structure:

$$ {}^{t}\mathbf{T}_c = \begin{bmatrix} 1 & 0 & 0 & 0 \\ 0 & 1 & 0 & 0 \\ 0 & 0 & 1 & 0 \\ 0 & 0 & 0 & 1 \\ -1 & -1 & -1 & -1 \end{bmatrix}, \quad {}^{f_1}\mathbf{T}_c = \begin{bmatrix} 1\,0\,0 \\ 0\,0\,0 \\ 0\,1\,0 \\ 0\,0\,1 \end{bmatrix}, \quad {}^{f_2}\mathbf{T}_c = \begin{bmatrix} 1\,0 \\ 0\,0 \\ 0\,1 \\ 0\,0 \end{bmatrix}. $$

The transformed system (5.22) can be written explicitly as:

$$ \begin{bmatrix} L_{11} L_{12} L_{13} L_{14} \\ L_{12} L_{22} L_{23} L_{13} \\ L_{13} L_{23} L_{22} L_{12} \\ L_{14} L_{13} L_{12} L_{11} \end{bmatrix} \begin{bmatrix} \dot{I}_{s1} \\ \dot{I}_{s2} \\ \dot{I}_{s3} \\ \dot{I}_{s4} \end{bmatrix} = - \begin{bmatrix} 2R_s & R_s & R_s & R_s \\ R_s & 2R_s & R_s & R_s \\ R_s & R_s & 2R_s & R_s \\ R_s & R_s & R_s & 2R_s \end{bmatrix} \begin{bmatrix} I_{s1} \\ I_{s2} \\ I_{s3} \\ I_{s4} \end{bmatrix} - \begin{bmatrix} E_{s1} - E_{s5} \\ E_{s2} - E_{s5} \\ E_{s3} - E_{s5} \\ E_{s4} - E_{s5} \end{bmatrix} + \begin{bmatrix} V_{s1} - V_{s5} \\ V_{s2} - V_{s5} \\ V_{s3} - V_{s5} \\ V_{s4} - V_{s5} \end{bmatrix}. \tag{C.6} $$

When $t_1 \leq t \leq t_2$, using the congruent transformation ${}^{f_1}\mathbf{I}_s = {}^{f_1}\mathbf{T}_c \, {}^{c}\mathbf{I}_s$ one obtains the following reduced system:

$$ \underbrace{\begin{bmatrix} L_{11} & L_{13} & L_{14} \\ L_{13} & L_{22} & L_{12} \\ L_{14} & L_{12} & L_{11} \end{bmatrix}}_{{}^{f_1}\mathbf{L}_s} \underbrace{\begin{bmatrix} \dot{I}_{s1} \\ \dot{I}_{s3} \\ \dot{I}_{s4} \end{bmatrix}}_{{}^{f_1}\dot{\mathbf{I}}_s} = - \underbrace{\begin{bmatrix} 2R_s & R_s & R_s \\ R_s & 2R_s & R_s \\ R_s & R_s & 2R_s \end{bmatrix}}_{{}^{f_1}\mathbf{R}_s} \underbrace{\begin{bmatrix} I_{s1} \\ I_{s3} \\ I_{s4} \end{bmatrix}}_{{}^{f_1}\mathbf{I}_s} - \underbrace{\begin{bmatrix} E_{s1} - E_{s5} \\ E_{s3} - E_{s5} \\ E_{s4} - E_{s5} \end{bmatrix}}_{{}^{f_1}\mathbf{E}_s} + \underbrace{\begin{bmatrix} V_{s1} - V_{s5} \\ V_{s3} - V_{s5} \\ V_{s4} - V_{s5} \end{bmatrix}}_{{}^{f_1}\mathbf{V}_s} $$

which is obtained from the previous one eliminating the 2nd row and the 2nd column. The time derivative ${}^{f1}\dot{\mathbf{I}}_s$ of the current vector necessary to calculate the voltage ${}^{f_1}V_2$ defined in (5.27) can be obtained using equation (5.28). The voltage ${}^{f_1}V_2$ has the following structure:

$$ {}^{f_1}V_2 = \begin{bmatrix} 0 \\ 1 \\ 0 \\ 0 \end{bmatrix}^{\mathrm{T}} \left[\begin{bmatrix} L_{11} & L_{12} & L_{13} & L_{14} \\ L_{12} & L_{22} & L_{23} & L_{13} \\ L_{13} & L_{23} & L_{22} & L_{12} \\ L_{14} & L_{13} & L_{12} & L_{11} \end{bmatrix} \begin{bmatrix} 1\,0\,0 \\ 0\,0\,0 \\ 0\,1\,0 \\ 0\,0\,1 \end{bmatrix} \begin{bmatrix} \dot{I}_{s1} \\ \dot{I}_{s3} \\ \dot{I}_{s4} \end{bmatrix} + \begin{bmatrix} 2R_s & R_s & R_s & R_s \\ R_s & 2R_s & R_s & R_s \\ R_s & R_s & 2R_s & R_s \\ R_s & R_s & R_s & 2R_s \end{bmatrix} \begin{bmatrix} 1\,0\,0 \\ 0\,0\,0 \\ 0\,1\,0 \\ 0\,0\,1 \end{bmatrix} \begin{bmatrix} I_{s1} \\ I_{s3} \\ I_{s4} \end{bmatrix} + \begin{bmatrix} E_{s1} - E_{s5} \\ E_{s2} - E_{s5} \\ E_{s3} - E_{s5} \\ E_{s4} - E_{s5} \end{bmatrix} - \begin{bmatrix} V_{s1} - V_{s5} \\ V_{s2} - V_{s5} \\ V_{s3} - V_{s5} \\ V_{s4} - V_{s5} \end{bmatrix} \right] $$

Note that the matrix product between the transformation matrix ${}^{f_1}\mathbf{T}_c$ with the current vector ${}^{f_1}\mathbf{I}_s$ and its time derivative ${}^{f_1}\dot{\mathbf{I}}_s$ are equal to vectors where the 2-nd component is zero. Since the 2-nd vector of the standard basis $\mathbf{e}_2^4$ select the 2-nd component of the corresponding right

vector, one obtains:

$$\begin{aligned} {}^{f_1}V_2 &= (\mathbf{e}_2^4)^{\mathrm{T}}\Big[{}^{c}\mathbf{L}_s\,{}^{f_1}\mathbf{T}_c\,{}^{f_1}\dot{\mathbf{I}}_s + {}^{c}\mathbf{R}_s\,{}^{f_1}\mathbf{T}_c\,{}^{f_1}\mathbf{I}_s + {}^{c}\mathbf{E}_s - {}^{c}\mathbf{V}_s\Big] \\ &= L_{12}\dot{I}_{s1} + L_{13}\dot{I}_{s3} + L_{13}\dot{I}_{s4} + R_sI_{s1} + R_sI_{s3} + R_sI_{s4} + E_{s2} - E_{s5} - V_{s2} + V_{s5}. \end{aligned}$$

The vector ${}^{c}\mathbf{V}_{Fs}$ to be added to system (5.22) is: ${}^{c}\mathbf{V}_{Fs} = \begin{bmatrix} 0 & {}^{f_1}V_2 & 0 & 0 \end{bmatrix}^{\mathrm{T}}$. In this case equation (5.25) is: $L_{22}\,{}^{c}\dot{I}_{s2} = -2R_s\,{}^{c}I_{s2}$ and the condition ${}^{c}I_{s2} = I_{s2} = 0$ is reached with an exponential law and a settling time $T_a = 3\,L_{22}/2R_s$.

When $t > t_2$ the reduced system (5.26) is:

$$\underbrace{\begin{bmatrix} L_{11} & L_{13} \\ L_{13} & L_{22} \end{bmatrix}}_{{}^{f_2}\mathbf{L}_s} \underbrace{\begin{bmatrix} \dot{I}_{s1} \\ \dot{I}_{s3} \end{bmatrix}}_{{}^{f_2}\dot{\mathbf{I}}_s} = - \underbrace{\begin{bmatrix} 2R_s & R_s \\ R_s & 2R_s \end{bmatrix}}_{{}^{f_2}\mathbf{R}_s} \underbrace{\begin{bmatrix} I_{s1} \\ I_{s3} \end{bmatrix}}_{{}^{f_2}\mathbf{I}_s} - \underbrace{\begin{bmatrix} E_{s1}-E_{s5} \\ E_{s3}-E_{s5} \end{bmatrix}}_{{}^{f_2}\mathbf{E}_s} + \underbrace{\begin{bmatrix} V_{s1}-V_{s5} \\ V_{s3}-V_{s5} \end{bmatrix}}_{{}^{f_2}\mathbf{V}_s}.$$

It is obtained from (C.6) eliminating the 2nd and 4th rows and columns, i.e. by applying the transformation ${}^{f_2}\mathbf{T}_c$. The voltages ${}^{f_2}V_2$ and ${}^{f_2}V_4$ are given by:

$$\begin{aligned} {}^{f_2}V_2 &= (\mathbf{e}_2^4)^{\mathrm{T}}\Big[{}^{c}\mathbf{L}_s\,{}^{f_2}\mathbf{T}_c\,{}^{f_2}\dot{\mathbf{I}}_s + {}^{c}\mathbf{R}_s\,{}^{f_2}\mathbf{T}_c\,{}^{f_2}\mathbf{I}_s + {}^{c}\mathbf{E}_s - {}^{c}\mathbf{V}_s\Big] \\ &= L_{12}\dot{I}_{s1} + L_{13}\dot{I}_{s3} + R_sI_{s1} + R_sI_{s3} + E_{s2} - E_{s5} - V_{s2} + V_{s5} \\ {}^{f_2}V_4 &= (\mathbf{e}_4^4)^{\mathrm{T}}\Big[{}^{c}\mathbf{L}_s\,{}^{f_2}\mathbf{T}_c\,{}^{f_2}\dot{\mathbf{I}}_s + {}^{c}\mathbf{R}_s\,{}^{f_2}\mathbf{T}_c\,{}^{f_2}\mathbf{I}_s + {}^{c}\mathbf{E}_s - {}^{c}\mathbf{V}_s\Big] \\ &= L_{14}\dot{I}_{s1} + L_{12}\dot{I}_{s3} + R_sI_{s1} + R_sI_{s3} + E_{s4} - E_{s5} - V_{s4} + V_{s5} \end{aligned}$$

Since the voltage applied to the first broken phase neglects the current in the last broken phase, in the fault transient the current I_{s2} is different from zero. During this second fault transient to hold the current in the first faulty phase equal to zero (i.e. $I_{s2} = 0$) the additional voltage ${}^{f_2}V_i$ must be recalculated taking into account the current in the second faulty phase I_{s4}.

The new additional voltage ${}^{f_1}V_2$ applied to the first broken phase 2 must be recalculated considering this reduced system where the current I_{s4} and the voltage ${}^{f_2}V_4$, of the last faulty phase are taken into account.

$$\underbrace{\begin{bmatrix} L_{11} & L_{13} & L_{14} \\ L_{13} & L_{22} & L_{12} \\ L_{14} & L_{12} & L_{11} \end{bmatrix}}_{{}^{f_1}\mathbf{L}_s} \underbrace{\begin{bmatrix} \dot{I}'_{s1} \\ \dot{I}'_{s3} \\ \dot{I}'_{s4} \end{bmatrix}}_{{}^{f_1}\dot{\mathbf{I}}_s} = - \underbrace{\begin{bmatrix} 2R_s & R_s & R_s \\ R_s & 2R_s & R_s \\ R_s & R_s & 2R_s \end{bmatrix}}_{{}^{f_1}\mathbf{R}_s} \underbrace{\begin{bmatrix} I_{s1} \\ I_{s3} \\ I_{s4} \end{bmatrix}}_{{}^{f_1}\mathbf{I}_s} - \underbrace{\begin{bmatrix} E_{s1}-E_{s5} \\ E_{s3}-E_{s5} \\ E_{s4}-E_{s5} \end{bmatrix}}_{{}^{f_1}\mathbf{E}_s} + \underbrace{\begin{bmatrix} V_{s1}-V_{s5} \\ V_{s3}-V_{s5} \\ V_{s4}-V_{s5} \end{bmatrix}}_{{}^{f_1}\mathbf{V}_s} + \underbrace{\begin{bmatrix} 0 \\ 0 \\ {}^{f_2}V_4 \end{bmatrix}}_{{}^{f_1}\mathbf{V}_s}.$$

Hence the new additional voltage ${}^{f_1}V_2$ given to the first broken phase has the following structure:

$${}^{f_1}V_2 = L_{12}\dot{I}'_{s1} + L_{23}\dot{I}'_{s3} + L_{13}\dot{I}'_{s4} + R_sI_{s1} + R_sI_{s3} + R_sI_{s4} + E_{s2} - E_{s5} - V_{s2} + V_{s5},$$

where the second faulty phase current is considered. Note that the new components $\dot{I}'_{s1}$, $\dot{I}'_{s3}$ and $\dot{I}'_{s4}$ of vector ${}^{f1}\dot{\mathbf{I}}_s$ are different from the previous one $\dot{I}_{s1}$, $\dot{I}_{s3}$ and $\dot{I}_{s4}$. Using ${}^{f_2}V_4$ and ${}^{f_1}V_2$ calculated above the vector ${}^{c}\mathbf{V}_{Fs}$ to be added to the system (5.22) is ${}^{c}\mathbf{V}_{Fs} = \begin{bmatrix} 0 & {}^{f_1}V_2 & 0 & {}^{f_2}V_4 \end{bmatrix}^{\mathrm{T}}$. In this way the condition $I_{s2} = 0$ during the fault transient is achieved.

C.5.2 Example: 7-phase motor

Let consider the example of a 7-phase motor where a first failure occurs at time t_1 on the phase $i_1 = 4$ and a second and third failures occur at time $t_2 > t_1$ on the phases $i_2 = 5$ and $i_3 = 2$ when the current of the first faulty phase is zero.The transformation matrices ${}^{t}\mathbf{T}_c$, ${}^{f1}\mathbf{T}_c$ and ${}^{f3}\mathbf{T}_c$ have the following structure:

$$
{}^{t}\mathbf{T}_c = \begin{bmatrix} 1 & 0 & 0 & 0 & 0 & 0 \\ 0 & 1 & 0 & 0 & 0 & 0 \\ 0 & 0 & 1 & 0 & 0 & 0 \\ 0 & 0 & 0 & 1 & 0 & 0 \\ 0 & 0 & 0 & 0 & 1 & 0 \\ 0 & 0 & 0 & 0 & 0 & 1 \\ -1 & -1 & -1 & -1 & -1 & -1 \end{bmatrix}, \quad {}^{f1}\mathbf{T}_c = \begin{bmatrix} 1\,0\,0\,0\,0 \\ 0\,1\,0\,0\,0 \\ 0\,0\,1\,0\,0 \\ 0\,0\,0\,0\,0 \\ 0\,0\,0\,1\,0 \\ 0\,0\,0\,0\,1 \end{bmatrix}, \quad {}^{f3}\mathbf{T}_c = \begin{bmatrix} 1\,0\,0 \\ 0\,0\,0 \\ 0\,1\,0 \\ 0\,0\,0 \\ 0\,0\,0 \\ 0\,0\,1 \end{bmatrix}.
$$

The transformed system (5.22) can be written explicitly as:

$$
\underbrace{\begin{bmatrix} L_{11} & L_{12} & L_{13} & L_{14} & L_{15} & L_{16} \\ L_{12} & L_{22} & L_{23} & L_{24} & L_{25} & L_{15} \\ L_{13} & L_{23} & L_{33} & L_{34} & L_{24} & L_{14} \\ L_{14} & L_{24} & L_{34} & L_{33} & L_{23} & L_{13} \\ L_{15} & L_{25} & L_{24} & L_{23} & L_{22} & L_{12} \\ L_{16} & L_{15} & L_{14} & L_{13} & L_{12} & L_{11} \end{bmatrix}}_{{}^{c}\mathbf{L}_s} \underbrace{\begin{bmatrix} \dot{I}_{s1} \\ \dot{I}_{s2} \\ \dot{I}_{s3} \\ \dot{I}_{s4} \\ \dot{I}_{s5} \\ \dot{I}_{s6} \end{bmatrix}}_{{}^{c}\dot{\mathbf{I}}_s} = - \underbrace{\begin{bmatrix} 2R_s & R_s & R_s & R_s & R_s & R_s \\ R_s & 2R_s & R_s & R_s & R_s & R_s \\ R_s & R_s & 2R_s & R_s & R_s & R_s \\ R_s & R_s & R_s & 2R_s & R_s & R_s \\ R_s & R_s & R_s & R_s & 2R_s & R_s \\ R_s & R_s & R_s & R_s & R_s & 2R_s \end{bmatrix}}_{{}^{c}\mathbf{R}_s} \underbrace{\begin{bmatrix} I_{s1} \\ I_{s2} \\ I_{s3} \\ I_{s4} \\ I_{s5} \\ I_{s6} \end{bmatrix}}_{{}^{c}\mathbf{I}_s} - \underbrace{\begin{bmatrix} E_{s1} - E_{s7} \\ E_{s2} - E_{s7} \\ E_{s3} - E_{s7} \\ E_{s4} - E_{s7} \\ E_{s5} - E_{s7} \\ E_{s6} - E_{s7} \end{bmatrix}}_{{}^{c}\mathbf{E}_s} + \underbrace{\begin{bmatrix} V_{s1} - V_{s7} \\ V_{s2} - V_{s7} \\ V_{s3} - V_{s7} \\ V_{s4} - V_{s7} \\ V_{s5} - V_{s7} \\ V_{s6} - V_{s7} \end{bmatrix}}_{{}^{c}\mathbf{V}_c}
$$

When $t > t_2$ the reduced system (5.26) is:

$$
\underbrace{\begin{bmatrix} L_{11} & L_{13} & L_{16} \\ L_{13} & L_{33} & L_{14} \\ L_{16} & L_{14} & L_{11} \end{bmatrix}}_{{}^{f3}\mathbf{L}_s} \underbrace{\begin{bmatrix} \dot{I}_{s1} \\ \dot{I}_{s3} \\ \dot{I}_{s6} \end{bmatrix}}_{{}^{f3}\dot{\mathbf{I}}_s} = - \underbrace{\begin{bmatrix} 2R_s & R_s & R_s \\ R_s & 2R_s & R_s \\ R_s & R_s & 2R_s \end{bmatrix}}_{{}^{f3}\mathbf{R}_s} \underbrace{\begin{bmatrix} I_{s1} \\ I_{s3} \\ I_{s6} \end{bmatrix}}_{{}^{f3}\mathbf{I}_s} - \underbrace{\begin{bmatrix} E_{s1} - E_{s7} \\ E_{s3} - E_{s7} \\ E_{s6} - E_{s7} \end{bmatrix}}_{{}^{f3}\mathbf{E}_s} + \underbrace{\begin{bmatrix} V_{s1} - V_7 \\ V_{s3} - V_7 \\ V_{s6} - V_7 \end{bmatrix}}_{{}^{f3}\mathbf{V}_c}
$$

It is obtained from (C.6) eliminating the 2nd, the 4th and 5th rows and columns, i.e. by applying the transformation ${}^{f3}\mathbf{T}_c$. The adding voltage vector ${}^{c}\mathbf{V}_{Fs}$ (defined in (5.38) has the following structure:

$$
\begin{aligned}
{}^{c}\mathbf{V}_{Fs} &= \left[{}^{c}\mathbf{L}_s \, {}^{f3}\mathbf{T}_c \, {}^{f3}\mathbf{L}_s^{-1} \left(- {}^{f3}\mathbf{R}_s \, {}^{f3}\mathbf{I}_s - {}^{f3}\mathbf{E}_s + {}^{f3}\mathbf{V}_s \right) + {}^{c}\mathbf{R}_s \, {}^{f3}\mathbf{T}_c \, {}^{f3}\mathbf{I}_s + {}^{c}\mathbf{E}_s - {}^{c}\mathbf{V}_s \right] = \\
&= \begin{bmatrix} 0 & {}^{f3}V_{s2} & 0 & {}^{f3}V_{s4} & {}^{f3}V_{s5} & 0 \end{bmatrix}^T
\end{aligned}
$$

where:

$$
\begin{aligned}
{}^{f3}V_2 &= L_{12}\dot{I}_{s1} + L_{23}\dot{I}_{s3} + L_{15}\dot{I}_{s6} + R_sI_{s1} + R_sI_{s3} + R_sI_{s6} + E_{s2} - E_{s7} - V_{s2} + V_{s7}, \\
{}^{f3}V_4 &= L_{14}\dot{I}_{s1} + L_{34}\dot{I}_{s3} + L_{13}\dot{I}_{s6} + R_sI_{s1} + R_sI_{s3} + R_sI_{s6} + E_{s4} - E_{s7} - V_{s4} + V_{s7}, \\
{}^{f3}V_5 &= L_{15}\dot{I}_{s1} + L_{24}\dot{I}_{s3} + L_{12}\dot{I}_{s6} + R_sI_{s1} + R_sI_{s3} + R_sI_{s6} + E_{s5} - E_{s7} - V_{s5} + V_{s7}.
\end{aligned}
$$

During this second fault transient to hold the current in the first faulty phase equal to zero the additional voltage ${}^{f3}V_4$ must be recalculated considering the reduced system where the current I_{s2}, I_{s5} and the voltage ${}^{f3}V_{s2}$, ${}^{f3}V_{s5}$ of the last faulty phases are taken into account. In this case $n = 3$, $o = 1$, $\mathcal{S}_o = \{i_1 = 4\}$, $\mathcal{S}_g = \{i_2 = 5\,,\, i_3 = 2\}$ and the reduced system (in which the currents and the voltages of phases belonging to $\mathcal{S}_o$ are considered) has the following structure:

$$\underbrace{\begin{bmatrix} L_{11} & L_{12} & L_{13} & L_{15} & L_{16} \\ L_{12} & L_{22} & L_{23} & L_{25} & L_{15} \\ L_{13} & L_{23} & L_{33} & L_{24} & L_{14} \\ L_{15} & L_{25} & L_{24} & L_{22} & L_{12} \\ L_{16} & L_{15} & L_{14} & L_{12} & L_{11} \end{bmatrix}}_{{}^{f1}\mathbf{L}_s} \underbrace{\begin{bmatrix} \dot{I}_{s1} \\ \dot{I}_{s2} \\ \dot{I}_{s3} \\ \dot{I}_{s5} \\ \dot{I}_{s6} \end{bmatrix}}_{{}^{f1}\dot{\mathbf{I}}_s} = - \underbrace{\begin{bmatrix} 2R_s & R_s & R_s & R_s & R_s \\ R_s & 2R_s & R_s & R_s & R_s \\ R_s & R_s & 2R_s & R_s & R_s \\ R_s & R_s & R_s & 2R_s & R_s \\ R_s & R_s & R_s & R_s & 2R_s \end{bmatrix}}_{{}^{f1}\mathbf{R}_s} \underbrace{\begin{bmatrix} I_{s1} \\ I_{s2} \\ I_{s3} \\ I_{s5} \\ I_{s6} \end{bmatrix}}_{{}^{f1}\mathbf{I}_s} - \underbrace{\begin{bmatrix} E_{s1}-E_{s7} \\ E_{s2}-E_{s7} \\ E_{s3}-E_{s7} \\ E_{s5}-E_{s7} \\ E_{s6}-E_{s7} \end{bmatrix}}_{{}^{f1}\mathbf{E}_s} + \underbrace{\begin{bmatrix} V_{s1}-V_7 \\ V_{s2}-V_7 \\ V_{s3}-V_7 \\ V_{s5}-V_7 \\ V_{s6}-V_7 \end{bmatrix}}_{{}^{f1}\mathbf{V}_s} + \underbrace{\begin{bmatrix} 0 \\ {}^{f3}V_{s2} \\ 0 \\ {}^{f3}V_{s5} \\ 0 \end{bmatrix}}_{{}^{f1}\mathbf{V}_{Fs}}$$

where the voltages ${}^{c}\mathbf{V}_{Fsg} = \mathbf{F}_g\, {}^{c}\mathbf{V}_{Fs}$ and ${}^{f1}\mathbf{V}_{Fs} = {}^{f1}\mathbf{T}_c^{\mathrm{T}}\, {}^{c}\mathbf{V}_{Fsg}$ are:

$${}^{c}\mathbf{V}_{Fsg} = \begin{bmatrix} 0&0&0&0&0&0 \\ 0&1&0&0&0&0 \\ 0&0&0&0&0&0 \\ 0&0&0&0&0&0 \\ 0&0&0&0&1&0 \\ 0&0&0&0&0&0 \end{bmatrix} \begin{bmatrix} 0 \\ {}^{f3}V_{s2} \\ 0 \\ {}^{f3}V_{s4} \\ {}^{f3}V_{s5} \\ 0 \end{bmatrix} = \begin{bmatrix} 0 \\ {}^{f3}V_{s2} \\ 0 \\ 0 \\ {}^{f3}V_{s5} \\ 0 \end{bmatrix}, \quad {}^{f1}\mathbf{V}_{Fs} = \begin{bmatrix} 1&0&0&0&0&0 \\ 0&1&0&0&0&0 \\ 0&0&1&0&0&0 \\ 0&0&0&0&1&0 \\ 0&0&0&0&0&1 \end{bmatrix} \begin{bmatrix} 0 \\ {}^{f3}V_{s2} \\ 0 \\ 0 \\ {}^{f3}V_{s5} \\ 0 \end{bmatrix} = \begin{bmatrix} 0 \\ {}^{f3}V_{s2} \\ 0 \\ {}^{f3}V_{s5} \\ 0 \end{bmatrix}$$

Then it is possible to obtain the faulty vector ${}^{c}\mathbf{V}_{Fo}$ in which the only component different form zero is related to the 4-th phase.

$$\begin{aligned} {}^{c}\mathbf{V}_{Fo} &= \mathbf{F}_o \left[{}^{c}\mathbf{L}_s\, {}^{f1}\mathbf{T}_c\, {}^{f1}\mathbf{L}_s^{-1} \left(- {}^{f1}\mathbf{R}_s\, {}^{f1}\mathbf{I}_s - {}^{f1}\mathbf{E}_s + {}^{f1}\mathbf{V}_s + {}^{f1}\mathbf{V}_{Fs} \right) + {}^{c}\mathbf{R}_s\, {}^{f1}\mathbf{T}_c\, {}^{f1}\mathbf{I}_s + {}^{c}\mathbf{E}_s - {}^{c}\mathbf{V}_s \right] \\ &= \begin{bmatrix} 0 & 0 & 0 & {}^{f1}V_{s4} & 0 & 0 \end{bmatrix}^T \end{aligned}$$

where the new additional voltage ${}^{f1}V_{s4}$ given to the first broken phase has the following structure:

$$\begin{aligned} {}^{f1}V_{s4} = {} & L_{14}\dot{I}'_{s1} + L_{24}\dot{I}'_{s2} + L_{34}\dot{I}'_{s3} + L_{23}\dot{I}'_{s5} + L_{13}\dot{I}'_{s6} + .. \\ & .. + R_sI_{s1} + R_sI_{s2} + R_sI_{s3} + R_sI_{s5} + R_sI_{s6} + E_{s2} - E_{s5} - V_{s2} + V_{s5}, \end{aligned}$$

where also the phase currents I_{s2} and I_{s5} are considered. Note that the new components $\dot{I}'_{s1}$, $\dot{I}'_{s3}$ and $\dot{I}'_{s6}$ of vector ${}^{f1}\dot{\mathbf{I}}_s$ obtained from (5.39) are different from the previous one $\dot{I}_{s1}$, $\dot{I}_{s3}$ and $\dot{I}_{s4}$ of vector ${}^{f3}\dot{\mathbf{I}}_s$. Using the vectors ${}^{c}\mathbf{V}_{Fg}$ and ${}^{c}\mathbf{V}_{Fo}$ calculated above the vector ${}^{c}\mathbf{V}_{Fs}$ to be

added to system (5.22) is:

$$ {}^{c}\mathbf{V}_{Fs} = {}^{c}\mathbf{V}_{Fg} + {}^{c}\mathbf{V}_{Fo} = \begin{bmatrix} 0 \\ {}^{f_3}V_{s2} \\ 0 \\ 0 \\ {}^{f_3}V_{s5} \\ 0 \end{bmatrix} + \begin{bmatrix} 0 \\ 0 \\ 0 \\ {}^{f_1}V_{s4} \\ 0 \\ 0 \end{bmatrix} = \begin{bmatrix} 0 \\ {}^{f_3}V_{s2} \\ 0 \\ {}^{f_1}V_{s4} \\ {}^{f_3}V_{s5} \\ 0 \end{bmatrix} $$

In this way the condition $I_{s4} = 0$ during the fault transient and the steady-state condition $I_{s2} = I_{s4} = I_{s5} = 0$ are achieved.

Bibliography

[1] Levi E. , "Multiphase Electric Machines for Variable-Speed Applications" *IEEE Transactions on Industrial Electronics*, vol.55, no.5, pp.1893-1909, May 2008.

[2] Parsa L., "On advantages of multi-phase machines" *31st Annual Conference of IEEE Industrial Electronics Society*, IECON 2005.

[3] Barcaro M., Bianchi N., Magnussen F., "PM Motors for Hybrid Electric Vehicles" *The Open Fuels & Energy Science Journal*, 2009, pp 135-141.

[4] Mecrow, B.C.; Jack, A.G.; Haylock, J.A.; Coles, J.; , "Fault-tolerant permanent magnet machine drives", Electric Power Applications, IEE Proceedings -, vol.143, no.6, pp.437-442, Nov 1996

[5] Ertugrul, N.; Soong, W.; Dostal, G.; Saxon, D.; , "Fault tolerant motor drive system with redundancy for critical applications", Power Electronics Specialists Conference, 2002. pesc 02. 2002 IEEE 33rd Annual , vol.3, no., pp. 1457- 1462 vol.3, 2002

[6] Welchko, B.A.; Lipo, T.A.; Jahns, T.M.; Schulz, S.E.; , "Fault tolerant three-phase AC motor drive topologies: a comparison of features, cost, and limitations", IEEE Transactions on Power Electronics, vol.19, no.4, pp. 1108- 1116, July 2004

[7] Naidu, M.; Gopalakrishnan, S.; Nehl, T.; , "Fault Tolerant Permanent Magnet Motor Drive Topologies for Automotive X-By-Wire Systems," Industry Applications Society Annual Meeting, 2008. IAS '08. IEEE , vol., no., pp.1-8, 5-9 Oct. 2008

[8] Abolhassani, M.T.; Toliyat, H.A.; , "Fault tolerant permanent magnet motor drives for electric vehicles", Electric Machines and Drives Conference, 2009. IEMDC '09.

[9] Bianchi, N.; Bolognani, S.; Pre, M.D.; , "Strategies for the Fault-Tolerant Current Control of a Five-Phase Permanent-Magnet Motor", IEEE Transactions on Industry Applications, vol.43, no.4, pp.960-970, July-aug. 2007

[10] Dwari, S.; Parsa, L.; , "Fault-Tolerant Control of Five-Phase Permanent-Magnet Motors With Trapezoidal Back EMF", IEEE Transactions on Industrial Electronics, vol.58, no.2, pp.476-485, Feb. 2011

[11] Dwari, S.; Parsa, L.; , "An Optimal Control Technique for Multiphase PM Machines Under Open-Circuit Faults", IEEE Transactions on Industrial Electronics, vol.55, no.5, pp.1988-1995, May 2008

[12] Kestelyn, X.; Semail, E.; , "A Vectorial Approach for Generation of Optimal Current References for Multiphase Permanent-Magnet Synchronous Machines in Real Time", IEEE Transactions on Industrial Electronics, vol.58, no.11, pp.5057-5065, Nov. 2011

[13] Tani, A.; Mengoni, M.; Zarri, L.; Serra, G.; Casadei, D.; , "Control of Multiphase Induction Motors With an Odd Number of Phases Under Open-Circuit Phase Faults", IEEE Transactions on Power Electronics, vol.27, no.2, pp.565-577, Feb. 2012

[14] Locment, F.; Semail, E.; Kestelyn, X.; , "Vectorial Approach-Based Control of a Seven-Phase Axial Flux Machine Designed for Fault Operation", IEEE Transactions on Industrial Electronics, vol.55, no.10, pp.3682-3691, Oct. 2008

[15] Semail E. , Kestelyn X. , Bouscayrol A., "Right Harmonic Spectrum for the Back-Electromotive Force of a n-phase Synchronous Motor", *39th Annual Meeting of Industry Applications Conference*, IAS 2004, ISBN: 0-7803-8486-5.

[16] Parsa L. and Toliyat H.A. , "Five-Phase Permanent-Magnet Motor Drives", *IEEE Transactions on Industry Applications* , 2005, Vol. 41, No. 1, pp. 30-37.

[17] Levi, E.; Jones, M.; Vukosavic, S.N.; Toliyat, H.A.; , "Operating principles of a novel multiphase multimotor vector-controlled drive", Energy Conversion, IEEE Transactions on , vol.19, no.3, pp. 508- 517, Sept. 2004

[18] Levi, E.; Jones, M.; Vukosavic, S.N.; Toliyat, H.A.; , "A novel concept of a multiphase, multimotor vector controlled drive system supplied from a single voltage source inverter", Power Electronics, IEEE Transactions on , vol.19, no.2, pp. 320- 335, March 2004

[19] Hyung-Min Ryu, Ji-Woong Kim, Seung-Ki Sul, "Synchronous frame current control of multiphase synchronous motor - part I Modeling and Current Control Based on Multiple d-q Spaces Concept Under Balanced Condition", Conference Record of the 2004 IEEE Industry Applications Conference, 39th IAS Annual Meeting.

[20] R. Zanasi, "Power Oriented Modelling of Dynamical System for Simulation", *IMACS Symp. on Modelling and Control of Technological System*, MCTS'91, vol. 2, pp. 31-35, Lille, France, May 1991.

[21] R. Zanasi, "The Power-Oriented Graphs Technique: system modeling and basic properties", *Vehicular Power and Propulsion Conference*, Lille, France, September 2010.

[22] X. Kestelyn, F. Locment, Y. Crevits, E. Semail, "Easy-to-Implement Integral Numerical Simulation of Multi-phase Drives under Fault Supply Condition", IEMDC 07, IEEE International Conference Electric Machines & Drives, vol.2, no., pp.1131-1135, 3-5 May 2007

[23] Park R. H. (1929) "Two-reaction theory of synchronous machines", Trans. AIEE , vol. 48, pp. 716, 1929.

[24] Clarke E. (1950) "Circuit Analysis of AC Power System", New York: Wiley, 1950, vol.I.

[25] Fortescue C.L. , "Method of Symmetrical Coordinates Applied to the Solution of Polyphase Networks". *Trans. AIEE* , pt. II, vol. 37, pp.1027-1140, 1918.

[26] Kestelyn X., Semail E., Hautier JP. , "Vectorial Multi-machine Modeling for a Five-Phase Machine", in Proc. Int. Conf. Electrical Machines (ICEM), Bruges, Belgium, 2002, CD-ROM, Paper 394.

[27] White D.C. and Woodson H. H. , "Electromechanical Energy Conversion", *New York: Wiley*, 1959.

[28] Grandi G. , Serra G. , Tani A. , "General Analysis of Multi-Phase Systems Based on Space Vector Approach", *Power Electronics and Motion Control Conference* , EPE-PEMC 2006, pp.834-840, 2006.

[29] R. Zanasi, F. Grossi, M. Fei, "Complex Dynamic Models of Multi-phase Permanent Magnet Synchronous Motors", IFAC 2011, 18th IFAC World Congress, Milano, Italy, 28 Aug. - 2 Sept. 2011.

[30] R. Zanasi, F. Grossi, M. Fei, "Real and Complex Models of Multi-phase Permanent Magnet Synchronous Motors", Int. J. Power and Energy Conversion, Vol., No., **h**pp.

[31] R. Zanasi, F. Grossi, "Optimal Rotor Flux Shape for Multi-phase Permanent Magnet Synchronous Motors", *Proceedings of International Power Electronics and Motion Control Conference*, September 1-3 2008, Poznan, Poland.

[32] R. Zanasi, F. Grossi, "Multi-phase Synchronous Motors: POG Modeling and Optimal Shaping of the Rotor Flux", *Proceedings of ELECTRIMACS 2008*, Québec, Canada, June 2008.

[33] F. Grossi, "Dynamic Modeling and Control of Hybrid Automotive Systems", PhD Dissertation

[34] Paap G.C. , "Symmetrical Components in the Time Domain and Their Application to Power Network Calculations",*IEEE Transactions on Power Systems* , Volume 15, Issue 2, pp.522-528, 2000.

[35] Toliyat H.A. , Rahimian M.M. , Lipo T.A. , "dq Modeling of Five Phase Synchronous Reluctance Machines Including Third Harmonic of Air-Gap MMF", *Industry Applications Society Annual Meeting* , 1991., Conference Record of the 1991 IEEE pp. 231-237 vol.1.

[36] Figueroa J. , Cros J. and Viarouge P. , "Generalized Transformations for Polyphase Phase-Modulation Motors", *IEEE Transactions on Energy Conversion* , 2006, Vol. 21, No. 2, pp. 332-341.

[37] Shan X., Xuhui W., Zhao F., "Multiphase Permanent Magnet Motor Drive System Based on A Novel Multiphase SVPWM", *Proceedings of CES/IEEE 5th International Power Electronics and Motion Control Conference IPEMC*, 2006, vol.1, pp.1-5.

[38] Casadei D., Dujic D., Levi E., Serra G., Tani A., Zarri L., "General Modulation Strategy for Seven-Phase Inverters With Independent Control of Multiple Voltage Space Vectors", *IEEE Transactions on Industrial Electronics*, vol.55, no.2, pp.1921 - 1932, 2008.

[39] Aller J.M., Bueno A., Paga T., "Power System Analysis Using Space-Vector Transformation", *IEEE Transactions on Power Systems*, Vol. 17, No. 4, pp. 957-965, 2002.

[40] R. Zanasi, M. Fei, "Star and Delta Complex Dynamic Models of Multi-Phase Synchronous Motors", ELECTRIMACS 2011, Paris, France, 6-8 June 2011.

[41] F. Locment, E. Semail, X. Kestelyn, "Optimum use of DC bus by fitting the back-electromotive force of a 7-phase Permanent Magnet Synchronous machine", European Conference on Power Electronics and Applications, EPE 2005, Dresden, Germany, Sep. 2005.

[42] L. Parsa, N. Kim, H.A. Toliyat, "Field Weakening Operation of a High Torque Density Five Phase Permanent Magnet Motor Drive", IEEE Int. Conference on Electric Machines and Drives, 15 May 2005.

[43] R. Zanasi, M. Fei, "Saturated Vectorial Control of Multi-phase Synchronous Motors", NOLCOS 2010 - 8th IFAC Symposium on Nonlinear Control Systems, Bologna, Italy, 1-3 September 2010.

[44] M. Fei, R. Zanasi, "Multi-phase Vectorial Control of Synchronous Motors with Currents and Voltages Saturations", CDC-ECC 2011 - 50th IEEE Conference on Decision and Control and European Control Conference, Orlando, Florida, 12-15 December 2011

[45] M. Fei, R. Zanasi, "Control of a Five-phase Synchronous Motors with Third Harmonic Constrained Injection", ICCA 2011 - 9th IEEE International Conference on Control & Automation, Santiago, Chile, 19-21 December 2011

[46] Vas P. (1990) *Vector Control of AC Machines*, Oxford University Press, 1990.

[47] Leonhard W., *Control of Electrical Drives*, 3rd Edition 2001, Springer-Verlag Berlin Heidelberg NewYork, ISBN 3-540-41820-2.

[48] Y. Crevits, X. Kestelyn, E. Semail, "Investigation on vector control of three-phase synchronous machines under supply fault condition" Proceedings of SPEEDAM 2006, pp.439-444.

[49] McCrow, B.C.; Jack, A.G.; Atkinson, D.J.; Haylock, J.A.; , "Fault tolerant drives for safety critical applications", New Topologies for Permanent Magnet Machines (Digest No: 1997/090), IEE Colloquium on , vol., no., pp.5/1-5/7, 18 Jun 1997

[50] M. Fei, R. Zanasi, "Modeling of Multi Open Phase Fault Condition of Multi-phase Permanent Magnet Synchronous Motors", ACEMP 2011 and ELECTROMOTION 2011, Istanbul, Turkey, 08-10 September 2011

[51] M. Fei, R. Zanasi, F. Grossi, "Modeling of Multi-phase Permanent Magnet Synchronous Motors under Open-phase Fault Condition", ICCA 2011 - 9th IEEE International Conference on Control & Automation, Santiago, Chile, 19-21 December 2011

[52] F. Locment,E. Semail, X. Kestelyn, "Vectorial Approach-Based Control of a Seven-Phase Axial Flux Machine Designed for Fault Operation", IEEE Transaction on Idustrial Electronics, Vol. 55, No. 10, Octorber 2008.

[53] Cruz, S.M.A.; Cardoso, A.J.M.; , "Stator winding fault diagnosis in three-phase synchronous and asynchronous motors, by the extended Park's vector approach", Industry Applications, IEEE Transactions on , vol.37, no.5, pp.1227-1233, Sep/Oct 2001

[54] M. Fei, R. Zanasi, "Multi-phase Synchronous Motors: Minimum Dissipation Fault-Tolerant Control", SPEEDAM 2012, International Symposium on Power Electronics, Electrical Drives, Automation and Motion, Sorrento, Italy, 20-22 June 2012.

[55] M. Fei, R. Zanasi, "Multi-phase Synchronous Motors: Minimum Dissipation Fault-Tolerant Control with Currents Saturation", CDC 2012 - 51st IEEE Conference on Decision and Control, Maui, Hawaii, 10-13 December 2012

[56] Peuget, R.; Courtine, S.; Rognon, J.-P.; , "Fault detection and isolation on a PWM inverter by knowledge-based model", Industry Applications, IEEE Transactions on , vol.34, no.6, pp.1318-1326, Nov/Dec 1998

[57] Nandi, S.; Toliyat, H.A.; Xiaodong Li; , "Condition monitoring and fault diagnosis of electrical motors-a review", Energy Conversion, IEEE Transactions on , vol.20, no.4, pp. 719- 729, Dec. 2005

[58] Meinguet, F.; Semail, E.; Gyselinck, J.; , "An on-line method for stator fault detection in multi-phase PMSM drives", VPPC 2010, Lille, France, Sept. 2010.

[59] Gandhi, A.; Corrigan, T.; Parsa, L.; , "Recent Advances in Modeling and Online Detection of Stator Interturn Faults in Electrical Motors", IEEE Transactions on Industrial Electronics, vol.58, no.5, pp.1564-1575, May 2011

[60] K. Muta, M. Yamazaki, and J. Tokieda, "Development of New-Generation Hybrid System THS II - Drastic Improvement of Power Performance and Fuel Economy", SAE Technical Paper 2004-01-0064, 2004

[61] Mansour, C., Clodic, D., "Dynamic modeling of the electro-mechanical configuration of the Toyota Hybrid System series/parallel power train", International Journal of Automotive Technology, vol.13, pp.143-166, 2012

[62] F. Grossi, M. Fei, R. Zanasi, "Dynamic Modeling and Control of Power-Split HEV with Multi-phase Electric Machines under Fault Condition", ECC 2013 IEEE European Control Conference, Zurich, Switzerland, 17-19 July 2013 (submitted)

[63] C. C. Chan, "The State of the Art of Electric, Hybrid, and Fuel Cell Vehicles", Proceedings of the IEEE , vol.95, no.4, pp.704-718, April 2007

[64] J. R. Bumby et al., "Computer modeling of the automotive energy requirements for internal combustion engine and battery electric-powered vehicles", Proc. Inst. Elect. Eng., vol. 132, pt. A, no. 5, pp. 265–279, 1985.

[65] T. Markel, A. Brooker, T. Hendricks, V. Johnson, K. Kelly, B. Kramer, M. O'Keefe, S. Sprik, K. Wipke, "ADVISOR: a systems analysis tool for advanced vehicle modeling", Journal of Power Sources, Volume 110, Issue 2, Pages 255-266, August 2002

[66] A. Rousseau, P. Sharer, F. Besnier, "Feasibility of Reusable Vehicle Modeling: Application to Hybrid Vehicles", SAE 2004-01-1618, SAE World Congress, Detroit, March 2004

[67] S. Halbach, P. Sharer, P. Pagerit, C. Folkerts, A. Rousseau, "Model Architecture, Methods, and Interfaces for Efficient Math-Based Design and Simulation of Automotive Control Systems", SAE 2010-01-0241, SAE World Congress, Detroit, April 2010

[68] Miller, J.M., "Hybrid Electric Vehicle Propulsion System Architectures of the e-CVT Type", IEEE Transactions On Power Electronics, Vol. 21, No. 3, May 2006.

[69] J. Liu, H. Peng "Modeling and Control of a Power-Split Hybrid Vehicle", IEEE Transactions on Control System Technology, Vol. 16, no. 6, pp.1242-1251, November 2008

[70] K. Chen, W. Lhomme, A. Bouscayrol, A. Berthon "Comparison of two series-parallel Hybrid Electric Vehicles focusing on control structures and operation modes", Vehicular Power and Propulsion Conference VPPC 2009, Dearborn, Michigan, USA, 2009

[71] R. Zanasi, F. Grossi "The POG Technique for Modeling Planetary Gears and Hybrid Automotive Systems", in Proc. of Vehicular Power and Propulsion Conference VPPC 2009

[72] R. Zanasi, F. Grossi "Modelling Hybrid Automotive Systems with the POG Technique", Journal of Asian Electric Vehicles, Volume 8, Number 1, June 2010

[73] R. Willis, "Principles of Mechanism", second edition, Longmans, Green and Co., 1870

[74] F. Grossi, A. Palladino, G. Fiengo, and R. Zanasi, "The POG technique for modelling engine dynamics based on electrical analogy", American Control Conference, Saint Louis, Missouri, USA, 2009.

[75] F. Grossi, A. Palladino, R. Zanasi, and G. Fiengo, "Modelling of an internal combustion engine using power-oriented graphs and electrical analogy", Int. J. Modelling, Identification and Control, Vol. 16, No. 2, 2012

[76] R. Zanasi, F. Grossi "Modeling and control of Power-split hybrid electric vehicles", in Proc. of IEEE Vehicle Power and Propulsion Conference (VPPC) 2010, pp.1-6, 2010

[77] M. Fei, R. Zanasi, "Multi-phase Synchronous Motors: Minimum Dissipation Fault-Tolerant Control", Proc. of SPEEDAM 2012, International Symposium on Power Electronics, Electrical Drives, Automation and Motion, Sorrento, Italy, 2012

[78] C. C. Chan, A. Bouscayrol, and K. Chen, "Electric, Hybrid, and Fuel-Cell Vehicles: Architectures and Modeling", IEEE Transactions On Vehicular Technology, Vol.59, no.2, pp.589-598, February 2010

[79] D. W. Gao, C. Mi, A. Emadi, "Modeling and Simulation of Electric and Hybrid Vehicles", Proceedings of the IEEE , vol.95, no.4, pp.729-745, April 2007

[80] R. Zanasi, "Dynamics of a n-links Manipulator by Using Power-Oriented Graph", *SYROCO '94*, Capri, Italy, 1994.

[81] R. Morselli, R. Zanasi, "Modeling of Automotive Control Systems Using Power Oriented Graphs", *32nd Annual Conference of the IEEE Industrial Electronics Society, IECON 2006*, Parigi, 7-10 Novembre, 2006.

[82] D. C. Karnopp, D.L. Margolis, R. C. Rosemberg, "System dynamics - Modeling and Simulation of Mechatronic Systems", *Wiley Interscience*, ISBN 0-471-33301-8, 3rd ed. 2000.

[83] V. Duindam, A. Macchelli, S. Stramigioli, H. Bruyninckx "Modeling and Control of Complex Physical Systems", *Springer Berlin Heidelberg*, 2009.

[84] Paynter, H.M., "Analysis and Design of Engineering Systems", *MIT-press*, Camb., MA, 1961.

[85] X. Guillaud, P. Degobert, J. P. Hautier, "Modeling, control and causality: the Causal Ordering Graph", 16th IMACS World Congress, CD-ROM, Lausanne (Switzerland), August 2000.

[86] J. C. Mercieca, J. N. Verhille, A. Bouscayrol, "Energetic Macroscopic Representation of a subway traction system for a simulation model", *IEEE-ISIE'04*, Ajaccio (France), May 2004.

[87] A. Bouscayrol, B. Davat, B. de Fornel, B. Fran**c**cois, J. P. Hautier, F. Meibody-Tabar, M. Pietrzak-David, "Multimachine Multiconverter System: application for electromechanical drives", Eur. Physics Journal - Appl. Physics, vol. 10, no. 2, pp. 131-147, May 2000.

[88] R. Zanasi, F. Grossi, "Differences and common aspects of POG and EMR energy-based graphical techniques", Proc. of IEEE Vehicle Power and Propulsion Conference (VPPC), 2011

[89] Bouscayrol, A.; schoenfeld, R.; Dauphin-Tanguy, G.; Geitner, G.-H.; Guillaud, X.; Pennamen, A.; Hautier, J.P.; , "Different energetic descriptions for electromechanical systems", European Conference on Power Electronics and Applications, Dresden, Germani, Sept. 2005

[90] R. Zanasi, G. H. Geitner, A. Bouscayrol, W. Lhomme, "Different energetic techniques for modelling traction drives", ELECTRIMACS 2008, Québec, Canada, June 8-11 2008

[91] Zanasi, R.; Grossi, F.; , "Differences and common aspects of POG and EMR energy-based graphical techniques", VPPC 2011 - Vehicular Power and Propulsion Conference, Chicago, USA, 7-9 September, 2011.

[92] R. Zanasi, F. Grossi, "The POG Technique for Modeling Planetary Gears and Hybrid Automotive Systems", Vehicular Power and Propulsion Conference VPPC 2009, Dearborn, Michigan, USA 7-11 September 2009.

Acknowledgements

First and foremost, I want to express my gratitude to my advisor Prof. Roberto Zanasi for the valuable guidance. He is the advisor that every student would like to have and I will never be able to thank him enough for his support and help.
I would like to express my heartfelt thanks to Federica and Giovanni for these wonderful years in the Autolab.
I want to express my love and gratitude to my families for their understanding and encouragement when it was most required.
Last, but not least, I would like to thank my "wife" Chiara for her endless patience and love. Without her editing assistance I would not have finished this dissertation.